

DISS. ETH NO. 26786

MULTI-SCALE, IMAGE-BASED MODELLING  
AND OPTIMIZATION OF  
NEUROSTIMULATION BY EXTRINSIC  
ELECTRIC FIELDS AND FOCUSED  
ULTRASOUND

A dissertation submitted to attain the degree of

DOCTOR OF SCIENCES of ETH ZURICH  
(Dr. sc. ETH Zurich)

presented by

HAZael FABRIZIO MONTANARO OCHOA  
MSc UZH und ETH in Neural Systems and Computation

born on 06.11.1987  
citizen of Paraguay

accepted on the recommendation of

Prof. Dr. Qiuting Huang, examiner  
Prof. Dr. Niels Kuster, co-examiner  
Prof. Dr. Silvestro Micera, co-examiner

2020

Hazael Fabrizio Montanaro Ochoa: *Multi-scale, Image-Based Modelling and Optimization of Neurostimulation by Extrinsic Electric Fields and Focused Ultrasound*, © 2020

In loving memory of Camuel Montanaro and David Burt,  
*siempre conmigo*



## ABSTRACT

---

Stimulation of the central nervous system (CNS) via electromagnetic (EM) fields and acoustic pressure waves (mostly low intensity focused ultrasound – LIFUS) is used for treatment of a variety of medical disorders (e.g., stroke, movement disorders, pain, depression). Targeted stimulation is required to ensure efficacy and to avoid stimulation of non-targeted neural tissue. Computational tools and models are becoming increasingly important in this regard to inform treatment planning, the development and optimization of stimulation devices, treatment efficacy and safety assessment, and to provide an improved understanding for the underlying physical and physiological mechanisms. They offer a high degree of control, facilitate the exploration of large parameter spaces, and provide dense information, while avoiding ethical issues. Importantly, in particular for use in clinical treatments, computational modelling must be accurate and reliable, with known parameter and prediction uncertainties.

The aims of this thesis are: (i) to develop and validate a comprehensive biophysical modelling framework, based on the Sim4Life computational life sciences platform, for the reliable simulation and optimization of electric and ultrasonic neurostimulation, (ii) to apply this framework to advance innovative therapeutic approaches (in the domains of bioelectronic medicine and neuroprosthetics), and (iii) to support precision medicine through personalized, image-based modelling.

Based on a review of the current state-of-the-art in the domain of EM and FUS neurostimulation modelling, requirements and knowledge gaps were identified. To close these gaps, important extensions of Sim4Life were realized, including the implementation of a multi-GPU-accelerated solver for acoustic propagation and of support for medical image-derived tissue heterogeneous anisotropy in the EM and LIFUS simulations. This allowed to establish unprecedentedly realistic multi-scale modelling of physical exposure and induced electrophysiological responses.

Verification of the modelling framework with analytical and experimental benchmarks was complemented by experimental *ex* and *in vivo* validation in three application areas: (i) retinal prosthetics (joint work with the FDA), (ii) spinal-cord stimulation (SCS) for the treatment of paraplegics (as part of the RESTORE project), and (iii) transcranial ultrasound sonication (tcFUS; with the Hvidovre Hospital, Denmark).

(i) Retinal Prosthetics: In addition to providing the necessary confidence in the modelling framework, the retinal stimulation study also provided a) unique morphologically-detailed electrophysiological ganglion cell models, b) insights into three distinct ganglion cell stimulation mechanisms, and c) requirements for regulatory-grade neurostimulation modelling (including an uncertainty assessment).

(ii) SCS: As part of the RESTORE project, personalized EM-neural-modelling-based optimization was used to redesign the SCS implant and to allow for patient-tailored treatments (device placement and stimulation parameters), yielding vastly superior stimulation selectivity than achieved by clinical experts. Successful restoration of locomotion to paraplegics could be achieved.

(iii) tCFUS: Computational modelling is recognized as a promising solution to address the difficulty of focusing tCFUS across the highly heterogeneous structure of the skull, but reliable predictions have proven elusive. Careful computational and experimental studies on requirements and pitfalls of acoustic transducer and image-based skull modelling were therefore performed. The importance of properly characterizing and modelling the internal structure and physics of the transducer was demonstrated. Standing-wave effects in the skull were found to impact transcranial sonication efficiency to a larger extent than previously believed. The need to use computed tomography (CT)-based modelling to account for inter-subject variability was demonstrated. It was shown that not only the heterogeneity of the skull, but also its structure has an important impact, and that CT-based mapping requires imaging-parameter-dependent calibration, which prevents simple translation between clinical sites. All these investigations were experimentally validated (using explanted skulls and 3D-printed obstacles) and complemented by extensive sensitivity and uncertainty analyses.

In addition to these validation studies, simulation studies on deep brain stimulation (DBS) and SCS modelling were performed. The results not only provided mechanistic understanding, but also gave rise to a novel, activating-function-based multi-contact stimulation optimization approach that combines the benefits of physiological impact-driven optimization with those of rapid physics-based optimization. Using this approach, superior stimulation selectivity and targeting could be achieved.

The confluence of the developed multi-physics and physiological modelling across a wide range of spatial scales was further illustrated in an application example: transcranial LIFUS neuromodulation. A neural-mass model of cortical activity was extended with a model of LIFUS-induced,

membrane-cavitation-mediated modulation of excitatory pyramidal neurons and inhibitory interneurons, resulting in testable predictions of induced changes in the electroencephalogram (EEG).

Finally, the limitations of this work are discussed and new research directions are suggested.





## ZUSAMMENFASSUNG

---

Die Stimulation des Zentralnervensystems (ZNS) über elektromagnetische (EM) Felder und akustische Druckwellen (meist durch fokussierter Ultraschall mit geringer Intensität- LIFUS) wird zur Behandlung einer Vielzahl von medizinischen Störungen (z. B. Schlaganfall, Bewegungsstörungen, Schmerzen, und Depressionen) eingesetzt. Eine gezielte Stimulation ist erforderlich, um die Wirksamkeit sicherzustellen, sowie um die Stimulation von nicht-betroffenen Nervengewebe zu vermeiden. Rechnergestützte Modelle gewinnen in dieser Hinsicht zunehmend an Bedeutung; sei es zwecks der Behandlungsplanung, der Entwicklung und Optimierung von Stimulatoren, der Beurteilung der Wirksamkeit und Sicherheit der Behandlung, oder um ein besseres Verständnis für die zugrundeliegenden physikalischen und physiologischen Mechanismen zu erreichen. Sie bieten ein hohes Mass an Kontrolle, erleichtern die Erkundung grosser Parameterräume, liefern detaillierte Informationen und vermeiden dabei auch ethische Probleme. Insbesondere für die Verwendung in klinischen Behandlungen muss die rechnergestützte Modellierung exakt und zuverlässig sein, sowie bekannte Parameter- und Vorhersageunsicherheiten aufweisen.

Die Ziele dieser Dissertation sind: (i) Die Entwicklung und Validierung eines umfassenden, biophysikalischen Modellierungssystems (auf der Basis der Sim4Life-Plattform für rechnergestützte Biowissenschaften) zur zuverlässigen Simulation und Optimierung von elektrischer und ultraschallbasierter Neurostimulation; (ii) die Anwendung des entwickelten Systems auf innovative, therapeutische Ansätze (in den Bereichen bioelektronische Medizin und Neuroprothetik); und (iii) die Ermöglichung von Präzisionsmedizin durch personalisierte, bildgestützte Modellierung.

Basierend auf einer Überprüfung des aktuellen Standes der Technik im Bereich EM- und LIFUS-Neurostimulationsmodellierung wurden Anforderungen und Wissenslücken identifiziert. Um diese Lücken zu schliessen, wurden wichtige Erweiterungen von Sim4Life realisiert, einschliesslich der Implementierung eines multi-GPU-beschleunigten Löser für akustische Simulationen und der Unterstützung von heterogenen, anisotropen Gewebemodellen in EM- und LIFUS-Simulationen. Dies ermöglichte eine beispiellos realistische Multiskalenmodellierung der physikalischen Exposition und der induzierten elektrophysiologischen Reaktionen.

Die Verifizierung des Modellierungssystems mit analytischen und experimentellen Richtwerten wurde durch die experimentelle *ex* und *in vivo*-Validierung in drei Anwendungsbereichen ergänzt: (i) Retina-Prothetik (gemeinsame Arbeit mit der FDA); (ii) Rückenmarkstimulation (SCS) zur Behandlung von Querschnittslähmungen (im Rahmen des RESTORE-Projekts); und (iii) transkranielle Ultraschallstimulation (tcFUS; zusammen mit dem Hvidovre Hospital, Dänemark).

(i) Retina-Prothetik: Zusätzlich zum erforderlichen Vertrauen in das Modellierungssystem lieferte die Retina-Stimulationsstudie auch a) einzigartige, morphologisch detaillierte, elektrophysiologische Ganglienzellmodelle, b) Einblicke in drei verschiedene Ganglienzell-Stimulationsmechanismen, und c) die Identifikation von Anforderungen zur regulatorischen Neurostimulationsmodellierung (inklusive einer Unsicherheitsabschätzung).

(ii) SCS: Im Rahmen des RESTORE-Projekts wurde eine personalisierte EM-neuronale, Modellierungs-basierte Optimierung verwendet, um das SCS-Implantat neu zu gestalten und patientenspezifische Behandlungen (Stimulatorpositionierungen und -parameter) zu ermöglichen. Die dadurch erzielte Behandlungsqualität (Stimulationsselektivität) ist der von klinischen Experten und Expertinnen überlegen. Dadurch wurde Paraplegikern/-innen das Gehen erfolgreich wiederermöglicht.

(iii) tcFUS: Computermodellierung gilt als vielversprechender Lösungsansatz für die Schwierigkeit tcFUS durch die überaus heterogene Struktur des Schädels zu fokussieren. Zuverlässige Vorhersagen wurden bisher jedoch noch nicht erreicht. Aus diesem Grund wurden sorgfältige rechnerische und experimentelle Studien zu den Anforderungen und Fallstricken von akustischer Transducermodellierung und bildbasierten Schädelmodellen durchgeführt. Es wurde aufgezeigt wie wichtig es ist die interne Struktur und Physik des Transducers richtig zu charakterisieren und zu modellieren. Es wurde festgestellt, dass Stehwelleneffekte im Schädel die transkranielle Beschallungseffizienz in einem höheren Grad beeinflussen als bisher angenommen wurde. Des Weiteren wurde die Notwendigkeit demonstriert eine Computertomographie-basierte Modellierung zu verwenden, um die Variabilität zwischen Patienten/-innen zu berücksichtigen. Es wurde gezeigt, dass nicht nur die Heterogenität des Schädels, sondern auch dessen Struktur einen wichtigen Einfluss haben, und dass die Computertomographie-basierte Extraktion von Gewebeeigenschaftskarten eine bildgebungsparameterabhängige Kalibrierung erfordert, die eine einfache Übersetzung zwischen klinischen Standorten verhindert. All diese Untersuchungen wurden experimentell validiert (unter Verwendung explantierter Schädel und

3D-gedruckten Hindernissen) und durch umfangreiche Sensitivitäts- und Unsicherheitsanalysen ergänzt.

Zusätzlich zu diesen Validierungsstudien wurden Simulationsstudien zur tiefen Hirnstimulation (DBS) und zu SCS durchgeführt. Die Ergebnisse lieferten nicht nur ein mechanistisches Verständnis, sondern führten auch zu einem neuartigen und auf Aktivierungsfunktionen-basierenden Ansatz zur Optimierung einer multipolaren Stimulation. Dieser Ansatz kombinierte die Vorteile einer impactorientierten Physiologie-basierten Optimierung mit denen einer schnelleren Physik-basierten Optimierung kombiniert. Mit der Verwendung dieses Ansatzes konnten eine überlegene Stimulationsselektivität und -anvisierung erzielt werden.

Die Integration der entwickelten multi-physikalischen und -physiologischen Modellierverfahren über eine Vielzahl von räumlichen Grössenordnungen wurde an einem Anwendungsbeispiel weiter veranschaulicht, nämlich der ranskranielle LIFUS-Neuromodulation. Ein neurales Massmodell der kortikaler Aktivität wurde mit einem Modell der LIFUS-induzierten und durch einer Membrankavitation vermittelten Modulation von exzitatorischen pyramidalen Neuronen und inhibitorischen Interneuronen erweitert, was zu überprüfbareren Vorhersagen von induzierten Veränderungen im Elektroenzephalogramm (EEG) führte.

Abschliessend werden die Grenzen dieser Arbeit diskutiert und neue Forschungsrichtungen vorgeschlagen.



## ACKNOWLEDGEMENTS

---

This thesis work would not have been possible without the help, encouragement, and unconditional support from the following people:

*Esta tesis no hubiese sido posible sin la ayuda, aliento y apoyo incondicional de las siguientes personas:*

- **Niels Kuster**, who took a chance with me, welcomed me to the Z43 family, and stuck his neck out for me when I needed him most
- **Esra Neufeld**, a mentor, friend, role model; his incalculable contribution to this thesis and my development as a researcher and a person could never be understated; no permutation of words could fully capture my gratitude and indebtedness to him, instead I hope my friendship, respect, and admiration serves as a more suitable means of expression
- **Mi familia**, *por darme el amor, la fuerza, la confianza y la fe necesaria para finalizar este trabajo; este trabajo es reflejo de su esfuerzo y dedicación para conmigo*
- **Sabine Regel**, and her excellent (and always patient) proofreading work
- **Sae Paliwal**, for her edits throughout and a strong and beautiful friendship; for her unwavering (and questionable) belief in me, giving me a fighting chance at a Doctorate in Switzerland
- **Katie Zhuang**, for her help and edits in Chapter 2
- **Andreas Rowald** for help with Chapter 3; always a pleasure (and a pain) to hack our way through *Sim4Life*
- **Nives Radoja** and **Klára Kult** for their help and dedication in formatting Chapter 4
- **Giuliano Montanaro**, for learning new tools at a moment's notice to help prepare the figures in Chapter 5
- **Gabriela Michel**, for her help with formatting in Chapter 5

- **Cristina Pasquinelli** and **Axel Thielscher**, for the fruitful collaborations of Chapters 7 and 8
- **Joe Tharayil** and **Théo Lemaire**, for their talent and dedication, which made Chapter 9 possible
- **Rhiana Spring**, for making the german abstract intelligible (and more gender inclusive)
- **Antonino Cassarà**, for the friendship and fruitful discussions and collaborations leading to most of the neuro-related work in this thesis
- **Redi Poni** and **Cindy Karina**, without whom this work would not be completed in time; thank you for caring and for the friendship
- **Bryn Lloyd**, **Manuel Guidon**, **Stefan Benckler**, **Stefan Schild**, **Pedro Crespo**, **Nik Chavannes**, for their patience, willingness to help, and for always leaving the door open to me for questions and discussions; respect and admiration for this talented developer team
- **Frederico Teixeira** and **Philipp Wissmann**, for their encouragement, thoughtfulness, and advise throughout the Doctorate
- **Jacqueline Pieper** and **Yvonne Mader** for being there and standing behind me when I needed them most in all administrative matters
- **Saray Soldado**, with **Gabriela Michel**, sisters, for showing me the way forward and pushing me to be a better version of myself
- **Sergey Burnos**, for the unwavering support, inspiration, and beers
- **Daniel Neil**, for his friendship and silent leadership
- **Familia Sosa**, *por darme un lugar en su mesa, como uno más de la familia; por siempre cuidarme y alentarme*
- **Patricia y familia Vitale Lesme**, *por hacerme parte de su familia, por preocuparse y siempre creer en mí*
- **Christian Luraschi**, *un hermano, por siempre estar para darme la mano en momentos de necesidad*

To everybody listed here (and a few more), I owe more than a debt of gratitude, to be paid with the same token onto others.

## ACRONYMS

---

<b>BLS</b>	Bilayer sonophore	<b>HWHM</b>	Half width at half maximum
<b>CNS</b>	Central nervous system	<b>IPG</b>	Implantable pulse generator
<b>CSF</b>	Cerebrospinal fluid	<b>IS-SD</b>	Initial segment-somato dendritic
<b>CT</b>	Computed tomography	<b>LAPWE</b>	Linear acoustic pressure wave equation
<b>DBS</b>	Deep brain stimulation	<b>LFP</b>	Local field potential
<b>DCS</b>	Direct current stimulation	<b>LIFUS</b>	Low intensity focused ultrasound stimulation
<b>DTI</b>	Diffusion tensor imaging	<b>MIDA</b>	Multimodal imaging-based detailed anatomical computer model
<b>EEG</b>	Electroencephalogram	<b>MIP</b>	Maximum intensity projection
<b>EES</b>	Epidural electrical stimulation	<b>MMS</b>	Method of manufactured solutions
<b>EMG</b>	Electromyography	<b>MRI</b>	Magnetic resonance imaging
<b>EM</b>	Electromagnetic	<b>NIBS</b>	Non-invasive brain stimulation
<b>FDTD</b>	Finite difference time domain	<b>NICE</b>	Neuronal intramembrane cavitation excitation
<b>FEM</b>	Finite element methods	<b>NMM</b>	Neural mass model
<b>FS</b>	Fast spiking	<b>PET</b>	Positron emission tomography
<b>FUS</b>	Focused ultrasound		
<b>FWHM</b>	Full width at half maximum		
<b>HIFU</b>	High intensity focused ultrasound		
<b>HU</b>	Hounsfield Units		

<b>PML</b>	Perfectly matched layer	<b>tcFUS</b>	Transcranial focused ultrasound
<b>PNS</b>	Peripheral nervous system	<b>TMS</b>	Transcranial magnetic stimulation
<b>RS</b>	Regular spiking	<b>TUS</b>	Transcranial ultrasound stimulation
<b>SCS</b>	Spinal cord stimulation	<b>TVB</b>	The Virtual Brain
<b>SEFT</b>	Single-element focused transducer	<b>VB</b>	Veroblack
<b>SNR</b>	Signal-to-noise ratio	<b>VNS</b>	Vagus nerve stimulation
<b>SONIC</b>	Multi-scale optimized neuronal intramembrane cavitation	<b>WLE</b>	Westervelt–Lighthill equation



# CONTENTS

---

1	INTRODUCTION	1
1.1	Thesis motivation	2
1.2	Thesis structure	2
2	BACKGROUND	7
2.1	Neuromodulation applications	7
2.1.1	EM neuromodulation	7
2.1.2	Acoustic neuromodulation	22
2.2	Computational modelling	27
2.2.1	Why computational modelling?	27
2.2.2	EM simulations for neuromodulation	29
2.2.3	Finite Difference Time Domain method	30
2.2.4	Low frequency approximations	31
2.2.5	Electrophysiological neuromodulation	33
2.2.6	Applications	34
2.2.7	Acoustic exposure	37
2.2.8	Acoustic stimulation for neuromodulation	38
2.3	Needs, limitations, and thesis motivation	41
3	MODELLING FRAMEWORK	45
3.1	Sim4Life	45
3.1.1	Framework	45
3.1.2	Quasistatic EM modelling	45
3.1.3	Acoustic modelling	46
3.1.4	Neural modelling	46
3.1.5	Acoustic neuromodulation	46
3.2	Extensions	47
3.2.1	Anisotropy verification	48
3.3	Spinal cord stimulation to restore locomotion	55
3.3.1	Background	55
3.3.2	Method	55
3.3.3	Results	62
3.4	Conclusions	63
4	ALPHA RGC MODEL OF EXTRACELLULAR STIMULATION	65
4.1	Introduction	66
4.2	Methods	67
4.2.1	Preparation	67

4.2.2	Recordings	68
4.2.3	Extracellular stimulation	68
4.2.4	Immunohistochemistry	69
4.2.5	Morphological reconstruction	70
4.2.6	NEURON ganglion cell model	70
4.2.7	Sensitivity analysis	72
4.3	Results	73
4.3.1	Measurement results	73
4.3.2	Estimating ion channel distribution	75
4.3.3	Spike adaptation in alpha cells	78
4.3.4	Extracellular electrode stimulation	80
4.3.5	Simulation results	83
4.3.6	Sensitivity and uncertainty analysis	83
4.4	Discussion	85
4.5	Conclusions	90
4.A	Appendix	92
4.A.1	Results tables	92
4.A.2	NaV1.6 channel model	95
4.A.3	Calcium clearance mechanism	96
5	NEUROSTIMULATION OPTIMIZATION	97
5.1	Introduction	97
5.2	Methods	98
5.2.1	EM-electrophysiological modelling	98
5.2.2	Activation functions and optimization	99
5.2.3	Generic neurostimulation model	101
5.2.4	DBS model	101
5.2.5	SCS model	106
5.3	Results	110
5.3.1	Verification	110
5.3.2	Activation function and stimulation location	110
5.3.3	Activation region	114
5.3.4	Activating function threshold	114
5.3.5	SCS selectivity	114
5.3.6	Anisotropy	120
5.4	Discussion	123
5.4.1	Activation function as predictor	123
5.4.2	Targeting optimization	123
5.4.3	Performance	124
5.4.4	Anisotropy	125

5.4.5	Generalization	126
5.5	Conclusions	128
5.A	Appendix	130
6	ACOUSTIC MODELLING OF TCFUS	137
6.1	Motivation	137
7	TRANSDUCER MODELLING FOR TCFUS SIMULATIONS	139
7.1	Introduction	140
7.2	Methods	142
7.2.1	Bone samples and phantoms	142
7.2.2	US transducer and water tank measurements	142
7.2.3	Actual measurements with objects	146
7.2.4	Calculation intensity from measurements	146
7.2.5	CT imaging of the objects	146
7.2.6	Simulation framework	148
7.2.7	Transducer modelling	151
7.2.8	Metrics	152
7.2.9	Backpropagation	157
7.2.10	Human head models	157
7.3	Results	158
7.3.1	Acoustic beam in a pure water background	158
7.3.2	Transmission through the VB plate	160
7.3.3	Transmission through the VB 3D-printed skulls	160
7.3.4	Transmission through the bone skull samples	161
7.3.5	Other parameters	161
7.3.6	Backpropagation	163
7.3.7	Human head models	165
7.3.8	Impact of non-linearity	165
7.4	Discussion	165
7.5	Conclusions	171
7.A	Appendix	173
7.A.1	Results tables and figures	173
8	CT IMAGE PARAMETERS AND SKULL TCFUS MODELLING	183
8.1	Introduction	184
8.2	Methods	187
8.2.1	Bone sample	187
8.2.2	Measurements	187
8.2.3	Simulation framework	188
8.2.4	Varied parameters	189
8.2.5	Agreement metrics	196

8.3	Results	201
8.3.1	CT parameters	201
8.3.2	Skull properties and mappings from CT	203
8.3.3	Positioning	207
8.4	Discussion	212
8.5	Conclusions	217
8.A	Appendix	219
8.A.1	Adjustment of CT noise levels	219
8.A.2	Results figures	221
9	COUPLED US-ELECTROPHYSIOLOGY-EEG MODELLING	227
9.1	Background	227
9.2	Method	227
9.2.1	Multi-scale model	227
9.2.2	Anatomical head model	228
9.2.3	Acousto-neural interaction model	228
9.2.4	Cortical oscillation model	231
9.2.5	Acoustic propagation model	238
9.2.6	Coupling	240
9.2.7	EEG computation	241
9.3	Results and discussion	242
9.3.1	Limitations	245
9.4	Conclusions	246
9.A	Appendix	248
9.A.1	Tables and figures	248
10	CONCLUSIONS	249
10.1	Achievements	249
10.2	Next steps and future research	253
	BIBLIOGRAPHY	255

## INTRODUCTION

---

Stimulation of the central nervous system (CNS) via electromagnetic (EM) fields and acoustic pressure waves is used for treatment of a variety of medical disorders such as stroke rehabilitation [1], pain palliation [2], depression [3], and tremors [4]). Typically, targeted stimulation is required to improve treatment efficacy and avoid unintended stimulation of other neural tissue. Computational tools and models are becoming increasingly important in this regard to inform treatment planning, the development and optimization of stimulator devices, treatment efficacy and safety assessment, and to provide an improved understanding for the underlying physical and physiological mechanisms. Consequently, these computational methods need to be accurate and reliable with known parameter and outcome uncertainty, in particular for use in clinical treatments.

Brain stimulation can be achieved via external electric ( $E$ -) or magnetic ( $H$ -) fields that typically stimulate large volumes, primarily in the cortex [5]. More localized or deep CNS stimulation is attained via implanted electrodes, such as deep brain stimulation (DBS) devices targeting the subthalamic nucleus for Parkinson's disease therapy [6], and spinal cord stimulators [7] targeting specific dermatomal zones for pain relief. Spinal cord stimulation (SCS) is typically achieved by delivering currents through an implanted multi-electrode array in the dorsal epidural space. To date, optimization of stimulation parameters and placement of the stimulator device for an individual patient (for treatment safety and efficacy) is very time-consuming and frequently produces sub-optimal results. Computational models are the tool of choice for a more systematic and optimal personalization approach.

SCS is an essential and established therapeutic approach for chronic pain treatment [7]. More recently, the use of SCS (or more specifically, spinal root stimulation) to restore locomotion in paraplegics, has been demonstrated [8, 9] – an example of neuroprosthetic medicine. Another neuroprosthetic application that has reached regulatory submission level is retinal prosthetics, where the U.S. Food and Drug Administration (FDA) required guidance on how regulatory grade computational EM and electrophysiology modelling for safety and efficacy assessment could be performed and to gain mechanistic understanding (Chapter 4).

Focused ultrasound (FUS) is a promising alternative to electric and magnetic stimulation of the CNS or PNS where ultrasonic energy is non-invasively deposited at a millimeter sized focal volume deep inside the body. Low intensity focused ultrasound (LIFU / LIFUS) has been shown to stimulate neurons [10] and modulate neural activity inside the brain [11, 12]. Multi-element phased array transducers have been used to achieve highly focused, non-invasive energy delivery deep in the brain, e.g., for functional neurosurgery [13], and could potentially be applied for targeted neurostimulation or brain mapping. Computational models are essential for predicting and compensating the pressure-wave distorting effects of the complex, heterogeneous skull structure. This is currently the biggest obstacle to achieving reliable and efficient targeting and presents an unsolved modelling challenge [14].

Multi-scale, multi-physics computational modelling frameworks for life sciences applications in the complex environment of the human body – such as the *Sim4Life* simulation platform (co-developed by our lab and ZMT Zurich MedTech AG [15]) – are perfectly suited to model and improve neurostimulation scenarios in clinical settings. *Sim4Life* offers an advanced, full-wave 3D linear and non-linear pressure wave solver optimized for FUS applications. It also provides functionality for personalized image-based anatomical model generation and EM modelling, which can be coupled with neuronal electrophysiology modelling.

## 1.1 THESIS MOTIVATION

*The aim of this thesis is to develop, validate, and apply a new multi-scale modelling framework that can use personalized imaging data for the optimized electric and ultrasonic stimulation of neurons. The work performed in this thesis addresses various of the currently existing challenges in highly relevant therapeutic areas, ranging from neuroprosthetics to DBS, SCS, and the application of LIFUS for brain neuromodulation.*

## 1.2 THESIS STRUCTURE

This thesis is structured into the following chapters:

**CHAPTER 2** An overview of therapeutic neuromodulation applications is provided and the need for computational modelling is discussed. Subsequently, a critical review of the current state-of-the-art in EM, acoustic, and

electrophysiology modelling in the context of therapeutic neuromodulation is provided. Important requirements, limitations, and knowledge-gaps are identified which motivated parts of the work performed in this thesis.

CHAPTER 3 The *Sim4Life* computational life sciences platform is introduced that was used for all computational modelling work in this thesis. The necessary extensions, based on the needs identified in Chapter 2, are discussed, along with the associated verification work. The most important extensions are the addition of support for heterogeneous material properties (as required for proper acoustic modelling of skull heterogeneity) and anisotropic material properties (important because of the high anisotropy of white matter and nerves), which were verified using analytical benchmarks and the method of manufactured solutions. The application of the extended *Sim4Life* platform is illustrated through the SCS treatment planning and optimization activities performed as part of the RESTORE project to achieve restoration of locomotion to paraplegics.

CHAPTER 4 The coupled EM-electrophysiological modelling is successfully validated in a controlled retinal stimulation experimental setup. In addition to providing the necessary confidence in the modelling framework, this study also provides mechanistic insights into epiretinal ganglion cell stimulation. The work, performed jointly with the U.S. Food and Drug Administration (FDA), addresses the current lack of suitable approaches to perform safety and efficacy assessment for the regulatory approval of an FDA-submitted retinal prosthetic device. A unique aspect of that work is that the biophysical properties of the model, as well as the cells' morphologies, were obtained from the very same cells that were also used to obtain electrophysiological validation measurements. Extensive uncertainty quantification work complements the validation and is used to determine an objective validation criterion.

CHAPTER 5 A highly detailed, image-based neuro-functionalized head model for investigating DBS has been created. Inspired by the success of activation-function-based considerations [16] in explaining features of the observed behavior (IC fiber stimulation thresholds and locations), a novel (pre-)optimization approach is established that provides acceleration by more than three orders of magnitude. A coupled EM-electrophysiological model of SCS is constructed, based on [7], and used to assess and optimize SCS selectivity for pain treatment. The activation-function optimization ap-

proach proves highly computationally efficient in determining multi-contact electrode steering parameters with superior stimulation selectivity. However, due to the impact of activating function narrowness on the stimulation threshold, coupled EM-electrophysiological modelling is still required to reliably predict stimulation and to refine the stimulation parameters. The activation-function concept is also helpful to understand the unexpectedly strong impact of neural tissue anisotropy on the penetration depth of e.g., epidural stimulation.

**CHAPTER 6** Provides a brief introduction and motivation for Chapters 7 and 8, which deal with the modelling of transcranial FUS (tcFUS) stimulation. Due to the difficulty of tightly focusing FUS across the highly heterogeneous skull (scattering, aberration), computational-modelling-based compensation has long been sought [17]. However, the reliable prediction and optimization of transcranial transmission, focus location, and focality has proven elusive. Therefore, careful computational and experimental studies on requirements and pitfalls of acoustic transducer and image-based skull modelling have been performed.

**CHAPTER 7** The importance of properly characterizing and modelling the internal structure and physics of the transducer is demonstrated through sensitivity analysis and comparison of experimental and simulation data on trans-obstacle sonication involving skull samples and 3D-printed obstacles, and using powerful comparison metrics previously introduced by our lab. Results show that some compromises on modelling detail can be acceptable when coupled with experimentally derived corrections, and that standing-wave effects in the skull play a more important role than previously believed, explaining some of the sensitivity in accurately predicting transcranial sonication efficiency.

**CHAPTER 8** The need to use computed tomography (CT) image-based modelling to account for inter-subject variability and personalize treatments is demonstrated and a detailed sensitivity analysis on imaging, application, and modelling parameters is performed. It is shown that not only the heterogeneity of the skull, but particularly its structure has an important impact of transcranial sonication, and that CT-based mapping requires imaging-parameter-dependent calibration (accounting for noise level, tube voltage, filter sharpness, etc.), which prevents simple translation between different clinical sites. Furthermore, the need for accurate applicator po-



sitioning and reproduction of that placement in the treatment planning model is evidenced.

CHAPTER 9 The confluence of the multi-physics simulation, physiological modelling, and scales discussed in previous chapters is illustrated for the example application of tcFUS-based neuromodulation. A neural-mass model of cortical activity is extended with terms accounting for the duty-cycle-dependent specific response to LIFUS of regular (pyramidal) spiking neurons and inhibitory interneurons, and testable predictions about the impact on the electroencephalogram (EEG) are made. The results of this initial study demonstrate the potential for future research and applications in this area.

CHAPTER 10 The final chapter of this thesis summarizes the achievements of the presented work, discusses its limitations, and suggests a number of new research directions.



## BACKGROUND

---

### 2.1 NEUROMODULATION APPLICATIONS

Electromagnetic and acoustic neuromodulation are applied in a wide range of therapeutic applications. The following section aims to provide both a basic overview of these applications, as a motivation for this thesis, and an understanding of the role and need for computational modelling in this research area. Background information on electromagnetism, acoustics, and their interaction with biological tissues, more specifically the nervous system, are provided alongside a discussion of different neuromodulation applications. We will also present a summary of existing computational models, along with some of their limitations.

#### 2.1.1 *EM neuromodulation*

*EM neuromodulation* refers to the use of electric or magnetic fields to inhibit, excite, synchronize, regulate, or otherwise affect the dynamics of the nervous system. It has been shown to directly impact neurological and neuropsychiatric conditions, in ways that can be therapeutically valuable, particularly when pharmacological approaches are unsuitable, in that they do not yet exist, are not sufficiently targeted or effective, or cause too many undesired side-effects. EM neuromodulation has been successfully applied in conditions such as Parkinson's disease [18, 19], essential tremors [20, 21], chronic pain [22], epilepsy [23], motor rehabilitation [24], medication resistant depression [25], addiction [26], and anorexia [27]. It is also a treatment approach to reverse sensory deficiencies, such as neural deafness [28] or blindness [29], or to restore a sense of touch, e.g., in neuroprosthetic applications involving robotic limbs [30].

*EM fields* are induced in biological tissues through exposure to electric or magnetic field sources outside or inside the body. Magnetic fields are generated by creating a time varying current (frequently in coiled wire) which induces electric fields and currents in the biological tissue. Electric exposure typically involves electrodes in direct contact with or close prox-

imity of the body. In EM neuromodulation applications, the human body primarily acts as a heterogeneous resistive medium.

The human body is composed of *tissues with varying dielectric properties*, namely permittivity and resistivity. The permittivity of the tissue is related to the ability of a material to polarize (atomic alignment of its constituent charges), thus affecting the internal field. The resistivity governs the flow of electric charges (ionic currents). While isotropic conductivity always results in currents that are aligned with the field orientation, anisotropic materials have an electric-field-orientation dependent conductivity, and produce currents that are not necessarily aligned with the field. Due to their spatially organized, fibrous structure, this is particularly relevant for white matter and nerve fibers [31–35].

The *nervous system* consists of the central nervous system (CNS) and the peripheral nervous system (PNS). The CNS comprises the brain and spinal cord, from which the roots and nerves of the PNS branch off. Nerves contain bundles of nerve fibers which are embedded in the epineurium and can be organized in fascicles surrounded by a semi-insulating membrane called the perineurium.

*Neurons* are electrically excitable cells that make up the nervous system and transmit information (see Figure 2.1). They process and transmit electrochemical signals and can be divided into the following components. The *soma* is the cell body which houses the nucleus. The *dendritic tree* is an extension of the soma that collects and processes synaptic input signals from connected cells. The non-linear, active nature of neural membranes can give rise to all-or-nothing electrical signals called *action potentials*. These action potentials then propagate, e.g., along a long projection of the cell called the *axon*. Axons are sometimes covered by a protective and insulative layer called the *myelin sheath*, which also serves to accelerate signal conduction. Axon can connect to other neural cells, e.g., synaptically, or can activate a motor response.

The cell membrane features ion channels that actively or passively mediate the in- and outflow of particular ions – mainly sodium  $\text{Na}^+$  and potassium  $\text{K}^+$ ). The magnitude of these ionic current typically depends on the transmembrane voltage. Given a large enough potential difference, the sodium ion channels open and let in enough ions to change the local cellular charge concentration which then activates the adjacent ion channels (sensitive to the same or different ions). This complex voltage interaction with ion channels along the axon ensures that the *action potential* gets propagated down the long axon without signal degradation, as the signal is constantly

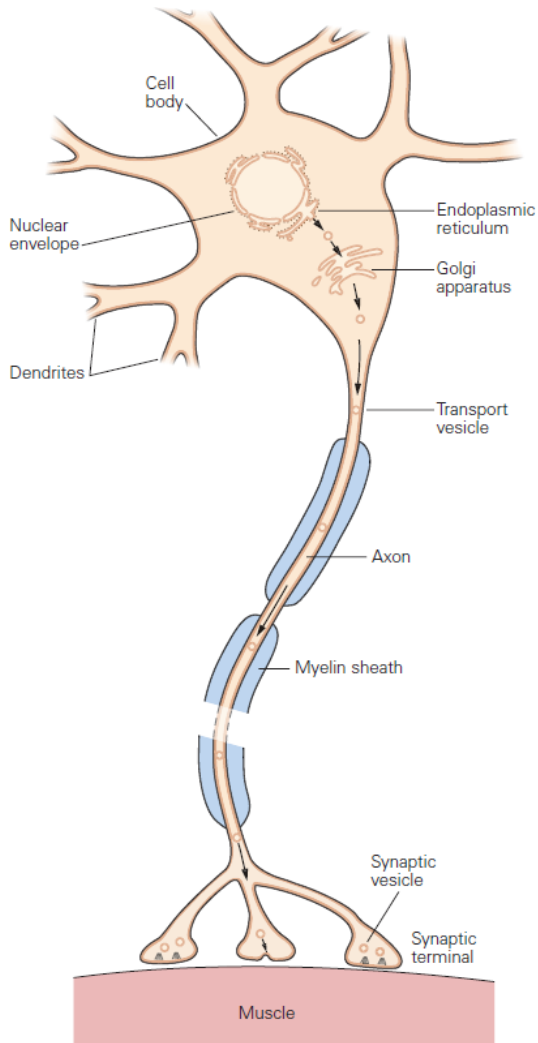


FIGURE 2.1: Schematic representation of a neuron structure. (Figure adapted from [36])

bolstered along the way. Action potentials are frequently followed by a *refractory* period during which the cell is silent and does not fire again.

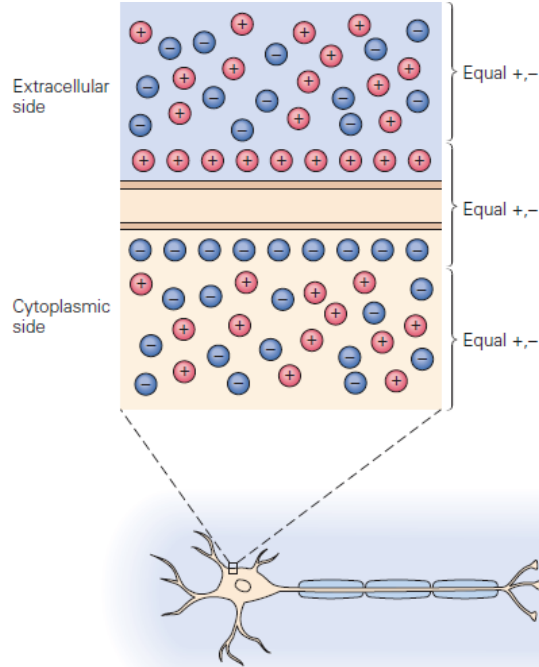


FIGURE 2.2: Illustration of ionic imbalances and the resulting transmembrane voltage. (Figure adapted from [36])

Neural *fibers* in fascicles are axons that can be divided into different subtypes based on their function, morphology, and speed of conduction. Neurons in the spinal cord can be broadly divided in three main classes: sensory / afferent, motor / efferent, and interneurons. Sensory neurons are afferent, in that they receive stimuli from the environment or internal organs. These neurons can be further classified into A, B, and C fibers based on the morphology on their axons, taking into account their conduction speed, diameter and myelination. Motor neurons are responsible for eliciting muscle activity. Interneurons can form networks and connect afferent and efferent fibers. Neurons in the brain are much more diverse and specialized.

Neurons in a rest state have a transmembrane voltage around  $-70$  mV that needs to rise in order for an action potential to be generated. The terms

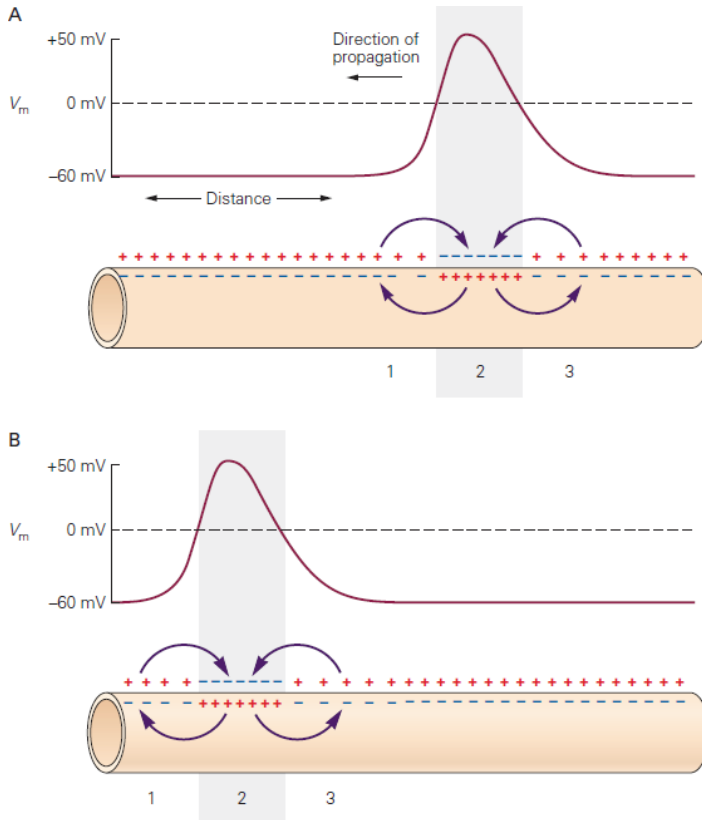


FIGURE 2.3: Schematic illustration of action potential propagation. (Figure adapted from [36])

hyper- and depolarization refer to a change of the transmembrane potential. Hyperpolarization is associated with lowering the neuron's excitability, and depolarization with increasing the neuron excitability. Even though action potentials typically start from the initial segment of the axon, ion channels along the axon can be driven to start the complex interaction leading to action potential propagation, e.g., by EM exposure. The *activating function* is a useful predictor for the initiation of an action potential along an axon [16]. It is related to the derivative of the tangential electric field along an axon trajectory (see Chapter 5). Electric fields can also induce activity at dendritic or axonal endings, or modulate activity in the subthreshold regime. The EM-modulated neural response depends on cell type, morphology, orientation, ion channel dynamics, tissue inhomogeneity, and synaptic connections [37].

The *brain* features large and complex networks of neurons that are frequently described on the level of neuron populations that are arranged in networks represented by connectivity maps. Electroencephalograms (EEG) and local field potential (LFP) recordings measure averaged activities of neuron populations at different scales and distances. Such measurements provide information about network activity at different frequencies, brain states, network coherence, etc. Models of neural networks, such as neural mass and mean field theory approaches, model these populations as recurrent feedback and feedforward nodes of excitation and inhibitions affecting population firing rates. Connectivity maps, known as the connectome, are attained through either the staining of neurons with special dyes or light-sensitive enzymes that reveal connections, or through the use of imaging modalities that track the diffusion of molecules, such as Diffusion Tensor Imaging (DTI). Attempts at creating detailed maps of the brain and its connectivity exist in the form of the Blue Brain Project [38], the Virtual Brain project [39], and the Connectome Project [40].

#### 2.1.1.1 *Modalities and applications*

*EM neuromodulation* is applied using different techniques and modalities. Typically, either direct or alternating currents are applied by adding a pair or array of electrodes either on the scalp, for noninvasive stimulation, or invasively using implanted electrodes (epidurally, subdurally, transcortically, or deep inside the brain or spinal cord). Implanted electrodes typically target nearby areas which are specifically chosen based on the neurological conditions that needs treatment.



### 2.1.1.2 *Direct current stimulation*

Direct current stimulation (DCS) and transcranial direct current stimulation (tDCS) have been successfully used for a variety of neurological and psychiatric conditions such as Parkinson's disease, essential tremor, chronic pain, epilepsy, and medication resistant depression. In these cases, anode and cathode surface electrodes are placed over the scalp. The anode electrode is placed over the regions of the head that needs depolarization (excitation) and the cathode over the regions that need to be hyperpolarized (inhibited or to create a strong enough gradient such that excitation can occur away from the cathode) [41]. The two surface electrodes (or more than two, in the case of high definition (HD-)DCS where one anode is used with four cathode electrodes) inject a low amplitude subthreshold current (typically, 0.5–2 mA) which changes the cortical excitability and the resulting spontaneous firing patterns [42, 43]. Electrode placement and voltages are set according to different anodal, cathodal, or bihemispheric stimulation protocols. Effects outlast the duration of the stimulation: there is an assortment of short and long term local and regional effects. The applied electrodes are relatively large, so focality is not possible and brain networks are targeted instead. Due to the rapid field strength drop with distance, transcranial direct current stimulation (tDCS) is generally restricted to stimulating the cortex. Given the susceptibility of neurons to field gradients and orientations, the excitability of the different cells depend heavily on electrode placement [44]. Experimental work has shown that response rates to these kinds of treatments may be around 50 % [45, 46]. Invasive forms of DCS (epidurally, subdurally, or intracortically) have also been applied.

Since the target of DCS is the cortex, epidural stimulation necessarily needs the injected current to flow through the dura, a membrane surrounding the brain, and the highly conductive cerebro-spinal fluid (CSF), acting as a shunt, before reaching the intended area of stimulation. Computational modelling work has shown that the resulting exposure is attenuated by roughly a factor of two [47–49] and spread-out. This highlights the importance of computational modelling to inform treatment parameters / setups and improve the success of target stimulation. These treatments need to be tailored or at least be partly informed by the patient's anatomy, as patient physiology can vary wildly, especially in the case of neurological diseases (shown, for example, in patients with cortex atrophy [24]). More specific and targeted treatments can be achieved with more invasive methods, such as intracortical stimulation with implanted electrodes, but these carry additional risks (e.g., infection, CSF leak, seizures [50], and foreign body

response which also affects impedance [51, 52]) and can be sensitive to small positioning inaccuracies [53].

While precise mechanistic understanding of DCS is elusive, a number of experimental and computational works have explored its impact on recruited neuron types and activation sites (i.e., synaptic modulation of interneurons), and the relation between baseline neurotransmitter and metabolite concentrations on cortical response [54–56].

### 2.1.1.3 *Deep brain stimulation*

An important area of EM stimulation application is Deep Brain Stimulation. This technique has important applications in psychiatry [57], movement disorders [58], and chronic pain [59] with proven effectiveness and benefits when compared to lesional surgery alternatives [21]. An electrode is implanted deep inside the brain near regions such as the subthalamic nucleus (STN) or the ventral intermediate nucleus (VIM) of a patient to modulate nearby brain networks involved in the neurological diseases (local cells, afferent inputs) or tangentially related to them (fibers of passage) [60]. These cells have similar thresholds for activation [61].

Stimulation depends on many parameters, such as frequency, amplitude, pulse width, and shape. Computational models can be helpful in optimizing these parameters. Electrodes typically have a quadripolar design to tune focality and polarity of stimulation and a battery powered implantable pulse generator (IPG) elsewhere in the body to deliver the electrical stimulation [62]. Typical operation of the device for treatment of Parkinson’s disease creates repeated bipolar stimulation at 130 Hz with 0.1 ms pulses with anode and cathode electrodes at 3 and  $-3$  V respectively (a reference 0 V is set at the IPG). To ensure safety and efficacy of treatments, clinicians typically come up with metrics and heuristics to guide treatment for different patients. Total charge injection is used as one measure for safety, and is affected by the electrode type, the anatomy, dielectric properties and electrode contact. Because of this, aspects such as electrode-tissue interface impedance, and tissue and field heterogeneity and anisotropy must be considered. Accurate quantification of charge injection relies on computational models. There is still uncertainty over the most effective targets for particular treatments; multiple possible targets have been identified and approximated with the use of brain atlases which are then superimposed on the patient’s anatomy attained from imaging modalities [19, 20, 63–67]. Computational models of DBS neuromodulation have been useful in eluci-

dating the neural targets and to predict the volume of tissue activated [37, 68, 69].

#### 2.1.1.4 *Spinal cord stimulation*

Another relevant and promising area of application is spinal cord stimulation (SCS), in particular, for the treatment of chronic neuropathic and ischemic pain, and for rehabilitation and locomotion restoration for patients with spinal cord injuries. The anatomy of the spinal cord can be seen in Figure 2.4. It is composed of white and gray matter that transmit neural signals to and from the brain, encode reflexes and motion patterns, and implement relatively simple circuits. The butterfly shape that can be seen on cross-sectional images consists of grey matter and the rest is white matter (rich in spatially organized axons). Typical targets for pain treatment are specific dermatomal zones in the dorsal column (see Figure 2.5). These are populated with different fibers associated with different somatosensory sensations. The spinal cord is divided into segments and roots which branch off from the spinal cord and form the different branches of the peripheral nervous system.

Initial theories of spinal cord stimulation (SCS) come from the *gate control theory* [70] which proposes that pain sensation modulation relates to the recruitment of specific fibers with differing diameters. Recruitment of large diameter sensory fibers (A-beta afferents), which induce a (non-painful) prickling sensation known as paresthesia, can override feelings of pain by inhibiting nociceptive small diameter fibers. While this initial theory has since been substantially expanded and revised to account for different neuromodulation effects, it has served as the basis of epidural and transcutaneous stimulation of the dorsal column for neuropathic pain therapy. Feelings of paresthesia associated with stimulation of different subregions of the dorsal column have served for topographical mapping for pain relief and sensation.

Initial work in SCS was guided mostly by empirical observations of effective and ineffective stimulation areas and pulse waveforms. Suitable computational models enable more systematic and extensive studies. Pulse waveforms (repetition frequencies: 40–100 Hz) based on empirical knowledge and computational models are employed to achieve appropriate target specificity and selectivity. Targets are axons in the dorsal column, and activation of axons in the dorsal roots are avoided [71]. Stimulation is typically done epidurally; however, transcutaneous spinal cord stimulation is also being investigated as a non-invasive alternative. Treatments are not always

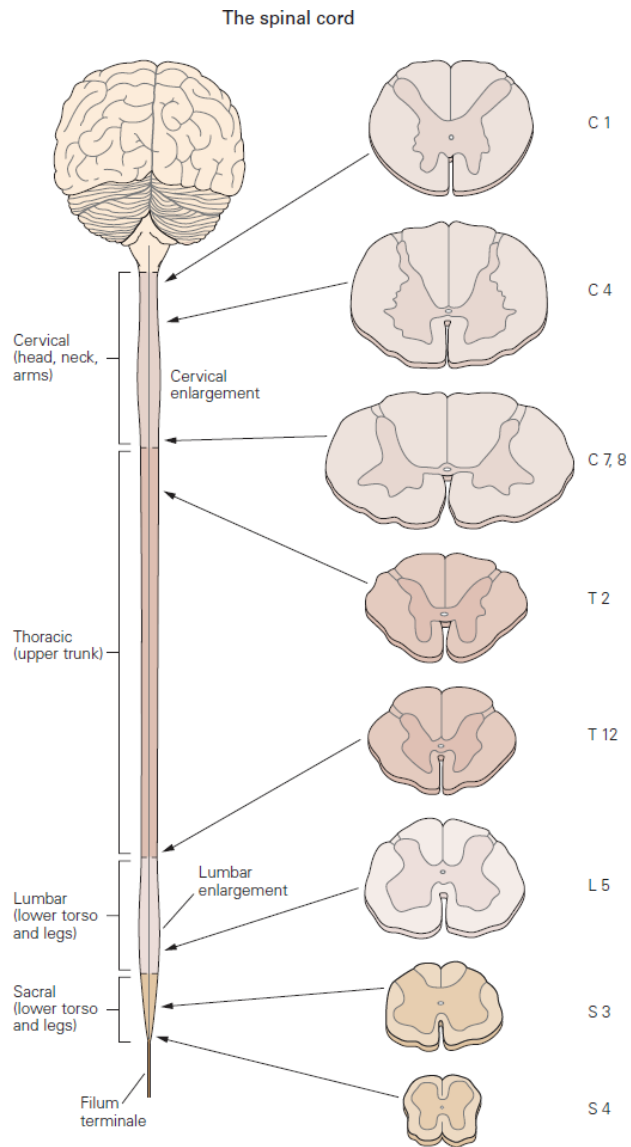


FIGURE 2.4: Schematic representation of the CNS, with a focus on spinal cord structure. (Figure adapted from [36])

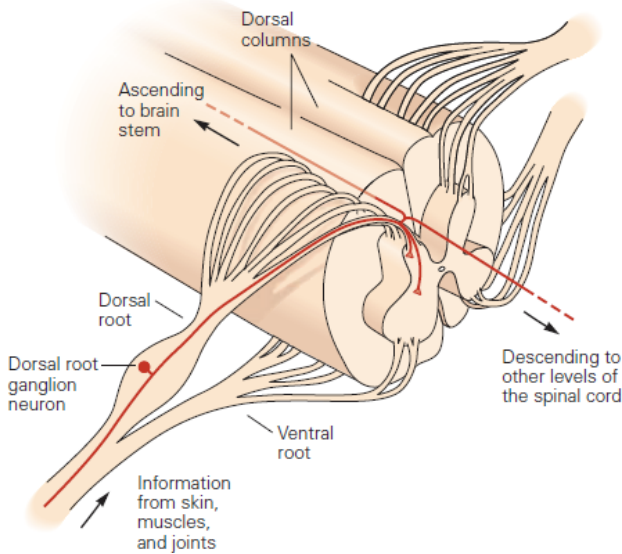


FIGURE 2.5: Schematic representation of the spinal-cord and its roots, with different sub-structures. (Figure adapted from [36])

effective, and tailor made computational models have the potential to explain and improve this situation. Treatment has been successfully applied to different neuropathic and nociceptive conditions such as failed back surgery syndrome (FBSS) and complex regional pain syndrome (CRPS). More than half of the patients with chronic pain conditions have reported significant levels of pain reduction with this kind of treatment [72]. Typical electric epidural stimulation (EES) treatments involve patients undergoing initial neuromodulation trials with external electrodes before a surgical paddle lead is implanted via laminotomy. High frequency (HF-SCS) and burst SCS are two sample stimulation modalities that employ subthreshold currents in an attempt to avoid the unpleasantness of paresthesia while alleviating pain.

Spinal cord stimulation has also been shown to evoke motor responses by activating proprioceptive circuits, which in turn activate motor neurons (i.e., lower-limb antagonists). As such, its use in motor rehabilitation has been investigated, in particular for people with spinal cord injury. Different spatiotemporal epidural stimulation patterns in the lumbosacral spinal cord below the injury site can be used to induce rhythmic patterns of locomotion. Coupled with physical therapy and extensive training, preserved (but

functionally silent) spinal circuits in paralyzed patients can reorganize. This allows for the possibility of voluntary motion, even in the absence of external electric stimulation. Motor responses can then be measured by surface electromyography (EMG) which correlates with muscle movement strength.

Complex stimulation patterns informed by computational models were used by [9] to ease voluntary locomotion in three patients with full paralysis. Patients participated in 100–278 sessions of rehabilitation over a period of 5–21 months. Encouragingly, the stimulator allowed for real time coordinated stepping movements and even voluntary action. Other research groups, like [73] and [74], have experimented with continuous direct EES to induce locomotion. Continuous EES, however, has been shown to interfere with proprioceptive information on the leg’s position, an effect mitigated using spatiotemporal EES patterns [74].

In both pain relief and locomotion rehabilitation, *pulsed waveforms* are a critical component that needs to be fully understood for effective treatments. Parameters such as pulse frequency, duty cycle, intensity, and waveform can be utilized to elicit different effects, such as selective fiber recruitment and zone targeting. They must also be taken into consideration for safety reasons; injected charge per second should be limited and pulses should be followed by corresponding pulses with opposite sign to prevent any unwanted effects from charge buildup. Computational models involving patient-specific anatomies populated with different neuron fiber types are a valuable tool to model the impact of these parameters, allowing researchers to identify stimulation thresholds and selectivity, charge injection, etc.

#### 2.1.1.5 *Transcranial magnetic stimulation*

Transcranial magnetic stimulation (TMS) is a neuromodulation modality that has been effective in combating clinical depression [75–79]. The effects of TMS resemble those of DCS. The electric fields are induced by a time varying magnetic field from a alternating current driven circuit or figure-eight coil positioned near the scalp. Increasing stimulus amplitudes result in the activation of a greater volume of tissue, and also affects the distribution of neuron subtypes that are recruited. Figure-eight coils are used because they create stronger, more focal fields, but still stimulate large sections of the cortex [80]. There are multiple stimulation waveforms and protocols for TMS, the most common being monopolar, bipolar and half sine, and more are being actively explored. Repetitive TMS (rTMS) is applied at fixed stimulation frequencies [81]. Typical observed effects at  $< 1$  Hz result in

transient inhibition of cortical activity. Above 1 Hz, increased excitability has been observed [82]. The involved mechanisms remain unclear. Long-term depression and potentiation effects have been proposed as candidate mechanisms, potentiating or depressing synapses, dynamically changing neuron excitation levels. However, inter-patient variability is large, and occasionally even inverse responses (excitation when inhibition is expected) are observed [83, 84]. Personalized computational approaches could help understand and mitigate this situation.

Other TMS modalities have been proposed that change the pulse wave forms and / or operate in the subthreshold region. Low intensity magnetic stimulation (LFMS), first discovered through chance observations of MRI scanning improving subjects' moods [85], was then proposed as a therapeutic intervention for depression and anxiety. Transcranial pulsed electromagnetic fields (T-PEMF) apply very small alternating magnetic fields with different waveforms to induce enhanced excitatory or decreased inhibitory neurotransmission [86, 87].

#### 2.1.1.6 *Bioelectric medicine*

Bioelectronic medicine [88] aims to replace conventional pharmacology-based approaches with novel, localized neurostimulation technologies to improve therapeutic precision. Its ultimate goal is to use neurostimulation to modulate organ functions (e.g., cardiac activity [89], breathing [90], digestion [91]), as well as to treat neurological disorders [92]), and to relieve conditions by manipulation of brain-to-organ and organ-to-brain communication at the level of – primarily – the autonomic component of the PNS (e.g., vagus nerve). This is achieved primarily through recently introduced physics-based neuromodulation approaches such as smart, miniaturized, implantable neural interface called 'electroceuticals' [93, 94], optogenetics [95–98], and localized ultrasound application (e.g., 'neural dust') [99]. Electroceuticals, such as vagus nerve stimulators (VNS), typically consist of pair- or multicontact electrodes in direct contact (e.g., wrapped) to a nerve or complex nerve structure (e.g., neurovascular bundles) of interest that is powered by internal batteries, connected to an IPG (implanted pulse generator), or remotely charged (via wireless power transfer [100, 101]). VNSs were the first type of electroceuticals approved by the US Food and Drug Administration (FDA) (for the treatment of drug-resistant depression [102]).

However, wide-spread success of bioelectronic medicine requires a wide range of additional technical developments and improved knowledge in the following key areas:

- organ electrophysiology and neural mapping: for many organs – such as the stomach [91] – neuroelectric characterization (neuronal populations and their role in regulating organ function) is still missing
- organ innervation: connectome maps for different organs are incomplete
- characterization of the internal structure of complex nerves such as the VN (anatomical structure, including fascicles, spatial functional organisation, distribution of axonal populations – myelination and fiber diameters) required for functional targeting [103, 104])
- mechanisms of interaction for various physical exposure conditions (EM fields, ultrasound, temperature, etc.) to permit the development of corresponding interface technology
- device development and optimization: this includes the development of smart, precise, and controllable implantable technologies (from their conception through all the prototyping stages until the clinical trials [105]).

In 2017, the US National Institute of Health (NIH) began the SPARC initiative (Stimulating Peripheral Activity to Relieve Conditions, <https://commonfund.nih.gov/sparc>) aimed at advancing research in these focus areas in order to further develop bioelectronic medicine technologies in the next decade. An important role is being played by multi-physics and multi-scale *in silico* modelling that simulates the interactions between EM fields, ultrasound, or heat and the neuroelectric activity of neurons and nerves. Hybrid physico-(electro)physiological simulations involving detailed geometrical representations of neuroelectric interfaces, image-based models of nerves (including features, such as a multi-fascicular structure, the presence of perineurium and epineurium, and dielectric heterogeneity and anisotropy), and realistic anatomical human or animal phantoms permit quantitative predictions of the outcome of electroceuticals interventions. This approach is currently employed in the following areas: (i) for the design and optimization of electroceuticals, (ii) to support translational clinical studies, and (iii) for treatment planning and optimization. Experimentally validated *in silico* models of neurostimulation are used to investigate factors such as the impact of electrode geometry, pulse waveforms, and the presence / absence of foreign body response. *In silico* models have also been used to interpret failures of clinical studies [106] and to define guidelines for the selection of stimulation parameters for treatment [107]. Closed-loop



technologies that combine adaptive stimulation with the recording of bioelectric activity (e.g., measurable as compound action potentials) could permit further advances in treatment precision and personalization. From a modelling point-of-view, this also requires the prediction of neural-activity-induced extracellular fields at distant locations and the extraction of activity / state-related information from such measurable signals.

#### 2.1.1.7 Neuroprosthetics

Neuroprosthetic devices aim to restore lost body functions such as motility, vision, or tactile sensations [108]. SCS to restore locomotion, nervous-system-interfaced robotic arms or legs (bidirectional interfacing can be used to relay sensor information from prosthetic devices to the CNS and to enable CNS control of prosthesis motion), as well as cochlear and vision implants are examples of such technologies. Neuroprosthetic devices require selective stimulation of specific functional sub-units of the nervous system within anatomical structures (e.g., spinal roots) through selective stimulation / inhibition of corresponding fibers and neurons, which is achieved through stimulation parameter, device placement, and device design optimization. Typically, implants consist of multicontact electrode geometries with the possibility of applying specific temporal stimulation patterns to individual or groups of electrodes. SCS electrode arrays range from four unidimensionally arranged electrodes to large arrays (such as the 32 contact Pentalead stimulator from Abbott) and have mostly been designed with pain therapy applications in mind. In current clinical practice, stimulation settings are still optimized / defined iteratively, based on patient response. *In silico* models can be used to achieve spatial selectivity (i.e., stimulate / inhibit specific target regions in the nerve or spinal cord) and fiber selectivity (i.e., target only large or small fibers) by optimization of pulse shapes or multi-contact array steering parameters. *In silico* solutions, based on hybrid EM neuronal simulations have repeatedly been shown to be crucial for personalized precision medicine. In [9], image-based personalized *in silico* models of spinal cord stimulation were used to optimize stimulator placement and to dynamically adapt the treatment parameters. Both the surgical intervention and the subsequent neurostimulation treatment to restore lost motor function were performed on the basis of modelling predictions.

### 2.1.2 *Acoustic neuromodulation*

*Acoustic neuromodulation* achieves the modulation (activation, inhibition, synchronization) of neurons through acoustic exposure. Acoustic sources do not directly electrically excite neurons, as the waves are mechanical in nature. The exact mechanisms underlying acoustic neuromodulation are an active area of research. An increasing amount of experimental evidence in mice, rats, monkeys, and even humans allows us to test mechanistic hypotheses around acoustic neuromodulation and to generate computational models (discussed in Section 2.2.8) [10, 11, 109–115]. Whereas EM neuromodulation is an established technique, acoustic neuromodulation is still in its infancy, and applications have yet to be translated to clinical settings. Acoustic neuromodulation already provides valuable advantages over its EM counterpart in the form of noninvasive, targeted deep stimulation. Non-invasive EM stimulation is not well localized and can only act at short distances from the source (when compared to the size of the brain). For deep and targeted stimulation, invasive surgery is necessary, and subsequent target steering is very limited without further surgery. Ultrasound, however, holds the promise of non-invasive stimulation at depth as the mechanical waves can safely travel through tissues and focus at mm-sized focal regions deep within tissues [116].

*Acoustic waves* are elastic in nature and encompass sound waves. They have an associated speed, wavelength, and frequency. Ultrasonic waves vibrate in the human non-audible regime ( $> 20$  kHz). Unlike EM waves that can propagate even in empty space, ultrasonic waves cannot exist in vacuum as they are synchronized vibrations of the carrier medium (e.g., air or human tissue) that rely on elastic forces in the medium. Longitudinal waves are the most common mode of propagation. They are pressure waves, exist in gases, liquids, and solids, and feature a displacement direction that is aligned with the wave propagation direction. Shear waves feature displacements that are orthogonal to the propagation direction, and are restricted to solid media, as they rely on directional bonds. Other wave modes include Rayleigh and Lamb waves that are restricted to surfaces and interfaces.

Of particular importance for the modelling of FUS applications are absorption (primarily thermal losses; occasionally, other losses, such as scattering losses in heterogeneous materials, are also modelled as absorption) and reflection / transmission / refraction [17]. Reflection and refraction occur at locations where acoustic impedance (related to the product of acoustic ve-

locity and density) varies. Mode conversion can also occur. It is challenging to individually characterize different absorption mechanisms experimentally, which is why absorption is typically described as a bulk property (e.g., obtained through frequency-dependent fitting of experimental data). Power deposition through absorption is often quantified as (time averaged for harmonic exposure) acoustic intensity:

$$I = \frac{p^2}{2Z} = \frac{p^2}{2\rho c}$$

where  $I$  is measured in  $\text{W}/\text{m}^2$ ,  $p$  denotes pressure,  $Z$  acoustic impedance,  $\rho$  density, and  $c$  is speed-of-sound in the media. This is also a safety-relevant and a therapeutic effect-relevant quantity. Diffraction occurs at borders, but is of limited relevance in soft tissue. The wave nature of acoustic waves results in constructive and destructive interference phenomena, which are crucial for FUS applications. At high intensities beyond the LIFUS-regime, various non-linear effects become important.

Therapeutic ultrasound is typically generated using piezoelectric crystals called *transducers* that convert alternating currents to oscillatory motion and can take various shapes to help shape the wave. The transducers used for focused ultrasound applications are typically cut from a spherical shell of a given radius at a given aperture. Alternatively, they can be flat and fitted with a curved acoustic lens with appropriate impedance to achieve the desired focusing [117]. Multi-element transducers, such as the ExAblate 4000 system which has  $> 1000$  elements with individually controllable phases and amplitudes, can be used to achieve superior focusing and steering control [118, 119] (see Figure 2.6). Such devices necessitate numerical optimization algorithms that can involve simulations for increased accuracy. A coupling medium, such as (degassed) water or gel, with acoustic impedance similar to that of soft tissue is used to avoid impedance mismatch and associated reflections. Bone has considerably higher acoustic impedance and attenuation losses than soft tissues, resulting in acoustic aberration, defocusing, focus shifting, undesired secondary hot-spots, and low transmission efficiency [120]. Skull bone is highly heterogeneous and is composed of a layer of porous or trabecular bone that is sandwiched between two very dense layers of cortical bone.

Two other relevant FUS effects are cavitation [121] and the radiation force [122]. *Cavitation* refers to the formation of gas bubbles, their oscillation (stable cavitation), and their occasionally violent bursting / collapse (inertial cavitation, which can cause tissue damage). Inertial cavitation is avoided by

imposing limits on peak negative pressure. Proper determination of such safety-relevant quantities in complex anatomical environments requires adequate computational models. Cavitation will be discussed again in Section 2.2.8 in the context of acoustic neuromodulation, as membrane-sonophore-cavitation is one of the candidate mechanisms. At the boundary between two media with different acoustic impedances there is a pressure buildup that can cause steady-state stresses. This is known as the *radiation force*, and has been measured to be several orders of magnitude smaller in biological tissues than the pressure forces associated with the acoustic wave itself. It is therefore mostly neglected, but could also be mechanistically involved in acoustic neuromodulation.

#### 2.1.2.1 *Neuromodulation*

Different forms of acoustic neuromodulation have been shown *in vitro* and *in vivo*, for CNS and PNS stimulation, in species such as mice, frogs, cats, monkeys, and humans [10, 11, 109–115]. *Peripheral nerve stimulation* in humans showed an increase in thermal, heat, and pain sensation [123–125]. This sensation was frequency dependent; however, the threshold for sensation depended exclusively on intensity, indicating that acoustic peripheral nerve stimulation is mechanical and not thermal in nature.

Changes in visual evoked potentials measured by EEG in the visual cortex have been observed in cats subject to ultrasound stimulation of the LGN and the optic tract [126]. Ultrasound was shown to produce reversible *modulation of brain activity*. In the case of LGN stimulation, the response was immediately measurable, whereas stimulation in the optic tract delayed the response by around five minutes, suggesting a transient spreading of the depolarization activity [127]. Complete and persistent recovery was achieved. Large scale modulation of brain excitability was also observed from electrocorticographic (ECoG) recordings in the exposed cortex of cats and rabbits in the form of suppression of gamma and beta waves [128]. Several experiments also show the impact of US stimulation on nerves in the CNS in anesthetized rats and rabbit [111, 129]. The level of anaesthetics played a big impact in the neuron's susceptibility. Degraded and improved task performance were observed in monkeys and humans undergoing different US stimulation protocols [12, 130].

*Ultrasonic neuromodulation effects* are exposure parameter dependent and include: impaired conduction, elevated compound action potentials, reduced latencies, time-locked action potential generation, evoked potentials, firing rate modulation, muscle activity, and reduction of epileptic activ-

ity [11, 109, 113, 131, 132]. Typically, sinusoidal stimulation is applied (continuous- (CW) or pulsed-wave (PW) stimulation are used). Timescales for modulation are longer than the corresponding ones for electric stimulation (tens to hundreds of milliseconds of high duty cycle stimulation at 250–650 kHz PW), suggesting mechanical effects at play. For pulsed excitation, the duty cycle level is associated with a change from inhibition to excitation of the neuron population. *In vivo* nerve stimulation was achieved using medium to high ultrasound intensities at frequencies ranging between 0.5 and 3 MHz [133–135]. Short low intensity pulses were used to cause neurons in mouse brain slice cultures to fire action potentials [136]. Low intensity and high frequency (2 MHz) stimulation caused reversible conduction block in peripheral nerves [137]. For excitation, pulse wave-forms were nearly continuous; for suppression, they were short and discontinuous. These effects are reproducible, but there is a high degree of variability between subjects, complicating translation into the clinic.

#### 2.1.2.2 *Therapeutic ultrasound*

The main modalities for therapeutic focused ultrasound are *high intensity focused ultrasound* (HIFU) and *low intensity focused ultrasound* (LIFU / LIFUS). HIFU applies sharply focused ultrasonic waves with high pressures and intensities (10–30 MPa) at varying frequencies (0.5–3.5 MHz). Intended applications focus mostly on ablation of malignant tissues, particularly in oncology [138]. LIFU applications (e.g., for neuromodulation) use pressure values of a few MPa (or even lower) at frequencies typically between 200 kHz and 2 MHz. Other applications of FUS include blood brain barrier opening, sonoporation, and thrombolysis.

HIFU is a procedure in which high intensities are used to ablate tissue and induce cell death, while avoiding damage to surrounding tissues [139]. This has been successfully applied in the treatment of essential tremors, in Parkinson’s disease, in certain movement disorders, and in neuro-oncology. At the moment, improvements are modest when compared to more established alternatives [140], and HIFU is mostly applied to avoid invasive treatments, or when alternatives are not viable. Clinical acceptance has been achieved for HIFU treatment of prostate cancer, uterine fibroids, and pain palliation. Neuro-oncological applications involve inducing temperatures higher than 55°C in brain neoplasms. Epilepsy can be treated by ablation of the epileptogenic zone or, at lower intensities, by disturbing brain networks [141]. Continuous wave forms are typically used and temperature increases are monitored by MRI or US thermometry (e.g., making use of the

temperature-dependence of the proton resonance frequency) [142]. LIFU applications typically involve pulsed wave-forms

### 2.1.2.3 *Transcranial FUS*

Transcranial FUS (tcFUS) can ideally achieve focusing precision in the order of 2 mm [143]. Transcranial targeting and stimulation present an additional level of challenge over other FUS applications, as the thick skull is highly heterogeneous and absorbs and scatters waves. Focused waves are aberrated and attenuated which affects treatment efficacy [120]. Consequently, multi-element transducers are sometimes utilized, such as the ExAblate with individually controllable amplitudes and phases [119]. Computational approaches, such as the virtual source method, can be used to compensate for the phase aberrations induced by the skull [144]. This electronic phase correction algorithm uses imaging information on skull inhomogeneity to build a computational model of the clinical setup and the patient's anatomy [145]. A point source is placed at the intended target location and the outwards wave propagation through the modelled anatomy is simulated. The resulting steady-state wave amplitude and phase is measured at the location of each of the transducer elements. By applying the conjugated signal during treatment administration, phase delays and aberration can be compensated, resulting in superior focusing and targeting. Proper skull modelling is highly dependent on the accurate representation of the skull's acoustic property distribution. However, simulations that do not consider individual variability and skull heterogeneity are not sufficiently accurate for that purpose. CT imaging can be used to estimate bone density. Works by [146] and [147] have established linear and non-linear mapping functions relating CT image data to the different acoustic properties. However, it is unclear how much these mapping functions depend on imaging parameters, age, or inter-species differences.

When applying transcranial FUS, special safety considerations must be taken to account for skull surface heating, blood vessel proximity to the stimulation site, and inertial cavitation [120]. Cavitation can cause blood vessels to rupture, resulting in hemorrhage. If the intended application involves thermal ablation, blood vessels also act as local heat sinks which cool the tissue and might necessitate unsafe levels of energy deposition to achieve the desired temperature increase [148].

Treatment efficacy for transcranial ultrasound is heavily influenced by the skull transmission [120]. Skull thickness, incident beam angle, standing waves, and the level of bone heterogeneity have an important impact on

transmission. The skull density ratio (SDR) between cortical and trabecular bone is typically measured using computed tomography (CT). Patients with SDR above 0.4 are typically not eligible for treatment. Properly validated computational skull models and efficient focusing algorithms are a necessary step in broadening the applicability of transcranial FUS.

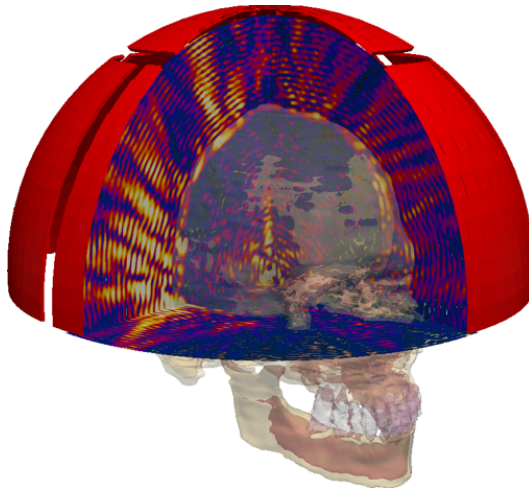


FIGURE 2.6: Simulation of tcFUS acoustic propagation from an ExAblate 4000 transducer model. (Figure adapted from [17])

## 2.2 COMPUTATIONAL MODELLING

This section gives an overview of the relevant computational models for the applications discussed of EM and acoustic neuromodulation. We begin by first giving a basic overview of EM, EM-neuro, acoustic, and acoustic-neuro models and how they can be solved with numerical methods. We continue by discussing the most relevant methodologies for the different applications, the latest advances and limitations, with a special interest in the topics that are addressed in this thesis.

### 2.2.1 Why computational modelling?

Computational models are valuable tools to improve the effectiveness of clinical applications. They can help with device design, positioning,

operation, and targeting to improve treatment efficacy. By placing clinical treatments in a mathematical and quantifiable, validated framework, it is possible to gain mechanistic insight and to form and test varying hypothesis where direct or indirect observation of certain relevant quantities are not feasible. As therapies become more complex and refined, the parameter space of stimulation configurations becomes too large to explore manually. Computational methods and algorithms are better suited to explore this space and find optimal patient-specific parameters. Coupled with real time measurements of biological signals, adaptive (closed-loop) control of treatments becomes possible.

Before the advent of computational models for virtual treatment exploration, stimulation protocols were based on empirical evidence based on patient reports and indirect measures of treatment effectiveness. Heuristics were constructed to inform treatments; however, there was little in the ways of tools to understand why certain treatments would not work on certain patients. Nonetheless, extensive experimental work on the subject has been recorded. The growth of computational resources, improvements in imaging modalities and mathematical frameworks explaining observed phenomena has now made it possible to work in virtual environments and consolidate the empirical data into models. Imaging modalities like MRI and CT can be used to construct a model of a patient's anatomy and to inform critical clinical considerations. Improvements in resolution and derived imaging modalities can even be used to visualize and quantify brain connectivity maps and small relevant brain structures. Computational models can be used to assess the activated neural tissue volume and which specific cells are being recruited, and parameters of stimulation protocols can be further tuned and optimized based on needs and real-time treatment feed-back.

Computational models have been successfully applied in a variety of therapeutic applications and have led to key insights and novel tools, resulting in improved safety, understanding, and treatment of neurological disorders. They have been applied successfully to assess the activated brain region in DBS, to see which neuron fibers are preferentially recruited within each tissue and which networks are activated. The impact of pulse waveforms is an active area of research used for safety and to selectively recruit specific neuron fibers. In the case of spinal cord injury rehabilitation, different motor neurons need to be recruited from the spinal cord in highly specific temporal pattern to initiate walking motions. They have been successfully used for improved SCS targeting and selectivity in patients with chronic pain. Safety standards employ computational modelling when



certain safety-relevant quantities, such as charge injection, cannot be directly measured and must be estimated.

It is important, before translating any of these models to the clinical setting, that they are constrained and validated with physiological data and that their context-of-use and limitations are fully understood.

### 2.2.2 EM simulations for neuromodulation

Electromagnetic fields, their propagation and tissue interaction, are described by Maxwell's equations.

$$\begin{aligned}\nabla \cdot \mathbf{E} &= \frac{\rho}{\epsilon_0} \\ \nabla \cdot \mathbf{B} &= 0 \\ \nabla \times \mathbf{B} &= \mu_0 \mathbf{J} + \mu_0 \epsilon_0 \frac{\partial \mathbf{E}}{\partial t} \\ \nabla \times \mathbf{E} &= -\frac{\partial \mathbf{B}}{\partial t}\end{aligned}$$

where  $\mathbf{E}$  is the electric  $E$ -field,  $\mathbf{B}$  the magnetic  $B$ -field,  $\epsilon_0$  and  $\mu_0$  are the permittivity and permeability of free space,  $\rho$  is the charge density, and  $\mathbf{J}$  is the current density. These equations are valid on the microscopic level in vacuum. On a macroscopic, averaged level, dielectric materials and their interactions with fields are better handled by introducing auxiliary fields (constitutive relations):

$$\begin{aligned}\mathbf{D} &= \epsilon \mathbf{E} \\ \mathbf{B} &= \mu \mathbf{H} \\ \mathbf{J} &= \sigma \mathbf{E} + \mathbf{J}_0\end{aligned}$$

where  $\epsilon := \epsilon_0 \epsilon_r$  and  $\mu := \mu_0 \mu_r$  and  $\epsilon_r$  and  $\mu_r$  are the relative permittivity and permeability of the medium. The third equation is Ohm's law where  $\sigma$  is the conductivity of the medium and  $\mathbf{J}_0$  is an external current source. The macroscopic Maxwell equations read:

$$\begin{aligned}\nabla \cdot \mathbf{D} &= \rho \\ \nabla \cdot \mathbf{B} &= 0 \\ \nabla \times \mathbf{H} &= \mathbf{J} + \frac{\partial \mathbf{D}}{\partial t} \\ \nabla \times \mathbf{E} &= -\frac{\partial \mathbf{B}}{\partial t}\end{aligned}$$

Given a source and a simple geometry and medium, the resulting  $E$ - and  $B$ -fields can be derived analytically. However, an analytical approach quickly fails when more complex geometries and mediums are involved, as is the case for setups involving the highly heterogeneous and irregularly shaped human body. In such cases, a numerical approach is useful. The spatio-temporal domain and equations are discretized into elements (voxels, tetrahedrons, etc.) and nodes. Each element / node has associated equations (derived from Maxwell's equations) with the corresponding source, electric, and magnetic terms. These equations are coupled to those of neighboring elements / nodes, giving rise to a large set of coupled equations. The discretization resolution affects the accuracy of the numerical approximation. Computational and algorithmic advances allow for modern machines and workstations to handle such tasks efficiently in reasonable time.

### 2.2.3 Finite Difference Time Domain method

A frequently approach approach to solve Maxwell's equations is the Finite Difference Time Domain (FDTD) method. Maxwell's equations are discretized and the spatial and temporal derivatives are approximated using finite differences:

$$\frac{\partial F[i, j, k, n]}{\partial x} = \frac{F^n[i + 1/2, j, k] - F^n[i - 1/2, j, k]}{\Delta x}$$

$$\frac{\partial F[i, j, k, n]}{\partial t} = \frac{F^{n+1/2}[i, j, k] - F^{n-1/2}[i, j, k]}{\Delta t}$$

where  $i, j, k$  are spatial variables indexed as cell integer values and  $n$  refers to the time step.  $E$ - and  $B$ -fields are typically discretized on spatially and temporally staggered grids (Yee discretization [149], hence the half-steps in the equation above) to reduce discretization errors. Finite differences are applied to Maxwell's equations in the following form:

$$\nabla \times \mathbf{H} = \frac{\partial}{\partial t} \epsilon \mathbf{E} + \sigma \mathbf{E}$$

$$\nabla \times \mathbf{E} = -\frac{\partial}{\partial t} \mu \mathbf{H} - \sigma \mathbf{H}$$

In FDTD, typically uniform or adaptive rectilinear grids are used for spatial discretization. Adaptive grids allow to increase the resolution near sources, sharp features, and other accuracy relevant regions. Domain truncation necessitates boundary conditions (such as the Perfectly Matched

Layer (PML) boundary condition) that absorb outgoing waves, to prevent reflections reentering the computational domain.

For harmonic (sinusoidal) excitation, results are typically analyzed in the frequency domain (once the numerical solution has converged and becomes periodic). Systems with a high energy input and slow energy dissipation may take a long time before they converge.

On uniform rectilinear meshes, it can be demonstrated that stability is ascertained, provided that the time-step  $\Delta t$  remains below a discretization- and material properties-dependent limit (CFL criterion):

$$\Delta t \leq \frac{1}{c \sqrt{\frac{1}{(\Delta x)^2} + \frac{1}{(\Delta y)^2} + \frac{1}{(\Delta z)^2}}}$$

where  $c$  and  $\Delta$  are the speed-of-sound and dimensions of a given cell. Heuristic experience has shown, that the same criterion is usually also sufficient when applying an adaptive rectilinear discretization.

#### 2.2.4 Low frequency approximations

The FDTD formulation solves the full wave equations. This can be computationally demanding – particularly when structures have characteristic length scales well below the wavelength, resulting in a large number of required time-steps (to satisfy the CFL criterion). Under some conditions, Maxwell's equations can be further simplified by neglecting negligible terms to decouple the equations. For exclusively mono-frequential harmonic sources, temporal derivations become trivial and the system is further simplified. For that purpose, it is useful to consider the electric and magnetic quantities as complex phasors (the real part corresponds to the actual fields):

$$\begin{aligned}\nabla \times \mathbf{E} &= -j\omega\mathbf{B} \\ \nabla \times \mathbf{H} &= j\omega\mathbf{D} + \mathbf{J} \\ \nabla \cdot \mathbf{D} &= \rho \\ \nabla \cdot \mathbf{B} &= 0\end{aligned}$$

where  $j = \sqrt{-1}$  and  $\omega$  is angular frequency.

These four equations can be further simplified as two equations by introducing auxiliary potentials. As per the Helmholtz's decomposition, fields can be decomposed as a sum of a rotational and an irrotational

component. As the divergence of the  $B$ -field is always zero, a potential  $\mathbf{A}$  can be constructed, such that:

$$\mathbf{B} = \nabla \times \mathbf{A}.$$

This is known as the vector potential of the magnetic field. Using this new potential one obtains:

$$\nabla \times (\mathbf{E} + j\omega\mathbf{A}) = 0$$

Similarly, in the absence of internal sources a divergence-free scalar potential  $\phi$  can be constructed, such that

$$\mathbf{E} + j\omega\mathbf{A} = -\nabla\phi.$$

(the sign is a matter of convention). Maxwell's equations can then be rewritten as:

$$\begin{aligned} \nabla \times \frac{1}{\mu} \nabla \times \mathbf{A} &= \omega^2 \tilde{\epsilon} \mathbf{A} - j\omega \tilde{\epsilon} \nabla \phi + \mathbf{J}_0 \\ \nabla \cdot \tilde{\epsilon} \nabla \phi &= -j\omega \nabla \cdot \tilde{\epsilon} \mathbf{A} \\ \tilde{\epsilon} &:= \epsilon_r \epsilon_0 + \frac{\sigma}{j\omega} \end{aligned}$$

where all constitutive equations are grouped into a single complex permittivity  $\tilde{\epsilon}$ .

Subsequently, *quasistatic* approximations are applied to further simplify the system. If the characteristic temporal and spatial scales of the problem are sufficiently small compared to the temporal and spatial scales of the wave propagation, selected terms become negligible. As an example, in the full wave equation, a changing  $E$ -field  $\mathbf{E}_0$  induces a changing  $B$ -field  $\mathbf{B}_0$  which induces another  $E$ -field  $\mathbf{E}_1$  and so forth. In the quasistatic approximation,  $\mathbf{B}_1$  and  $\mathbf{E}_0$  are ignored as they are orders of magnitude smaller than the principal terms. Under this approximation, Maxwell's equation reduces to

$$\begin{aligned} \nabla \times \frac{1}{\mu} \nabla \times \mathbf{A} &= \mathbf{J}_0 \\ \nabla \cdot \tilde{\epsilon} \nabla \phi &= -j\omega \nabla \cdot \tilde{\epsilon} \mathbf{A} \end{aligned}$$

The resulting Poisson equation-like problems can be efficiently solved using the finite element method (FEM), and in homogeneous cases using Fast Fourier Solvers. The relevant fields are readily obtained from the

scalar and vector potentials. Dedicated solvers exist for problems with and without source currents  $\mathbf{J}$  and for cases where Ohmic terms dominate the complex permittivity  $\tilde{\epsilon}$ :

Electro Quasistatic	$\nabla \cdot \tilde{\epsilon} \nabla \phi = 0$	
Electro Static	$\nabla \cdot \epsilon \nabla \phi = 0$	$(\sigma \ll \omega \epsilon)$
Ohmic Quasistatic	$\nabla \cdot \sigma \nabla \phi = 0$	$(\sigma \gg \omega \epsilon)$
Magneto Quasistatic	$\nabla \cdot \tilde{\epsilon} \nabla \phi = -j\omega \nabla \cdot \tilde{\epsilon} \mathbf{A}_0$	
M-QS: Displacement	$\nabla \cdot \epsilon \nabla \phi = -j\omega \nabla \cdot \epsilon \mathbf{A}_0$	$(\sigma \ll \omega \epsilon)$
M-QS: Ohmic	$\nabla \cdot \sigma \nabla \phi = -j\omega \nabla \cdot \sigma \mathbf{A}_0$	$(\sigma \gg \omega \epsilon)$

*Sim4Life* includes efficient quasistatic FEM solvers for structured and unstructured discretizations.

FEM solvers are used to model the electromagnetic fields in the highly heterogeneous human body. In white-matter, nerves, and other fibrous tissues, such as muscle, it can be important to consider anisotropy, as the longitudinal and transversal conductivities differ greatly. Imaging modalities, such as DTI [150–152], can be used to obtain anisotropy maps. Dielectric tissue properties have been compiled in databases such as [153–155].

Frequent boundary conditions in quasistatic FEM problems are Dirichlet and Neumann boundary conditions. Dirichlet boundary conditions set a fixed potential (voltage) value at a given boundary. Neumann boundary are typically applied to fix the normal component of the current density (flux leaving / entering the domain) or  $E$ -field. A special variant of the Neumann boundary condition is the insulating boundary condition (no flux leaving the domain).

### 2.2.5 Electrophysiological neuromodulation

Computational models of neurons are frequently based on the work of [156, 157] who modelled the temporal evolution of transmembrane potential as a result of transmembrane currents from leakage channels, active channels and capacitive currents, using coupled first-order non-linear ordinary differential equations. The conductance of the active channels depend on rate constants that evolve as a function of the transmembrane voltage. Spatially extended variants can be used to model fibers and action potential propagation, complex neuron morphologies (e.g., featuring dendritic structures), and neural networks with synaptic contacts. These models can also

be represented or implemented as non-linear electric circuits. Commonly employed fiber models include the Sweeney [158] and MRG [159] models.

Numerical integration methods, such as Euler and Runge-Kutta methods, can be used to solve the coupled differential equations. The most commonly employed software for that purpose is *NEURON* [160], which also supports high-performance computing applications. Large repositories of neuron models, such as the ModelDB [161], exist.

Work by [162] introduced coupling to an extracellular potential distribution (see Figure 2.7). Extracellular voltage compartments are added at each of the nodes of the discretized neuron model and an external potentials is applied. This can be used to study electromagnetic neurostimulation.

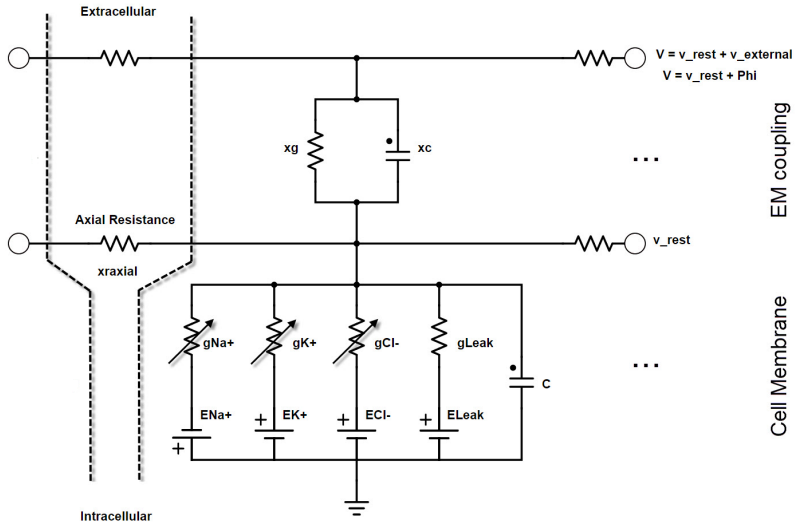


FIGURE 2.7: Circuit representation of Hodgkin-Huxley-like neuronal dynamics model.

### 2.2.6 Applications

Computational tools have proven valuable for treatments such as DBS and SCS. Below are brief reviews of the current state-of-the-art in computational modelling for these applications, their limitations, and current needs.

**DBS** In the context of DBS, improvements in neuro-imaging have enabled more precise electrode implantation, while improvements in computational modelling have enabled superior targeting and control. Multimodal MRI imaging techniques (e.g., T1- / T2-weighted, DTI) are employed to directly visualize and identify brain regions and to establish brain maps and atlases, instead of having to rely on indirect biomarkers. Imaging enables patient-specific fiber tractography, and image-based registration of detailed atlases further facilitates the identification of targets and regions [163–166].

Two types of models are applied: network models to assess the impact of DBS on brain activity and rhythms, and personalized hybrid EM-neuronal modelling for the evaluation of the volume of tissue activation (VTA).

Downstream thalamic activity following DBS in patients with Parkinson's disease (PD) was modelled by [167]. The model predicted the varying firing rates of the STN, GPe, GPi, and the thalamus under healthy and PD conditions. Models by [168] looked at the impact of GPi firing patterns on thalamic outputs. Neural models were built from fits of data obtained through *in vivo* micro-electrode recordings in primates. Work by [168] extended the model from [167] by including additional signaling pathways and networks. Work by [169] explored the frequency dependence of STN DBS and found a mixture of excitatory and inhibitory responses from the basal ganglia.

Personalized DBS models featuring fiber tracts and atlas-based brain-region parcellation, are used to calculate the VTA for specific implant geometries and pulse waveforms and to assess axonal activation in the electrode proximity [170, 171]. Different axons in different regions get recruited with increasing pulse strength and duration. Modelling has guided clinical application by superimposing simulation results with diffusion tensor imaging, brain atlases and post operative images [171]. Such computational models are also used for the design of new multi-contact implants and for pulse waveform optimization [172, 173]. Efficient algorithms are critical to achieve real-time adaptive control based on measurable neural activity signals, such as local field potentials (LFP). Another example is the use of computational modelling to enable current steering [174].

These modelling approaches suffer from some important limitations: (i) Hybrid modelling focuses on impact of DBS on STN neurons, GPi fibers, cortico-spinal fiber tracts (CST) to assess safety issues related to unwanted side effect stimulation. However, conventional DTI cannot reliably extract fiber trajectories (e.g., due to crossing fibers in low-anisotropy regions). (ii) Electrophysiological models of human STN neurons are unavailable

(rat models are used), while fiber tracts are modelled as generic mammalian myelinated fibers (MRG), and other electrically excitable cells are ignored. The impact of these issues on computational modelling predictions in humans need to be carefully evaluated. (iii) The applicability of these models to newer DBS approaches that involve higher frequencies or acoustic stimulation is unclear. (iv) Network and feedback effects are hardly considered [168]. (v) The same is true for interface effects and foreign-body response.

In spite of these limitations, DBS computational models are essential tools to diagnose disease states, evaluate surgical targets, predict networks recruitment and activity, and optimize treatment protocols.

**scs** Several computational models of the spinal cord, featuring simplified, antropomorphic or image-based and personalized spinal cord structures combined with electrophysiological models of fibers and neurons, have been built to enhance understanding and identify effective therapeutic strategies to treat chronic pain disorders and restore locomotion to paraplegics (through the activation of large myelinated proprioceptive fibers in spinal roots, which in turn activate complex motion patterns encoded in the spinal cord [8, 175–178] – motor neurons in other regions in the spinal cord are only stimulated at much higher exposure [179]). Hybrid EM-neuronal simulations have been used to investigate fiber recruitment and achieve the dynamic spatial stimulation steering required for natural gait. While original stimulation protocols were devised from empirical mapping experiments in the mid-line spinal cord [180], hybrid EM-neuronal models have permitted a deeper understanding of the mechanisms at play and improved stimulation control. Computational studies [8, 176] enable *in silico* optimization of electrode placement and stimulation protocols for the selective recruitment of individual posterior roots using multi-contact electrode arrays – a precondition for the restoration of the complex locomotion patterns involved in natural gait.

The first 2D volume conductor spinal cord model was generated by [181]. A 3D geometrically realistic model of the lumbo-sacral spinal cord with embedded epidural electrodes was established by [176]. It distinguished gray matter, white matter, CSF, epidural fat, the vertebral column, and the dura, and includes realistically positioned dorsal and ventral root fibers. The model was used to investigate fiber recruitment and studied the impact of fiber curvature and conductivity discontinuities on stimulation predictions. Work by [8] built a detailed EM-electrophysiological



computational model of a rat spinal cord to study intrafascicular EES in rodents. Work by [182] built a full human thoracic spinal cord model and compared intradural and epidural stimulation modalities for chronic pain. More recent work by [183] was centered on investigating kHz-frequency epidural stimulation for the treatment of chronic back pain.

Recent efforts are focused on the development of image-based, personalized spinal cord anatomies to enable patient specific, precise multi-electrode placement and optimized multipolar stimulation protocols. These models are functionalized with realistic neuronal trajectories, occasionally even neural circuits, and consider image-based tissue anisotropy and inhomogeneity information (unpublished work with our collaborators).

### 2.2.7 Acoustic exposure

Ultrasonic waves are represented via the wave equation. The full wave equations are based on stress-strain relationships and consider vectorial displacements in a typically tensorial equation. However, when shear-waves can be neglected (e.g., in primarily gaseous, liquid, and soft environments) this equations can be reduced to the scalar pressure wave equation, which can be solved with much reduced computational effort (in terms of memory and computational time requirements). While this is a strong and problematic simplification, it is frequently required to handle the complexity of therapeutic exposure scenarios with realistic computational resources. However, users must be aware that shear waves and mode conversions are not represented in the pressure-wave approximation. The commonly employed linear acoustic pressure wave equation reads:

$$\rho \nabla \frac{1}{\rho} \nabla p - \frac{1}{c^2} \frac{\partial^2 p}{\partial t^2} - \frac{\tilde{a}}{c^2} \frac{\partial p}{\partial t} = 0$$

$$\tilde{a} = 2a \sqrt{\frac{a^2 c^4}{\omega^2} + c^2}$$

where  $\rho$  is density,  $c$  is speed-of-sound,  $\alpha$  is attenuation,  $p$  is pressure,  $t$  is time, and  $\omega$  is angular frequency.

When non-linearity cannot be neglected, the more general Westervelt-Lighthill equation [184] can be employed:

$$\rho \nabla \frac{1}{\rho} \nabla p - \frac{1}{c_0^2} \frac{\partial^2 p}{\partial t^2} + \frac{\delta}{c_0^4} \frac{\partial^3 p}{\partial t^3} + \frac{\beta}{2\rho_0 c_0^4} \frac{\partial^2 p^2}{\partial t^2} = 0$$

where  $\delta$  is diffusivity,  $\beta$  is the nonlinearity coefficient.

It is important to properly consider interfaces using the term:

$$\rho \nabla \frac{1}{\rho} \nabla p$$

rather than the commonly implemented simplified version  $\nabla^2 p$ .

The full wave equation in highly heterogeneous and irregular geometries can again be efficiently solved using the FDTD method (as described for EM in Section 2.2.3) and similar considerations, e.g., concerning stability and absorbing boundary conditions, apply. Other commonly employed numerical methods include the angular spectrum method (suitable when a principal propagation direction exists) and the pseudospectral method. Rayleigh-Sommerfeld integral methods are frequently employed in homogeneous environments and can occasionally produce analytical results.

### 2.2.8 Acoustic stimulation for neuromodulation

The Hodgkin-Huxley [156] model for neurons is based on purely electric phenomena and can not explain mechanical wave stimulation, such as US induced neurostimulation. Thermal effects cannot sufficiently explain acoustic stimulation, as was shown by [135, 185, 186]. Several mechanistic models with differing levels of biological plausibility and quantitative agreement with experimental data have been proposed in the recent years.

Several models have been suggested in an attempt to explain this. These try to couple mechanical and electrical actions in the cell's membranes, motivated by the different observed mechanical effects in axons during action potential propagation. On initiation of an action potential, reversible heat, length contraction, and thickness changes are observed [187–189]. The normal force exerted in phase with the action potential propagation has been measured to be around 1 nm; higher than what can be explained by physical changes in the ion channels.

The first such model is the rather exotic *soliton model* which proposes that action potentials travel as pressure soliton waves due to phase transitions of the membrane lipids between a liquid and gaseous state [190]. The term soliton refers to a solitary self-reinforcing wave that, due to non-linear dynamics of the medium and dispersion, propagates while maintaining its shape and intensity. Changes in density result in changes in the local field potential (via large electric dipole moments in the lipid molecules) which induces a piezoelectric wave effect – polarization of charges due to compression and expansion. While such an approach naturally lends

itself to incorporate electro-mechanical coupling, it does not account for the known importance of ion-channels and considering the important body of evidence supporting the common model of action potential propagation, the soliton model appears to be highly questionable.

Another theory to explain acoustic neuromodulation is the flexoelectricity hypothesis. In this theory, membrane curvature changes affect the transmembrane potential, resulting in action potentials that propagate as flexoelectric wave [191, 192]. In this theory, ion channels play a fundamental role (while phase-changes in the lipid layer do not). There is no mathematical formulation of this model that predicts action potential generation and propagation.

The two most likely mechanistic theories are the membrane cavitation model (the Neuronal Intramembrane Cavitation Excitation (NICE) model from [193]; see Figure 2.8) and the acoustic radiation force [194] model.

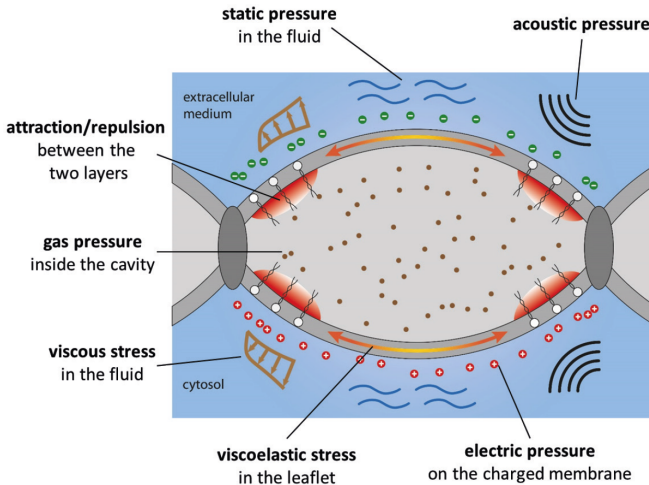


FIGURE 2.8: Schematic representation of the sonophore cavitation (NICE) model of acoustic neuromodulation.

The NICE model [193] is promising, as it produces predictions which are in good quantitative and qualitative agreement with experimental data. Also, it has a mathematical framework that lends itself to implementation and the formulation of testable hypotheses. It assumes that sonophores (nanometer sized bubbles) in the double-lipid membrane start cavitating under acoustic exposure (due to gas-transfer related to pressure changes, see Chapter 9) and thereby cyclically affect the transmembrane capacitance,

which – due to the electric non-linearity of membrane channels – results in a net-charge transfer that can in turn trigger action potentials. The typical Hodgkin-Huxley like models are modified to account for the intramembrane sonophore cavitation.

The electrical system is modelled by the following equations:

$$\frac{dV}{dt} = -\frac{1}{C_M} \left[ V \frac{dC_M}{dt} + g_{Na} (V - E_{Na}) + g_K (V - E_K) + g_M (V - E_K) + g_L (V - E_L) \right]$$

$$\frac{dn}{dt} = \alpha_n (1 - n) - \beta_n n$$

$$\frac{dm}{dt} = \alpha_m (1 - m) - \beta_m m$$

$$\frac{dh}{dt} = \alpha_h (1 - h) - \beta_h h$$

$$\frac{dp}{dt} = \frac{p_\infty - p}{\tau_p}$$

where the transmembrane voltage  $V$  is a deflection dependent quantity which can in turn affect capacitive displacement currents. The mechanical coupling is modelled via the following equations:

$$\frac{d^2 Z}{dt^2} = -\frac{3}{2R} \left( \frac{dZ}{dt} \right)^2 + \frac{1}{\rho_l R} [P_G + P_M + P_{EC} + P_0 + P_{AC} + (P_E) + P_{VS} + P_{VL}]$$

$$\frac{dn_g}{dt} = \frac{2SD_a}{\xi} \left( C_g - \frac{P_g}{k_H} \right)$$

where it is important to note that  $P_E$  is a charge dependent quantity. Further explanation of the terms and further accompanying equations are detailed in [193].

By focusing on the evolution of membrane charge density and applying cycle averaging and other mathematical techniques, a highly efficient and physiologically interpretable variant of the NICE model was derived – the multiScale Optimized Neuronal Intramembrane Cavitation (SONIC) model [195].

Alternatively, stress-induced ion channels' mechanosensitivity has also been suggested as a possible biophysical mechanism by which mechanical waves may induce neural activity. This theory is simple in nature, and

supported by strong empirical evidence at the cellular level [196, 197]. However, it lacks universality, as it intrinsically depends on the heterogeneous mechanosensitivity of various types of ion channels expressed across nervous systems. Moreover, the driving force responsible for the hypothesized membrane stress has yet to be clarified. Acoustic radiation force has been shown to play a significant role in neuromodulatory effects in *in vitro* and *ex vivo* studies [194, 198], and therefore received strong support in the community. However, the high US frequencies used in these studies ( $> 10$  MHz) contrast with the low US frequencies used to trigger significant neuromodulatory effects *in vivo* [10]. Consequently, a predictive mathematical model based on this mechanical hypothesis has yet to be formulated.

### 2.3 NEEDS, LIMITATIONS, AND THESIS MOTIVATION

Based on the reviewed literature, the following needs and limitations of hybrid EM / FUS-neuro modelling for therapeutic applications in CNS and PNS neuromodulation were identified:

- Computational modelling of therapeutic applications typically focus on determination of physical exposure. This is particularly true for modelling in the context of treatment planning. However, physical exposure metrics (such as field- or pressure-strength) are not always strongly correlated with the physiological impact. It is important to also model the resulting physiological impact – even if only to identify a suitable exposure metric that can serve as safety and / or efficacy estimator. Improved mechanistic insights resulting from hybrid modelling have repeatedly revealed that previously considered exposure quantities are not suitable. The presented thesis work systematically employs hybrid physico-physiological modelling approaches.
- Computational modelling necessarily simplifies the represented reality. However, the acceptability of the degree of simplification is rarely investigated in the context of hybrid neuromodulation modelling.
  - *EM*: The simulated dielectric models typically feature a small number of distinguished tissues, a strongly simplified anatomical geometry, and assume isotropic, homogeneous dielectric properties throughout a given tissue. For example, in spinal cord modelling the important anisotropy of neural tissue is frequently not represented at all, or only considered in overly simplistic 2.5D models, where longitudinal and transversal directions can easily

be distinguished. Head models for transcranial EM stimulation modelling usually only distinguish scalp, bone, cerebro-spinal fluid, as well as white and grey brain matter. The insulating impact of dura, the different skull layers, and the important conductivity differences between skin, fat, and muscle in the scalp are rarely considered. Spinal cord models neglect the crucial role of spinal roots and rootlets, which have a highly patient-specific geometry that crucially affects stimulation and stimulation selectivity. In this thesis, work on generating more realistic and detailed EM models (in terms of 3D anatomy and dielectric property distributions) is performed and the importance of accurate anisotropy representation is quantified.

- *FUS*: The difficulty of predicting the magnitude, focality, secondary hot-spots, and focus location in transcranial FUS application, as well as the potentially valuable contribution that computational modelling could make in this regard, have long been recognized, and modelling is frequently performed. Nevertheless, the computational prediction of transcranial FUS remains unreliable. This thesis systematically investigates the assumption that the lack of reliability is due to oversimplified representation of the sonication device and the skull heterogeneity.
- *Neuro-electrophysiology*: Neuron or network models of relevance to the intended neuromodulation must be realistically embedded in their anatomical environment to simulate meaningful exposure conditions (not just intensity, but also its heterogeneous distribution, especially when elongated axons are concerned). This requires the establishing of complex neuro-functionalized anatomical models that include representative fiber trajectories and the dynamics of excitatory and inhibitory neurons in networks. Such neuro-functionalized models are exceedingly rare, and need to be developed. A range of neuro-functionalized models for specialized purposes (e.g., retinal neuroprosthetics, SCS for locomotion restoration, acoustic neuromodulation of brain activity) are established and investigated in the presented thesis work. It remains to be seen, if models of more general applicability can be developed in the future, or if such models continue to be application-specific.
- *Verification, validation, sensitivity analysis, and uncertainty quantification*: When modelling is applied for therapeutic (e.g., treatment optimiza-

tion) or regulatory (e.g., device safety and efficacy assessment) purposes, a high degree of reliability is required. The modelling tools must be verified (i.e., ascertaining that the intended model is correctly implemented) and validated (i.e., ascertaining that the chosen model accurately represents reality within its intended context of use), and the factors which most strongly impact the modelling must be understood (sensitivity analysis), and hence must be highly controlled and accurately modelled. The uncertainty associated with model predictions must be quantified. For computational modelling of neuromodulation and the underlying (e.g., acoustic) exposure modelling, little verification, validation, and uncertainty quantification has been performed, and no systematic sensitivity analyses have been found in literature, prior to this thesis' work.

- *Personalized treatment optimization*: Large inter-subject variability is characteristic of the neuromodulation field. Nevertheless, the use of personalized modelling remains limited and tedious manual adjustment over a long time period is frequently required to personalize and optimize stimulation parameters. Placement of implants relies on expert knowledge and is hardly guided by systematic physico-physiological assessment. Furthermore, multipolar stimulation electrode arrays promise more targeted stimulation – however, heuristic, trial-based optimization is hardly possible, due to the large number of involved stimulation and steering parameters. Hence, an important aspect of the work in this thesis is the study of image-based personalized model creation and the development of efficient, physiological impact driven treatment optimization. That work also informed the optimization of SCS implant design.
- *Mechanistic understanding*: Mechanistic understanding is not only required to gain understanding of the underlying principles of neuromodulation, but also to reliably assess treatment risk and to optimize treatment efficacy. In this thesis, insights into the mechanisms behind neuromodulation applications such as retinal neuroprosthetics, acoustic neuromodulation of brain activity, spinal-cord stimulation for the restoration of locomotion to paraplegics are sought.
- *Complexity of implementing hybrid modelling*: The few groups that have performed hybrid physico-neurophysiological modelling had to establish complicated pipelines involving a large number of independently developed own and third-party tools for that purpose. An

framework that integrates all steps facilitates usability, and allows improvements / addition of components (e.g., addition of specialized methods for anatomical model generation and neuro-functionalization – as developed in the present work for SCS) to easily benefit the entire pipeline. This thesis has pursued the integration of complete workflows for the image-based modelling of EM- and LIFUS-neuro-modulation.

These needs and limitations motivated and guided the work presented in this thesis. Important progress on all of these points was achieved.



## MODELLING FRAMEWORK

---

### 3.1 SIM4LIFE

#### 3.1.1 *Framework*

*Sim4Life* is an advanced computational life sciences platform developed by the IT'IS Foundation in collaboration with ZMT Zurich MedTech AG (Zurich, Switzerland). It has been developed to enable multi-physics simulations within complex anatomical environments and encompasses a range of dynamic tissue and physiology models. The platform features detailed presegmented anatomical models, such as the IT'IS Virtual Population models [199], a medical image-segmentation framework for the creation of patient-specific models, geometric (computer aided design – CAD) modelling functionalities, high-performance computing-enabled physics solvers (electromagnetism, acoustic, thermal, flow, etc.), integrated neuronal dynamics modelling, analysis and visualization functionalities, and a *Python* scripting framework, as well as a range of specialized modules (e.g., for implant safety assessment).

#### 3.1.2 *Quasistatic EM modelling*

A range of quasistatic EM solvers have been developed that are optimized for the simulation of low-frequency exposure of large, highly heterogeneous, and geometrically irregular models, such as anatomical body models. These solvers are implemented in C++ and high-performance computing-enabled through message passing interface (MPI) parallelization. The PETSc [200] library is used for preconditioning and solving.

Two families of solvers exist: solvers for (i) structured (rectilinear) meshes and solvers for (ii) unstructured meshes. They can be further distinguished according to the simplifications of Maxwell's Equations that are employed to facilitate simulations in the low frequency regime (for efficiency or stability reasons). For the work in this thesis, the 'Ohmic Current-Dominated Electro-Quasistatic Solver' is employed in its structured and unstructured variants.

It solves the equation:  $\nabla\sigma\nabla\phi = 0$  with Neumann or Dirichlet boundary conditions, where  $\phi$  is the electric potential and  $\sigma$  is the electric conductivity.

### 3.1.3 Acoustic modelling

*Sim4Life* provides a GPU-accelerated acoustic solver. It solves the linear acoustic pressure wave equation (LAPWE) [17]:

$$\rho\nabla\frac{1}{\rho}\nabla p - \frac{1}{c^2}\frac{\partial^2 p}{\partial t^2} - \frac{\tilde{a}}{c^2}\frac{\partial p}{\partial t} = 0$$

$$\tilde{a} = 2\alpha\sqrt{\frac{\alpha^2 c^4}{\omega^2} + c^2}$$

where  $\rho$  is density,  $c$  is speed-of-sound,  $\alpha$  is attenuation,  $p$  is pressure,  $t$  is time, and  $\omega$  is angular frequency. The solver implements a finite-differences time-domain (FDTD) scheme, which is well suited to deal with complex anatomical models.

### 3.1.4 Neural modelling

*Sim4Life* integrates the *NEURON* solver from [160] for the simulation of compartmental neuron models. These can be defined through a *Python* interface or through a hoc file. Ion channel dynamics can be inserted by defining and precompiling corresponding functions and mechanisms, as specified in mod files. *Sim4Life* facilitates the coupling of electric potentials and fields with neuronal dynamics through the ‘extracellular potential’ mechanism of *NEURON*, to permit simulation of EM-induced neuromodulation. Furthermore, *Sim4Life* provides a range of predefined fiber models, allowing users to define spline-trajectories that are then automatically converted into parameterized compartmental axon models (myelinated and unmyelinated).

### 3.1.5 Acoustic neuromodulation

An efficient approach to model the impact of acoustic exposure on neural activity, based on the membrane sonophore cavitation hypothesis [193], has been co-developed by IT’IS [195]. It parameterizes the ion channel dynamics to represent an ‘effective’ dynamics that depends on sonication intensity and duty cycle. The cavitation mechanism hypothesis – i.e., the

assumption that closed intramembrane compartments that oscillate due to the periodic pressure variation and related gas transfer result in temporal variations of the membrane capacitance, which in combination with the nonlinearity of membrane electrophysiology leads to a net current – has been found to be well suited in predicting neurostimulation and neural inhibition for a certain range of acoustic intensities [10]. At high intensities, radiation pressure appears to dominate. The effective channel dynamics can be precomputed and stored as look-up tables, which are evaluated in dedicated *NEURON*-mechanisms that are specified in `mod`-files.

### 3.2 EXTENSIONS

A range of *Sim4Life* extensions were implemented within the framework of this thesis:

- Neural tissues can display strong *anisotropy* (i.e., up to a factor 10 higher longitudinal than transversal electrical conductivity). Therefore, the low-frequency EM simulation framework (pre-processing, solving, post-processing, GUI) was extended to also handle tensorial electrical conductivities  $\vec{\sigma}$ . This also affected the computation of derived quantities (such as current density  $\mathbf{j} = \vec{\sigma} \cdot \mathbf{E}$  from the electric field  $\mathbf{E}$ ).
- Modelling of electrical conduction or acoustic properties *heterogeneity*, can be crucial e.g., for transcranial sonication modelling (see Chapter 8). For that purpose, support for heterogeneous material maps has been added to *Sim4Life*. Initially, binning into a discrete number of material classes (solver preprocessing) was implemented, which is readily compatible with all the available postprocessing. However, to support heterogeneous anisotropy maps that are required for the SCS simulations (see Section 3.3), the *Sim4Life* low-frequency EM solver framework was extended to also handle heterogeneous material properties.
- For the investigation of non-linear acoustic effects, frequency-mixing / higher-harmonics formation, a solver for the Westervelt–Lighthill Equation (WLE) has previously been implemented into *Sim4Life* at IT'IS [17]. The WLE model's dispersion and frequency mixing ex-

tended the LAPWE equation through additional terms. The WLE equation is reproduced below:

$$\rho \nabla \frac{1}{\rho} \nabla p - \frac{1}{c^2} \frac{\partial^2 p}{\partial t^2} + \frac{\delta}{c^4} \frac{\partial^3 p}{\partial t^3} + \frac{\beta}{2\rho c^4} \frac{\partial^2 p^2}{\partial t^2} = 0$$

where  $\delta$  is the diffusivity of the medium and  $\beta$  is the nonlinearity coefficient. The WLE solver implementation was suffering from stability issues that could only be addressed using very small time-steps. The formulation has been revised and both a modified stencil and update-scheme were implemented, resulting in considerably improved stability behavior. Analytical analysis was used to establish a stability criterion for the time-step. A Fourier-like approach has been implemented to convert the transient signal of any simulation period into complex phasors at multiples of the carrier frequency.

- To achieve a performance level of the acoustic solver that permits simulations with the required large number of degrees-of-freedom, *multi-GPU* hardware accelerated parallelization was implemented with a performance increase of two orders of magnitude.
- *User-defined sources* were implemented to enable the simulation of transient, non-sinusoidal pressure-sources. The user can either specify an analytical expression or provide a time-series for the source scaling.
- To make use of symmetries and thus reduce the computational domain, periodic and mirror *boundary conditions* were implemented in the acoustic solver to complement the existing Perfectly Matched Layers (PML) boundary conditions. The different boundary conditions can be flexibly combined.
- For the needs of the detailed and realistic SCS simulations performed in the context of neuroprosthetics for paraplegics (see Section 3.3), a powerful *meshing* tool for the discretization of complex anatomical domains with thin features and layers (spinal roots, semi-insulating membranes) and irregular shapes was developed by the *Sim4Life* development team. Some minor contributions have been made to this development as part of this thesis.

### 3.2.1 Verification of the heterogeneous anisotropy modelling

In order to verify the implementation of heterogeneous tissue properties and the support for anisotropy in the quasi-static solver framework, the

'Method of Manufactured Solutions' (MMS) was employed (published in parts in [201]).

Solver features that require verification are: (i) the correct solving of the underlying equation ( $\nabla \cdot \bar{\sigma}(x) \nabla \phi(x) = 0$ , where  $\bar{\sigma}$  is the conductivity tensor and  $\phi$  is the electric potential from which the electric field is obtained as  $\mathbf{E} = -\nabla \phi$ ), (ii) the convergence to the precise solution with increasing refinement and stricter convergence tolerance criteria, (iii) the correct handling of sharp dielectric interfaces, and (iv) proper implementation of boundary conditions (Dirichlet and Neumann).

To verify (i) and (ii), the MMS was used: a  $\bar{\sigma}$  distribution and a reference solution  $\phi_{ref}(x)$  are defined, allowing the analytical determination of a source distribution  $S(x) := \nabla \cdot \bar{\sigma}(x) \nabla \phi_{ref}(x)$ . Subsequently, the equation  $\nabla \cdot \bar{\sigma}(x) \nabla \phi(x) = S(x)$  is solved using the LF FEM solver and the obtained  $\phi(x)$  can be compared to  $\phi_{ref}(x)$ . Four MMS cases with spatially varying sources and / or conductivities were created: one isotropic with spatially varying source  $\bar{\sigma}$  (CaseIa), one homogeneous anisotropic with spatially varying source  $\bar{\sigma}$  (CaseIb), one heterogeneous anisotropic  $\bar{\sigma}$  (CaseIc), and one heterogeneous anisotropic with spatially varying source  $\bar{\sigma}$  (CaseId). In all cases, a cube with 1 mm edge length is simulated. Care was taken for CaseId to ensure that both the orientation of the conductivity tensor eigenvectors and the corresponding eigenvalues varied spatially, while the latter remained larger than zero. To verify (iii) and (iv), a discontinuous case (CaseII) with scalar  $\sigma$  was implemented where the left half of the cube was assigned a three times larger conductivity than the right half. The left side was fixed (Dirichlet) to 0 V, the right to 1 V, and the other four sides were treated as insulating (Neumann). The reference solution has 0.75 V at the interface with linear variation from there to the left and right sides. In all cases, simulations were performed using second order tetrahedral meshes at four resolutions ranging from 0.05–0.3 mm (200–24 000 elements; in some cases also 0.02 mm, 300 000 elements) to ascertain convergence. The error was quantified as maximal deviation from the reference solution.

The exact equations solved for the different cases are presented below.

#### CASEIA *Isotropic diffusion, spatially varying source*

The diffusivity tensor was defined as:

$$\sigma = 1$$

and the potential function (theoretical and expected) as:

$$\varphi = x^3 - z^3$$

The solver solves the following equation:

$$\nabla \cdot (\sigma \nabla \varphi') - S_0 = 0$$

(note that the prime does not denote a derivative, but rather the unknown potential). With the source term:

$$S_0 = \nabla \cdot (\sigma \nabla \phi) = 6(x - z)$$

The problem was solved in a rectangular box mesh, centered at 0 with edges of length 1 discretized by 7146 second order tetrahedral elements. The mesh for  $\varphi$  and  $\varphi'$  was kept constant across all verification cases. For the boundary conditions, we set:

$$\varphi(x, y, z)|_{\Omega} = \varphi'(x, y, z)|_{\Omega}$$

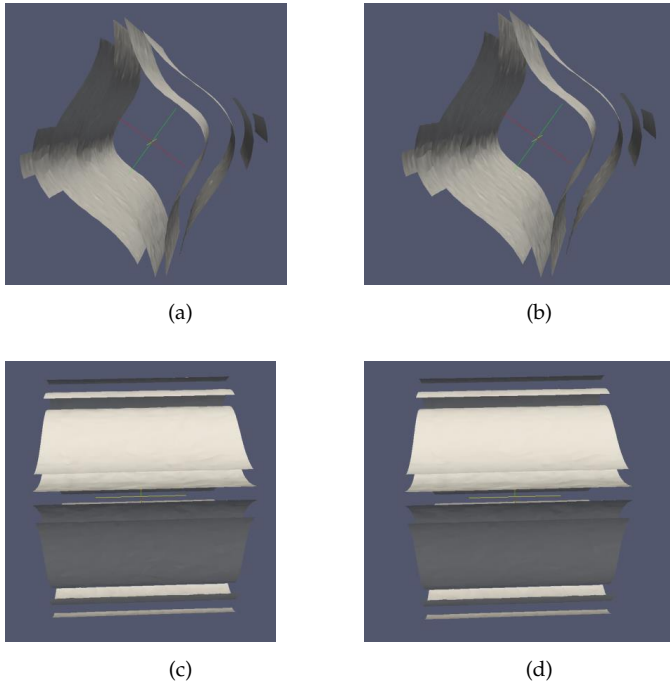


FIGURE 3.1: Expected (left) and numerical (right) solutions for CaselA: *isotropic diffusion, spatially varying source*.

CASE1B *Anisotropic diffusion, spatially varying source*

The diffusivity tensor is changed to:

$$\bar{\sigma} = \begin{bmatrix} 1 & 0 & 0 \\ 0 & 1 & 1 \\ 0 & 1 & 1 \end{bmatrix}$$

The remaining parts of the equations remain unchanged.

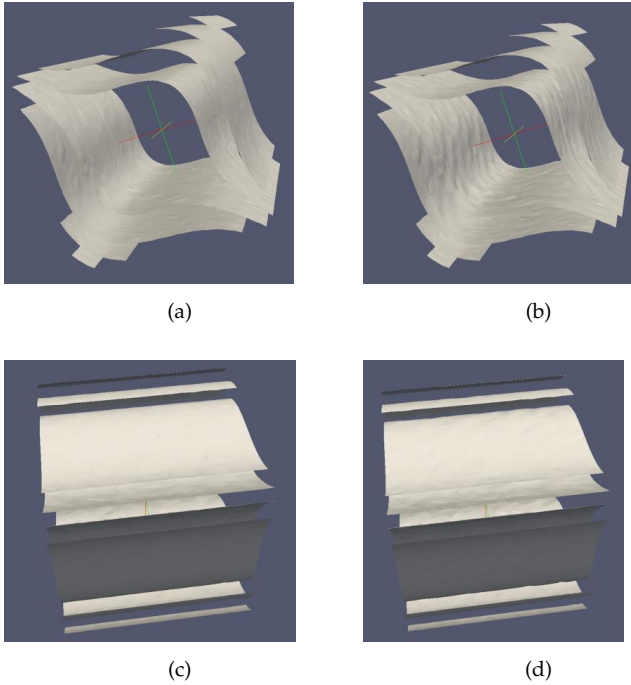


FIGURE 3.2: Expected (left) and numerical (right) solutions for Case1b: *anisotropic diffusion, spatially varying source*.

CASE1C *Spatially varying anisotropic diffusion, constant source*

The equations are given by:

$$\bar{\sigma} = \begin{bmatrix} z^2 + 0.1 & 0 & 0 \\ 0 & y^2 + z^2 + 0.1 & z^2 \\ 0 & z^2 & x^2 + 0.1 \end{bmatrix}$$

$$\varphi = -x + z$$

$$S_0 = \nabla \cdot (\bar{\sigma} \nabla \phi) = 0$$

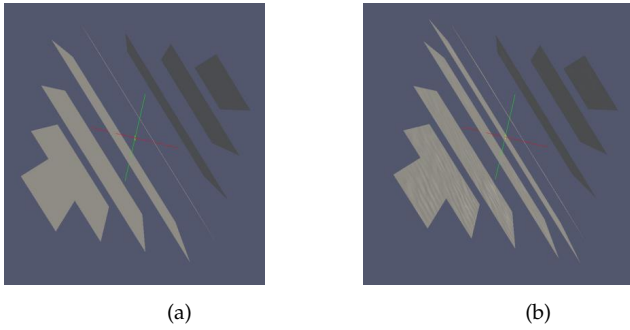


FIGURE 3.3: Expected (left) and numerical (right) solutions for CaseIc: *spatially varying anisotropic diffusion, constant source*.

CASEID *Spatially varying anisotropic diffusion and source*

The equations are given by:

$$\bar{\sigma} = \begin{bmatrix} \sigma_{xx} & 0 & 0 \\ 0 & \sigma_{yy} & f_1 \\ 0 & f_1 & \sigma_{zz} \end{bmatrix}$$

$$\varphi = x + y + z$$

$$S_0 = 2x + 4zf_6^2 - 4zf_5f_6 - 4zf_4f_6 + 4zf_3f_6$$

$$= 2zf_4f_5 - 2zf_3f_5 - \frac{2zf_4f_6^2}{f_5} + \frac{2zf_3f_6^2}{f_5}$$



where:

$$\sigma_{xx} = x^2 + 0.1$$

$$\sigma_{yy} = (4x^2 + 1.2) f_1 - (2z^2 + 1.1) (f_2 - 1)$$

$$\sigma_{zz} = (2z^2 + 1.1) f_2 - (4x^2 + 1.2) (f_2 - 1)$$

$$f_1 = \frac{\sqrt{1 - f_2} (1000x^4 + 500x^2z^2 - 55x^2 - 500z^4 + 65z^2 - 2)}{250}$$

$$f_2 = (x^2 + z^2 - 0.08)^2$$

$$f_3 = 2z^2 + 1.1$$

$$f_4 = 4x^2 + 1.2$$

$$f_5 = \sqrt{1 - f_6^2}$$

$$f_6 = x^2 + z^2 - 0.08$$

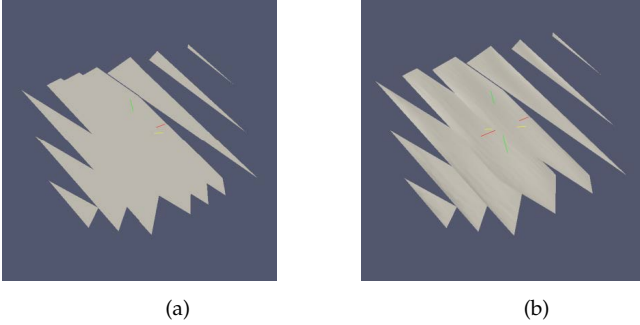


FIGURE 3.4: Expected (left) and numerical (right) solutions for CaseId: *spatially varying, anisotropic diffusion and source*.

The above expressions were derived in order to ensure a diffusion that is always positive on the given mesh. This was achieved as follows: the first row and first column of the matrix are set. Then, a submatrix  $\sigma$  is derived that always provides positive eigenvalues across the domain. For this, a real symmetric matrix is constructed by using an orthogonal matrix and

a diagonal matrix with the targeted eigenvalues of the resulting matrix (spectral decomposition):

$$\begin{aligned}
 a &= x^2 + z^2 - 0.08 \\
 U &= \begin{bmatrix} a & \sqrt{1-a^2} \\ \sqrt{1-a^2} & -a \end{bmatrix} \\
 V &= \begin{bmatrix} 4x^2 + 1.2 & 0 \\ 0 & 2z^2 + 1.1 \end{bmatrix} \\
 \sigma &= \begin{bmatrix} 2 & 3 \\ 2 & 3 \end{bmatrix} = U^T V U
 \end{aligned}$$

### 3.2.1.1 Results

All four cases CaseIa-d showed the expected exponential convergence to the reference solution as evident in log-log plots of maximum deviation against resolution that can be fitted linearly with an  $R^2 > 0.998$  (see Figure 3.5 for the convergence of CaseIc). All resolutions of CaseII result in maximum deviations of  $< 3 \times 10^{-7}$  V, limited by the adaptable solver convergence tolerance criterion.

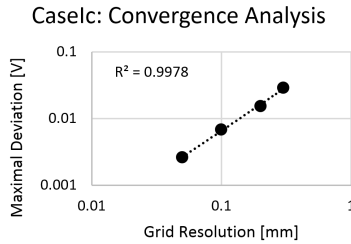


FIGURE 3.5: Exponential reduction of error due to solution convergence with increasing mesh refinement, shown for CaseIc.

The verification demonstrates the correctness of the heterogeneous anisotropic LF FEM solver implementation. For more detail on the verification of the coupled EM-neuro modelling, see [201].

### 3.3 SPINAL CORD STIMULATION TO RESTORE LOCOMOTION

#### 3.3.1 *Background*

Spinal cord injury can interrupt communication between the brain and the neuro-muscular system, potentially resulting in an inability to control and elicit motion. Recently, a unique approach, based on SCS, has been developed to trigger motion units that are hard wired in the spinal cord with the correct temporal dynamics, resulting in regained locomotion [9]. It is assumed that the underlying mechanism is based on inducing neural activity in spinal-roots, selectively and in the right sequence, to mimic proprioceptive input to the spinal cord, triggering, in return, the right sequence of motion patterns.

For that purpose, highly selective stimulation of individual spinal roots is required, which can be achieved by implanting a suitable multi-contact stimulation electrode in the spinal epidural space [202]. Computational modelling has been used within the European RESTORE consortium (<https://www.eurostars-eureka.eu/project/id/10889>; partners: Foundation For Research On Information Technologies In Society (IT<sup>2</sup>S), Ecole Polytechnique Federale De Lausanne (EPFL), Universitair Medisch Centrum Utrecht, G-Therapeutics B.V., ZMT Zurich Medtech AG) to personalize and optimize treatments (required to achieve the necessary root stimulation selectivity), to develop a suitable implant electrode geometry that is capable of such selective stimulation, and to assess the impact of anatomical variability throughout the patient population on treatment efficacy, and to confirm that the chosen electrode design is sufficiently broad to cover the bulk of the relevant population.

Full publication of the RESTORE modelling work is currently planned for the end of 2020 and results are still embargoed. Therefore, only selected technical results can be presented in this thesis.

#### 3.3.2 *Method*

##### 3.3.2.1 *Anatomical model generation (EPFL)*

RESTORE partners at EPFL have developed an image segmentation pipeline combining classic computer vision approaches with machine learning and template-based segmentation to transform optimized MRI and CT images of a patient's spine into a detailed geometric model, distinguishing white

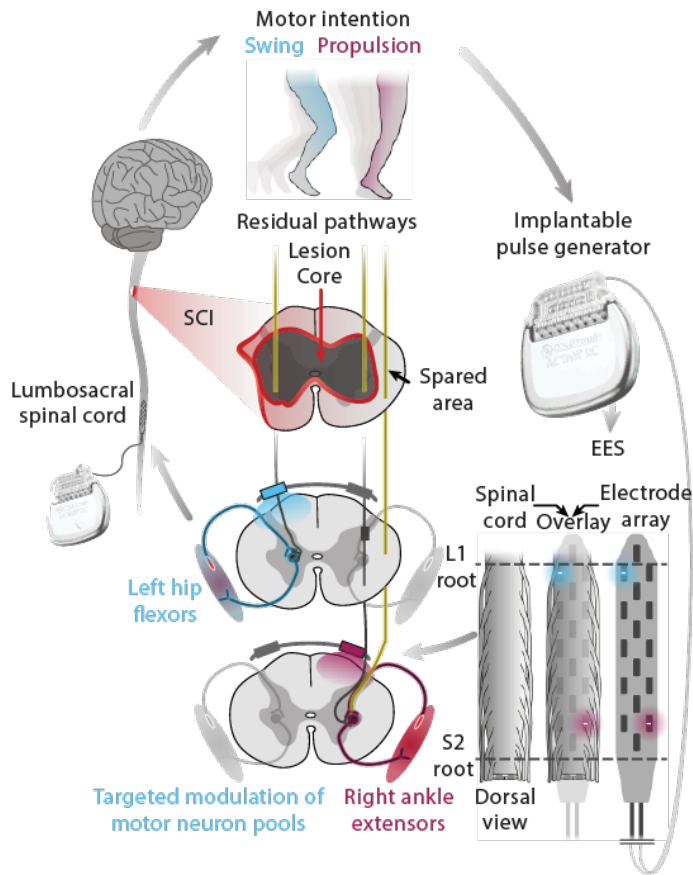


FIGURE 3.6: Illustration of the use of SCS to compensate for lost supra-spinal input.

and grey spinal cord matter, spinal roots, cerebrospinal fluid, spinal dura mater, epidural fat, and vertebrae (see Figures 3.6–3.9).

A stimulator electrode model is inserted in the epidural space of the model and its position is parameterized. The electrode features a large number of contacts (see Figure 3.8) which can be assigned individual voltages and parameterized for the purpose of treatment optimization.

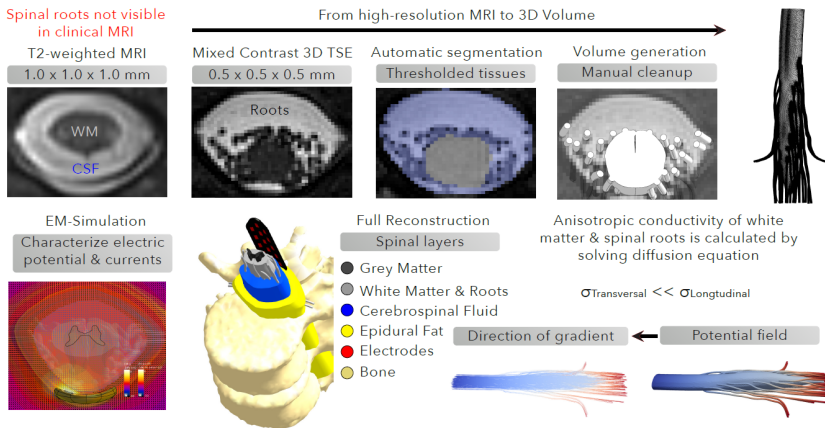


FIGURE 3.7: The steps from medical image data to patient-specific stimulation selectivity predictions.

### 3.3.2.2 Tissue property assignment

While most of the tissue properties are assigned according to the IT'IS tissue properties database [155], a special approach had to be established to properly model the spinal roots and white matter. These tissue feature very high anisotropy, with principal electrical conductivity direction aligned with the fiber orientation. Due to the complex, curved shape of these structures, it is not easily possible to define an associated curvilinear coordinate system.

This challenge has been addressed by performing a diffusion simulation that is restricted to the root and white matter domains. For this, the low-frequency EM solver is used in combination with a constant scalar conductivity  $\sigma_C$  to solve the equation  $\nabla \sigma_C \nabla \phi_H = \sigma_C \Delta \phi_H = 0$  and obtain a helper potential  $\phi_C$ . The boundary conditions of the diffusion problem are set to insulating, except for the rostral end of the spinal cord white matter, where a Dirichlet boundary condition  $\phi_H = 1$  is set, and the caudal end of the spinal cord white matter, where – as for the spinal root endings – a

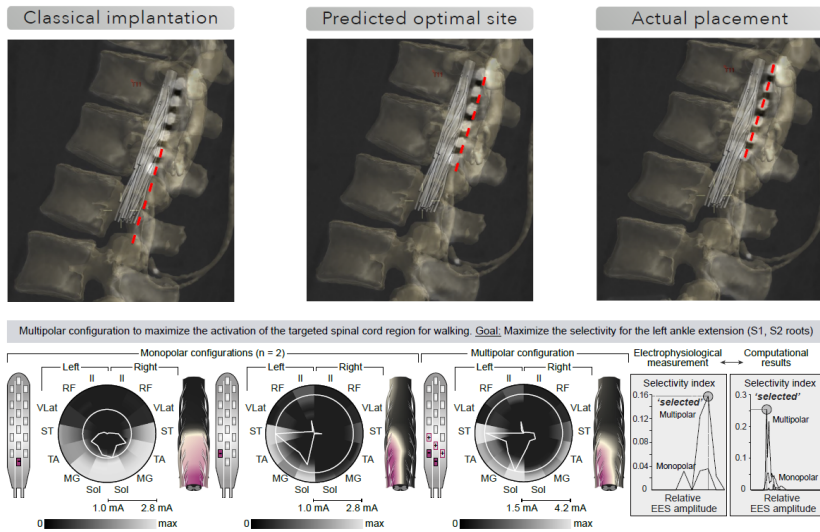


FIGURE 3.8: Simulation-based optimization of implant positioning (top) and electrode voltages (bottom). The simulation-based optimized placement differed greatly from the expert-suggested optimal site and was found to produce vastly superior stimulation selectivity. Similarly, simulation-based multipolar stimulation configurations result in superior selectivity than achievable using monopolar stimulation, as experimentally confirmed.

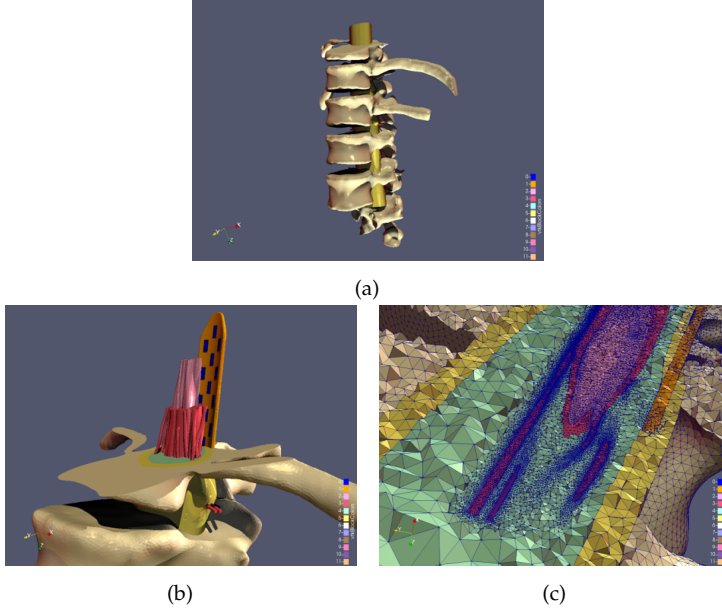


FIGURE 3.9: Unstructured tetrahedral meshes of the spinal cord stimulation setup.

Dirichlet boundary condition  $\phi_H = 0$  is assigned. The orientation of the gradient  $\nabla\phi_H = -\vec{E}_H$  is used as principal axis of the conductivity tensor  $\vec{\sigma}$ , which is computed according to  $\vec{\sigma} = \sigma_l \cdot P + \sigma_t \cdot (I - P)$  ( $\sigma_l, t$  are the longitudinal and transversal conductivity values,  $P = (\vec{E}_H \otimes \vec{E}_H) / (\vec{E}_H \cdot \vec{E}_H)$  is the normalized projection matrix along the direction  $E_H$ , and  $I$  is the identity matrix).

### 3.3.2.3 Fiber integration

The helper potential  $\phi_H$  is also used to identify fiber trajectories. For that purpose, streamline tracing of  $\nabla\phi_H$  was performed using *vtk* [203]. Seed points were placed randomly following a top-hat distribution at the end cross-sections of the spinal roots. Streamlines that exit the root or white matter domains are discarded (see Figure 3.10). *Sim4Life* functionality is employed to convert the remaining streamline trajectories into parameterized Sweeney fiber models [158] or motor and sensory MRG models [159]. At least 10 fibers were modelled per spinal root, and up to 100 fibers where the resolution was sufficient (see Figure 3.11).

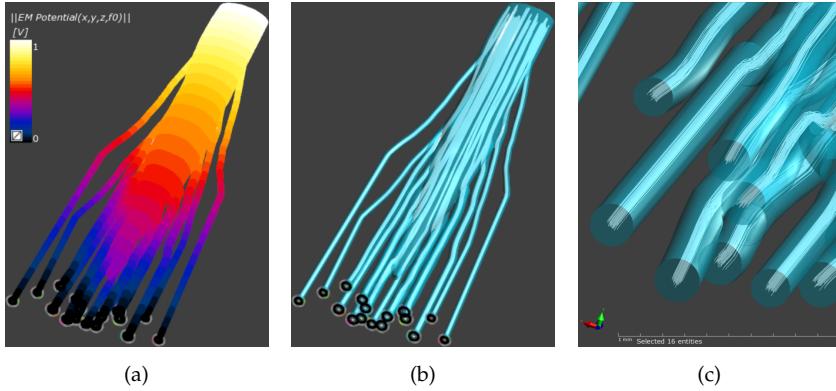


FIGURE 3.10: (A) Helper Potential  $\phi_H$ , used to define the conductivity tensor orientations and for fiber tracking, with seed points at base of roots. (B) Tracked root fibers and (C) close-up.

#### 3.3.2.4 EM simulation

Based on the dielectric property distributions obtained using the approaches from Section 3.3.2.2, ohmic current-dominated E-QS simulations were performed, prescribing the voltages at the different electrode contacts as boundary conditions (insulating boundary conditions at the domain boundaries).

#### 3.3.2.5 Neuro simulation

Neuro-electrophysiology simulations according to the Sweeney model were performed and the *Sim4Life* titration functionality was used to establish fiber-recruitment curves for the different spinal roots.

Pulse shape was biphasic and done in accordance with the pulses available with the implantable pulse generator (IPG; Medtronic PLC, Dublin). Pulse phase was altered to observe its impact on recruitment patterns.

#### 3.3.2.6 Optimization

To perform automatic optimization of the electrode contact steering parameters, the contact voltages were parameterized. Subsequently, the genetic optimization for global optimization variant of the *Sim4Life* optimization framework was used, in combination with the selectivity index goal function from [204] (see Figure 3.12).



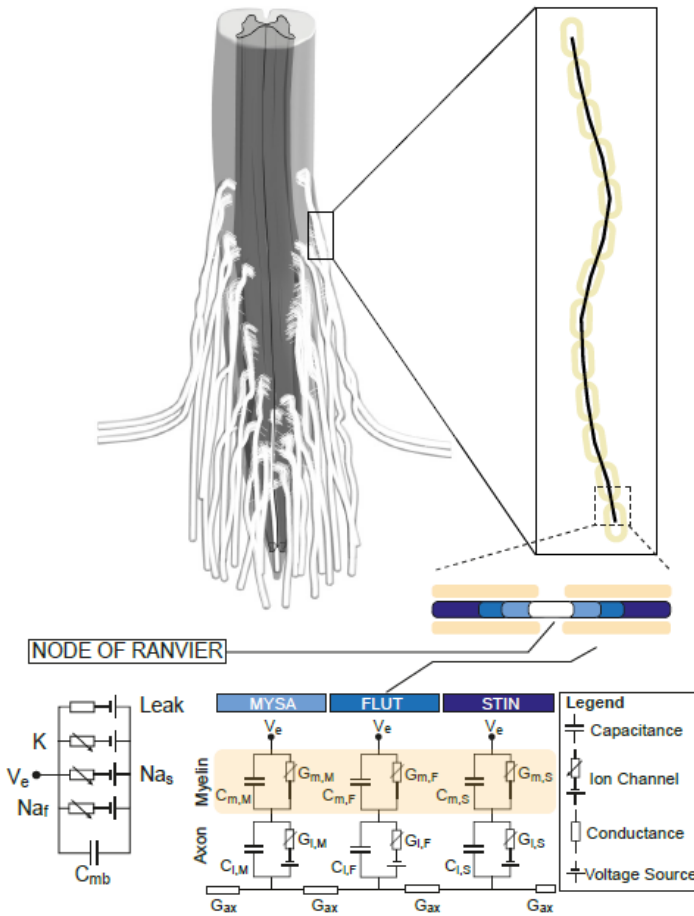


FIGURE 3.11: Spinal cord model with fiber trajectories along roots. Close up of discretization of single fiber, its different compartments, and equivalent circuit model.

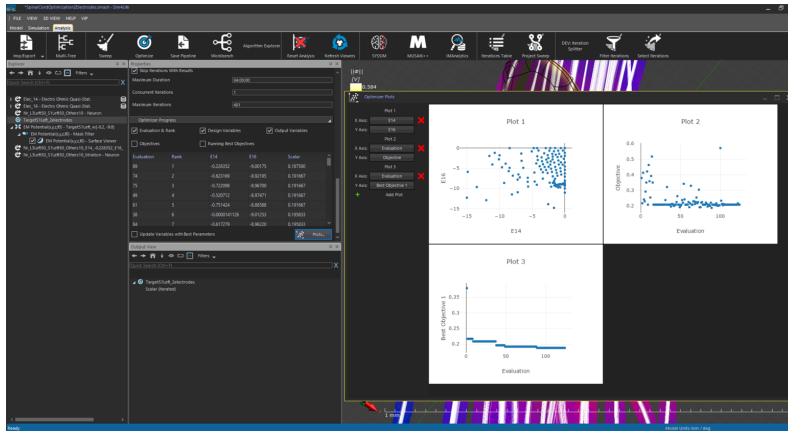


FIGURE 3.12: Implementation of the SCS optimization within *Sim4Life* and illustration of optimization convergence (bottom graph), along with the performance of two optimization goals.

Electrode lead placement is optimized by varying its position in 5 mm steps. Approximately 10 positions are evaluated and selectivity indices, consisting of the euclidean distance between desired recruitment and actual recruitment for the L<sub>1</sub>, L<sub>2</sub>, L<sub>4</sub>, S<sub>1</sub>, S<sub>2</sub> roots are computed (these roots are primarily responsible for Iliopsoas, vastus lateralis (VLat), tibialis anterior (TA), medial gastrocnemius (MG), and soleus (Sol) muscle activation, respectively). The coarsely identified 5 mm interval with the highest selectivity is then further refined with 1 mm steps and the optimal position is identified.

To achieve and accelerate convergence, a preselection of candidate contacts was performed by determining selectivity indices for all combinations of electrode contact configurations (on / floating / ground). Thus, we restricted the parameter space during the genetic optimization step.

While pulse-shapes were not optimized, the established framework would readily allow for that possibility.

### 3.3.3 Results

Detailed results of the RESTORE project, including the medical follow-up of the treated patients, will be part of a forthcoming publication targeted for end of 2020. The following illustrative results, obtained by the RESTORE

project partners, serve to highlight the value of the established modelling approaches:

- The treatment modelling functionality has played a fundamental role in allowing the successful restoration of locomotion to paraplegics [9].
- The model predictions about spinal root activation selectivity could be experimentally confirmed by measuring EMG activity in key muscles after single pulse application in an inter-operative and post-operative setting.
- Computational modelling was also used to design a dedicated electrode that replaced the previously employed commercial electrode. Besides spatially rearranging the electrode contacts, an additional contact belt was added, as it was predicted to have important benefits in stimulation targeting (validated in rodents). The therapeutic performance of the original implant design was compared to that of the redesigned implant, demonstrating therapeutic benefits of the redesign.
- Optimized implant placement and steering parameters were predicted that were very different from the treatment parameters the surgeons would have selected. Subsequent experimental analysis confirmed the important superiority of the simulation-based optimized treatment parameters.

### 3.4 CONCLUSIONS

*Sim4Life* is a powerful platform for the modelling of EM and acoustic (ultrasound) exposure, as well as induced neuromodulation. The following important extensions of the platform were developed for the purpose of this thesis and carefully verified: support for anisotropic and heterogeneous materials, non-linear acoustic propagation modelling, multi-GPU solver acceleration, user-defined (non-sinusoidal) sources, extended boundary conditions, and unstructured mesh generation. The extended platform functionality has played a critical role in enabling restoration of locomotion to paraplegics through SCS (as part of the European RESTORE project) by providing patient-specific treatment planning and optimization, as well as device optimization capabilities.



## DEVELOPMENT OF AN ALPHA RETINAL GANGLION CELL MODEL OF EXTRACELLULAR STIMULATION

---

### ABSTRACT

Retinal ganglion cells are the primary stimulation target of epiretinal electrode prostheses, as their action potentials encode the visual signals to the brain. Coupled electromagnetic / neuron-electrophysiology simulations involving faithful ganglion cell models with realistic physiology could support prosthetic device design multi-physics models and safety / efficacy assessments / optimization. However, most ganglion cell models have been constructed by combining cell morphologies and ion channel distributions obtained from different neuron types. In this study, we apply whole-cell recording, simultaneously measure intracellularly the biophysical behavior of OFF-alpha rabbit ganglion cells, and use epiretinal electrodes to determine spatial stimulation threshold maps to extracellular current pulses. We immunolabeled the recorded alpha ganglion cells and reconstructed them through confocal microscopy and then utilized the measured action potential phase plots and spike trains to estimate the ion channel distributions and generate computational *NEURON* models. Several alpha cell models were evaluated with a novel electromagnetic (EM)-induced neurostimulation platform, which combines an existing, well validated, EM solver and the open-source *NEURON* modelling package. Modelling revealed three electrode location dependent stimulation mechanisms (listed in order of increasing threshold): initial segment stimulation (potentially mediated by a low threshold sodium channel), axonal stimulation at locations of high field inhomogeneity, and extracellular stimulation of dendritic termini (potentially a modelling artifact). Simulated, location-dependent, extracellular current pulse action potential stimulation thresholds were compared to measurements on the same cell. The computationally predicted threshold magnitude spatial maps and experimental measurements agree within the combined (experimental and measurement) uncertainty, thereby validating the ganglion cell *NEURON* model and the novel EM-induced neurostimulation platform.

## NEW AND NOTEWORTHY

Retinal ganglion cells are the stimulation target of many retinal prostheses. Modelling this computationally can support device development and safety / efficacy assessment. We developed detailed rabbit OFF-Alpha ganglion cell *NEURON* models by combining cell-type specific whole-cell recording and confocal microscope reconstructions. The models and a novel simulation platform for coupled EM-neurophysiology were validated by epiretinal stimulation experiments, including careful uncertainty assessment. Stimulation sensitivity maps are established and different activation mechanisms are identified.

## 4.1 INTRODUCTION

Retinal ganglion cells are the main stimulation target of epiretinal prosthesis electrodes, as their axons send action potentials to the visual areas of the brain. However, the current models of epiretinal electrode extracellular stimulation of ganglion cells do not analyze these properties on single ganglion cells as the biophysical properties of ganglion cell types differ [205–208]. Currently, many extracellular ganglion cell stimulation models are generated by incorporating voltage-gated channels and ganglion cell morphologies taken from different species and retinal eccentricities [209–211]. In this paper, we have developed rabbit ganglion cell models of epiretinal stimulation that are based on the actual physiologically recorded properties of alpha retinal ganglion cells and then validated the model against the recorded extracellular activation properties (e.g., spatial maps of stimulation current thresholds) of ganglion cells exposed to extracellular epiretinal stimulation by large, prosthetic-sized stimulation electrodes near the inner retinal surface.

The alpha ganglion cell is a morphological type present in many mammalian species [212–214] with similarities to the magnocellular retinal ganglion cell, their anatomical homologue in human and primates. It has a large soma, a wide dendritic field, and a large-diameter axon with a fast conduction velocity [215]. Here, we have used the whole-cell recording technique to selectively record from OFF-center alpha retinal ganglion cells. The biophysical properties of a small group of OFF-alpha cells were measured, and the dendritic arborizations of two recorded cells have been reconstructed with confocal microscopy. *NEURON* models were developed based on the measured stimulation data with incorporation of a low thresh-

old initial segment zone on the alpha cell axon [216, 217]. These models, when compared to the extracellular stimulation data of two alpha cells by means of whole-cell recording, produced phase plot profiles and electrical stimulation sensitivity profiles similar to the data measured in the real cells. The main goals of this paper are to:

- Present the development of morphologically and electrophysiologically detailed alpha ganglion cell models, based on the morphology and electrophysiology from single cells.
- Validate these retinal ganglion cell models by comparing simulations of the measurement setup against the experimentally measured data, specifically electrode stimulation ganglion cell thresholds, pulse shape, and transmembrane voltage traces.
- Apply these models to study mechanisms involved in stimulation of alpha ganglion cells and study the sensitivity of stimulation thresholds to a range of parameters to assess simulation and measurement uncertainty.
- Use the measurements and simulations to validate and demonstrate the applicability of our newly developed simulation platform for coupled electromagnetic-neuronal dynamics modelling [201].

## 4.2 METHODS

### 4.2.1 Preparation

Dutch belted rabbits (2–3 lbs) were anesthetized with ketamine-xylazine (35–50 mg/kg, 5–10 mg/kg), in accordance with an animal protocol approved by the Food and Drug Administration (FDA) Institutional Animal Care and Use Committee (IACUC). The eyes were denucleated and the retina was isolated under dim red light. The isolated retina was attached to nitrocellulose filter paper which had 3 mm holes in it, mounted over fine nylon mesh, and perfused with Ames Ringer's solution [218] which contained the following salts (in mM): NaCl, 120; KCl, 3.1;  $\text{KH}_2\text{PO}_4$ , 0.5;  $\text{NaHCO}_3$ , 23.0;  $\text{Mg}_2\text{SO}_4$ , 1.2;  $\text{CaCl}_2$ , 1.15; and 26 vitamins and amino acids (US Biologicals, Salem, MA). The Ringer's solution was allowed to flow by gravity at a rate of approximately 5 mL/min and was heated to 35°C with an in-line heater just before entering the retinal chamber. The temperature was monitored with a thermocouple at the entrance to the chamber. To

visualize the ganglion cell bodies, the isolated retina was stained with dilute 0.006% Azure B vital dye [219]. The retinal terminal axon bundles from the optic radiations were oriented to the left of the viewing field using a Zeiss Axioskop FS upright microscope equipped with IR Normarski interference contrast illumination, a rotating stage, a 40× water-immersion objective lens, and an infrared (IR) surveillance camera / monitor.

#### 4.2.2 *Recordings*

Whole-cell recordings of ganglion cells were made using borosilicate glass patch electrodes (1.5 mm outer diameter, 0.9 mm inner diameter, 5–7M $\Omega$ ) held in a Model 5177 Eppendorf micromanipulator (Eppendorf, Hamburg, GE), a DAGAN 3900A patch-clamp amplifier (Dagan Corp, Minneapolis, MN), and the pClamp 10 data acquisition program (Molecular Devices, Sunnyvale, CA). The potassium-based internal solution (pH 7.2) contained (in mM): potassium methanesulfonate, 120; KCl, 4; MgCl<sub>2</sub>, 2; HEPES, 5; EGTA, 5; glutathione, 1; NaATP, 1; NaGTP, 0.5; all reagents were obtained from Sigma-Aldrich (St. Louis, MO). In addition, 0.05% lucifer yellow, lithium salt (Invitrogen, Grand Island, NY) was added to the internal solution for visualization and labeling of the recorded ganglion cell. To target an alpha cell for whole-cell recording, a small hole was made in the inner limiting membrane on the side opposite the axon bundles with a patch electrode to allow membrane access. Whole-cell recordings in current clamp mode were digitized at 25 kHz with a Molecular Devices Digidata 1440A data acquisition system (Molecular Devices Corp, Sunnyvale, CA). Cell resting potentials used AgCl as the reference electrode and were corrected for a liquid junction potential of 7 mV [220, 221].

#### 4.2.3 *Extracellular stimulation*

A Pt-Ir stimulus electrode 100  $\mu$ m in diameter insulated with a thin  $\sim$ 10  $\mu$ m layer of Epoxylite resin was placed opposite the recording electrode and used to stimulate the ganglion cell extracellularly. The conducting disc electrode surface (FHC Inc., Bowdoin ME), was beveled at an angle of 30° relative to the retinal surface, and positioned 50  $\mu$ m above the surface of the inner limiting membrane of the retina. The X/Y position of the stimulus electrode was controlled by computer (MP285 Sutter Instruments, Novato CA). To determine the action potential threshold at each point tested around the cell body, a model A395 linear stimulus isolator (WPI,



Inc., Sarasota FL) was used to generate an ascending series of ten 0.5 ms biphasic current pulses (2 or 4  $\mu\text{A}$  increments) with a 20 ms interphase period, under computer control. A long 0.25 mm diameter Pt-Ir wire in the bath served as the counter electrode. See Figure 4.1 for a schematic representation of the experimental setup.

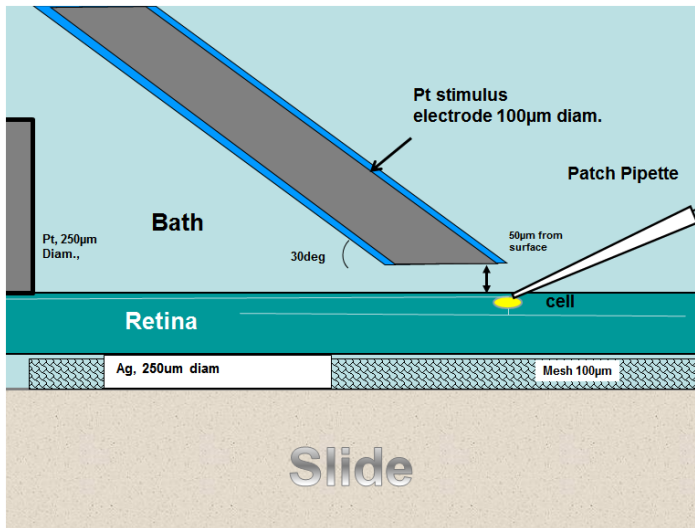


FIGURE 4.1: Schematic diagram of the platinum stimulation electrode and the patch pipette used for whole-cell recording alpha retinal ganglion cells in the isolated rabbit retina.

#### 4.2.4 Immunohistochemistry

After whole-cell recording, the alpha cell dendritic morphology of the Lucifer yellow filled cell was visually confirmed by means of epifluorescence microscopy, and the cell was photographed with a digital camera. The retina was removed and placed in 4% paraformaldehyde fixative in phosphate buffer overnight at 4°C. To recover the complete dendritic morphology of the recorded ganglion cell, we used a modified anti-Lucifer yellow antibody immunolabeling technique [222, 223]. The retina was washed 3 times in phosphate-buffered saline (PBS) (Sigma-Aldrich, St. Louis, MO), incubated in 0.5% Triton X-100 in 6% normal goat serum (NGS) in PBS for 2 hours, then incubated at room temperature (RT) for 2 days in Invitrogen anti-

lucifer yellow biotin tagged antibody (Thermo Fisher Scientific, Waltham, MA), diluted 1:500 in PBS with 3% NGS and 0.5% azide. To visualize the antibody, the retina was washed 6 times in PBS with 3% NGS, then incubated overnight in Alexa 488 streptavidin secondary label (Jackson ImmunoResearch, West Grove, PA) 1:100 in PBS with 3% NGS. After 6 washes in PBS, the retina was mounted on a slide in Fluoro-Gel (Electron Microscopy Sciences, Hatfield, PA), a coverslip was added, and it was examined for fluorescent immunolabeled recorded ganglion cells. After processing, four alpha retinal ganglion cells were recovered for morphological analysis.

#### 4.2.5 *Morphological reconstruction*

The immunolabeled alpha cell dendritic arborizations were reconstructed on an Olympus Fluoview 1000 confocal microscope at 20 $\times$  magnification as a series of 0.6  $\mu$ m Z-section image stacks. In some cases, the retinal borders were also post-labeled with the red nuclear dye propidium iodide. The dendritic morphologies of the 2 alpha ganglion cells were manually digitized from the confocal image stacks with the NeuroLucida reconstruction program (MBF Neuroscience, Williston VT). The resulting files were exported and edited to generate hoc ganglion cell morphology files for import into the *NEURON* modelling program [224].

#### 4.2.6 *NEURON ganglion cell model*

##### 4.2.6.1 *Simulation and fitting*

Custom *MATLAB* (The Mathworks, Natick, MA) scripts were used to convert pClamp *ascii* files of the real ganglion cell spikes recorded during depolarizing current steps into phase plot files for reading in the *NEURON* vector file format. Using the *NEURON* graphical interface, the real alpha ganglion cell action potentials were displayed as spike phase plots which allowed direct comparison in real-time to the phase plot spikes generated from the model alpha ganglion cell ion channel conductance mechanisms. A modified 5-channel Hodgkin and Huxley (H-H) model [156, 225, 226] with an additional low threshold initial segment sodium channel was used to fit the real cell impulse spiking properties to current steps and the spike phase plots to the model cell (see Tables 4.1 and 4.2). The simulation step for most preliminary fits was 0.001 ms; we also investigated simulation steps of

$1 \times 10^{-4}$  and  $1 \times 10^{-5}$  s. The phase plots of the same model data for the 3 integration time steps are superimposable, which suggests negligible error, however the final figures and fits reported herein are made from the data sets of the  $1 \times 10^{-4}$  s step.

#### 4.2.6.2 Coupled EM-neuronal dynamics modelling

Coupled electromagnetic-neuronal dynamics modelling of the experimental setup has been performed to help validate the computational ganglion cell model and to gain an understanding about the underlying mechanisms, the parameters that impact measured and simulated retinal stimulation thresholds, and their related experimental uncertainties. The mechanistic insights and sensitivity analysis aided our understanding of the electrode position-dependent extracellular EM exposure-induced ganglion cell activation by stimulus electrode pulses (see Figure 4.7 and Table 4.3). The setup allowed the *NEURON* ganglion cell model obtained to be evaluated against the actual whole-cell recorded ganglion cell extracellular stimulation thresholds. EM and neuronal dynamics models were set up within the computational life sciences simulation environment of *Sim4Life* (developed jointly with ZMT Zurich MedTech AG, Zurich, Switzerland).

#### 4.2.6.3 EM model of ganglion cell stimulation

The computational model of the experimental stimulation setup consists of a planar layer that represents the isolated retina in a saline bath solution and a stimulus electrode (see Figure 4.7). The dimensions and placement of the Pt stimulus and return electrode, including their insulation, are as shown in Figure 4.1 and these were modelled as perfect electrical conductors. The retinal thickness, conductances, and dielectric parameters (see Table 4.1 and 4.2) were derived from [227] and electrical conductivities values of 0.357 S/m for the sensory retina and 1.282 S/m for the saline were assumed [227]. The large pore size nylon mesh support was modelled as saline. The simulations were performed with the *Sim4Life* ‘Ohmic Current Dominated Electro-Quasistatic’ solver, which solves the equation  $\nabla \sigma \nabla \phi = 0$ , where  $\sigma$  is the electrical conductivity and  $\phi$  is the electric potential from which the electric ( $E$ -) field can be obtained as  $\mathbf{E} = -\nabla \phi$ . This quasi-static approximation is valid, as the following criteria are satisfied:  $\omega^2 \epsilon \mu d^2 \ll 1$  and  $\omega \sigma \mu d^2 \ll 1$ ; i.e., the wavelength is large compared to the characteristic domain length  $d$ ; where  $\omega$  denotes the angular frequency,  $\epsilon$  the permittivity,  $\mu$  the permeability; and  $\sigma \gg \omega \epsilon$ ; i.e., ohmic currents

dominate over displacement currents. Dirichlet boundary conditions were applied to the electrode, and the current flux density was integrated over a surface enclosing one electrode for current normalization purposes. The computational domain was discretized with a graded rectilinear mesh of 21 million voxels; the minimal grid step in the region surrounding the neuron model and the stimulation electrode was 0.02 mm, and the coarsest grid step in regions with mostly constant potential was 1.25 mm. A grid convergence study was performed to ascertain that the discretization and the convergence tolerance criterion, a relative reduction of the residuum by 8 orders of magnitude, was found sufficient.

#### 4.2.6.4 *Neuronal dynamics model*

The neuronal dynamics was modelled with the T-NEURO module of *Sim4Life*, which uses the integrated *NEURON* library [224] to unidirectionally couple EM fields to electrophysiological modelling by means of the ‘extracellular mechanism’ of *NEURON* [201]. The ganglion cell morphology and channel distribution model developed above was imported, embedded within the retinal layer at a depth of 5  $\mu\text{m}$  from the inner limiting membrane surface, and shifted relative to the electrode to investigate the dependence of the stimulation thresholds on lateral position in 20  $\mu\text{m}$  step increments over a range of 0.8 mm in both X-Y plane directions to cover the neuron area. Titrations (bifurcation search for spike threshold) were performed to identify the extracellular stimulation thresholds and current strengths, and in each case, the spatial location of the spike initiation at the threshold level was recorded.

#### 4.2.7 *Sensitivity analysis*

To evaluate the impact of modelling parameters on the stimulation threshold, the depth of the neuron within the retina, the thickness of the retina, the electrical conductivities of the retina and the saline solution, the distance from the electrode to the retina, the position and the relative angle of the electrode over the retina, diameter of the electrode and the insulation, and the simulation resolution were assessed, also over a range of 0.8 mm but with a coarser step-size of 0.1 mm. Subsequently, the change in the stimulation threshold was assessed for each electrode placement location. By dividing the threshold changes (in dB) by the parameter change, the sensitivity factors were determined. Multiplication of the sensitivity factors with the uncertainty of the underlying parameters yielded the contribu-

tion to the stimulation threshold uncertainty. The discretization related numerical uncertainty was assessed by comparing a simulation with finer resolution (grid step reduction factor  $1.5\times$ ) with the reference simulation. The parameter values, sensitivities, underlying parameter uncertainties, and contributions to the uncertainty in the stimulation threshold examined, as well as the combined simulation uncertainty, is reported in Tables 4.3–4.5. The combination of the measurement and simulation uncertainty produces the total uncertainty, which also serves as the criterion for the success of the validation. The uncertainty analysis was performed according to the approach described in [228].

## 4.3 RESULTS

### 4.3.1 *Measurement results*

We targeted large ganglion cell bodies for whole-cell recording by pre-labeling the retinal ganglion cells with dilute Azure B vital dye (see Figure 4.2). Access to the ganglion cell bodies was obtained by loosening a patch of the inner limiting membrane on one side adjacent to the cell body, opposite from the axon fibers from the optic radiations. The patch pipette was filled with a potassium-based Ringer’s solution and a fixable Lucifer yellow dye, which allowed identification post-recording of the alpha cell morphology using the epifluorescent illumination of the microscope. We recorded from 5 alpha cells, and their resting potentials averaged  $-61.4 \pm 5.5$  mV. After biophysical characterization, stimulation, fixation and immunocytochemical processing of the cells, we were able to recover the complete axonal arborizations and dendritic trees of 4 cells (see Section 4.2.5). These all had large cell bodies averaging  $30.7 \pm 3.8$   $\mu\text{m}$  ( $n = 4$ ), and a wide field dendritic morphology as originally described for rabbit alpha ganglion cells by [213] and as type G11 by [229]. The light-response of the 5 ganglion cells studied in cell-attached or whole-cell configurations all showed transient firing at light-OFF. Each of the 4 recovered ganglion cells had thick ascending primary dendrites with dendritic arbors that averaged  $907.3 \pm 148.6$   $\mu\text{m}$  in diameter. Confocal microscopic reconstructions of the dendrites showed arborization in the OFF-sublamina of the inner plexiform layer (IPL).

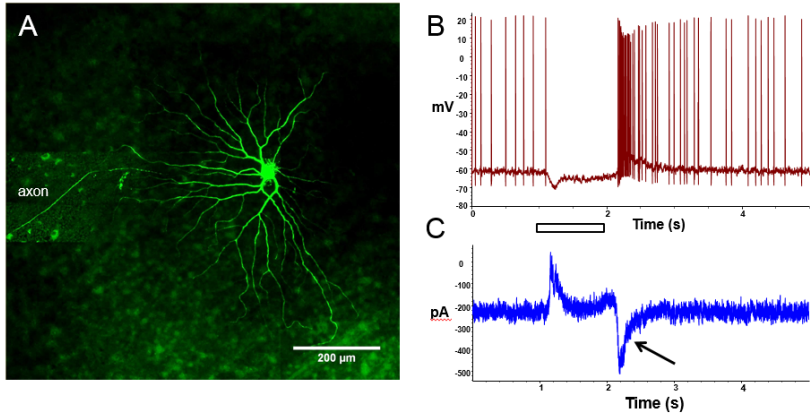


FIGURE 4.2: Examples of reconstructed OFF-alpha ganglion cells whole-cell recorded and their light-evoked responses. (A) Confocal microscopic Z-stack reconstruction of an immunostained whole-cell-recorded alpha ganglion cell, showing the typical wide-field dendritic tree morphology and large cell body (Cell 1). The overlying ganglion cell's axon is shown as an inset on the left side of the image. (B) Light-evoked action potentials of the alpha retinal ganglion cell shown in A recorded in current clamp mode to full field stimulation showed a hyperpolarization at light-ON and a transient depolarizing burst of spikes at light offset. (C) Voltage clamp recording of another OFF-alpha cell shows an outward current at light-ON, and an inward excitatory current at light-OFF, similar to those reported in the cat [206].

### 4.3.2 Estimating ion channel distribution

We examined the kinetics of the real alpha cell action potential using phase plot analysis to estimate the voltage-gated channel distributions in the axon, soma, and dendrites of the *NEURON* model. We previously showed that phase plots of  $dV/dT$  vs.  $V$  of the spikes for a ganglion cell recorded at the soma is functionally equivalent to the ganglion cell capacitive membrane current in  $\mu\text{A}/\text{cm}^2$  (given the membrane capacitance  $C_m = 1 \mu\text{F}/\text{cm}^2$ ). This allows direct comparison and fitting of the real alpha cell phase plot to its *NEURON* model to estimate ion channel distributions directly in *NEURON* [226]. To avoid any possible influence of depolarization on the action potential shape or multispikes adaptation mechanisms, we chose to analyze either spontaneous action potentials of the alpha cell at rest or spikes to small current steps to make an accurate fit. Each spike appeared to be followed several milliseconds later by a small, delayed afterdepolarization [230]. An example of the fitting process is shown in Figure 4.3. The phase plots of all axon-bearing alpha cells showed a prominent initial segment-somato dendritic (IS-SD) break at the action potential threshold. The peak  $dV/dT$  of the alpha cells was  $0.6\text{--}0.9 \text{ V/ms}$  ( $\mu\text{A}/\text{cm}^2$ ).

A single action potential of the recorded alpha ganglion cell and the corresponding spike action potential phase plot, compared with that of the *NEURON* model of the action potential are superimposed in Figure 4.3. Alpha ganglion cell action potentials were very rapid, with half-widths of  $180\text{--}250 \mu\text{s}$  at  $35^\circ\text{C}$ . The action potential model of [226] provided a good fit to real alpha cell data along the main portion of the phase plot curve [226]. A careful balance of sodium and potassium channel densities was used to start the empirical fitting process. At  $35^\circ\text{C}$ , the size of the loop reflected largely the sum of the magnitudes of voltage-gated sodium current  $I_{\text{Na}}$  and delayed rectifier channel densities  $I_{\text{K}}$  on the soma and dendrites. The positive peak velocity of the phase plot loop reflected the density of voltage-gated sodium channels on the soma and dendrites, while the negative peak velocity reflected the balance of the soma and dendrite potassium channels. Voltage-gated calcium currents appear to contribute weakly to the peak voltage of the action potential, while calcium-activated potassium and A-type currents had little effect on phase plot shape.

While the Fohlmeister model [226] provides a good fit to the main portion of the action potential phase plots, there was one region where the model did not appear to provide a good fit to the real anatomical and physiological data. Phase plots of the alpha cell action potentials often display

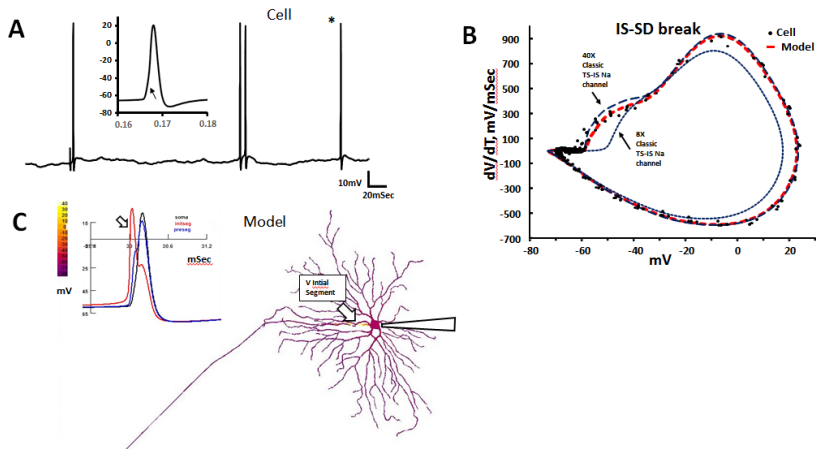


FIGURE 4.3: Example of the process for fitting the ganglion cell action potentials to generate the alpha cell models in *NEURON*. (A) Raw spike data of alpha cell 1 (see Figure 4.2a) to a 180 pA current step generated weak action potentials. Inset: A single action potential (\*) is shown. The sloped rising phase of the action potential (arrow) denotes the IS-SD break. (B) Spike phase plot of the real action potentials (black dots) compared to data of the *NEURON* model (red trace) show close correspondence when a sodium channel mechanism with a lower threshold is incorporated in the axon's initial segment. Black dashed phase plot curves show attempts to match the IS-SD break with different classic H-H Na channel model initial segment current densities. (C) *NEURON* model voltage plot of the reconstructed ganglion cell 1 responding to spike activation (arrow) by a depolarizing current pulse of 600 pA injected in the soma with the patch electrode (right). Note the trigger segment region or initial segment (color scale in mV at the left) has the lowest threshold for sodium channel spike activation (yellow zone) compared to the cell body shown in the voltage plot box. The action potential then simultaneously back propagates into the soma / dendrites and down the axon from the trigger initial segment zone. Inset: Comparison of action potential activation from the initial segment (red trace), into the presegment region (blue trace), and into the soma (black trace).



IS-SD breaks (see Figure 4.3a). Such a break is currently thought to reflect a high density of low-threshold sodium channels in the axon initial segment; originally detected by means of immunocytochemistry [216]. Work by [217] reported that the initial segment of rabbit ganglion cell axons also exhibit a high sodium channel density immunolabeling in this region. Confocal reconstructions of all our axon-bearing rabbit alpha ganglion cells showed that the axon exited the cell body without the constricted axon diameter region trigger segment (TS) previously reported in ganglion cell models based on amphibian ganglion cells [205, 225]. The thickness range of the alpha cell axons was 1.9–2.2  $\mu\text{m}$ . While an IS-SD bump could be generated by increased axonal conductance of H-H Na channels in the unconstricted trigger segment region of the axon, the recorded IS-SD breaks of the real ganglion cell spike phase plots (red traces) could not be reproduced, except at very high IS channel densities (see Figure 4.3b). Therefore, we incorporated in our alpha ganglion cell models an initial segment axon zone of low-threshold sodium channels similar in location and width to the high sodium channel density region reported by [217], shown in Tables 4.1 and 4.2. We refer to this trigger segment region of the axon as the initial segment (IS), where the action potentials initiate and propagate down the axon and also back through the pre-segment to elicit a regenerative spike in the soma and dendrites [231].

On real alpha cell phase plots, spike threshold averaged  $-57.6 \pm 5.5$  mV ( $n = 4$ ). However, the model H-H Na channel phase plot based on the channel kinetic densities of [226] had a spike voltage onset of  $-53$  mV. A comparison of the actual ganglion cell threshold data and the model suggested a threshold voltage difference of approximately 5 mV. We found that the best way to fit the actual IS-SD bump was to develop a voltage-shifted H-H model of a NaV1.6 sodium channel found in these initial segment regions with gating variables shifted 5 mV more negative than normal (see Figure 4.3, and Tables 4.1 and 4.2) [216, 232]. The development of this empirically estimated inner segment Na channel mechanism is shown in Figure 4.3 with phase plot comparison of the final model (red dashed curve) to the real ganglion cell phase plot spike data (black dots). In initial attempts to model the IS-SD activation, we used a trigger segment of classic H-H channels similar in channel density to those used in [226], which resulted in a model ganglion cell that needed large stimulus currents to reach spike threshold. The use of a classic H-H Na trigger segment channel density of  $\sim 800$  mS/cm<sup>2</sup> resulted in a diminished phase plot cycle of smaller amplitude spikes shown in Figure 4.3b (inner circle, fine dashed

line). While an extreme increase of  $40\times$  the normal density of H-H sodium channels could match the observed IS-SD spike activation voltage of the real cell, but resulted in a slight overshoot of the IS-SD hump in the phase plot (course dashed lines).

### 4.3.3 Spike adaptation in alpha cells

Current vs. spike frequency (f-I) curves were studied on all alpha cells whole-cell recorded. A series of 100 pA steps of depolarizing current were injected to analyze their firing patterns. Figure 4.4 shows examples of the firing patterns to large current steps of real and model alpha cells. In real cells, positive current injections caused action potentials to be evoked, and spike adaptation was observed (see Figure 4.4a), similar to previous reports for alpha ganglion cells in the cat retina [208, 233]. Similar to previous descriptions of alpha cells, the alpha cell membrane resistance was low:  $13.3 \pm 3.4 \text{ M}\Omega$  ( $n = 5$ ).

We used a 173 ms, 900 pA current step to analyze the spike adaptation kinetics of 5 alpha ganglion cells. On average, alpha cells fired  $8.2 \pm 3.4$  spikes, (mode 7,  $n = 5$ ) during the step. The adaptation kinetics of the spike trains were analyzed by binning the current step spike responses. Spike times during the current step were divided into 8 bins and normalized to the total spikes during the step. The spiking probability pattern of 5 ganglion cells were normalized and then multiplied by the average to indicate the average number of spikes per time bin. While there was often an initial burst of spikes at the step onset, the spiking rapidly declined to one spike per bin during most of the current step (see Figure 4.4c). The alpha cell calcium clearance mechanism time constants were adjusted to modulate the calcium-activated potassium currents in the model to show a similar spike adaptation pattern to the current pulse step as in the real cells (see Figure 4.4b, and Tables 4.1 and 4.2).

Phase plot analysis of real alpha cell spikes during the current injection step revealed that spikes with the largest and most negative activating IS-SD breaks occurred at step onset from the resting potential (blue curve, arrow), while spikes evoked later in the step at more positive potentials showed less IS-SD break (red curves), even though the repolarization phase of these action potentials were nearly as negative as the initial spike (see Figure 4.4d). On all cells displaying IS-SD breaks, current steps from more negative potentials evoked larger spikes and IS-SD breaks. Phase plots of 4 cells showed the first spike threshold to the current step averaged  $59.1 \pm 3.7 \text{ mV}$ .

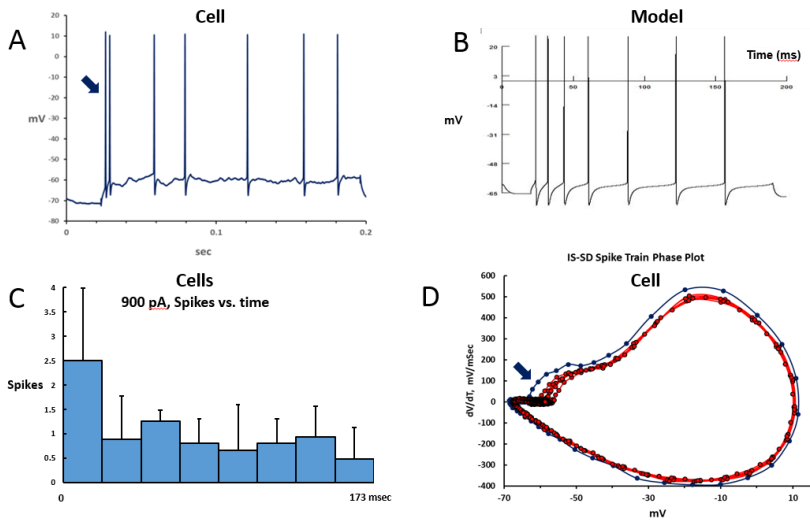


FIGURE 4.4: Comparison of the spiking properties of real and model alpha retinal ganglion cells. (A) Real recorded alpha cell action potentials generated by a 900 pA, 173 ms current step show spike adaptation (alpha cell 2). (B) Model alpha cell action potentials to the same 900 pA step also adapt. (C) Average spike probability histogram of real alpha cells to the same current pulse step: bars: mean  $\pm$  SD,  $n = 5$  cells. (D) Phase plots of real alpha cell action potentials during the current step (same cell as in A). Compared to the initial current step (blue trace), the IS-SD break onset voltages of the action potentials (arrow) become more positive later in the spike train (red traces).

In contrast, phase plots of the model alpha cell action potentials showed no spike adaptation in their IS-SD break onset voltage during the current step (data not shown).

#### 4.3.4 *Extracellular electrode stimulation*

Extracellular electrode stimulation using biphasic current pulses, also evoked IS-SD breaks when action potentials were elicited (see Figure 4.5). To better visualize the current phase generating the action potential during whole-cell recording, a short duration current pulse of 0.5 ms was used in combination with a 20 ms interphase interval to separate the cathodic and anodic phase contributions. We found that action potentials were elicited only when cathodal stimulation pulses were used [234]. The extracellular stimulation action potential phase plots often showed a prominent loop below the IS-SD break due to the cathodic stimulus pulse artifact, particularly on ganglion cells with higher stimulus current thresholds (see Figure 4.5c). We examined the extracellular stimulation spike threshold on 4 axon-bearing OFF-alpha ganglion cells with the 100  $\mu\text{m}$  diameter Pt insulated electrode 50  $\mu\text{m}$  above the surface of the retina with an ascending series of biphasic current pulses. Starting at the cell body / IS region, the spatial sensitivity of the spike threshold of a cell was determined in 100  $\mu\text{m}$  increments across the retina in a T-shaped pattern; the completeness of which depended on the duration of the whole-cell recording (see Figure 4.6). Examination of regions to the right of the cell body were physically blocked by the patch recording electrode. At the cell body / IS region, extracellular stimulation spike threshold averaged  $6.0 \pm 4.1 \text{ nC}$  ( $n = 4$  cells). In four cells, we studied the stimulation spike threshold along the axis near the estimated axon, which declined 200  $\mu\text{m}$  from the soma IS starting location. The precise axon direction could be determined only after histological processing post-recording, as only the orientation of the fine axon fiber bundles near the ganglion cell body were visible in the infrared (IR) viewer during recording. In two cells, we were able to study stimulation thresholds along 3 axes around the cell body that suggested threshold declined away from the cell body / IS region (see Figure 4.6). The results of these stimulation studies suggested that the lowest threshold zone of stimulation is a region at or near the cell body / IS itself.

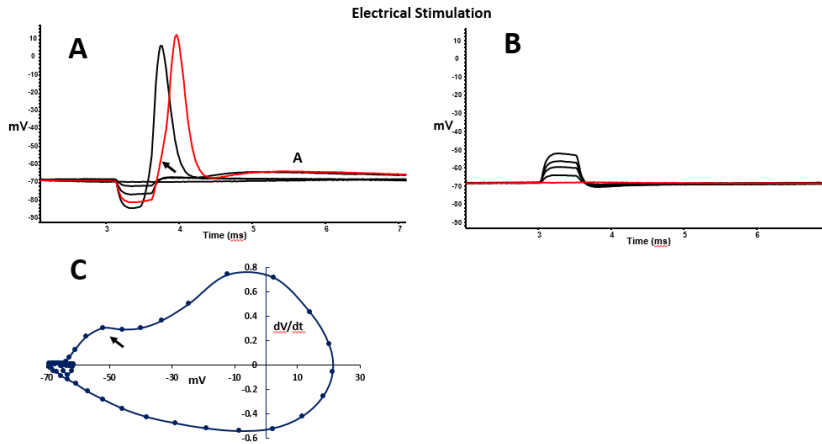


FIGURE 4.5: Comparison of action potentials generated by 0.5 ms steps of cathodic and anodic extracellular stimulation electrode current pulses. The stimulus electrode location was  $100\ \mu\text{m}$  down the axon (left) from the starting location (soma / IS). Same cell (cell 2) as in Figure 4.6. (A) Cathodic stimulus pulses elicited action potentials, with the red trace showing the first spike. Action potentials from cathodic stimulation showed a lagged rise time (arrow) during the onset of the action potential and a small post-spike after-depolarization was observed at A (see also Figure 4.3a) [235]. Traces have been aligned at the mean pre-stimulus resting potential for clarity. (B) Anodic pulses up to  $28\ \mu\text{A}$  did not elicit any action potentials on any cell studied. (C) Phase plot of a single cathodic-evoked stimulus electrode action potential on an alpha cell ( $8\ \mu\text{A}$ ) showed a prominent negative IS-SD break activating at  $-63\ \text{mV}$  in the waveform (arrow). Same cell as in Figure 4.2. Similar IS-SD breaks were seen on all stimulation sites tested eliciting action potentials ( $n = 5$  cells).

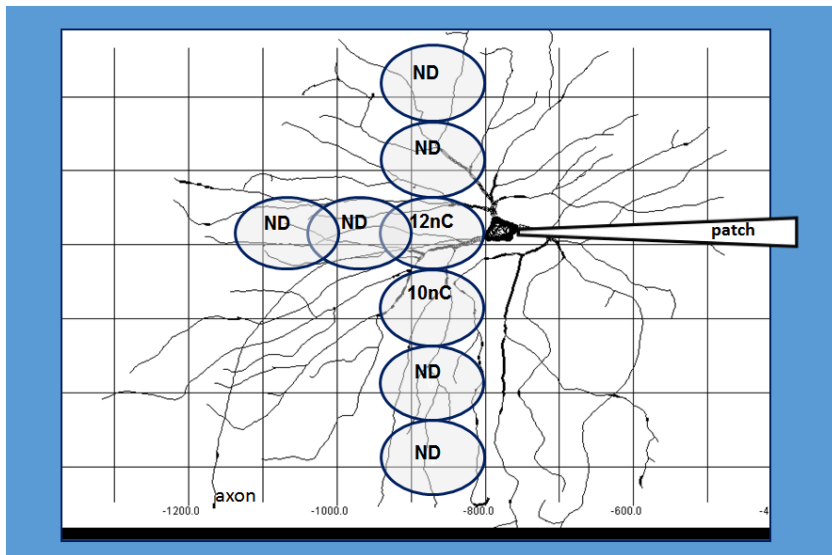


FIGURE 4.6: Stimulation electrode pulse charge sensitivity map of alpha ganglion cell 2 shown superimposed on the reconstructed ganglion cell for size comparison. With 100  $\mu\text{m}$  diameter stimulus electrodes, the lowest extracellular spike threshold was found in a region near the cell body / axon IS region. ND: No threshold for eliciting action potentials was detected at the maximal current steps tested in this region.

#### 4.3.5 *Simulation results*

We performed coupled EM-neuronal dynamics modelling of the experimental setup for stimulation to help validate the computational ganglion cell model and gain some understanding about spatial mechanisms and experimental parameters impacting ganglion cell stimulation thresholds. The electrode position was mapped in 20  $\mu\text{m}$  steps in a grid pattern across the alpha cell model. The experimentally measured spatial sensitivity of the threshold for action potential generation due to extracellular stimulation and the simulated spatial maps of the stimulation electrode position dependence of the threshold are similar in form and magnitude, as seen in Figures 4.6 and 4.7. The stimulation threshold is lowest when the electrode is near the axon IS, where the low threshold sodium channels were inserted. The threshold is also low for electrode positions on top of the axon trajectory. A few dendritic tip regions showed small peaks of sensitivity, possibly related to a sealed-end boundary modelling artefact. Electrode positions near the initial segment and cell body first activate the initial segment, while locations further down the axon first activate the axon. This is coherent with the observed stimulation threshold behavior. The simulations also suggest small peaked regions associated with the stimulation of different dendritic termini, which might however be simulation artifacts related to the simulated boundary conditions at the termini. The sensitivity profile of the model is close to the experimentally observed stimulation threshold behavior, with the cell body IS region being lowest in threshold and the axon being roughly double the threshold of the cell body. The thresholds for these locations remote from the cell body were often higher than the limits of the experimentally applied linear current step range tested, and hence activation could not be detected, in accordance with the computational model predictions.

#### 4.3.6 *Sensitivity and uncertainty analysis*

We performed a sensitivity analysis with regard to measurement and modelling parameters and, on that basis, established uncertainty budgets. Each of the following individual parameters were varied, and the impacts on the ganglion cell stimulation threshold were investigated. The uncertainty contributions to the stimulation threshold originating from the material properties, neuron location, electrode placement, electrode and retina geometries, and the numerical discretization (based on reported or estimated

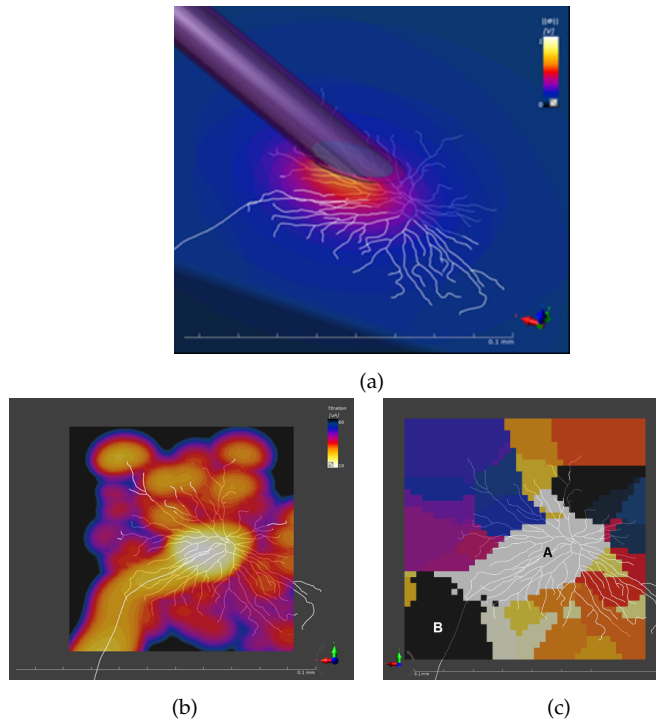


FIGURE 4.7: Assessment of ganglion cell stimulation (threshold and mechanism) using coupled electromagnetic-electrophysiological computational modelling. (A) Computational model of the alpha ganglion cell (Cell 1, see Figure 4.2) and the stimulation electrode ( $50\ \mu\text{m}$  above retinal surface). The cell body position is shown as an orthogonal bar at center. (B) Simulated spatial sensitivity map of current required to elicit action potentials in the model. The lowest simulated spike threshold ( $11\ \mu\text{A} / 5.5\ \text{nC}$ ) was found in a zone near the cell body / axon initial segment, as in the real cell threshold measurements ( $10\text{--}12\ \mu\text{A}$ ). The remaining axon had 2–3 times higher threshold. (C) Spatial regions associated with specific sites of predicted spike initiation. *A* demarks initiation at the initial segment and *B* initiation at the axon – the other regions are associated with the different dendritic termini and may be artefacts of the modelling.



uncertainties of the underlying parameters) can be found in Tables 4.3–4.5. The dominant uncertainty contribution is related to the uncertainty concerning the distance of the electrode from the retinal surface. Other important contributions stem from the electrode angle and the neuron depth within the retina. By estimation of the uncertainty of the underlying parameters and assuming them to be normally distributed and independent, the combined simulation uncertainty is obtained as the root-sum-square of the product of the sensitivities and parameter uncertainties. The combined stimulation threshold simulation uncertainty at the electrode position of maximal uncertainty is 2.6 dB ( $k = 1$ ). It should be noted that the uncertainty of the neuronal dynamics modelling was not included, as it is unclear how such an assessment could be performed. The principal contributor to the measurement uncertainty is the step size of the current used to search for the stimulation threshold (2  $\mu$ A) of the ganglion cell, while uncertainty related to amplifier linearity and calibration offset were small. The combined measurement uncertainty is 1.0 dB ( $k = 1$ ). The total uncertainty, combining simulation and measurement uncertainties, is 2.8 dB ( $k = 1$ ), which corresponds to  $\sim 35\%$  (see Table 4.5).

#### 4.4 DISCUSSION

We have developed a retinal ganglion cell model of extracellular epiretinal stimulation based on anatomical and physiological analysis of a large ganglion cell type in the rabbit retina. By recording from a single type of retinal ganglion cell, we attempted to understand the common properties of the OFF-alpha ganglion cell type in the rabbit retina. This cell type, the largest ganglion cell type found in rabbits, has a large diameter dendritic tree and cell body, a thick axon, and fast conduction velocity [213, 215]. Large diameter alpha cell axons are also thought to have the lowest extracellular electrode stimulation thresholds. We reconstructed two recorded OFF-alpha ganglion cells and digitized their dendritic arborizations to develop *NEURON* models to match their observed physiological properties [160, 224].

**FIRING RATES AND SPIKE ADAPTATION** We examined the firing patterns of alpha cells to current steps of up to 900 pA. All alpha cells showed spike adaptations to sustained current steps and low membrane resistance, similar to previous reports of alpha cells in the cat retina [208, 233]. This spiking adaptation was implemented in the *NEURON* alpha cell model by incorporation of a slow calcium-activated potassium current channel,

voltage-gated calcium currents, and a slow internal calcium clearance mechanism similar to that described by Destexhe [236] see also [225, 226]. The alpha cell model spike adaptation mechanism was designed to match the average spike adaptation probability profile of the alpha cell cohort. The activation of this calcium-activated potassium current, which was considerably slower than the faster voltage-gated sodium and delayed rectifier potassium currents involved in spike generation, appeared to constrain the spiking adaptation characteristics of the alpha cells to long current steps during current injection through the patch electrode. Therefore, given the delayed action of the calcium-activated potassium currents and the small contribution of the voltage-gated calcium channel currents to the action potential, these currents do not play a significant role in the action potentials evoked by the ms duration current pulses on extracellular stimulation electrodes.

**ACTION POTENTIAL** Close examination of individual spike phase plots during current steps shows that most alpha cells exhibit a prominent IS-SD break in their action potentials similar to those reported for classic studies of motoneuron activation [231, 237]. This specialized axonal site near the soma was referred to as the IS, which initiated the impulse and activated a regenerative response that propagates into the soma and dendrites. The one exception appeared to be an alpha retinal ganglion cell where the axon was accidentally cut in the process of exposing the cell body for whole-cell recording. The IS-SD breaks could be activated at voltages as negative as  $-63$  mV. To strong depolarizing current steps, phase plots of their spiking showed the IS-SD threshold break was largest on the initial ganglion spike from the resting potential, which occurred at more negative potentials, and the IS-SD break threshold of subsequent spikes decreased with continued depolarization, which suggests that a low-threshold process triggers the ganglion cell spike when resting at more negative potentials. However, close examination of the alpha cells bearing axons showed that the IS segment axon zone smoothly exits the cell body to enter the nerve fiber layer. No constriction of the axon IS was observed on any alpha ganglion cell axon recovered, unlike those reported for ganglion cells in amphibians [205]. We therefore used an unstricted axon to constrain our *NEURON* model voltage-gated axon channel densities to more closely resemble the actual recorded cell used for extracellular stimulation.

**CELL MODEL FITTING** We started the fitting of our model alpha cell using the Fohlmeister model [226] as a general template for sodium-, calcium-, and potassium-channel distributions. Good phase plot fits to the main loop of the action potential were obtained by employing a rough ratio of voltage-gated sodium / potassium (delayed rectifier) current conductances in a  $\sim 1:1$  ratio. However, fits according to the Fohlmeister model to the IS-SD portion bump of phase plots were poor when the real axon anatomical data – i.e., lacking a  $90\ \mu\text{m}$  trigger segment region that is 36% of the original axon diameter – was used for IS axon diameters, even after a large sodium-channel conductance  $8\times$  the conductance density of the soma was added to the axon IS (see Figure 4.3). This necessitated the addition of a modified sodium channel with empirically-based channel activation kinetics. Previous immunocytochemical studies of the proteins found in the axon IS (trigger zone) in mouse retinal ganglion cells indicated the presence of ankyrin G and the NaV1.6 sodium channel type are present on the IS in a zone  $15\text{--}20\ \mu\text{m}$  distal to the soma [216, 238–240]. This high conductance NaV1.6 channel zone was found to correspond to a zone of high immunoreactivity when a Pan sodium channel antibody was used. More recent studies, like the work from [217] using a Pan sodium channel antibody have shown a similar zone of high immunoreactivity on rabbit alpha cell axon on average  $30\ \mu\text{m}$  distal to the cell body, the dimensions of which have been incorporated in our current *NEURON* model. However, we were unable to fit the IS-SD break activation voltage of the real cell phase plot data to phase plots based on the Fohlmeister [226] channel kinetics on our unconstricted axon alpha cell models except at extreme channel densities, which may not be physiologically relevant [241] (see Figure 4.2). To approximate the more negative IS-SD break seen in the phase plots of our recorded alpha cells with unconstricted IS axons, we developed a modified NaV1.6 H-H model, with the gating parameters adjusted to be activated at voltages  $5\ \text{mV}$  more negative than previously. A NaV1.6 conductance density on the unconstricted axon IS,  $6\text{--}9\times$  higher than that of the soma, appeared to provide an acceptable fit to the alpha cell phase plots when combined with a higher density of axonal delayed rectifier potassium channels to stabilize the mechanism (see Table 4.1 and 4.2 for modelling details). Our realistic alpha cell models, while reproducing the physiological data, also show channel distributions that may reflect natural variation in morphological and physiological properties [242].

**STIMULATION SENSITIVITY** Many studies show that the trigger region of the IS plays an important role in controlling action potential activation of retinal ganglion cells to short (0.1–1 ms) electrical stimulation currents pulses evoked by epiretinal retinal prosthetic stimulus electrodes. Analysis of single electrically evoked spikes all show prominent IS-SD breaks in their phase plots. In this aspect, the electrically evoked spikes in simulations and, in the real cell, appear to fit the model, given the potential variability in electrode-retina proximity from our error analysis of the process. However, it is also likely that our model is an incomplete simulation of alpha cell dynamics; while our models exhibit sustained spike adaptation to large stimulus current pulses (500–900 pA), the voltage threshold for the NaV1.6 IS-SD break appeared to be reduced during current steps to more depolarized potentials in the real alpha cell but was invariant in the model. This changing threshold may be due to slow inactivation of NaV1.6 sodium channels previously reported at more positive potentials [243, 244]. Because electrical stimulation of retinal neurons by Pt electrodes largely relies on short current pulses, these differences may not be of practical significance, however synaptic activation of alpha cell stimulation by light or glutamate pulses may cause differences between real cells and our *NEURON* model in the observed firing patterns.

While our physical method of soma access for whole-cell recording could potentially lower the extracellular stimulus threshold of the recorded ganglion cell, we found the lowest extracellular current stimulation threshold values were near the soma IS, with thresholds similar to those reported from previous extracellular recording studies by [245] and [217]. Our stimulation electrode sensitivity mapping was physically limited by the presence of the patch recording electrode on the cell body. While our orientation of the axon to the cell body was based on the very visible nerve fiber orientation of the local axon bundles in the microscope, the orientation of the axon exiting from an individual ganglion cell body will vary slightly, as can be seen in two reconstructed ganglion cells (see Figure 4.2a). The data acquisition program we used only generated a series of linear stimulation electrode current steps to determine action potential threshold. As a consequence, the higher thresholds of distal axon and ganglion cell dendrites may have been beyond the range of stimulation current steps currently investigated.

**STIMULATION SIMULATION** The stimulation threshold and spike initiation maps of the models suggest that three distinct mechanisms are involved in stimulation of retinal ganglion cells by localized extracellular

electrodes: The lowest current stimulation threshold is observed when the electrode is in the vicinity of the IS, where spike initiation occurs. This agrees with previous experimental results and suggests that the IS is the most sensitive location. At twice that threshold, direct stimulation of the axon is obtained [245]. This mechanism is likely to be related to the field inhomogeneity, producing a high activating function, i.e., second potential derivative along the nerve fiber [210], that leads to a net charge injection and subsequent generation of the action potential. Finally, small peaked zones in the vicinity of the dendritic tree termini also appear to be weakly activating at a threshold  $2.2\times$  higher than the initial segment stimulation threshold, which may reflect simulation artifacts resulting from the modelled boundary condition. Termini have been modelled according to the approach commonly chosen when exposure safety is assessed [246], but sealed boundary conditions might be a better representation of the real electrophysiology. Currently, these zones have not been reported in real alpha cells stimulated with extracellular electrodes [217, 245].

**UNCERTAINTY ASSESSMENT** We performed a measurement and a simulation parameter sensitivity analysis of the stimulation threshold and established measurement and simulation uncertainty budgets to provide objective criteria of the model validation. Our results show that the uncertainty in the ganglion cell stimulation threshold is dominated by the impact of the distance between the neuron and the stimulation electrode, in terms of the proximity of the electrode to the retina, the tilt of the electrode, and the depth of the ganglion cell in the retina. This finding is consistent with previous studies, where it was shown that the electrode tissue access resistance or the ganglion cell spike threshold currents of stimulus electrodes change rapidly when positioned closer than  $100\ \mu\text{m}$  to retinal surface, which enhances small proximity errors in the measurements [245, 247]. Electrode proximity factors must be carefully controlled in future experiments. The uncertainty assessment presented does not take into consideration uncertainty related to the electrophysiological modelling. Such an analysis would be difficult to perform, as there are a very large number of parameters (e.g., channel distributions) and only limited knowledge about the equations that describe electrophysiological activity, and it is unclear how the constraining information on possible modelling parameters obtained from the patch clamp measurements (e.g., phase plot fits) can be taken into account.

**MODEL VALIDATION** We validated our alpha cell models of extracellular stimulation by comparing experimental stimulation thresholds to computational predictions. A stimulation threshold of 10–12 $\mu$ A was determined in repeated measurements for an electrode located above the soma; at 100  $\mu$ m further down the axon, the stimulation threshold increased to 10–14 $\mu$ A; another 100  $\mu$ m further down the axon, the stimulation threshold was 12–16 $\mu$ A. Simulations at corresponding locations yield thresholds of 11, 14.5, and 22  $\mu$ A respectively, which is within the range of the measured values with the uncertainty margin (2.8 dB, coverage factor  $k = 1$ ), even without the contribution of the neuronal dynamics modelling related uncertainty. Thus, it can be concluded that our simulations are in general agreement with the stimulation measurements. While the alpha cell neuronal dynamics model was influenced by measurement information about the action potential phase plots, no information about stimulation thresholds, or indeed stimulation by an external electrode, went into the model, such that validation by measured stimulation threshold maps can be considered to be mostly independent information and hence usable for validation purposes.

#### 4.5 CONCLUSIONS

Epiretinal electrode stimulation is often used to activate ganglion cells in the blind patient's retina [248–250]. We have developed an integrated ganglion cell model in *NEURON* of extracellular stimulation with the focus on the analysis of a single OFF-alpha ganglion cell type in the rabbit. The biophysical properties of the model were derived on the basis of whole-cell recording. To examine the parameters that affect the ganglion cell spiking thresholds, we performed a sensitivity analysis and related uncertainty assessment of our computational modelling and experimental measurements data. This assessment showed that computed and measured results agree within the combined uncertainty, thus validating our cell models. The results also contribute validation evidence for our coupled EM-electrophysiology modelling and the neurostimulation simulation platform.

The applied modelling approach may have clinical utility for the development of computational models of ganglion cells in the human fovea, which could aid the development of future retinal prostheses and other novel stimulating medical devices. As current epiretinal extracellular stimulation electrodes typically stimulate several hundreds of ganglion cells and can also activate the overlying axons of distal ganglion cells, resulting in bright, arc-shaped visual-artefacts, future work should be aimed towards genera-

tion of not only individual ganglion cell models, but also larger scale retinal models encompassing a representative range of ganglion cell types and retinal neurons, within a realistic layered dielectric tissue structure. Thus, computational modelling will be able to contribute to the development of not only safer but also more effective neurotherapeutic devices.

## 4.A APPENDIX

4.A.1 *Results tables*

Alpha Cell 1 Fitted Conductances G [mS/cm <sup>2</sup> ]					
Channel	Dendrites	Soma	Preseg.	Initial seg.	Axon
Na H-H	119.0	90.7	486.3	0	124.5
NaV1.6	0	0	0	528.9	0
K H-H	139.0	120.7	218.1*	797.7	49.9
Ca	2.5	3.0	2.5	0	0
Ca-activated K	2.2	2.2	2.2	2.2	2.2
A-current	2.7	3.8	0	0	0
Surface Area [μm <sup>2</sup> ]	47104.7	3569.7	496.7	281.6	5869.4
Process length [μm]	—	43.6	38.7	43.3	1297.8

TABLE 4.1: Distribution of ion channels and G-bar membrane conductances (mS/cm<sup>2</sup>) on the alpha ganglion cell model 1 for  $T = 35^\circ\text{C}$ . \* indicates values that are arbitrary for which changes cannot be distinguished in soma recording phase plots.  $g_{pas} = 0.0006$ ,  $e_{pas} = -65.0$ ,  $Ra = 143.2$ ,  $global\_ra = 143.2$ ,  $E_{Na} = 60.59\text{ mV}$ ,  $E_K = -95.31\text{ mV}$ .



Alpha Cell 2 Fitted Conductances G [mS/cm <sup>2</sup> ]					
Channel	Dendrites	Soma	Preseg.	Initial seg.	Axon
Na H-H	75.8	63.4	903.1	0	124.5
NaV1.6	0	0	0	562.0	0
K H-H	129.7	80.5	149.6*	199.4	49.8
Ca	2.5	3.0	2.5	0	0
Ca-activated K	2.2	2.2	2.2	2.2	2.2
A-current	2.7	3.8	0	0	0
Surface Area [μm <sup>2</sup> ]	71856.9	4885.1	315.0	258.2	8185.8
Process length [μm]	—	40.4	38.2	39.9	1194.6

TABLE 4.2: Distribution of ion channels and G-bar membrane conductances (mS/cm<sup>2</sup>) on the alpha ganglion cell model 2 for  $T = 35^\circ\text{C}$ . \* indicates values that are arbitrary for which changes cannot be distinguished in soma recording phase plots.  $g_{\text{pas}} = 0.0002$ ,  $e_{\text{pas}} = -65.0$ ,  $R_a = 143.2$ ,  $g_{\text{local\_ra}} = 143.2$ ,  $E_{Na} = 60.59$  mV,  $E_K = -95.31$  mV.

Uncertainty Factor	Unit	$\Delta_{\text{model}}$	$\sigma_{\text{model}}$	$\Delta_{\text{threshold}}$ [dB]	$f_{\text{max}}$ [dB/unit]	$U_{\text{max}}$ [dB]
Medium conductivity	%	10	5	1.58	0.16	0.79
Retina conductivity	%	10	10	0.65	0.065	0.65
Electrode distance to retina	mm	0.025	0.00577	8.52	340	1.97
Simulation grid resolution	$\times$	1.5	—	0.34	—	0.34
Electrode x-position	mm	0.025	0.001	6.47	260	0.26
Electrode y-position	mm	0.025	0.001	6.64	265	0.27
Electrode angle	$^{\circ}$	2	2	1.00	0.50	1.00
Electrode diameter	mm	0.05	0.00577	1.67	33.4	0.19
Insulator diameter	mm	0.005	0.003	1.13	225	0.68
Retina thickness	mm	0.005	0.011	0.35	70.7	0.78
Neuron depth	mm	0.05	0.003	15.8	315	0.95
<i>Combined uncertainty</i>						2.6
<i>(<math>k = 1</math>)</i>						

TABLE 4.3: Simulation uncertainty budget for the stimulation threshold

Uncertainty Factor	U [dB]
Current step (2 $\mu$ A)	0.95
Amplifier linearity	0.05
Calibration offset	0.05
<i>Combined uncertainty (k = 1)</i>	1.00

TABLE 4.4: Measurement uncertainty budget for the stimulation threshold.

Uncertainty Factor	U [dB]
Simulation	2.6
Measurement	1.0
<i>Total uncertainty (k = 1)</i>	2.8

TABLE 4.5: Total uncertainty for the stimulation threshold.

#### 4.A.2 *NaV1.6 channel model*

Hodgkin-Huxley style gating rate constants were used in this model for simulating voltage-gated sodium, potassium, and calcium channel kinetics were as reported for mammalian retinal ganglion cell action potentials [226]. However, the addition of a modified gating mechanism for NaV1.6 channels was required for the axon initial (trigger) segment (IS) of high sodium-channel density. Currently, there is large variability in the reported axon IS activation gating voltages of NaV1.6 channels and position in the literature, as they appear to be dependent on activity [251, 252]. We used an empirical solution-based approach to obtaining an adequate fit to the IS-SD break bump in the phase plot. The IS NaV1.6 m<sup>3</sup>h gating variable kinetics format was standard, but included a gating rate activation constant (m) shifted 5 mV more negative, although other values for the gating shift were investigated.

NaV1.6 m:

$$\alpha_m(V) = \frac{-2.725(V + 40)}{e^{-0.1(V+40)} - 1}$$

$$\beta_m(V) = 90.83e^{-(V+65)/20}$$

$$\tau_m = \frac{1}{\alpha_m(V) + \beta_m(V)}$$

$$m_\infty = \alpha_m(V)\tau_m$$

NaV h inactivation was left intact:

$$\alpha_h(V) = 1.817e^{-(V+52)/20}$$

$$\beta_h(V) = \frac{27.25}{1 + e^{-0.1(V+22)}}$$

$$\tau_h = \frac{1}{\alpha_h(V) + \beta_h(V)}$$

$$h_\infty = \alpha_h(V)\tau_h$$

#### 4.A.3 Calcium clearance mechanism

The calcium clearance model was based on the first-order decay internal calcium pump model `capump.mod` originally described by [236] and modified by Carnevale (unpublished) with improved integration, with the 4 model parameters passed to *NEURON* as global variables as shown below:

```
depth_cas = 15
taur_cas = 280 (alpha cell 1)
taur_cas = 150 (alpha cell 2)
kd_cas = 0.0002
cainf_cas = 1 × 10-5
```

The fits match the average number of spikes to 900 pA depolarizing current pulses. The initial calcium concentration parameters were  $[Ca^{2+}]_o = 1.8$  mM and  $[Ca^{2+}]_i = 0.0001$  mM.

## NEUROSTIMULATION OPTIMIZATION USING ACTIVATION FUNCTIONS AND COUPLED EM-ELECTROPHYSIOLOGICAL MODELLING

---

### ABSTRACT

A novel modelling approach to automatically tune the stimulation parameters of multi-contact electrodes in order to achieve targeted and steerable stimulation has been developed. The approach, which is based on pre-computed activating function contributions determined along individual neuron fiber trajectories, was successfully compared and validated against fully coupled EM-neurophysiological modelling in neuro-functionalized computational anatomical models. The approach provides acceleration by more than three orders of magnitude. The applications investigated include deep brain stimulation (DBS) and spinal cord stimulation (SCS). Proper consideration of tissue anisotropy has been found to be crucial for the prediction of fiber recruitment.

The development of an image-based, neuro-functionalized virtual head model for DBS-related modelling is also described.

### 5.1 INTRODUCTION

A wide range of therapies that rely on stimulation of neural activity through application of EM fields with external or implanted devices exist. In the majority of cases, a population of neurons is to be stimulated, while interference with the activity of other neurons is to be avoided [8]. Selective targeting can be achieved through application of multiple electrode contacts, for which the voltage or current amplitudes are individually controlled [253, 254]. However, when the number of independent electrodes becomes large and patient-specific treatment optimization is required, application of pre-defined steering parameters or manual tuning becomes suboptimal, time consuming, or even impossible. Optimization must take into consideration the field distribution within the complex inhomogeneity of the human anatomy, but also the trajectories and morphologies of neurons, as well as the electrophysiological behavior of these neurons (including pulse-shape-

dependent responses). While coupled EM-neuronal dynamics modelling within functionalized virtual anatomical models has recently become possible [201], the computational effort is typically still too costly to allow brute-force stimulation parameter optimization by means of, e.g., genetic algorithms – at least on ordinary computational hardware. Therefore, an alternative approach is needed.

In this study, DBS and SCS were studied by comparing coupled EM-neuro modelling with simplified predictions based on the activation function concept from [16]. A computationally efficient optimization scheme suitable for the latter is proposed and applied to SCS targeting. The limits of the activation function approximation are investigated, along with the impact and importance of considering spinal cord anisotropy. The extension of the proposed approach to pulse-shape optimization is discussed.

## 5.2 METHODS

### 5.2.1 *EM-electrophysiological modelling*

For the coupled EM-electrophysiological modelling *Sim4Life* (ZMT Zurich MedTech AG, Switzerland) is used that offers a range of EM solvers for the full Maxwell equations, as well as a range of (quasi-)static approximations suitable for electric or magnetic exposure at low frequencies. The EM solvers are optimized for the modelling of *in vivo* field conditions within complex virtual anatomical models. *Sim4Life* facilitates electrophysiological modelling of neuron models with complex channel dynamics and morphologies by integrating the *NEURON* libraries [255] and offers a range of predefined axonal dynamics models. Coupling between the electric  $E$ -field distributions or electric potentials and the compartmental neuron models is achieved using *NEURON*'s extracellular mechanism. Using this approach, it is possible to simulate neuronal dynamics within suitably functionalized anatomical models [201]. Titration functionality is available to determine, for a given field distribution, neuron model, and pulse shape, the scaling required to reach the stimulation threshold.

For all simulations below, *Sim4Life*'s ohmic-current-dominated electro-quasistatic solvers (structured and unstructured) have been employed, together with the low-frequency tissue parameters from [199].

### 5.2.2 Activation functions and optimization

The activation function (also sometimes referred to as ‘activating function’) is a quantity related to the second derivative of the electric potential  $\phi$  along a nerve fiber trajectory that was proposed as a means of assessing stimulation by fields applied extracellularly to the fiber. Axonal fibers can be stimulated by the tangential  $E$ -field at the fiber end, by field inhomogeneity along the fiber, and by bends in the fiber trajectory [246]. While the first is related to field strength, the latter two can be predicted based on the activation function. Activation functions  $A(l)$  can either be derived from the continuum partial differential equation representation of the electrophysiological model resulting in the formula

$$A(l) = \frac{d}{4\rho C} \frac{\partial^2 \phi(l)}{\partial l^2} \propto \frac{\partial^2 \phi(l)}{\partial l^2} =: A^*(l)$$

where  $l$  is the position along the fiber,  $d$  the fiber diameter,  $\rho$  the axoplasmic resistivity, and  $C$  the membrane capacitance. It can also be understood in a discretized way in myelinated nerves as the charge build-up resulting from the difference between the neural current flowing between a Ranvier node and the previous one as a result of their potential difference and the current flowing between the node and the subsequent one:

$$A_D(l_i) \propto A_D^*(l_i) = \left( \frac{\phi_{i+1} - \phi_i}{\Delta_l} - \frac{\phi_i - \phi_{i-1}}{\Delta_l} \right) / \Delta_l = \frac{\phi_{i+1} - 2\phi_i + \phi_{i-1}}{\Delta_l^2}$$

where  $\Delta_l$  is the internodal distance. Notice that this formula is equivalent to the central differences discretization of the second derivative along the nerve trajectory. Functionality to extract the activation function along fiber trajectories for a simulated EM field was implemented in *Sim4Life*.

While investigating the dependence of the activated regions and neurons on varying electrode configurations, it was found that the activating function (i.e., a quantity proportional to the second spatial derivative of the potential along the trajectories) is an excellent predictor for the stimulation of axonal fibers by field inhomogeneity – one of the principal stimulation mechanisms – (see Section 2.1.1). Whether the maximum or the absolute value of the minimum (depending on the polarity / shape of the pulse) of the activating function along a fiber is above a threshold  $A_T$  determines whether that fiber is activated. The threshold at which a neuron spikes depends on the type of neuron and its dynamics (e.g., motor vs. sensory, A / B-type, diameter), as well as the pulse shape of the applied field. It can

be determined from a single neuronal dynamics simulation per fiber type, diameter, and pulse shape, irrespective of electrode geometry, placement, local anatomy or tissue properties. For monopolar pulse shapes, action potentials are likely to be initiated in fibers where the activation function maximum (or the maximum of  $-A(l)$ , depending on cathodic vs. anodic stimulation) along the fiber exceeds the threshold, while other fibers are unlikely to respond. For bipolar pulses, the maximum of both  $A(l)$  and  $-A(l)$  can be relevant. An approach that relies on precomputed activating functions along all fibers and electrodes and uses an efficiently evaluable functional can be employed to optimize the stimulation parameters.

Due to the linearity of Maxwell's equations, the total potential for any steering parameter set is:

$$\phi(l) = \sum_i c_i \phi(l)_i$$

where  $c_i$  are the weights of the field generated by the  $i$ -th contact / channel; e.g., the applied voltage if the fields have been normalized accordingly. The activating function can then be evaluated as follows:

$$A^*(l, \vec{c}) = \frac{\partial^2 \phi(l)}{\partial l^2} = \frac{\partial^2 \sum_i c_i \phi(l)_i}{\partial l^2} = \sum_i c_i \frac{\partial^2 \phi(l)_i}{\partial l^2} = \sum_i c_i A_i^*(l)$$

Therefore, if the  $A_i^*$  have been precomputed for all individual channels,  $\max_l A^*(l, \vec{c})$  can be evaluated very efficiently for any  $\vec{c}$ , allowing optimization using standard approaches. A corresponding approach was implemented as a *Python* script in *Sim4Life* to maximize the functional:

$$w_+ \sum_{i \in F_+} S \left( \frac{\max_l \sum_i c_i A_i^*(l)}{A_T} - 1, d \right) - w_- \sum_{i \in F_-} S \left( \frac{\max_l \sum_i c_i A_i^*(l)}{A_T} - 1, d \right)$$

$$S(x, d) = \frac{2}{1 + e^{-x/d}} - 1$$

where  $S(x, d)$  is a sigmoid function,  $w_{+/-}$  are weighting coefficients for the activation of fibers that should be activated ( $F_+$ ) or not ( $F_-$ ; weight-ratio  $w := w_-/w_+$ ), and  $d$  is the sharpness of the sigmoid. (Note: there are about 20 times fewer targeted fibers than fibers to avoid – hence equal weighing would correspond to about  $w = 0.05$ .) The Nelder-Mead optimization method from SciPy was used [256, 257]. The ratio of the weighting coefficients expresses the importance of effective stimulation vs. unwanted side-effects.  $d$  is related to the importance of stimulation robustness (fibers



with activation function peaks within  $d \cdot A_T$  of the threshold are not considered fully activated or silent, reflecting the uncertainty about the exact activation threshold; see Section 5.4.1).  $d$  also influences optimization convergence, as with decreasing  $d$  the sigmoid approaches a step function that is flat nearly everywhere and does not provide gradient information anymore.

### 5.2.3 *Generic neurostimulation model*

The activating function-based stimulation assessment is an approximation. The activation function varies along the fiber resulting initially in a de- / hyperpolarization pattern resembling the activating function. However, conduction along the fiber subsequently leads to an influence from neighboring regions, especially for longer pulse durations. Therefore, the activation function threshold is expected to depend, e.g., on the width of the exposure. To investigate this, gaussian potentials with varying width (1–15 mm) were applied to a fiber model and the activation function threshold was determined by titration. A Sweeney fiber model [158] (diameter 12  $\mu\text{m}$ ; parameterized to mimic dynamics at 37°C) was used given its relevance for the SCS application studied in this chapter.

### 5.2.4 *DBS model*

Coupled EM-electrophysiological DBS models were developed by integrating the corresponding neurons and fibers within the detailed anatomical ‘MIDA’ head-model [258] that features the thalamic nuclei of interest. The MIDA model is based on high resolution (at least 0.5 mm isotropic), multimodal MRI data of a healthy volunteer that has been segmented into a large number of detailed tissue structures. It is complemented by high quality, non-rigidly registered diffusion tensor imaging (DTI) data of the same volunteer, which allows to assign inhomogeneous, anisotropic material property distributions to the neural tissues. Furthermore, an atlas of thalamic and subthalamic nuclei has been integrated in some versions of the MIDA model.

For the work presented here, the functionalization of the MIDA model involved two steps: the anatomo-morphological reconstruction and the electro-physiological functionalization. First, real, MIDA-specific nerve trajectories of the internal capsule (IC) fibers were derived from the acquired DTI data. Internal globus pallidus (GPi) fibers were reconstructed on the ba-

sis of the neuroanatomical description of the GPi fiber trajectories from [259]. A replica of the subthalamic nucleus (STN) neurons according to the models of Miocinovic [171] (see Figure 5.1) were positioned within the STN. Secondly, the compartmentalization and biophysical properties assignment according to [260] was performed for the myelinated GPi and IC axons, while the biophysics of the STN neurons was imported unchanged from the Miocinovic's model.

**STN NEURONS** In the work of Miocinovic [171], three different base models of STN neurons were used. All three models have identical neuronal bodies (i.e., soma and dendritic tree) but different axonal trajectories to account for anatomical differences. In the present work,  $N = 100$  replicas of the Miocinovic STN base neurons (see Figure 5.1) were positioned within the STN with the axon pointing toward the GPi. To position the neurons, three points were defined for each base neuron, marking the soma, as well as the first and the last axonal node. The coordinates of the axonal nodes were used to determine the orientation of the axon, while the coordinates of the first node, closest to the soma, was chosen for the positioning of the neuron within the STN.  $N$  points within the STN were randomly distributed to uniformly cover the entire STN volume. Then, each neuronal replica was positioned with its initial axonal node at one of these random point locations and rotated in order to orient the axonal axis toward the closest point of the GPi. A neuronal position was accepted when two conditions were satisfied: (i) the soma, including the dendritic arbour, was completely enclosed within the STN; and (ii) the neurons did not intersect with the electrode geometry. In case at least one of these conditions was violated, a new choice for the position was considered and conditions (i) and (ii) verified until a sufficient number of neurons could be placed.

**IC FIBERS** A DTI fiber tracking algorithm was implemented and used to identify trajectories of largest diffusion – hence identifying fibers – in a region of interest (ROI) that includes the whole GPi, STN, and the DBS stimulator geometry. 500 random fibers were created.

This large number of fibers permitted the exclusion of 'unrealistic' fibers, i.e., fibers with evident spatial irregularities in proximity of the electrodes and the STN, fibers which were too short, or fibers that were very similar to other fibers. This selection was performed visually and resulted in a reduction of the number of possible candidate fibers to 265 (52%), from which 50 fibers were finally chosen (see Figure 5.2). Specifically, ten random

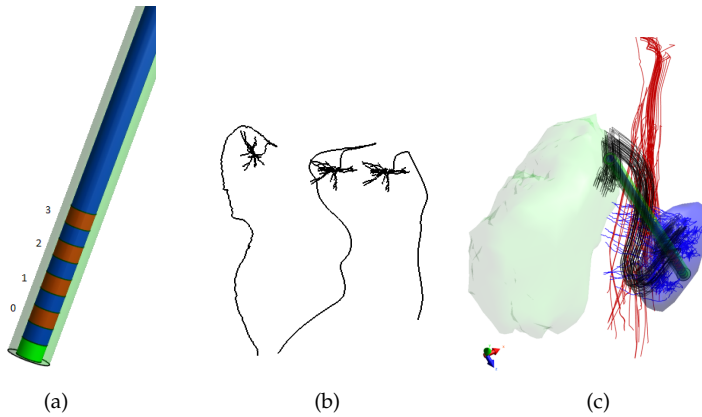


FIGURE 5.1: (A) Multi-contact ring electrode, (B) the three base STN neuron morphologies, (C) selected STN neurons (blue), GPi fibers (black), and IC fibers (red); the GPi is shown in light green and the STN in light blue.

permutations of always 50 fibers were chosen from the 265 visually selected ones. A statistical analysis was performed on the impact of the selection (ten permutations) on the titration factors for spike initiation in any IC fiber, which showed that the selection of 50 fibers from the 265 suitable candidates has only a minor impact on the functionalized model behavior (see Figure 5.3). The IC trajectories were converted into electrophysiological models comprising nodes, paranodal compartments (MYSA and FLUT) and internodes (STIN) compartments according to [171, 260].

**GPi FIBERS** To integrate the GPi fibers into the MIDA model, the following strategy was used: first, one basic GPi fiber running from the internal segment of the GPi to the ventral thalamus was traced, while referring to the description of the lenticular fasciculus trajectory from Parent and Parent [259]. In a second step, a population of fibers was obtained by cloning the basic geometry and distributing the clones in the model with random translations of  $10\mu\text{m}$  in all the three directions. This was followed by conversion into electrophysiological models [260].

**INTRINSIC NEURONAL ACTIVITY** STN neurons and GPi fibers possess intrinsic activity, also in the absence of external electric stimuli, as originally considered in Miocinovic's model. This intrinsic activity is enforced artificially in the GPi fibers by including a current source ('IClamp') with

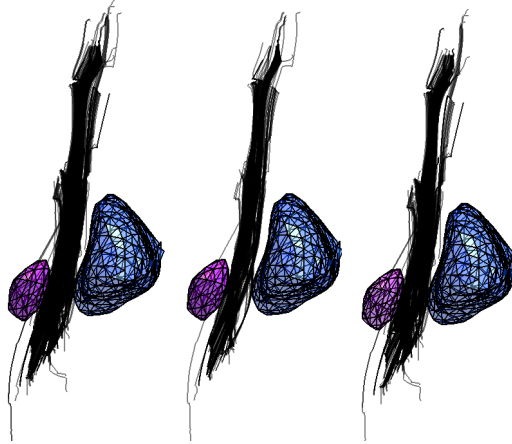


FIGURE 5.2: IC fiber candidates obtained from DTI-based fiber tracking. From left to right: all fibers, accepted fibers, and discarded fibers.

a frequency of 80 Hz at the initial node. For the STN neurons, the spontaneous activity emerges physiologically from the specific ionic channel distribution and conductivities.

**LIMITATIONS** A range of limitations of the neuron models still exist and should be considered, in particular with regard to predictions of the response to DBS stimulation in humans.

- The STN neurons are based on the ModelDB [161] models from Miocinovic and have been generated from macaque monkey data. The current nonexistence of similar neuronal models for humans limits the direct translation of the modelled single cell DBS stimulation response to humans. Moreover, the STN axons of the ModelDB models are not sufficiently long to reach the GPi, due to the larger STN-GPi distance in humans compared to macaques. However, it is not expected to affect the results obtained from studies of STN stimulation, as the STN axonal end-nodes are outside of the critical near field generated by the electrodes and hence largely unaffected by direct stimulation.
- Although the tracing of GPi fibers was performed for the specific human MIDA model and based on detailed atlas data and the neuroanatomical description from Parent and Parent [259], it is not expected to be fully accurate.

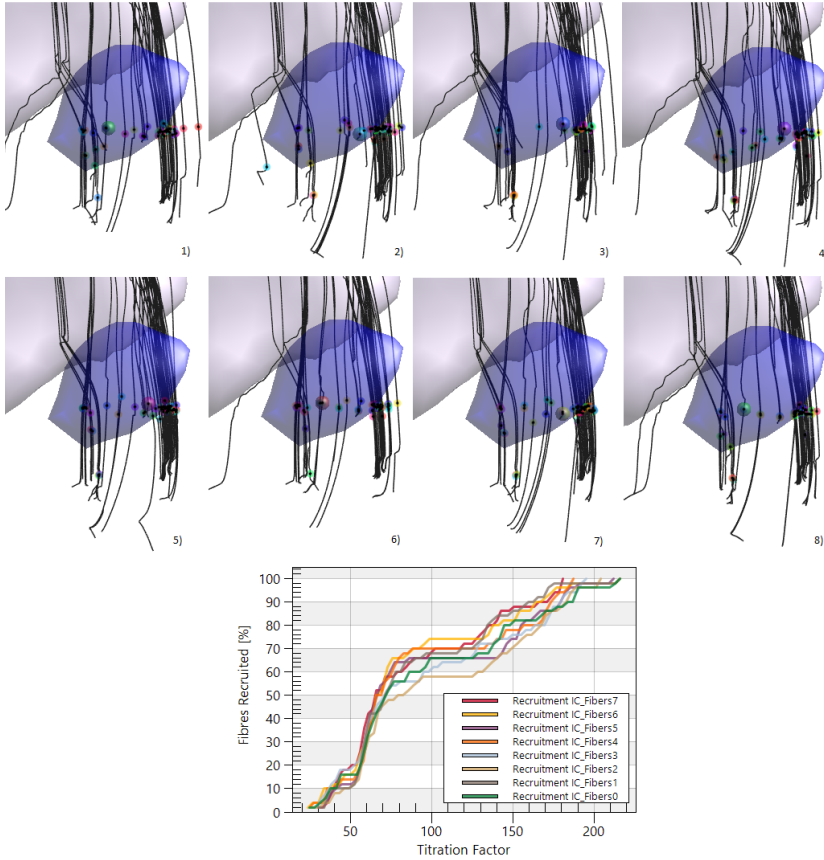


FIGURE 5.3: Top: different fibers sets randomly selected from the 265 suitable candidate fibers, including visualization of the spike initiation site at the stimulation threshold (indicated by spheres). For each image, the largest sphere indicates the location of the lowest threshold spike-initiation-site. Bottom: recruitment curves as a function of the titration factor for different sets of fibers.

- The fiber tracking algorithm used to trace IC fibers from the DTI data might not accurately follow fibers in regions of low fractional anisotropy, resulting in unrealistic bends. However, angle criteria as well as visual inspection were used to avoid the inclusion of unsuitable fiber trajectories – at the cost of reducing the density of usable fibers with trajectories passing regions of low fractional anisotropy.

**EM MODELLING** Here we focus on reporting the study-part related to IC fiber activation as the other neuron populations manifest spontaneous activity, complicating the discussion of exposure-related spike-initiation. Avoiding collateral activation of IC fibers is frequently an objective when adjusting DBS stimulation parameters or designing DBS implants.

A generic electrode with three active ring contacts was placed in a trajectory reaching the STN, mimicking a common implantation trajectory (see Figure 5.1). ‘Damaged’ neurons, i.e., neurons overlapping with the implant, were discarded. For the EM modelling, an unstructured quasistatic finite element method (FEM) solver has been used that properly accounts for the important anisotropy of the neural tissue. In the MIDA computational head model, the inhomogeneous map of anisotropic electrical conductivity was derived from DTI data [258], following the relationship between fractional DTI anisotropy and anisotropic conductivity reported by [150]. Two sets of Dirichlet boundary conditions were applied to the active contacts:  $[0/1/0]$  and  $[-1/0/1]$  (arbitrary scaling as basis for the titration procedure). Neuronal dynamics simulations were performed for the modelled IC fibers (including titration), and the location of spike initiation at the stimulation threshold was recorded for each fiber. The activating function along the fibers was computed from the simulated potential distribution.

### 5.2.5 SCS model

To investigate activation function-based stimulation parameter optimization, a SCS model similar to the one from [7] was constructed (see Figure 5.4). It includes a 2.5D spine model with epidural fat, dura, cerebrospinal fluid (CSF), grey and white matter, and distinguishes 22 dermatomal zones. A generic paddle electrode featuring an array of 5-by-4 contacts was placed in the epidural fat, in the position closest to the spinal cord (for most tests, only 5–10 contacts were included for optimization to reduce the optimization search-space). EM simulations were performed for each contact using the ohmic-current dominated real-valued electro-quasistatic solver, setting the

contact voltage to 1 V and the voltage of all others to 0 V, while isolating boundary conditions were applied at the domain boundary. From these simulations, any set of electrode current or voltage conditions can be obtained by superposition. 1952 axially-aligned Sweeney neuron models were positioned throughout the dorsal column at a density of 400 fibers/mm<sup>2</sup> (see Figure 5.4). These fibers run nearly the full longitudinal length of the spinal cord and are each randomly offset by a distance of maximally the internode distance (uniform offset probability distribution), such that the different fiber's nodes are not unrealistically aligned. Fibers are long enough to avoid non-physiological stimulation originating at either end of the fiber, as ascertained numerically. All fibers were set to have a fiber diameter of 12 $\mu$ m, as in [7].

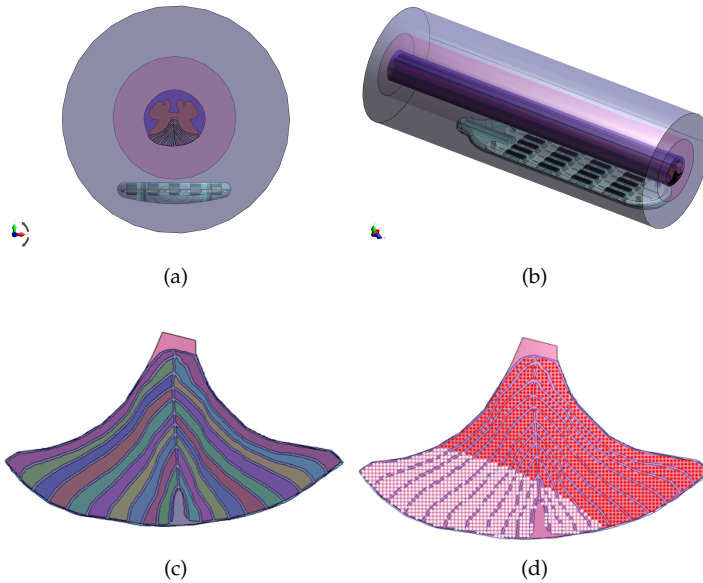


FIGURE 5.4: (A,B) Setup featuring the spinal cord with an inserted stimulator paddle model. (C,D) Close-ups of the 22 dermatomal zones and the neuron fibers running longitudinally along the dorsal column (density: 400 modelled fibers/mm<sup>2</sup>). White points indicate fiber activation for a given stimulation condition.

The stimulation conditions from [7, 261], reproduced in Figure 5.5, were simulated to verify that similar activation maps were obtained. Subsequently, stimulation threshold titration and activation function extraction

was performed for one of the fibers with a monopolar pulse of 0.1 ms, to determine the corresponding  $A_T$ . The spinal cord subdomains were assigned dielectric properties listed in Table 5.1, obtained from [7]. Four variants of the white matter electrical conductivity were simulated: (i) anisotropic (longitudinal: 0.72 S/m, transversal: 0.083 S/m; as in [7]); (ii) isotropic low (0.083 S/m); (iii) isotropic average (0.4015 S/m, corresponding to the average of the longitudinal and transversal conductivities from [7]); and (iv) isotropic high (0.72 S/m). Simulations were performed with different grid refinement to ensure that the impact of discretization on neural stimulation thresholds were negligible (less than 2%). A strong convergence criterion was used for the numerical solver (residuum reduction by nine orders of magnitude).

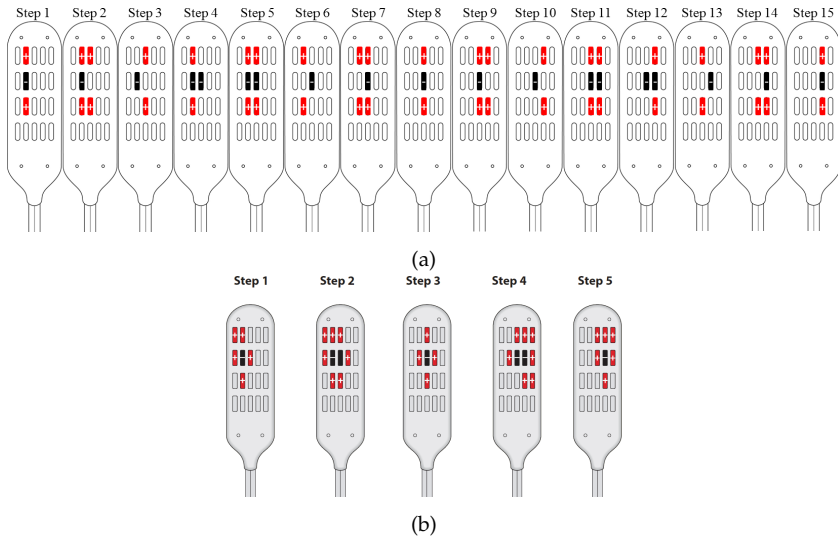


FIGURE 5.5: (A) Electrode configuration from [7] and (B) 'guarded' configuration from [261] indicating (+) and (-) potentials. (Figures adapted from original papers)

For the neuronal dynamics simulations, a stimulation waveform consisting of a cathodic  $100\ \mu\text{s}$  step pulse with an initial delay of  $100\ \mu\text{s}$  (for equilibration purposes) was employed.

**OPTIMIZATION** Automatic steering parameter optimization was performed by specifying which dermatomal zones should be activated. The suitability of this approach has been investigated in the spinal cord model



Material	Conductivity [S/m]
Epidural Fat	0.05
CSF	1.67
DC and White Matter	
<i>isotropic</i>	0.4015
<i>aniso. longitudinal</i>	0.72
<i>aniso. transversal</i>	0.083
Grey Matter	0.25
Paddle	0

TABLE 5.1: Material dielectric properties used in the SCS model

by defining regions of targeted activation and shifting them laterally (from the far left to the far right), as well as varying their size (1–11 consecutive zones). Initially, only the front row of neurons was considered, but subsequently the depth was extended to obtain the typical depth of activation in [262, 263]. Optimization was performed (i) for a single row (1D array) of five active contacts, (ii) a single row sandwiched between two grounded rows, and (iii) a 2D array (three rows, 15 contacts; to allow configurations similar to the ‘guarded’ ones in [261]). The initial guess  $c_{\text{Init}}$  of the  $c_i$  (identical for all  $i$ ) was varied, as well as the sigmoid parameter  $d$ , to assess the impact on optimization performance and to study optimization robustness.

**METRICS** The following metrics were used to quantify stimulation selectivity:

- *coverage ratio*: ratio of successfully activated fibers in the targeted region (as a measure of effectivity).
- *collateral ratio*: ratio of activated non-targeted fibers (as a measure of collateral side-effects).
- *stimulation robustness*:

$$\sum_{i \in F_+} S \left( \frac{\max_l \sum_i c_i A_i^*(l)}{A_T} - 1, 12.5\% \right) / |F_+|$$

as a measure of robustness of the intended stimulation. The 12.5% were chosen, reckoning that a safety distance of  $1/8 \cdot A_T$  from the

assumed activation-function-threshold should be sufficient to handle actual threshold-variations.

- *safety robustness:*

$$\sum_{i \in F_-} S \left( 1 - \frac{\max_l \sum_i c_i A_i^*(l)}{A_T}, 12.5\% \right) / |F_-|$$

as a measure of safety from unwanted stimulation.

## 5.3 RESULTS

### 5.3.1 Verification

When comparing the results obtained using the SCS model with those from [7], the minimal titration threshold of 1.95 mA is 3 % higher than the 1.89 mA found in [7], demonstrating a good agreement. Visual comparison of the predicted activated region at 2.6 mA (see Figure 5.6) also shows good agreement with [7], when anisotropic properties are used. This serves as additional verification of the coupled EM-neuro modelling implementation.

### 5.3.2 Activation function and stimulation location

The  $E$ -field generated by the DBS stimulator for the two electrode configurations ([0/1/0] and [-1/0/1]) has been characterized in homogeneous tissue with conductivity equal to the STN to obtain a clear idea of its spatial features. Figure 5.7 illustrates the  $E$ -field distributions for both electrode configurations, on a symmetry plane containing the electrode axis.

Titration predicts that a minimal current of 0.5 mA is required for IC fiber activation for configuration [0/1/0]. For configuration [-1/0/1], spike initiation in IC fibers occurs at a minimum threshold of 2.58 mA. Figure 5.8 compares the recruitment curves of IC-fibers for the two stimulation configurations. It illustrates the large effect of different choices of the electrode configuration on the threshold levels for IC fiber activation: configuration [0/1/0] has a threshold for IC fiber recruitment 5.4 larger than that of configuration [-1/0/1].

Figure 5.7 illustrates the activating function calculated for each IC fiber for the two electric configurations, with fiber-specific, symmetric color-scales ranging from  $[-m, m]$  ( $m$  being the maximum absolute value of the activating function along that fiber; the color-scale is thus different for each fiber).

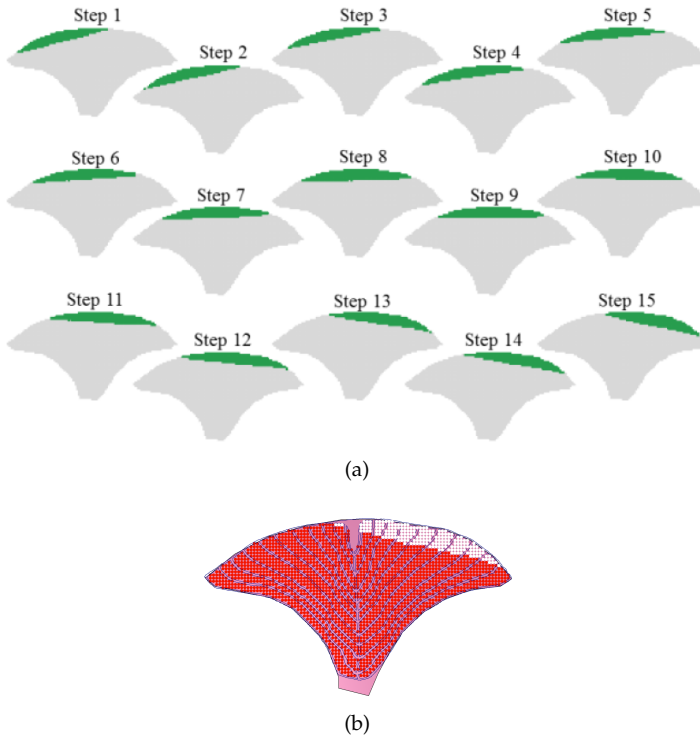


FIGURE 5.6: (A) Figure from [7] showing the fiber activation for a range of un-guarded configurations at a 2.6 mA stimulation magnitude. (B) Corresponding result obtained using the model from this study, for configuration 'Step 15'.

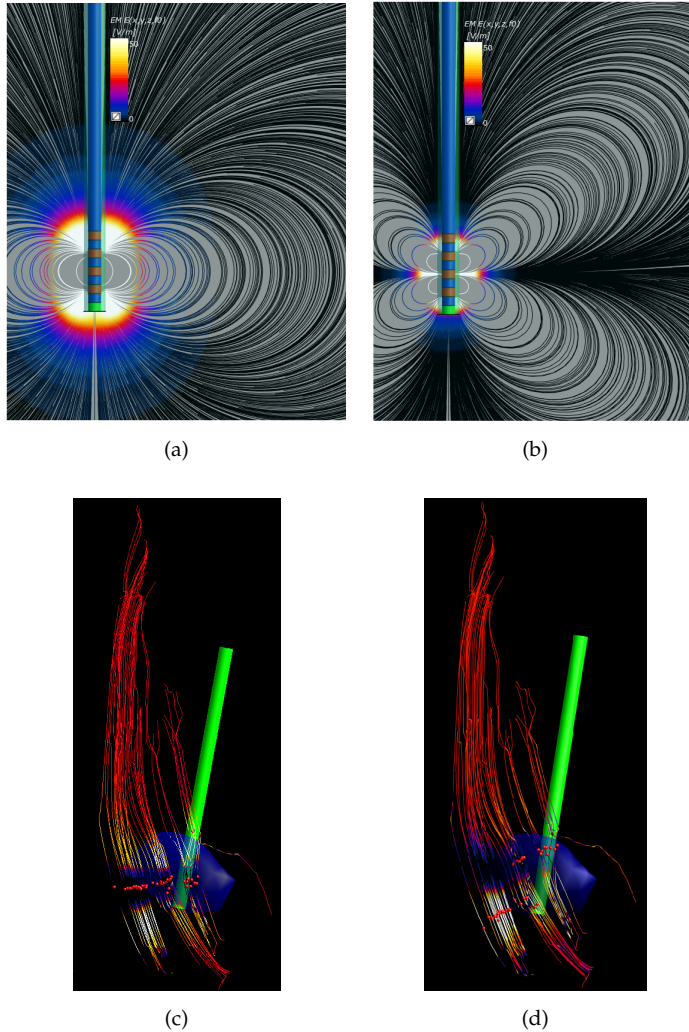


FIGURE 5.7: (Top) Combined slice-field and streamline views of the  $E$ -field in a plane containing the electrode axis for configuration (A)  $[0/1/0]$  and (B)  $[-1/0/1]$ . (Bottom) Surface line plots of the activating function along the IC fibers using fiber-specific but symmetric color-scales, i.e., with a range  $[-m, m]$  - (C)  $[0/1/0]$  and (D)  $[-1/0/1]$ . The locations of spike initiation at the threshold level, determined through the titration procedure, are indicated as red spheres.

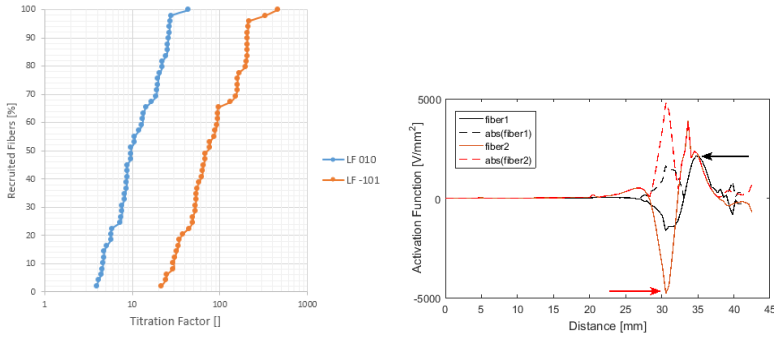


FIGURE 5.8: (Left) Comparison of the recruitment curves for the two investigated electrode configurations. (Right) Activation function along two fibers, as well as locations of recorded spike initiation (for electrode configuration  $[-1/0/1]$ ). The spike-initiation locations coincide with extrema of the activation functions.

The location of spike initiation at the threshold exposure level is visualized for each fiber, as a red sphere. The activating functions successfully predict the location of spike initiation for the IC fibers, therefore providing an alternative method to investigate the locations of spike initiation in axonal fibers and to roughly estimate thresholds without performing actual neuronal dynamics modelling.

While for the stimulation configuration  $[0/1/0]$  the sites of stimulation always occur at activating function minima, for the configuration  $[-1/0/1]$  the stimulation sites are partly located at maximal activating function locations. This can be understood when looking at the investigated pulse, which is a short, symmetric bipolar pulse, thus producing comparable stimulation thresholds for positive and negative activating function values of similar magnitude (unlike monophasic pulses which result in different thresholds for cathodic and anodic stimulation). For the stimulation configuration  $[0/1/0]$  the activating function magnitude is maximal at the level of the non-grounded electrode (where the activating function is negative), while for the stimulation configuration  $[-1/0/1]$  two levels (bands) with similar activation function magnitude, but opposite sign, exist. Depending on the distance between fibers and specific electrodes, the actual location of spike initiation will vary between the two levels.

### 5.3.3 Activation region

To compare the activation-function and the electrophysiological modelling-based stimulated region predictions, the maximum along the fiber direction of the second potential derivative is visualized across a spine cross-section (activation function maximal intensity project (MIP)), while the activation of fibers is indicated through color-coded dots (see Figure 5.9).

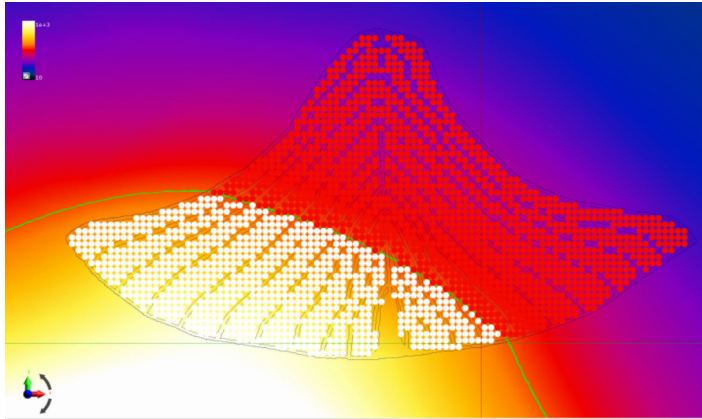


FIGURE 5.9: Comparison of fiber activation prediction methods. The white / red dots indicate stimulation predictions based on detailed coupled EM-neuro simulations, whereas the green line indicates the delineation of the region where the activation function along the fibers exceeds the activation function stimulation threshold. The color map in the background visualizes the projected activation function maxima along the fiber directions on a plane perpendicular to the fiber orientation.

### 5.3.4 Activating function threshold

The impact of the gaussian width on  $A_T$  in the generic model is shown in Figure 5.10.

### 5.3.5 SCS selectivity

Figures 5.11–5.14 illustrate the selectivity and robustness of activation with regard to safety and efficacy measures, as well as the impact of the sigmoid sharpness  $d$  and the ratio of the weights  $w = w_- / w_+$  – the latter expressing

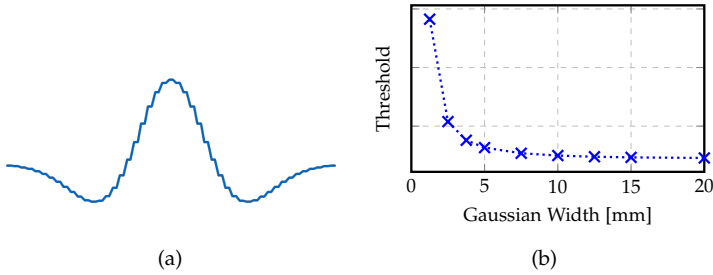


FIGURE 5.10: (A) Illustration of the second derivative of a gaussian curve, which features two side extrema with opposite sign next to the principal extremum. This means that a gaussian extracellular potential along a nerve fiber results in two opposing activation function regions on both sides of an activation function maximum. If the width of the gaussian becomes small, this results in a opposing transmembrane current flows that have a non-negligible impact on the activating function based stimulation threshold. (B) Gaussian width dependence on stimulation threshold.

the relative importance assigned to activating the targeted fibers vs. not activating unwanted fibers (for safety reasons).

Figure 5.11 shows stimulation robustness, safety robustness, coverage ratio, and collateral ratio (as defined in Section 5.2.5) for the chosen reference configuration: optimization of a single row of five contacts,  $w = 0.5$ ,  $d = 0.015$ , and  $c_{\text{Init}} = 75$ . Note that the values for  $c_i$  and  $c_{\text{Init}}$  depend on the computed activating function threshold and would need to be further normalized to translate to a physically meaningful quantity.

Figure 5.12 compares the coverage ratio, collateral ratio, stimulation robustness, and safety robustness plots for the reference configuration (single row with 5 electrode contacts) and a  $3 \times 5$  array .

Figure 5.13 compares the coverage ratio, collateral ratio, stimulation robustness, and safety robustness plots for the reference configuration for two different values of the relative weighting of avoidance of non-target regions vs. successful activation of targeted regions  $w$ .

Figure 5.14 compares the stimulation robustness, safety robustness, coverage ratio, and collateral ratio plots for the reference configuration for two different values of the sigmoid width  $d$ .

Figure 5.15 compares the coverage ratio, collateral ratio, stimulation robustness, and safety robustness plots for the reference configuration for two different values of the initial guess  $c_{\text{Init}}$ .

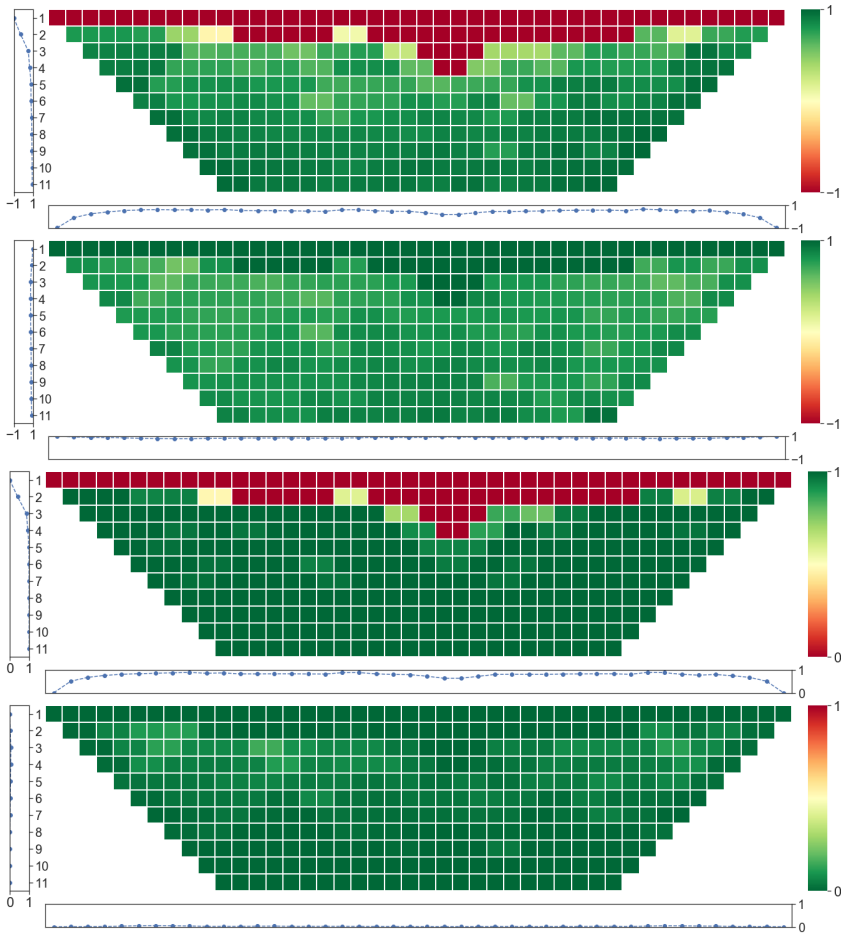


FIGURE 5.11: Stimulation robustness, safety robustness, coverage ratio, and collateral ratio (top to bottom) for the chosen reference configuration. The top row in the trapezoidal visualization corresponds to targeting a single dermatomal zone and the subsequent rows increase that to up to 11 zones. Left-to-right corresponds to corresponding lateral shifting of the targeted zones. The row averages are displayed on the left and the column averages below.



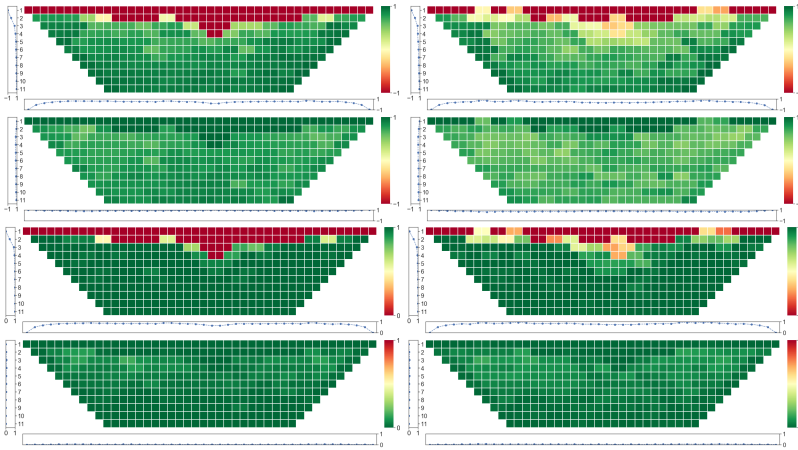


FIGURE 5.12: Comparison of the stimulation robustness, safety robustness, coverage ratio, and collateral ratio plots (top to bottom) from the reference configuration (single row with 5 electrode contacts; shown left), a single row sandwiched between two grounded rows (middle), and a  $3 \times 5$  array (right).

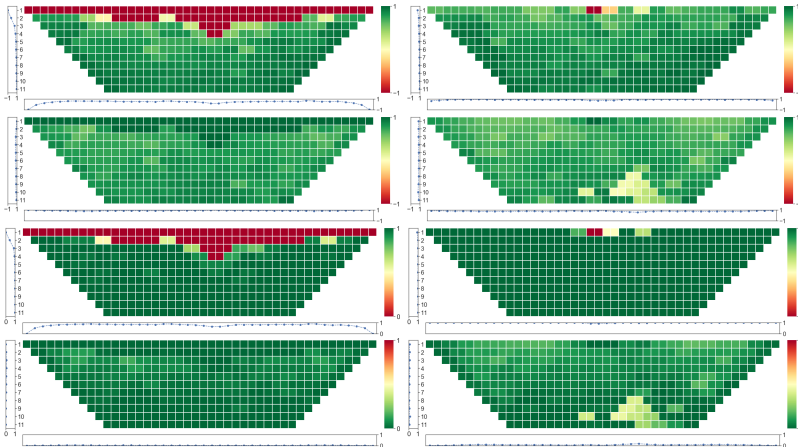


FIGURE 5.13: Impact of the relative weighting of avoidance of non-targeted regions vs. successful activation of targeted regions  $w = w_-/w_+$  on the stimulation robustness, safety robustness, coverage ratio, and collateral ratio plots (top to bottom) of the reference configuration. Left:  $w = 0.5$ ; right:  $w = 0.1$ .

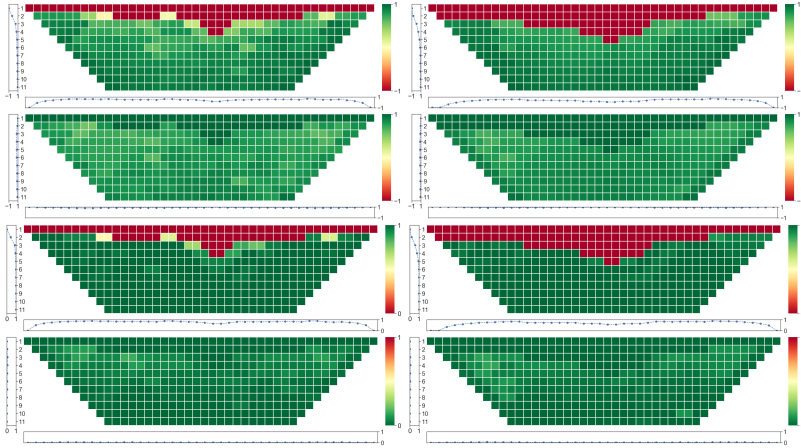


FIGURE 5.14: Impact of the sigmoid width  $d$  on the stimulation robustness, safety robustness, coverage ratio, and collateral ratio plots (top to bottom) of the reference configuration. Left:  $d = 0.015$ ; right:  $d = 0.050$ .

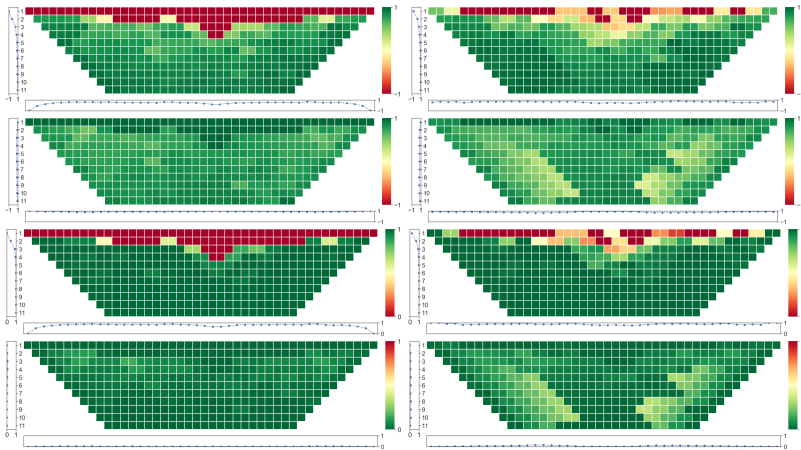


FIGURE 5.15: Impact of the initial guess  $c_{\text{Init}}$  on the stimulation robustness, safety robustness, coverage ratio, and collateral ratio plots (top to bottom) of the reference configuration. Left:  $c_{\text{Init}} = 75$ ; right:  $c_{\text{Init}} = 750$ .

The impact of varying  $w$ ,  $d$ , and  $c_{\text{Init}}$  on the robustness of stimulation is quantified in Figure 5.16. The monotonic decrease of the stimulation robustness, coupled to an increase of the safety robustness, with increasing  $w$  is evident and expected. The opposite trend is seen for the dependence on  $c_{\text{Init}}$ , demanding again a compromise between safety and efficacy. For  $d$ , an optimal choice (around 0.02) seems to be possible.

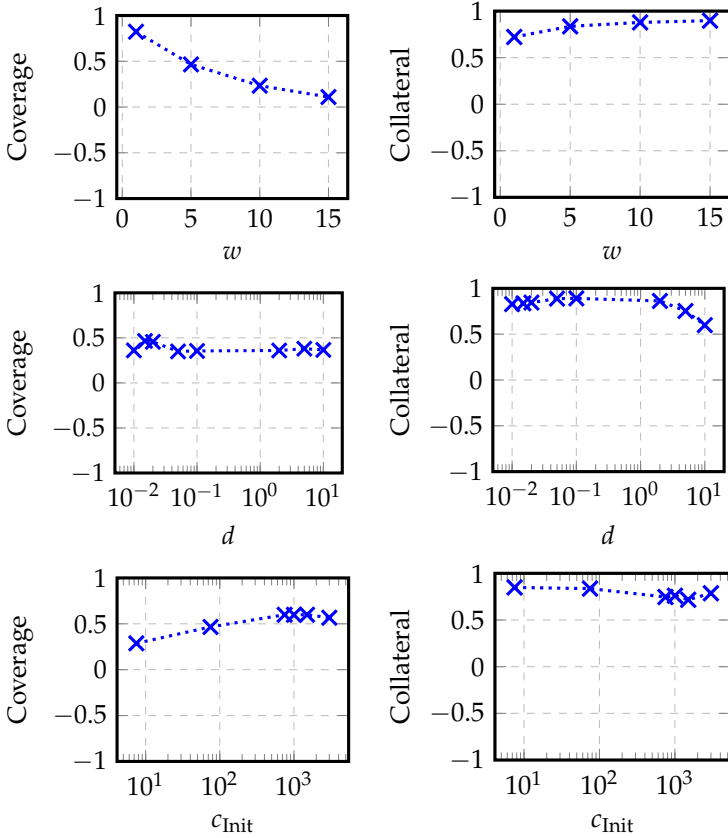


FIGURE 5.16: The parameter dependence of the coverage (left) and collateral (right) ratios, as a function of  $w$  (top),  $d$  (middle), and  $c_{\text{Init}}$  (bottom).

### 5.3.6 Anisotropy

To gain understanding of the impact of anisotropy, the influence on distributions of the potential in selected slices through the electrode center and between the anode and cathode electrodes (see Figures 5.23–5.26) and along selected lines (see Figures 5.18–5.19) has been studied for the four electrical conductivity models described in Section 5.2.5. Furthermore, the titration factors obtained using these four models were compared for three selected neuron fibers at different depths (see Table 5.2).

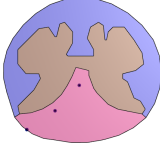
Depth	Unguarded	Guarded	
Front	2.6	4.0	
Middle	3.7	5.8	
Back	6.1	9.8	

TABLE 5.2: Stimulation thresholds (in mA) at the three selected fibers (varying depths – ‘Front’ is closest to the paddle).

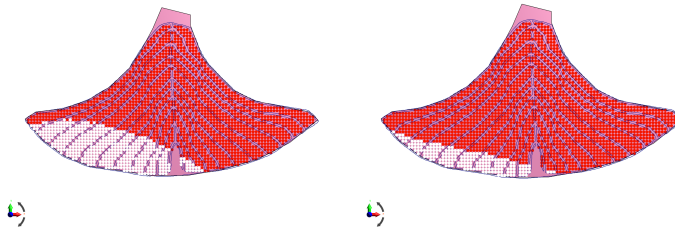


FIGURE 5.17: Predicted activated fibers at 2.6 mA stimulation current when assigning an average isotropic conductivity (left) and a more realistic anisotropic conductivity (right).

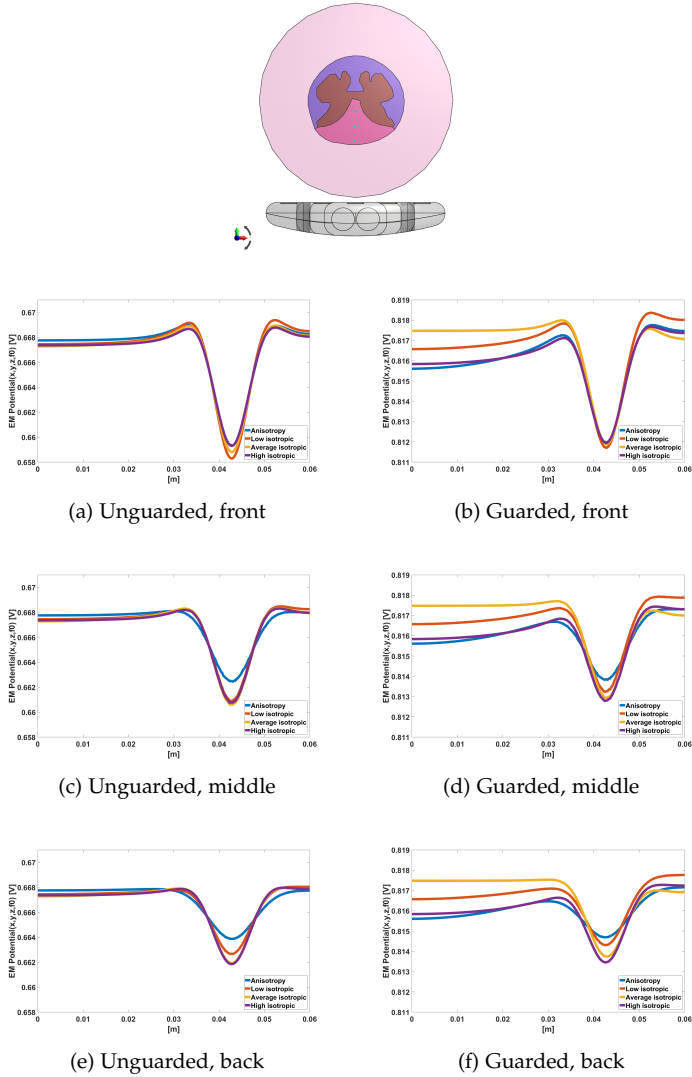


FIGURE 5.18: Longitudinal variation of EM potentials along longitudinal lines at different depths in the spinal column. Configurations are compared for anisotropic and isotropic tissue property assignments. The locations of the longitudinal lines in the DC along which the data was extracted are indicated by corresponding dots in the top figure.

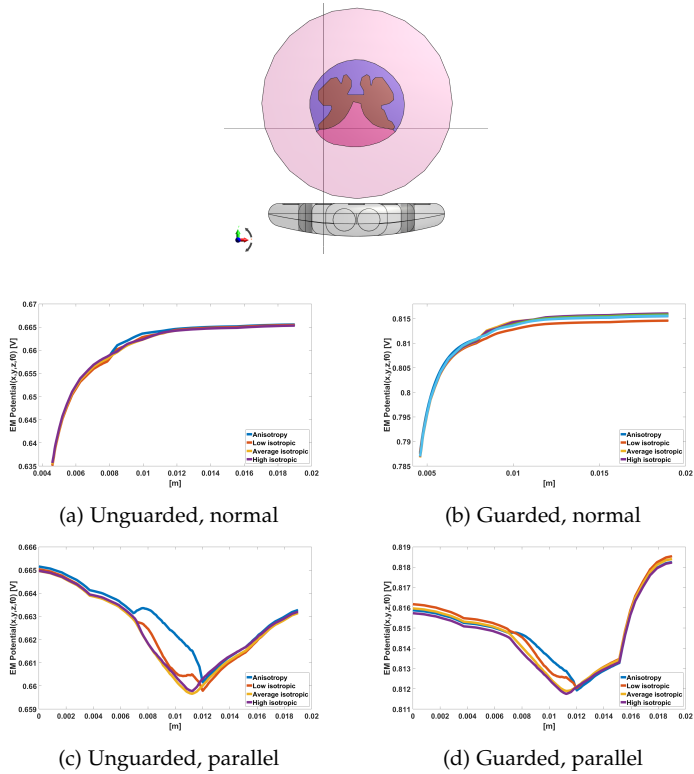


FIGURE 5.19: Potential variation along two lines for the unguarded and guarded configurations. The locations in the DC of the lines along which the corresponding data was extracted are illustrated in the top figure: a line normal to and through the active cathode ('normal') and a line across the spinal cord and parallel to the paddle ('parallel').

## 5.4 DISCUSSION

### 5.4.1 *Activation function as predictor*

**DBS** The large IC fiber activation threshold differences observed for the two stimulation voltage patterns (factor 5.4 between configurations [0/1/0] and [-1/0/1]) are a consequence of the change in localized potential width which strongly impacts the second derivative and hence the activation function. A rough estimation shows that the configuration-change from [0/1/0] to [-1/0/1] doubles the potential peak width and, hence, is expected to increase the stimulation threshold by a factor in the order of four. Interesting differences in spike initiation locations are found that can be readily understood by studying the activating function variation along the fibers.

**scs** It is evident in Figure 5.9, that an MIP isoline perfectly separates the region within which all fibers are activated from the non-activated region, confirming that the activating function can be used to predict fiber activation.

**$A_T$**  Figure 5.10 shows that  $A_T$  does not vary much more when the stimulation localization exceeds about 4–6 mm. For more localized exposures, thresholds increase, as neighboring transmembrane net-charge-transfer has a relevant inhibitory impact (for gaussian potential shapes, the second derivative features side-extrema with opposite sign). This must be compensated.

### 5.4.2 *Targeting optimization*

**SELECTIVITY** The automatic optimization is capable of identifying parameters that result in targeted activation of selected fibers / dermatomal zones, failing only when the target region is very narrow (1–2 zones) and centrally located (see Figure 5.11).

**1D VS. 2D CONTACT ARRAY** Targeting performance increases from a single row of five active electrode contacts, over the active row sandwiched between grounded rows, to the full 2D array ( $3 \times 5$ ). The robustness, however, shows the opposite trend (see Figure 5.12). This is to be expected as an increase of the number of optimization parameters (degrees-of-freedom)

enlarges the solution space, such that it encompasses solutions with better optimization functional values (higher stimulation selectivity). It does so, however, at the cost of the robustness of the stimulation configuration – probably as it relies on subtly balancing out the impact of the individual contacts (compensation), resulting in a reduced safety margin.

**OPTIMIZATION PARAMETERS** Depending on the number of steering parameters (contact voltages) to be optimized, the optimization (based on precomputed fields) takes between a few seconds and a few minutes, compared with 30 min for performing a single electrophysiology simulation of all the fibers (i.e., one optimization iteration; could be trivially parallelized, as long as the fibers are treated as disconnected). Selecting an initial guess of the right magnitude (voltage range) is required to ascertain convergence to an optimal solution. Increasing the sigmoid width  $d$  strongly accelerates convergence but reduces stimulation robustness – likely because changes of the activation function distance from the stimulation threshold have a smaller impact on the optimization functional. As expected, increasing the  $w_+/w_-$  ratio prioritizes achieving effective stimulation over safety, and vice versa. Thus, successful optimization is dependent on proper tuning of the optimization parameters (sigmoid width, magnitude of initial guess). More work is required to find a general approach to setting these parameters.

**VALIDITY OF APPROXIMATION** The predicted and optimized stimulation based on the activating function-related functional has been successfully compared and validated against full EM-electrophysiological modelling, with the complexity of the channel dynamics taken into consideration.

### 5.4.3 *Performance*

One full neuro-simulation featuring all 1952 took 30 min on the employed computational infrastructure (which allowed parallel execution of 20 fiber simulations), meaning that an optimization-run with 100 iterations (optimizations for the SCS setup in Chapter 3.3 typically required 100-200 iterations) would require in the order of 50 hrs. Using the activation function-based approach reduced the optimization time to  $< 2$  min (and below a minute when optimizing only a single row of contacts), without making use of parallelization. This corresponds to an acceleration of more than three orders of magnitude.



#### 5.4.4 *Anisotropy*

The titration factor behavior is not in agreement with the naive expectation that the anisotropic model should produce thresholds intermediate between those observed for the low-conductivity and high-conductivity isotropic models. Instead, the titration factors are similar for the different isotropic models, and the behavior of the anisotropic model is unique. It has a titration factor between the low and the average isotropic models for the closest fiber, but the titration factor rapidly increases with increasing depth.

This behavior can be better understood by observing the potential along these fibers (see Figure 5.18). While the potential variation along superficial fibers is similar in the isotropic and anisotropic cases, the curvature (second derivative) of the curves rapidly decreases with increasing fiber depth in the case of the anisotropic model compared to the curvature behavior observed for the isotropic cases. The stimulation threshold is known to be related to the second derivative [16, 246] and, thus, reduced curvature is related to an increased stimulation threshold. For a field line from the cathode to the anode (see Figure 5.20) to reach a location deep within the spine, the current has to travel to that depth when entering and exiting the spinal cord. Most of the voltage drop occurs along those path segments, where there is an important field component in the transverse direction (along which resistance is high). At the same time, the voltage drop along the part of the path in between is reduced due to the higher conductivity. This scenario can be compared to a serial arrangement of a large resistor, a small resistor, and another large one, where the voltage drop over the small resistor is comparably small. Furthermore, a trajectory that rapidly gains depth, then travels mostly in a longitudinal direction, and leaves the spinal cord again on a short path results in overall reduced resistivity – even if the overall field line length increases – thus further stretching the potential along the neuron fiber, reducing the curvature, and increasing the stimulation threshold. A field line that barely penetrates the spinal cord, however, will be little affected by the anisotropy, and its trajectory will not deviate much from that of a field line in the isotropic case. Therefore, the stimulation threshold of fibers near the stimulator remains similar in the anisotropic and in the isotropic case.

In conclusion, the important impact of tissue anisotropy on stimulation thresholds, selectivity, and recruitment curves is understandable, as conductivity is highest precisely along the direction of the fibers which is also the direction along which the second derivative of the potential is computed,

while it is low perpendicular to that direction. This configuration facilitates potential drops between fibers and simultaneously smooths the potential variation along fibers, thus reducing the activating function and the related stimulatability.

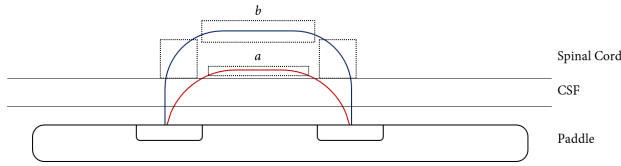
When comparing the anisotropic and isotropic models, it is important to remember that the spinal cord is surrounded by highly conductive CSF that mostly dominates the potential distribution across the entire geometry. The lower conductivity spinal cord locally distorts and compresses the isopotential surfaces, producing a higher field within the spine than in the surrounding CSF. This compression slightly increases the potential variation – and hence curvature – on the dorsal side, while decreasing it on the ventral side (see Figures 5.23–5.26). The degree of that effect depends on the exact conductivity value and explains the titration factor behavior observed for different isotropic models with varying conductivity: with increasing conductivity, the titration factor and stimulation threshold of neurons near the paddle (‘front’ neuron) increases slightly, while the titration factor of remote neurons (‘back’ neuron) decreases.

In conclusion, neural tissue anisotropy has an important impact neurostimulation thresholds and recruitment. While the limit stimulation threshold can be estimated with an isotropic model, the prediction of penetration depth and activation region size is considerably overestimated when an isotropic model is used, even if low transversal conductivity is applied.

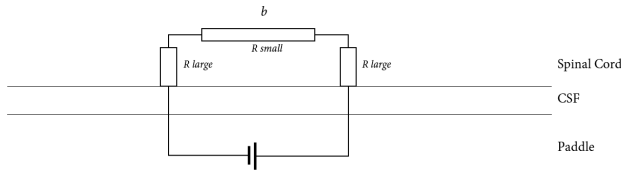
#### 5.4.5 *Generalization*

In future work, the use of activation functions for rapid optimization of targeted stimulation could be extended beyond the demonstrated application to steering parameter optimization for a homogeneous population of neural fibers.

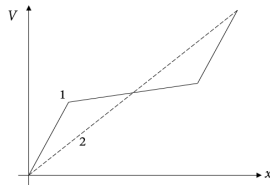
**HETEROGENEOUS FIBER POPULATION** In cases where different types of fibers need to be considered (e.g., myelinated and unmyelinated, varying diameters, varying channel characteristics and / or distribution), the principal adaptation of the presented scheme is that instead of a global  $A_T$  value, fiber-specific activation function thresholds  $A_T(\text{fiber-type})$  are required. Several applications, such as nerve stimulation selectivity optimization, e.g., in the context of neuroprosthetics [204] or bioelectronic medicine, could benefit from this finding.



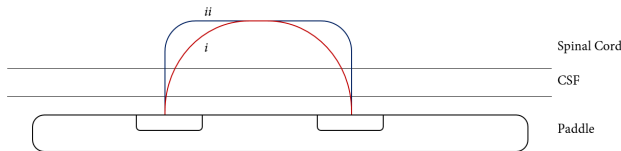
(a) Comparison of two field lines that reach different depth in the spinal cord.



(b) 'Equivalent circuit' for field line  $b$  (anisotropic conductivity).



(c) Potential variation along a field line that initially goes through a high-resistive region, then a low-resistive region, and then a high-resistive once again (1); comparison to the potential variation when going through a constant resistivity region (2).



(d) Two paths reaching the same depth. Path  $ii$  might be longer than path  $i$ , but it minimizes the parts with mostly transversal orientation and larger resistivity.

FIGURE 5.20: Interpretation of the observed strong impact of anisotropy on the stimulation. Anisotropy reduces the voltage variation in the part of the path with mostly longitudinal orientation, as understandable when looking at a simple circuit example with serial resistors (B), and favors paths with reduced length in transversal direction (D).

**PULSE SHAPE** In cases where the pulse-shape has to be optimized (e.g., to improve stimulation selectivity by fiber-type),  $A_T$  cannot be taken as constant anymore. Instead, in each optimization iteration, a single electrophysiological simulation per fiber-type must be performed, to determine the new  $A_T$ (pulse-shape).

## 5.5 CONCLUSIONS

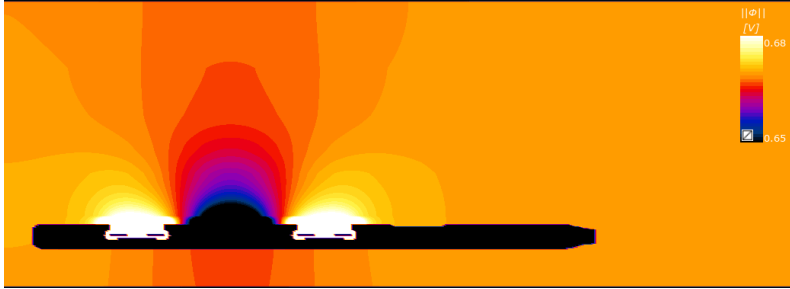
Inspired by the successful prediction of stimulation locations and thresholds in computational models of DBS and SCS based on activation function, a novel optimization approach for targeted stimulation with multi-contact electrodes that is capable of efficiently determining optimal stimulation parameters has been developed. It optimizes the physiological response based on features of the electric potential. The approach requires information about fiber orientation, but can be performed without the need for repeated coupled EM-neuronal dynamics modelling, resulting in computational acceleration by more than three orders of magnitude. The quality of the stimulated region predictions has been successfully validated against such coupled EM-neuronal dynamics modelling and applied in the context of SCS to obtain superior targeting (focus and steering). Extension of the approach to pulse-shape optimization and / or heterogeneous fiber populations (as relevant in neuroprosthetics and bioelectronic medicine) have been discussed. Adaptation of the approach is likely to be required when the distance between independent electrodes along the fiber direction drops below about 4 mm.

In the process of that work, a computational neuro-functionalized human head model for DBS was created based on the work by [171]. The computational 'MIDA' head model was employed for computational electromagnetics and as a source of information (DTI data, brain nuclei atlas) supporting neuron placement and fiber trajectory tracing. Populations of electrophysiological STN neurons, as well as GPi and IC fiber models were created, positioned realistically within the head anatomy, and can now be used for coupled electromagnetic-neuronal dynamics simulations. The neuro-functionalized MIDA model was applied to compare two different electrode configurations with similar inter-electrode voltage-differences. Large differences in IC fiber activation thresholds (factor of 5.4) were found and explained based on activation function considerations.

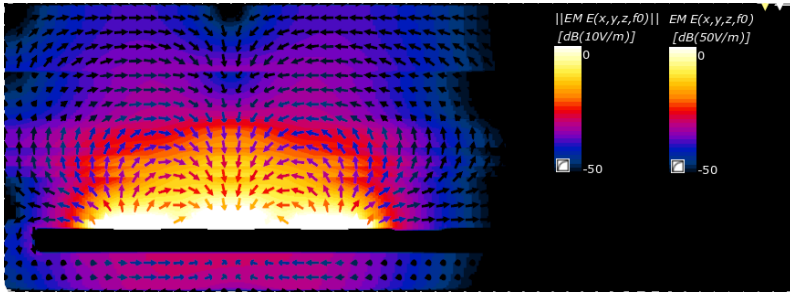
Activation function considerations also help to understand the unexpectedly strong impact of anisotropic conductivity of stimulation penetra-

tion depth (e.g., in epidural stimulation applications). The origin of that phenomenon is twofold: (i) increased longitudinal conductivity results in smoothed potential variations along the fiber orientation, reducing the activation function and increasing the stimulation threshold, and (ii) increased transversal resistance accelerates the field intensity decrease with increasing distance to the electrodes.

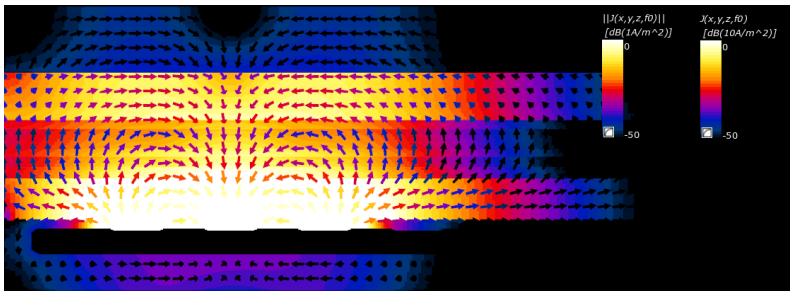
5.A APPENDIX



(a) Potential



(b) Electric field ( $E$ )



(c) Current Density ( $J$ )

FIGURE 5.21: Planes cutting longitudinally through the active electrodes, showing the potential,  $E$ -field, and current density distributions for the unguarded step 15 configuration from [7].



(a) Potential

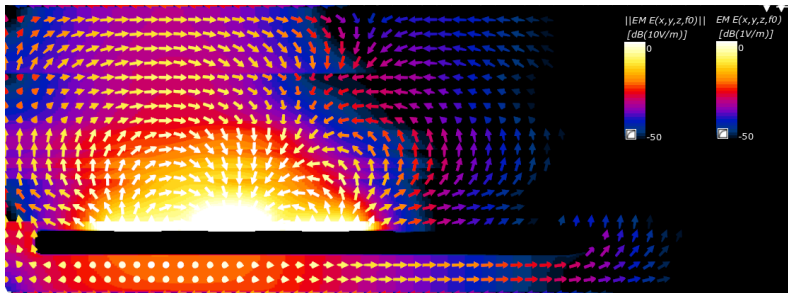
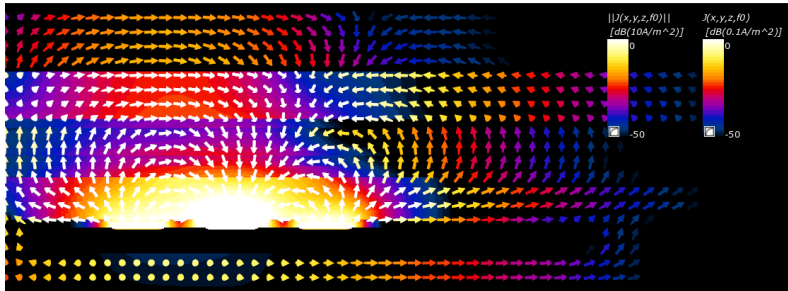
(b) Electric field ( $E$ )(c) Current Density ( $J$ )

FIGURE 5.22: Cross section planes cutting longitudinally through the active electrodes, showing the potential,  $E$ -field, and current density distributions for the guarded step 5 configuration from [261]. Note the different scales used for the Vector and Slice Field Viewers.

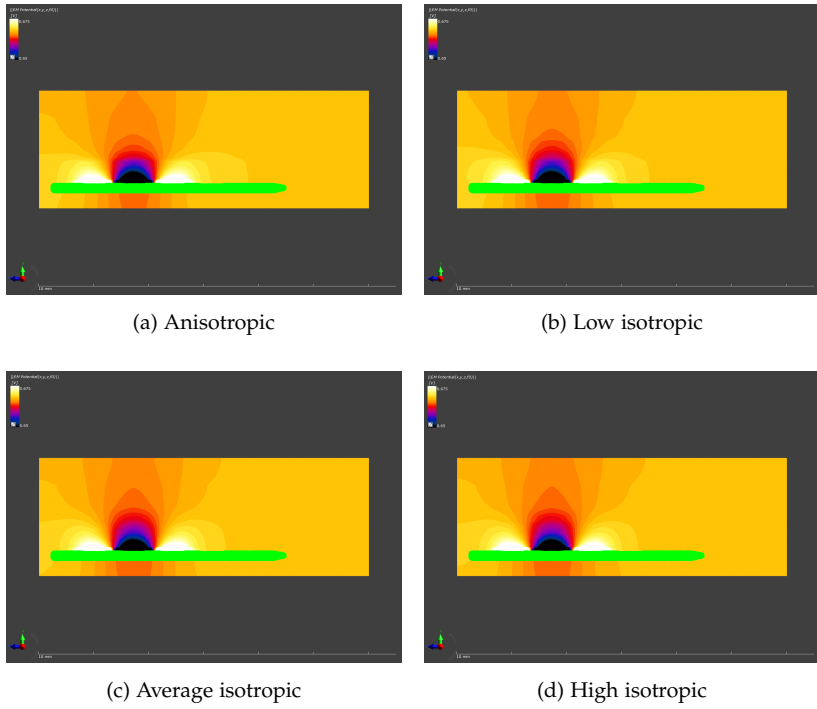


FIGURE 5.23: EM potential on a longitudinal plane across the cathode (Slice Field View); unguarded configuration with different conductivity models.



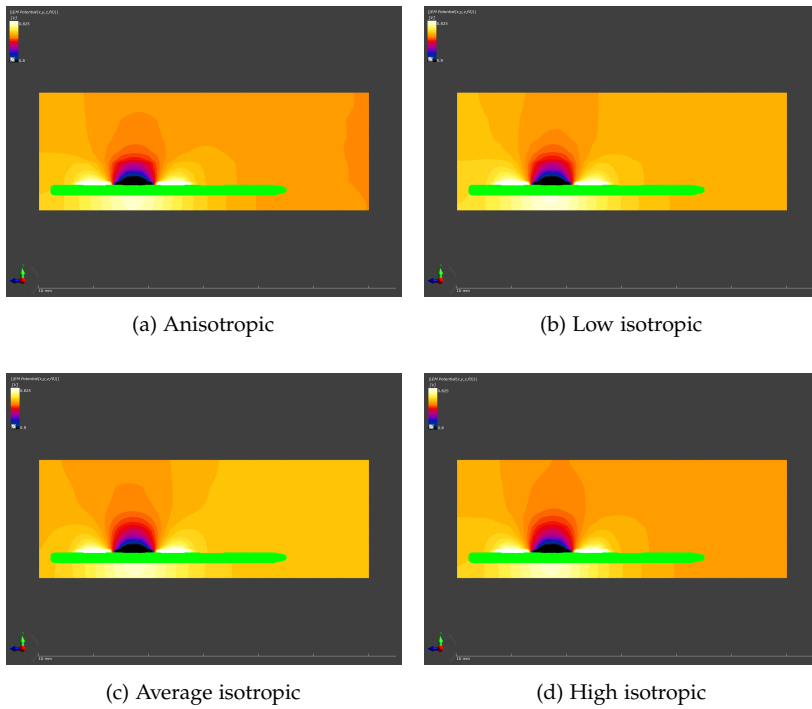


FIGURE 5.24: EM potential on a longitudinal plane across the cathode (Slice Field View); guarded configuration with different conductivity models.

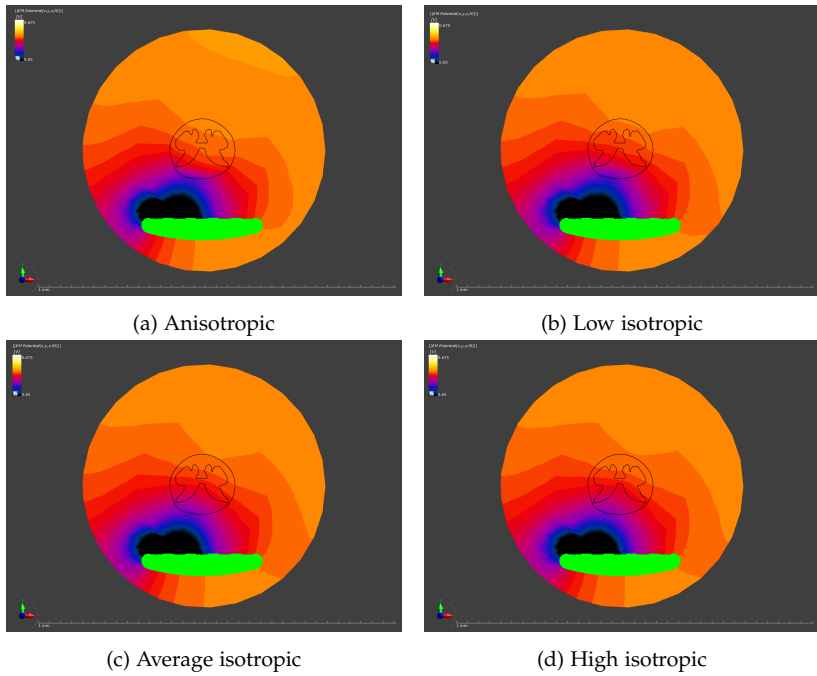


FIGURE 5.25: EM potential on a transversal plane across the cathode (Slice Field View); unguarded configuration with different conductivity models.

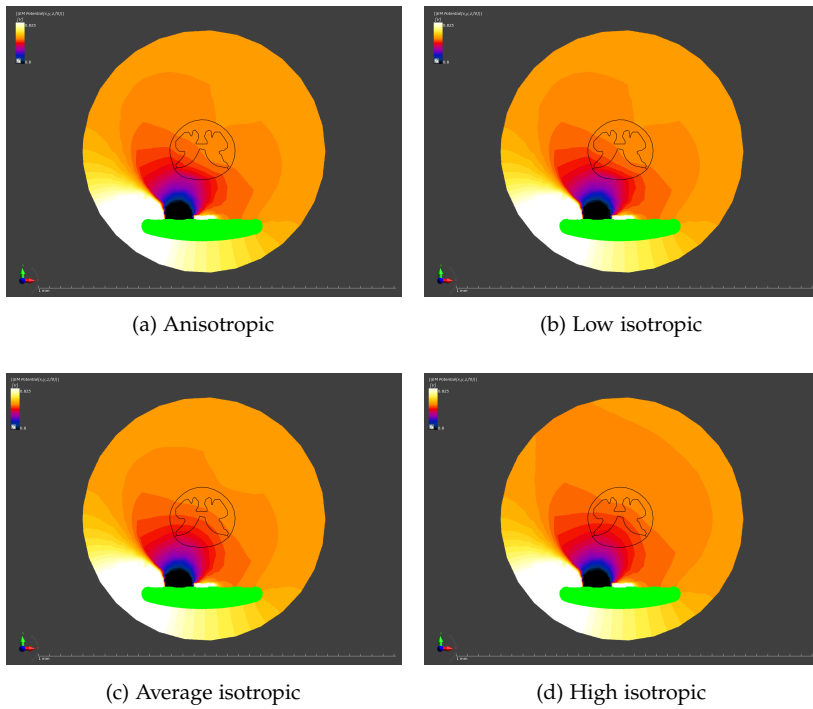


FIGURE 5.26: EM potential on a transversal plane across the cathode (Slice Field View); guarded configuration with different conductivity models.



## ACOUSTIC MODELLING OF TRANSCRANIAL FOCUSED ULTRASOUND

---

### 6.1 MOTIVATION

Transcranial FUS (tcFUS) was initially introduced for functional neurosurgery, starting with the treatment of chronic pain patients (stereotactic lesioning, [264]), but later also for applications in brain cancer surgery [265] and epilepsy therapy [141]. In all these applications, tissue lesioning (thermal coagulation) is performed by using high intensity tcFUS. Lower intensity tcFUS, on the other hand, has been found to achieve reversible blood-brain-barrier disruption [266], and to have neuromodulatory abilities [109].

However, since its introduction in 1947 by [267], it has become clear that achieving a sharp focus, precise targeting, and reliable prediction of transcranial sonication efficiency are difficult [268]. This is mostly due to acoustic scattering and aberration induced by the highly heterogeneous structure of the skull [120] which shows high inter-patient variability and is the principal cause for the need of personalized treatment planning and optimization. Therefore, modelling approaches also need to be patient-specific. This can be achieved by using medical image data to obtain information on the individual anatomy and tissue property distributions of each patient. Particularly CT scans offer valuable data on skull structure and properties.

Chapters 7 and 8 provide valuable contributions to the understanding of various factors that affect image-based personalized modelling of tcFUS, as well as the requirements of reliable modelling, along with pitfalls. These insights were obtained through careful, experimentally validated computational studies, including sensitivity analyses and mechanism elucidation. Particular focus is placed on the modelling of the acoustic transducer in order to get a reliable source model, and on image-based skull heterogeneity modelling.



## TRANSDUCER MODELLING FOR ACCURATE ACOUSTIC SIMULATIONS OF TRANSCRANIAL FOCUSED ULTRASOUND STIMULATION

---

### ABSTRACT

**Objective:** Low-intensity transcranial ultrasound stimulation (tcFUS) is emerging as non-invasive brain stimulation technique with superior spatial resolution and the ability to reach deep brain areas. Medical image-based computational modelling could be an important tool for individualized tcFUS dose control and targeting optimization, but requires further validation. This study aims to assess the impact of the transducer model on the accuracy of the simulations.

**Approach:** Using hydrophone measurements, the acoustic beam of a single-element focused transducer (SEFT) with a flat piezoelectric disc and an acoustic lens was characterized. The acoustic beam was assessed in a homogeneous water bath and after transmission through obstacles (3D-printed shapes and skull samples). The acoustic simulations employed the finite-difference time-domain method and were informed by computed tomography (CT) images of the obstacles. Transducer models of varying complexity were tested, representing the SEFT either as a surface boundary condition with variable curvature, or also accounting for its internal geometry. In addition, a back-propagated pressure distribution from the first measurement plane was used as source model. The simulations and measurements were quantitatively compared using key metrics for peak location, focus size, intensity and spatial distribution.

**Main results:** While a surface boundary with an adapted, 'effective' curvature radius based on the specifications given by the manufacturer could reproduce the measured focus location and size in a homogeneous water bath, it regularly failed to accurately predict the beam after obstacle transmission. In contrast, models that were based on a one-time calibration to the homogeneous water bath measurements performed substantially better in all cases with obstacles. For one of the 3D-printed obstacles, the simulated intensities deviated substantially from the measured ones, irrespective of the transducer model. We attribute this finding to a standing

wave effect, and further studies should clarify its relevance for accurate simulations of skull transmission.

**Significance:** Validated transducer models are important to ensure accurate simulations of the acoustic beam of SEFTs, in particular in the presence of obstacles such as the skull.

## 7.1 INTRODUCTION

Transcranial focused ultrasound (tcFUS) has been successfully applied for stereotactic neurosurgery, brain tumor ablation, and reversible blood brain barrier (BBB) disruption. More recently, tcFUS has also emerged as a promising non-invasive brain stimulation technique due to the smaller focal size and the possibility to reach deeper brain areas compared to other non-invasive stimulation techniques [123]. Both excitatory and inhibitory neuromodulatory effects of tcFUS have been repeatedly demonstrated in several animal species, including non-human primates [11, 109, 130, 269, 270] and humans [12, 269, 271, 272].

Safe application of tcFUS requires the precise control of the ultrasound dose in the brain. So far, this mostly relates to the control of the focus position and size of single element focused transducers (SEFT) that have been used in the majority of studies due to their relative ease of use and low cost, despite a more limited control of the energy deposition and spatial targeting compared to multi-element phased array transducers. The SEFT's beam profile can be characterized using hydrophone acoustic pressure measurements both in a homogeneous water environment and after the transmission through skull samples. These measurements, however, allow only for a limited assessment of the actual tcFUS dose in human *in vivo* applications as the beam profile depends strongly on the skull's heterogeneous and individually varying structure and thickness [14]. Computer simulations informed by imaging techniques like magnetic resonance imaging (MRI) and computed tomography (CT) could play an important role in a non-invasive dose control and treatment planning on an individual patient basis. Simulations typically make use of some numerical method (e.g., the Finite Difference Time Domain - FDTD method) to solve the pressure wave equation [17] for modelling the propagation of acoustic waves through inhomogeneous media. Their usefulness for dose control in practical applications directly depends on their accuracy.

Much prior work has focused on the geometry and acoustic properties of the skull [146, 147, 273–276], as inadequate skull models will cause



significant errors in transcranial simulations. However, special care also must be taken when modelling the transducer device. SEFTs typically consist of either a physically curved vibrating piezoelectric element or a flat piezoelectric disk with an acoustic lens shaped like a concave spherical cap. For the second case, SEFTs are frequently modelled by representing only the forward facing, spherical-cap-shaped surface and imposing a pressure or velocity boundary condition on it, neglecting the internal structure of the device. The simulated beam profile of this simplified model differs from the real profile when modelling the transducer surface curvature according to its real curvature, as shown in Figure 7.3b. Manufacturers therefore typically report an effective curvature to match the experimentally measured focus location [277] in a homogeneous water bath, as shown in Figure 7.3c. Simulations then model the transducer by using this reported effective curvature or by adapting the simulated curvature to fit experimental data on the focus location, and ignore the real and internal transducer geometry [14, 278–281].

While this approach allows matching the experimental location of the beam focus and its size (i.e., the peak dose location and full width at half maximum) in a test tank with water as medium and no obstacle, further validation is required when moving to more complex and heterogeneous obstacles, such as the skull. In this study, we used a SEFT with a flat piezoelectric disk and an acoustic lens and compared the simplified effective transducer model, as per the manufacturer's specification ( $S_{\text{eff}}$ ), against (1) physically realistic and detailed models of the transducer accounting for its internal geometry ( $P_{1-2}$ ; see Section 7.2.7), and (2) a source model derived by back-propagation ( $M_{\text{B-P}}$ ) of the measured pressure distribution to a virtual source plane. We investigated the sensitivity of the new models to the different underlying parameters and assessed their accuracy by comparing the results with hydrophone measurements of the beam in the presence of different obstacles. Obstacles consisted of two bone samples (sheep and pig) and three 3D-printed simple and skull-shaped phantoms made of Veroblack, a material of known acoustic properties. In addition, we acquired CT data of the obstacles with the transducer and obstacle holder for precise positioning and to derive estimates of the obstacle's geometry and acoustic property distributions in the case of the bone skulls. Finally, we assessed the sensitivity of simulations to the modelling parameters when employing full human head models instead of the obstacles. Our results show that the simplified, effective transducer model that was based on the specification sheet of the manufacturer produces substantial deviations between the

simulations and measurements. Specifically, clear deviations occurred in the presence of skull obstacles even though the correspondence was reasonable for the case of a homogeneous water background. This effect is even larger for a model that assigns a boundary condition to a surface reproducing the real, geometrically correct (physical curvature radius) transducer surface shape ( $S_{\text{geom}}$ ). The deviations were substantially reduced for the transducer models that were established based on calibration measurements in a pure water background.

## 7.2 METHODS

Figure 7.1 gives an overview of the methodological workflow, which is discussed in detail in the next sections.

### 7.2.1 *Bone samples and phantoms*

In this study, two animal skull samples (pig and sheep; see Figure 7.1a) and three phantoms were tested. The pig skull was bought from a butcher and the sheep skull was donated by a local farmer. Soft tissue from both skulls was mechanically removed with tweezers, and the samples were cut to maintain the upper parts of the skull. While the entire upper part of the sheep skull was preserved, only part of the pig skull was extracted to have a thickness comparable with that of the human cranium. A mostly flat surface was obtained where the pig skull was cut. The two bone samples were then glued to holders (see Figure 7.2) and subsequently continuously kept under phosphate-buffered saline (PBS) solution. The skulls were not degassed, but the CT data acquired before and after the measurements did not reveal the presence of gas inside the samples. In addition, three 3D-printed phantoms were constructed from Veroblack (acoustic properties in Table 7.1). Two of those phantoms replicated the outer shape of the pig and sheep skull samples, as reconstructed from CT data (see Figure 7.1a). The third phantom consisted of a printed rectangular slab obstacle ( $100 \times 100 \times 5 \text{ mm}^3$ ).

### 7.2.2 *US transducer and water tank measurements*

A single element spherical ultrasound transducer element with a flat piezoelectric disc and an acoustic lens (IPBD<sub>2</sub>, Hagisonic, South Korea, shown in Figure 7.1a) operating at 500 kHz, with an aperture diameter of 3 cm, a radius of curvature of 2.5 cm, and a reported focal length of

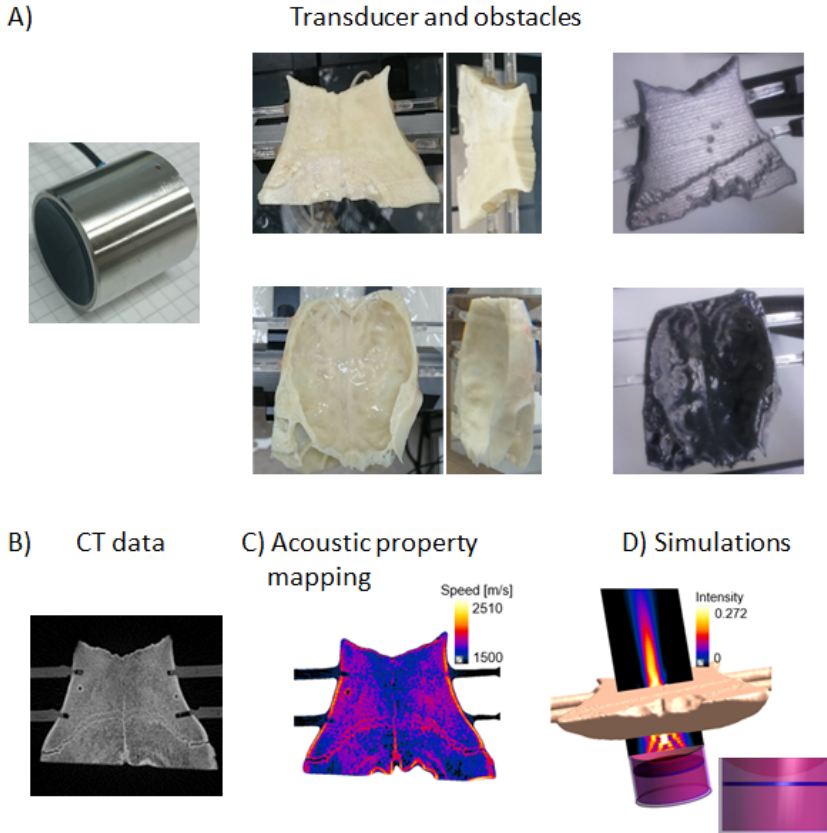


FIGURE 7.1: Workflow in the methods section. (A) The propagation of an ultrasound transducer (left) was characterized in a pure water background and after the transmission through obstacles. Specifically, the obstacles were a pig and a sheep skull (center, top and bottom, respectively), and the corresponding 3D printed phantoms (right). (B) The CT data of the obstacles were acquired, (C) to map their acoustic properties and to import their geometry in the simulation environment. (D) An example of the normalized intensity beam with the pig skull obstacle is shown, together with a view of the transducer model based on its actual internal geometry.

Material	$\rho$ [kg/m <sup>3</sup> ]	$c$ [m/s]	$\alpha$ [Np/m]	$Z$ [MRayl]
Water (generic)	1000	1500	0	1.5
Water (20°C)	1000	1482	0	1.5
Veroblack	1180	2495	21.3	2.9
Acrylic Resin	1190	2750	7.3	3.3
Acrylic M1-7	1180	2610	14.2	3.1
Human Cortical Skull	1908	2814	27.2	5.4

TABLE 7.1: Acoustic properties of different materials used in this paper, for a center frequency of  $f = 500$  kHz from [14, 155, 282]. In particular, the density ( $\rho$ ), the speed-of-sound ( $c$ ), the coefficient of attenuation ( $\alpha$ ) and the acoustic impedance ( $Z$ ) are indicated for each material. Different values for speed-of-sound in water that were used in the uncertainty assessment are included (see Section 7.2.6).

5 cm (incorrectly reported as radius of curvature by the manufacturer specification sheet [277]), was used to generate the acoustic pressure waves. The setup used for the bone samples employed two function generators (33220A, Agilent Technologies, California, United States) to generate a burst (20 pulses / burst) of sinusoidal waves with a center frequency of 500 kHz at a pulse repetition frequency of 1 kHz. The pulse was subsequently amplified by a power amplifier (5312, OPHIR, California, USA) and sent to the transducer. We first measured the pressure distribution along the symmetry axis from far to near field with different numbers of pulses (from 2 up to 30) per burst. In the far field, we observed that the measured beam intensity did not change beyond 15 pulses, meaning that the steady-state was reached. We chose a number of pulses / burst of 20, which, considering a speed-of-sound in water of 1500 m/s, corresponds to a travelled distance of 6 cm. A custom-designed 3D-printed holder was used to fix the transducer inside a tank filled with de-ionized water. The pressure wave was sampled with a calibrated needle hydrophone with an active diameter of 1 mm (NH1000, Precision Acoustic, Dorset, UK) carefully inserted in a holder surrounded by a sponge in order to minimize reflection, as tested for continuous waves. The sponge is an open-cell foam for packing material (see Figure 7.2a). More importantly, since the distance between the transducer and hydrophone holder was greater than 8 cm even when the hydrophone was close to the transducer, reflections from the

holder did not affect the measurements of the 20 pulses / burst. Before each measurement series, the position of the transducer inside the holder was measured using a caliper. The hydrophone was moved by a stepper-motor system (Sciencetown Co., Incheon, South Korea) with a plane sampling distance of 0.25 mm and controlled by custom written software in *MATLAB*. The signal from the hydrophone was transmitted and visualized with an oscilloscope (DSOX2022A, Agilent Technologies, California, United States). The raw data for each acquisition point were sent via USB to a computer and stored. In order to decrease noise, the signal was acquired using the average mode of the oscilloscope, with 32 samples averaged at each measurement position. For logistic reasons, the measurement setup used for the 3D-printed phantoms was changed to employ a different function generator (33500B, Keysight, California, United States), amplifier (240L, E&I, New York, United States) and oscilloscope (DSO-X 3024A, Agilent Technologies, United States), and an in-plane sampling resolution of 0.3 mm. The material of the hydrophone holder was Plexiglas in these measurements, rather than aluminum, to improve the acoustic impedance matching with water. Measurements of the beam profile in water confirmed that this change did not affect the recorded data.

Thirteen planes parallel and one perpendicular to the transducer aperture were acquired to fully characterize the beam profile. The distance between twelve of the parallel planes was 5 mm and an additional plane near the focus was acquired at a distance of 2.25 mm from the nearest plane to better sample the strong spatial variations of the beam. The axial distance between the nearest parallel plane and the center of the transducer was 2 cm. The aperture-perpendicular plane was chosen to traverse the beam position of maximum intensity. In the case a strong secondary focus was detected, an additional perpendicular plane was acquired to cover it appropriately. The number of points for each acquired plane varied. The largest plane had a size of  $3 \times 8 \text{ cm}^2$  with a sampling distance of 0.25 mm resulting in 38841 points. The smaller planes had a size of  $0.9 \times 0.9 \text{ cm}^2$  with a sampling distance of 0.3 mm (961 points in total). Prior to each plane measurement, the position of maximum intensity in water was determined as follows. First, two parallel planes with a separation of 2 cm were acquired near the focus and the positions of the peak intensities in each plane determined. Subsequently, measurements were performed along a line through these two positions. The obstacle was then put in place and several planes were acquired as stated above.

### 7.2.3 *Actual measurements with objects*

In order to precisely position the objects in the water tank, a holder was 3D-printed for each obstacle. This holder allows for the obstacle to be screwed in place at one of 5 different locations (position 1, 2A, 2B, 2C, and 3; see Figure 7.2).

The exact distance between transducer and obstacle was determined as follows: first, the location of the peak was determined in a water tank. Its position was recorded and used to define the symmetry axis. Then, the obstacle and its holder were inserted in the water tank. The distance along the symmetry axis between the forward facing obstacle surface and the previously determined focus location (in the absence of the obstacle) was measured. These measurements are used to accurately determine the position of the obstacle relative to the transducer. The complete set of obstacle distances to the transducer are shown in Figure 7.2. Beam profiles were measured after transmission through the two animal skull samples. A similar procedure was followed for the three 3D-printed Veroblack phantoms.

### 7.2.4 *Calculation of US intensity from the measured data*

The stored raw signals were first filtered with a high pass 4<sup>th</sup> order Butterworth filter with a cutoff frequency of 200 kHz to remove low-frequency noise. For each measured position, the intensity in  $W/m^2$  was then calculated as

$$I = \frac{p^2}{2\rho c}$$

where  $p$  is pressure in Pa,  $\rho$  is the density of water ( $1000 \text{ kg/m}^3$ ) and  $c$  is the speed-of-sound in water ( $1500 \text{ m/s}$ ). To calculate the signal phase, a Hanning window was applied to the time domain signal to select only a central period (10<sup>th</sup> pulse). The Fourier transform was then calculated and the phase for the center frequency determined.

### 7.2.5 *CT imaging of the objects*

We acquired CT data of all objects attached to their holders both in water and air backgrounds using a PET / CT scanner (positron emission tomography, Biograph 128, Siemens, Germany). For each object, we acquired CT data with tube current-time product of 115 mAs and tube potential of 80 kV, which would correspond to a low dose of 0.3 mSv for a human head

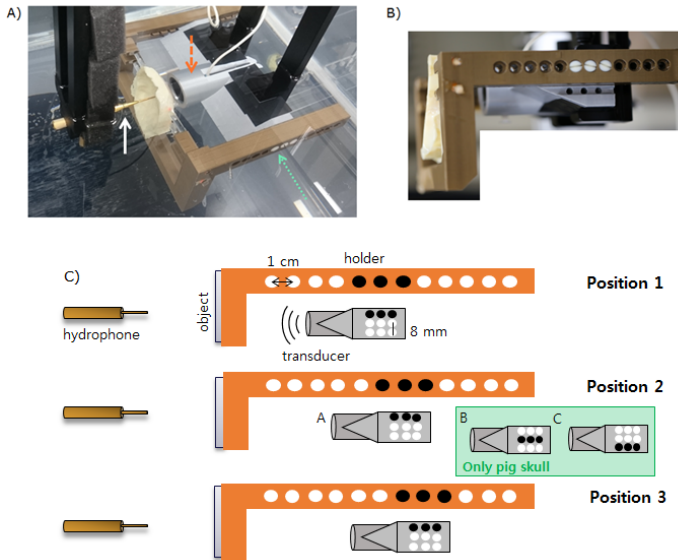


FIGURE 7.2: Details of the measurement setup. (A) The orange arrow points to the transducer, inside its 3D-printed holder (silver plastic). The transducer holder has an opening that allows the cable from the transducer to easily reach the amplifier and the curved face of the transducer to be positioned towards the hydrophone and the obstacles. The skull holder (gold plastic) is connected to the transducer holder with screws, in a way which is stylized by the black dotted line. The obstacle (here, the sheep skull) is glued to thin acrylic rods that are fixated in holes of the main part of the holder. The distance between the outer part of the transducer holder and the acrylic rods is 2.3 cm, as indicated in the figure. The white arrow points to the hydrophone. It is fixed in a holder, which is surrounded by sponge to absorb acoustic reflections. While the transducer and the skull stay in the same position throughout a measurement, the hydrophone holder is moved by a stepper-motor system. (B) Holders of the hydrophone and object seen from the side (indicated by the green arrow in A). The relative position of the skull and the transducer can be changed in steps using different screw holes. (C) A schematic of the employed configurations in this study. Black dots indicate the position of the screws, and the transducer holder is shown in grey. The transducer face is inside the cylindrical part of the holder, as displayed in the figure. The horizontal distance of the holes in the skull holder is 1 cm and the vertical one is 8 mm.

scan (roughly one third of the dose of clinical head scans). A sharp filter (H60s) was used during reconstruction. The nominal spatial resolution of the reconstructed images was  $0.36 \times 0.36 \times 0.6 \text{ mm}^3$ . An example of one slice of the CT data for the pig skull is shown in Figure 7.1b.

### 7.2.6 Simulation framework

Acoustic propagation was simulated within the *Sim4Life* (ZMT Zurich MedTech AG, Zurich, Switzerland) platform for computational life sciences, which encompasses functionality for image-based modelling, a range of acoustic propagation solvers, a *Python* scripting interface, as well as post-processing, visualization, and analysis functionality. For the purpose of this study, the linear acoustic pressure wave solver (LAPWE) from [17] was employed, which implements FDTD on rectilinear, inhomogeneous meshes and supports multiple graphical processing units (GPU) parallel execution to permit simulation of models with a large number of degrees-of-freedom within reasonable time. The LAPWE solver solves the wave equation:

$$\rho \nabla \frac{1}{\rho} \nabla p - \frac{1}{c^2} \frac{\partial^2 p}{\partial t^2} - \frac{\tilde{a}}{c^2} \frac{\partial p}{\partial t} = 0$$

$$\tilde{a} = 2\alpha \sqrt{\frac{\alpha^2 c^4}{\omega^2} + c^2}$$

where  $\rho$  is density in  $\text{kg/m}^3$ ,  $c$  is speed-of-sound in  $\text{m/s}$ ,  $\alpha$  is attenuation in  $\text{Np/m}$ ,  $p$  is pressure in  $\text{Pa}$ ,  $t$  is time in  $\text{s}$ , and  $\omega$  is angular frequency in  $\text{rad/s}$ . This equation accounts for reflections due to acoustic impedance ( $Z = \rho c$  in  $\text{kg}/(\text{m}^2 \text{ s})$  or  $\text{Rayl}$ ) variations and discontinuities, standing waves, and the combined impact of absorption and scattering. However, it neglects shear waves in the rigid skulls, as well as tissue non-linearities, which can lead to frequency mixing and higher harmonics, but are not relevant at the studied intensities [273]. Grid generation ensured that the voxel size in every material remained below a tenth of its wavelength. The coarsest grid step was  $0.3 \text{ mm}$  outside the skull region and  $0.1 \text{ mm}$  in the skull region, resulting in a simulation mesh with about 500 million voxels. To ascertain the suitability of the discretization, a grid convergence analysis was performed for all obstacles in the holder's first position, where the grid resolution was increased until the peak amplitude change remained below 1%. Perfectly Matched Layers (PML) boundary conditions with 16 layers were used to ascertain that reflections at the domain boundary remain negligible ( $< 2\%$  amplitude change [283]). Undulations are still



apparent in some of the simulations (see Figure 7.3). These result from imperfect wave absorption at the boundaries. It has been confirmed that enlarging the domain or increasing the number of PML layers indeed strongly reduces the undulations, at the cost of increased computation times. Detailed information about the verification and validation of this solver and its implementation can be found in [283].

In addition to performing simulations using the LAPWE solver, similar simulations were executed (for the sheep skull setup) with *Sim4Life*'s Westervelt-Lighthill Equation (WLE) solver. This solver implements a higher-order (larger stencil) finite-difference scheme and also accounts for non-linearity (e.g., frequency mixing) and a first order frequency dependence of acoustic properties. These simulations allow to assess the impact of the numerical solver implementation, as well as the impact of neglecting non-linearity. The non-linearity parameter of  $B/A = 374$  was assigned according to [284], which is described as a conservative choice [285].

Simulations of the experimental setup were performed for a pure water background, as well as for the two skulls and the 3D-printed Veroblack plate and skulls, at up to five positions each (see Figure 7.2). The skull models were generated by thresholding the normalized CT images at 500 Hounsfield Units (HU) and extracting the skull component. Image up-sampling (from 0.36 mm base resolution to 0.111 mm resolution) and gaussian smoothing ( $\sigma = 1$  mm) were applied to avoid surface staircasing related to the CT resolution which is large compared to the discretization step in the simulation domain (0.1 mm). The transducer holder geometry was readily available from the computer-aided-design model used for rapid prototyping. For more details on the transducer geometry modelling, see Section 7.2.7. Reflections from the hydrophone and the tank walls were not simulated and had a very low impact on the measurement data because of the use of pulsed rather than continuous sonication. Using sufficiently short pulses prevents returning (reflected) waves from interfering with the outgoing wave in the measurement volume, due to the different arrival times.

Water was assigned generic properties (speed-of-sound: 1500 m/s, attenuation: 0 Np/m) and the properties of Veroblack were set according to [14]. Some simulations also used 1482 m/s as the speed-of-sound in water in accordance with the IT'IS database (value at 20°C from [155]). For the acrylic acoustic lens material, properties were assigned within the range provided for acrylic resin and acrylic M1-7 in [282]. Acoustic properties of the different materials used in simulations are listed in Table 7.1. Transducer acoustic

lens properties are discussed in Section 7.2.7 and the employed values for the final models  $P_{1-2}$  can be found in Table 7.3. Further lens variations can be found in Figures 7.11 and 7.12. To simulate the inhomogeneity of the bone skulls, the approach from [146] was used, which assumes that the CT HU can be linearly mapped into bone density, which in turn maps to speed-of-sound according to the following linear relations:

$$\rho = \rho_{ref_1} + \frac{\rho_{ref_2} - \rho_{ref_1}}{HU_{ref_2} - HU_{ref_1}} HU$$

$$c = c_{ref_1} + \frac{c_{ref_2} - c_{ref_1}}{\rho_{ref_2} - \rho_{ref_1}} \rho$$

where  $ref_1$  and  $ref_2$  refer to the reference values used to anchor the linear mappings.  $ref_1$  was chosen as water, and  $ref_2$  was set to species specific average skull properties (density and speed-of-sound). For simplicity, attenuation in the skull was set to a constant value that was experimentally adjusted to match the maximum measured intensity when the skull was placed in the holder's first position. Typically, acoustic skull attenuation is experimentally inflated and adjusted to account for microscopic backscattering effects that cannot be effectively captured by even high resolution CT images [14, 146, 286]. As discussed in Section 7.4, attenuation primarily impacts the overall field scaling, but has little impact on focus shape and position. Skull mapping parameters are provided in Table 7.2. In order to determine them, a histogram of the skull CT HU data was extracted and clipped at the HU of water (0 HU). The very apparent subsequent peak towards higher HU was assumed to be the average HU in skull and assigned to the corresponding (species-specific) value, as found in the literature – [287] for pig, [280] for sheep.

HU-based property assignment was restricted to the skull region and linear interpolation was used to relate the finer voxel resolution (0.1 mm) to the coarser CT (0.335 mm). To efficiently handle inhomogeneity, voxels were assigned to 20 different bone classes based on HU binning. This permits precomputation and storage of update coefficient look-up tables for the GPU accelerated solver, thus increasing solver efficiency. An increase of the number of binning classes beyond 20 was found to not significantly affect the acoustic distributions anymore (< 1% change in peak intensity). Examples of a map of speed-of-sound in a cross section of pig skull and how the simulated beam appears are shown in Figure 7.1c and d, respectively. Acquiring the CT data of the skulls allowed also to replicate the exact position of the skulls in the simulation, and to correctly model their

thickness. The thickness of the skulls varied from 13 to 3.5 mm for the pig and from 6 to 8 mm for the sheep. The thickness of the sheep skulls along the ultrasound beam was 6 mm, while for the pig skull it varied because we shifted vertically the skull (see Figure 7.2). The impact of geometry segmentation, skull thickness, and inhomogeneous mappings using different CT scanner parameters (including the one in this work) is analyzed in [288].

Skull	$ref_1$ (Water)			$ref_2$ (Average Skull)			
	HU	$\rho$ kg/m <sup>3</sup>	$c$ m/s	HU	$\rho$ kg/m <sup>3</sup>	$c$ m/s	$\alpha$ Np/m
Pig	0	1000	1500	630	1260	1903	62.5
Sheep	0	1000	1500	1400	1710	2500	100
Human	0	1000	1500	<i>peak</i>	1908	2814	27

TABLE 7.2: Parameters used for skull property mappings, based on the approach from [146], but using species specific values from [287] [280] and [155]. *peak* corresponds to the peak HU value of the histogram of the segmented human skull.

### 7.2.7 Transducer modelling

Acoustic sources were modelled as time-harmonic sinusoidally varying Dirichlet pressure boundary conditions. The transducer casing was treated as a perfect reflector (zero pressure). Initially, an effective transducer model (termed  $S_{\text{eff}}$  in the following) was created using a spherical cap as pressure boundary, with an aperture diameter of 30 mm and an outer surface curvature radius of 50 mm, as provided in the manufacturer specification sheet. To confirm the given specifications of this model, ten simulations with varying curvature radii (25–70 mm) were performed, while the aperture diameter was held constant (30 mm). It was found that a curvature radius of 50 mm indeed optimally reproduces the measurements in water, both in term of peak location and Gamma metric (see Section 7.2.8), as shown in Figure 7.10.

As the curvature of the above effective model differed clearly from that of the real transducer surface, we explored the beam shape predicated by a model ( $S_{\text{geom}}$ ) consisting of a simplified spherical cap as pressure boundary,

but having the geometrical surface curvature (radius of 25 mm). As shown in Figure 7.3b and 7.4,  $S_{\text{geom}}$  expectedly failed to reproduce the intensity distribution in water, and was therefore excluded from further analyses.

A subsequent inquiry with the manufacturer revealed that the actual piezo element is in fact a flat piston and that an additional acrylic element with the measured surface shape is inserted on top of this disk (see Figure 7.3). Hence, a detailed transducer model was constructed that features a flat disk, which is assigned a time-harmonic sinusoidally varying pressure distribution, while the curved acrylic resin element on top (acoustic lens) is treated as a passive medium that shapes the wave-front (see Figure 7.1). The acoustic properties (density, speed-of-sound, and attenuation) of the acrylic layer were based on [282] and varied within the associated uncertainty range (see Figures 7.11 and 7.12) until simulation results matched the measured field in the obstacle-less water bath setup (using the Gamma metric introduced in Section 7.2.8 as criterion). The depth of the disk was set to a quarter of the wavelength in the lens as reported in [289] and also varied. Furthermore, a radial dependence  $p(r)$  of the pressure  $p_0$  on the disk was introduced (constant:  $p(r) = p_0$ , linear:  $p(r) = p_0(1 - r)$ , cosine:  $p(r) = p_0 \cos(\frac{\pi}{2}r)$ , and spherical:  $p(r) = p_0\sqrt{1 - r^2}$  for  $r \in [0, 1]$ ) to reflect the potential impact of the transducer walls on the vibrational mode ('aperture function') of the piezo source. That way, two candidate physical transducer models ( $P_{1-2}$ ; see Table 7.3) were generated. These fitted 'physical' models and the 'effective' model were then used to analyze how well they are able to predict transcranial ultrasound intensity distributions. The LAPWE solver typically employs 'hard' boundary conditions (i.e., the pressure at the source is imposed as a time varying Dirichlet boundary condition). This results in reflections of incoming (e.g., back-scattered) waves, which might not be completely accurate. Furthermore, a hard source impacts the pressure wave from the physical transducer models even in the absence of an obstacle, due to internal reflection in the transducer (e.g., by the transducer casing). Hence, a special version of the solver implementing the opposite extreme ('soft' sources, i.e., continuous addition of pressure at the source location) was used to study the resulting exposure change.

Table 7.3 summarizes the main transducer models employed in this paper.

### 7.2.8 Metrics

All simulated pressure distributions were normalized by the peak simulated pressure in the absence of a bone or printed skull obstacle. The following

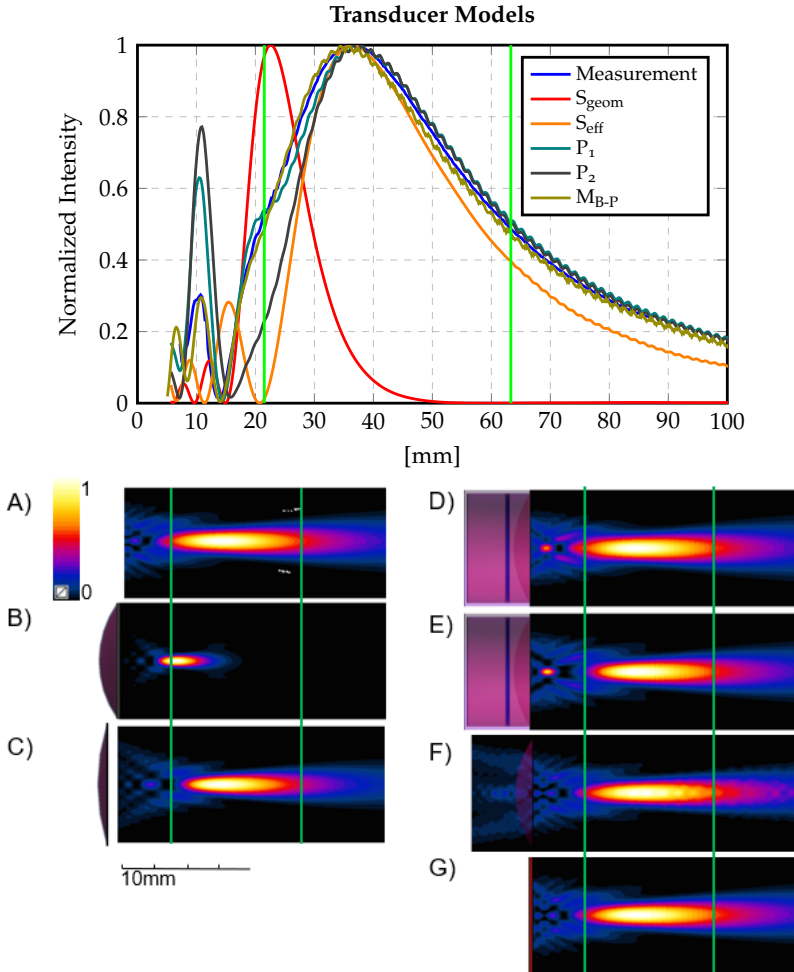


FIGURE 7.3: Transducer Models: (Top) Normalized acoustic intensity along the symmetry axis for different transducer models, compared to measurement data. The Full Width at Half Maximum extent of the measured focus is indicated by vertical green line. (A-G) Measured and simulated normalized intensity distributions. (A) Measurement, (B)  $S_{\text{geom}}$ , (C)  $S_{\text{eff}}$ , (D-E)  $P_{1-2}$  physical transducer models, (F) reconstruction using the plane-wave decomposition approach (from the first measurement plane), (G) simulation using the back-propagated pressure from the first measurement plane to the transducer aperture plane as pressure source.

Model	Description	Parameters
$S_{\text{geom}}$	Curved element with the actual transducer curvature (25 mm)	-
$S_{\text{eff}}$	Curved element with a curvature optimized to reproduce the focus location (50 mm)	-
$M_{\text{B-P}}$	Flat element, derived from holographic reconstruction	-
$P_1$	Transducer with an internal structure, flat element and cosine aperture function	$c = 2600 \text{ m/s}$ $\alpha = 50 \text{ Np/m}$
$P_2$	Transducer with an internal structure, flat element and spherical aperture function	$c = 2600 \text{ m/s}$ $\alpha = 14 \text{ Np/m}$

TABLE 7.3: Main transducer models employed in this paper. Parameters  $c$  and  $\alpha$  are the speed-of-sound and attenuation properties, respectively, of the acrylic acoustic lens.  $P_1$  and  $P_2$  are the best physical candidate models. For them, the density of the acrylic acoustic lens was set to  $\rho = 1180 \text{ kg/m}^3$  and the distance of the piezo element (in wavelengths of the lens material  $\lambda$ ) from the base of the lens surface was set to  $d = 0.25\lambda$

metrics were used for quantification and comparison purposes: (i)  $d_z$  and  $d$ : peak location as a measure of focus position (position along  $z$ -axis to quantify focal depth and  $(x, y, z)$ -position to quantify absolute focal shift); (ii)  $I_{\text{peak}}$ : peak intensity (normalized by the peak intensity in the absence of any obstacle); (iii)  $\text{FWHM}_z$ : extent of the focus full width at half maximum along the principal propagation axis (where available); (iv)  $\text{HWHM}_{z+}$ : half maximum past the location of the focus (or the length until the intensity has decayed by a factor of two, in case the obstacle prevents measuring the peak location); (v) Gamma: Gamma comparison value. These quantities were all obtained based on the field distribution past the obstacle. The metrics were selected (and adapted, as described above) depending on availability (particularly for configurations where obstacles are placed far from the transducer).

The Gamma comparison method was proposed by [290] to compare planned and administered radiological dose distributions. It permits to quantitatively compare fields that include both shape distortions and varia-

tions in amplitude, and its use in validation experiments has been advocated by [283]. Given spatial tolerances and an amplitude tolerance ( $\Delta d_{x,y,z}$  and  $\Delta D$ , respectively), the gamma index ( $\gamma$ ) compares every measurement point with all simulation points and finds the simulation point that minimizes an Euclidean distance norm combining distance and value ( $f(\vec{r})$ ) deviations (normalized by the corresponding tolerances):

$$\Gamma(\vec{r}_{\text{model}}, \vec{r}_{\text{meas},i}) = \sqrt{\frac{(f_{\text{model}}(\vec{r}_{\text{model}}) - f_{\text{meas}}(\vec{r}_{\text{meas},i}))^2}{\Delta D^2} + \sum_{j=x,y,z} \frac{(r_{j,\text{model}} - r_{j,\text{meas},i})^2}{\Delta d_j^2}}$$

The minimized Euclidean distance norm is subsequently assigned as the score of the corresponding measurement location:

$$\gamma(\vec{r}_{\text{meas},i}) = \min \{ \Gamma(\vec{r}_{\text{model}}, \vec{r}_{\text{meas},i}) \} \forall \vec{r}_{\text{model}}$$

A value of 0 corresponds to a perfect match for this point and a value of 1 reflects the limit of what lies within the total tolerance. The total tolerance is obtained as root-sum-square reflecting the simplified assumption of statistical independence. We report the gamma comparison value ‘Gamma’ as the percentage of measurement points that have been assigned a norm exceeding 1 (outside of the tolerance). Furthermore, the spatial distribution of  $\gamma(\vec{r}_{\text{meas}})$  provides an intuitive visualization of disagreement locations (see Figure 7.4 for an illustrative example of the Gamma comparison method).

$$\gamma(\vec{r}_{\text{meas},i}) > 1 : \text{disagreement exceeds combined tolerance}$$

The chosen agreement criteria were motivated by the intended application – i.e., the spatially precise targeting of a small cortical patch – and the physical beam properties. Given a focus size with a FWHM of 42 mm along the beam axis and 5 mm perpendicular to it (determined for pure water, see Figure 7.3), we set  $\Delta d_z = 5$  mm and  $\Delta d_{xy} = 2$  mm as upper thresholds for shifts of the focus position in these directions. Shifts exceeding these criteria would result in the undesired stimulation of a neighboring cortical patch, or in a peak position that is in cerebral spinal fluid (CSF) or white matter, rather than in gray matter. Based on the approximately sigmoidal dependence of tcFUS intensity on neural response as demonstrated in [291], a 15% difference in peak intensity maximally changes the stimulation success rate by 10%. For this reason,  $\Delta D = 15\%$  was set as the amplitude tolerance.

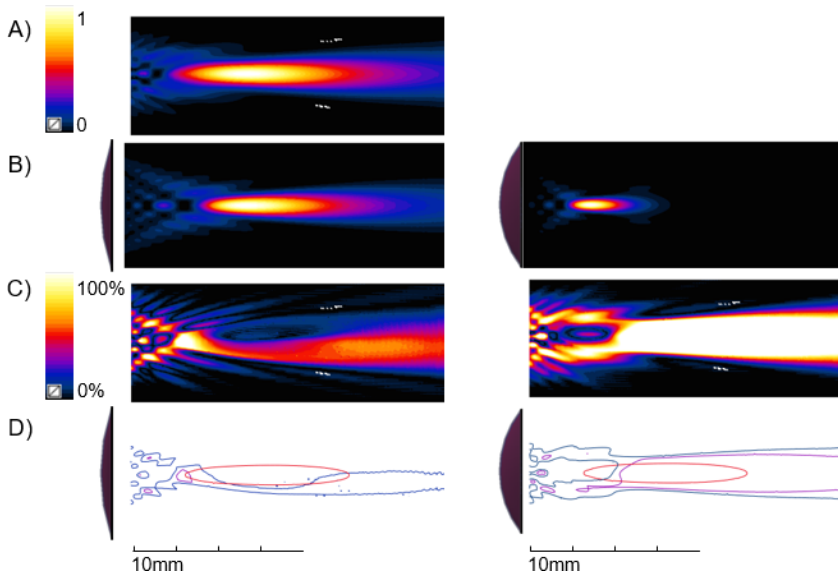


FIGURE 7.4: Illustrative example of a good (right) and a bad (left) Gamma comparison. (A) Measurement normalized to the peak intensity; (B)  $S_{\text{eff}}$ ,  $S_{\text{geom}}$ ; (C) Gamma comparison distribution ( $\gamma(r)$ ; tolerances: 5 mm longitudinal, 2 mm transverse, and 15% intensity); (D) FWHM of measurement profile in red, iso-curves of  $\gamma(r)$  at 100% in purple and at 50% in blue. Notice that the biggest differences for  $S_{\text{eff}}$  occur in the near field and in the region of the focus – the latter indicating that the measurement focus does not align perfectly with the symmetry axis. A  $\gamma$  value below 100% indicates deviation within the combined tolerance. The purple iso-curve demarks the regions that exceed the combined tolerance. For  $S_{\text{geom}}$ , almost the entire region of the measurement focus is outside the acceptable tolerance.



The same tolerance values were also used to normalize deviations in focus location and size. As we're measuring a euclidean distance for  $d$ , we used a single 5 mm deviation tolerance, independent of particular axial directions, for simplicity.

### 7.2.9 Backpropagation

To assess the choice of aperture functions (see Section 7.2.7), back-propagation from a plane parallel to the transducer aperture at an axial distance of 7.2 mm from the center of the transducer was performed (in the obstacle-free setup) and the resulting pressure distribution on the transducer surface was compared to those obtained in the different simulations. Back-propagation was performed using the plane-wave decomposition method (PWD, also known as angular spectrum method, [292, 293]) in free space – neglecting the attenuation in water –, which precluded propagation beyond the transducer surface into the heterogeneous transducer structure. Evanescent modi were not exponentially increased in the back-propagation to avoid inflating measurement errors and sampling-related errors. Apodization and zero-padding were used before the Fourier transformation step of the plane-wave decomposition to reduce ringing and folding artifacts. The backpropagated pressure field on the plane encompassing the transducer aperture was used as source ( $M_{B,P}$ ) in simulations with and without sheep skull obstacle.

### 7.2.10 Human head models

Simulations involving three different human head models ( $S_1$ ,  $S_2$ ,  $S_3$ ) from [294] were performed using the  $P_1$  and the  $S_{\text{eff}}$  transducer model (see Figure 7.8). These head models were created from multi-modal image data (different MRI sequences, as well as CT), permitting the consideration of skull heterogeneity. For a list of the 15 segmented tissues, see [294]. Tissue properties have been assigned according to [155], while the skull density and speed-of-sound were linearly mapped from the CT's HU according to Table 7.2. While no reference measurements exist to assess the validity of the simulated pressure distribution, these simulations can serve to illustrate the principal impact of transducer modelling on simulated transcranial sonication.

### 7.3 RESULTS

#### 7.3.1 Acoustic beam in a pure water background

Modelling the transducer as a pressure Dirichlet boundary condition on an ‘effective’ model that adapts the curvature radius in accordance with the effective radius provided by the manufacturer ( $S_{\text{eff}}$ ) results in a low Gamma error (0.2%; see Table 7.4). We confirmed that the chosen effective radius best reproduced the focus position in water and minimized the Gamma metric in water (see Figure 7.10). The physics-based transducer models further improve the agreement (Gamma = 0%), yet this is expected as they have been tuned to match water measurements. The impact of the various transducer parameters on the intensity distribution and along the symmetry axis is depicted in Figures 7.11 and 7.12.

Watertank Comparison [%]					
	Gamma	$d_z$	$d$	FWHM $_z$	HWHM $_{z+}$
$S_{\text{eff}}$	0.2	-26.5	28.7	-166.1	-90
$P_1$	0.0	-13.3	18	33.6	28.7
$P_2$	0.0	-16.3	19.8	-55.4	27.7
$M_{\text{B-P}}$	0.0	-16.3	22.4	-25.7	-0.01

TABLE 7.4: Differences between the measured and simulated intensities in a watertank setup without obstacle. The differences are expressed in percentages normalized to the tolerances from Section 7.2.8.

When a ‘soft’ source is used instead of Dirichlet boundary conditions, transducer-internal reflections by structures behind the piezo-element become relevant. Due to the lack of knowledge about the internal transducer structure, the region within the casing and behind the piezo was modelled as homogeneous material with varying absorption (50 and 150 Np/m), while the casing was treated as perfect reflector. In comparison to the Dirichlet pressure boundary condition, the secondary foci in the near field are less prominent and the focus length is shortened by 37% (see Figure 7.13).

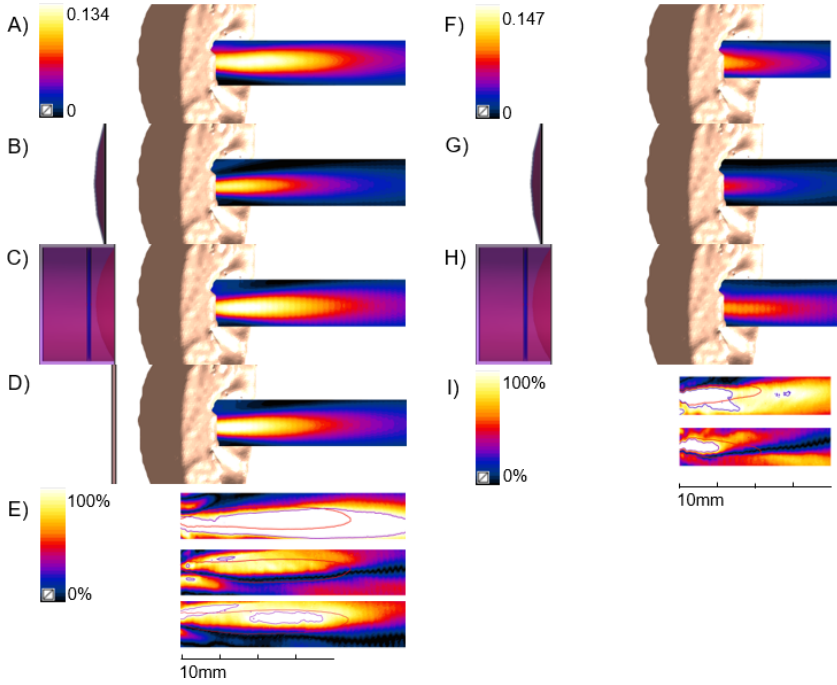


FIGURE 7.5: Sample measurement and simulation intensity distributions normalized to the peak intensity in water, and gamma comparison distribution past obstacles. (A-D) Illustrative ‘good’ simulation result (sheep skull, position 1) and (E-H) ‘bad’ simulation match (sheep skull, position 3) with measurement. (A,F) Measurement, (B,G)  $S_{\text{eff}}$ , (C,H)  $P_1$  physics-based transducer model, (D)  $M_{B-P}$  plane source, (E,I) Gamma comparison of normalized deviation between measurement and different transducer models (from top to bottom,  $S_{\text{eff}}$ ,  $P_1$ ,  $M_{B-P}$ , where available). The overlaid red contour denotes the Half Maximum isocontour of the measurement distribution; the purple contour indicates the region with a deviation that exceeds the combined tolerance.

### 7.3.2 *Transmission through the Veroblack plate*

Once the Veroblack plate obstacle is introduced, the ‘effective’ transducer model fails to reproduce focus location and size. The two physics-based transducer models, however, are capable of predicting the focus location, size, and overall pressure distribution reliably (0% disagreement of the Gamma metric vs. 15% and 19% of the points failing the Gamma comparison for the effective transducer model at two different positions; see Table 7.5).

### 7.3.3 *Transmission through the Veroblack 3D-printed skulls*

**FIG (THICK SKULL)** The 3D-printed pig skull is the thickest Veroblack obstacle (the thickness along the propagation axis can exceed 10 mm), resulting in standing wave patterns inside the obstacle. While one side is mostly flat (due to the cutting), the other is slanted such that small shifts in predicted focus position can result in clear changes of the standing waves in the obstacle and the related transmission efficacy (see Section 7.4). Depending on the skull position perpendicular to the propagation direction (positions 2A-C), the beam goes through the maximal thickness or partly passes outside the skull fragment border (2C). This results in two separate, prominent focal lobes and some weak secondary foci. In all the Veroblack printed pig skull cases, the peak intensity is within the (unmeasurable) region inside the skull or near its surface. Therefore, while the Gamma comparison is meaningful, reported peak intensity ( $I_{peak}$ ) and focus size comparisons ( $HWHM_{z+}$ ) are not. The ‘effective’ model is unable to predict focus intensity (the error is smaller than the tolerance only for position 3) and frequently fails to correctly predict focus extent. Consequently, it displays poor Gamma metrics. The physics-based transducer models produce good results, except for positions 2B and 3, where the intensity is off, despite very good agreement in the relative distribution pattern. The physics-based simulations are all well able to handle the challenging 2C case, where the focus is right at the border of the skull fragment (see Table 7.6).

**SHEEP** The 3D-printed sheep skull is thinner and curved and the agreement between simulations and hydrophone intensity measurements is better than for the 3D-printed pig skull. The physics-based models outperform the ‘effective’ model, based on the Gamma criterion, and, with the exception of

position 3 where the ‘effective’ model shows a  $> 30\%$  Gamma error rate, the Gamma criterion remains below 5% for all transducer models. However, the focus position error frequently exceeds the chosen 5 mm tolerance (see Table 7.7).

#### 7.3.4 *Transmission through the bone skull samples*

**PIG** The physics-based transducer models show near perfect Gamma metrics (always  $< 1\%$ ), whereas the percentage of data-points failing to agree with the hydrophone measurements (according to the Gamma criterion) can reach over 20% for the ‘effective’ transducer model. While the physics-based transducer model occasionally slightly exceeds the prescribed peak intensity tolerance of 15%, the ‘effective’ model nearly always fails and exceeds the tolerance threshold by up to 4.8 times (see Table 7.8).

**SHEEP** Simulation performance with the sheep skull obstacle is inferior to the accuracy achieved for the pig skull. However, the physics-based models again outperform the ‘effective’ model. The latter fails to pass the Gamma criterion for 7–40% of the measurement points, while the failure rate of the former is in the 4–20% range (see Figure 7.5). In most cases, the prediction of the peak intensity is insufficient (considering the defined 15% threshold), which seems to be related to the simulations predicting two distinct but overlapping intensity peaks, while the measurements show a single, merged peak of combined (higher) intensity (see Table 7.9).

**COMBINED RESULTS** Figures 7.6 show the averaged deviation between the measured and simulated distributions for the different transducer models. The physical transducer models clearly outperform the ‘effective’ model in terms of the Gamma metric and the accuracy of the focus location and size predictions. However, it is also apparent, that none of the models can always guarantee predictions within the desired tolerances. This is particularly true with regard to the peak intensity prediction and in cases where standing-wave effects occur (e.g., Veroblack pig skull). The performance of the two physical transducer models is comparable.

#### 7.3.5 *Other parameters*

**WATER SPEED-OF-SOUND** The speed-of-sound of water is temperature dependent. A slight difference in speed-of-sound in combination with a

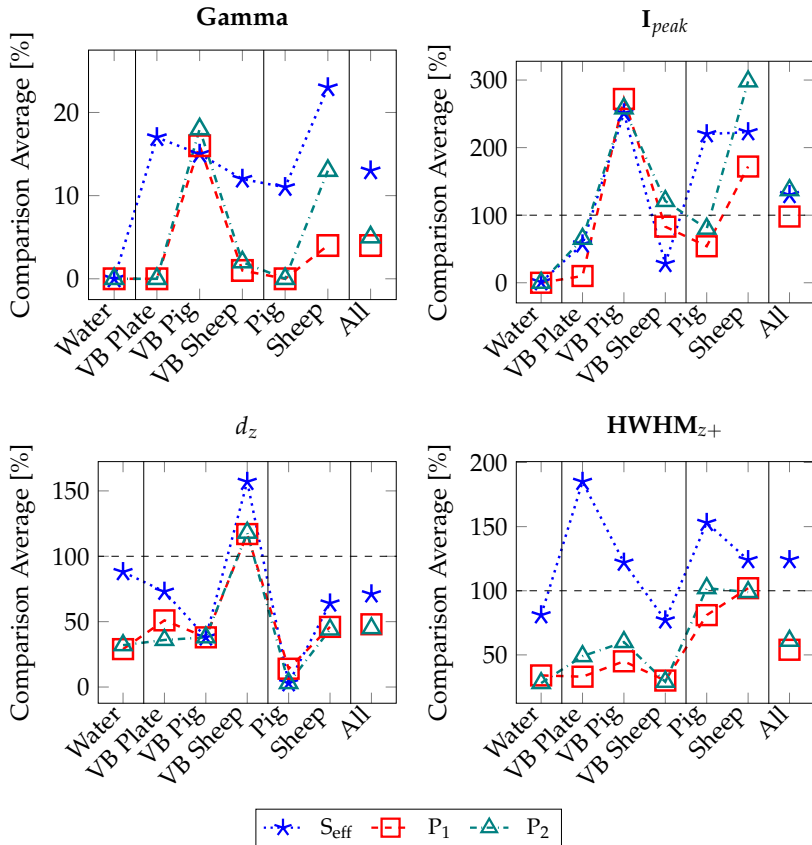


FIGURE 7.6: Averaged deviations for each obstacle at different positions between the measured and simulated distributions for the different transducer models:  $S_{eff}$  and  $P_{1-2}$ . Values normalized to the prescribed spatial (5 mm) and intensity tolerances (15%). Values above 100% fall outside the permitted tolerance. The data in the abscissa are in arbitrary order, so that the dotted lines do not indicate any trend, but are used for a better visual grouping of the results of the different transducers.

large distance (in terms of wavelengths) can result in a noticeable change of the interference pattern and pressure distribution. Changing  $c_{\text{water}}$  from 1500 to 1482 m/s has no visible impact on the pressure distribution in water. The impact is more pronounced after transmission through the sheep skull (see Table 7.9). Particularly the peak position shifts significantly. However, inspection of the pressure distribution as well as the Gamma metric reveal that this is due to small changes in the region of a flat peak and that the distribution difference remains small.

### 7.3.6 Backpropagation

The backpropagated pressure distribution on the transducer surface is depicted in Figure 7.7, which also shows the sonication intensity in water, as reconstructed from the first measurement plane using the angular spectrum method. The measured and reconstructed intensity distributions are in good agreement. When comparing the backpropagated radial dependence of the pressure with those obtained using the physical transducer models with varying aperture functions, it is found that the backpropagated one lies between the ‘cosine’ and the ‘spherical’ aperture function simulations. It does, however, also display a pronounced central maximum, similar to that observed with the ‘linear’ aperture function. The radial dependence of phase primarily reflects the varying path length from the piezo element to the transducer surface. All aperture functions result in similar phase patterns. In general, it can be seen that a pressure boundary condition with suitable aperture function is capable of reproducing the physical exposure, even though a velocity boundary condition might be more physically meaningful and can produce noticeable differences, particularly with regard to secondary maxima near the piezo-element.

The backpropagated pressure distribution on the plane encompassing the transducer aperture was used as source in simulations with and without sheep skull obstacle. Table 7.4 quantifies the obtained agreement with the measured intensity distribution. While the agreement in water is high, some differences are obtained in the presence of a skull (reflected in all of the metrics, see Table 7.9 and Figure 7.5). In particular, a large shift of the beam position occurs in that case. The disagreement metrics are larger than those observed for the physical transducer simulation models, but smaller than those obtained using  $S_{\text{eff}}$ . These differences could be due to limitations of the backpropagated source approach in handling multiple reflections or uncertainties in the measurements.

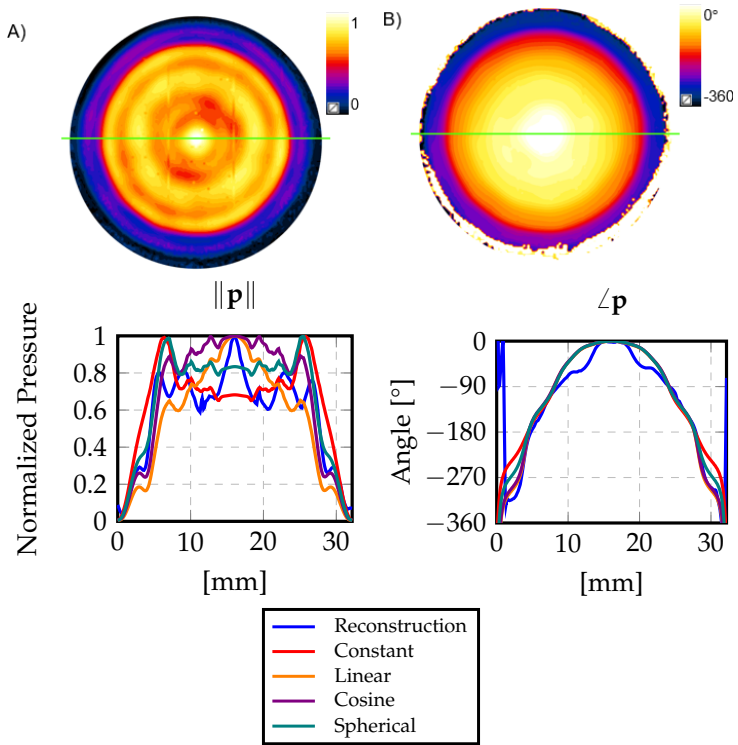


FIGURE 7.7: Top: (A) Absolute value and (B) angle of the reconstructed complex pressure at the curved surface of the transducer lens via backpropagation of measurements. Bottom: Line plots of different ‘aperture’ functions and the reconstruction, interpolated on an arc going through the center of the transducer’s curve (green line in top figures).



### 7.3.7 *Human head models*

The transcranial intensity distribution results obtained using the human head models can be seen in Figure 7.8. The different transducer models primarily affect the intensity scaling (skull transmission efficacy). The distribution is less affected.

### 7.3.8 *Impact of non-linearity and pressure wave approximation*

The WLE simulations of the sheep skull showed no non-linearity impact (differences  $< 1\%$  of the peak intensity) at the simulated exposure strength (tested by using WLE with and without non-linear term; in agreement with [285]). The negligible differences ( $> 1\%$  of the peak pressure) between the pressure fields obtained using the LAPWE solver and WLE solver without non-linear term can be readily explained by the differing stencil choices and time-integration schemes (higher order for the WLE solver).

## 7.4 DISCUSSION

**TRANSLATABILITY OF TRANSDUCER MODEL** While it is correct that the physical transducer model has been optimized to fit measurements, it is important to note that this optimization was only performed for the water measurements and the fitted model was subsequently used without further adaptation for all the different obstacle setups (bone and Veroblack obstacles).

**‘EFFECTIVE’ AND PHYSICAL TRANSDUCER MODEL** The results demonstrate that using the measured transducer surface geometry as pressure source fails to correctly predict the intensity distribution and results in strong deviations in focus location and shape. Applying the ‘effective’ model geometry provided by the manufacturer or artificially varying the curvature, as frequently done [14, 278–281], permits to mimic focus location, but results in important deviations in focus shape, both in terms of primary focus size and secondary foci in the near-field. Furthermore, the fact that this model is an unphysical model means that it is an ‘effective’ model only in the absence of obstacles. As the overall intensity distribution provided by the ‘effective’ model deviates substantially from that of the real transducer, the presence of the obstacle results in a completely different interference pattern that prevents reliable modelling even of focus location

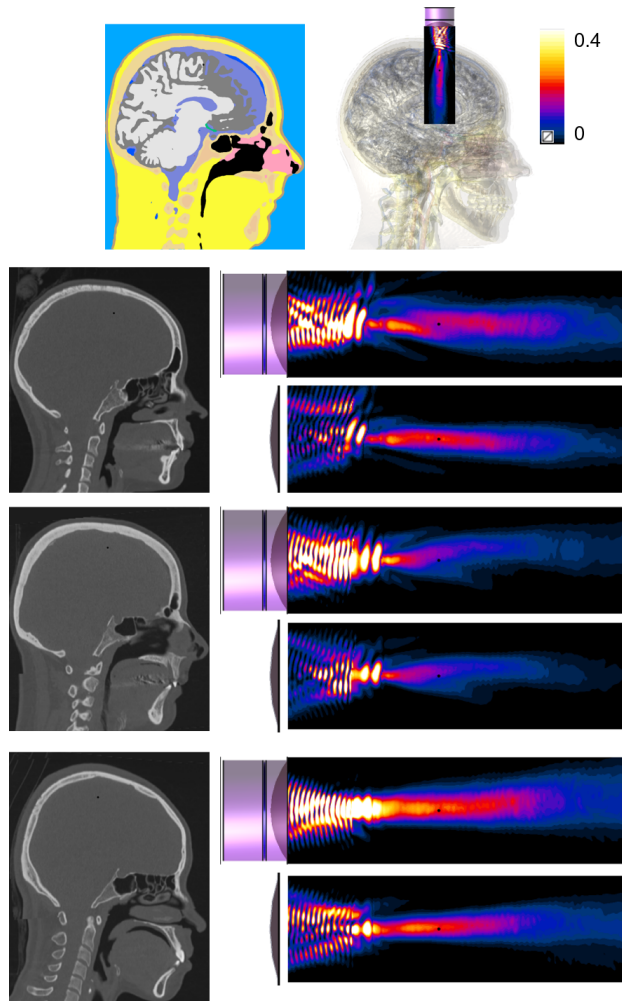


FIGURE 7.8: Transcranial intensity (normalized to water) of three different human head models with two different transducer models ( $P_1$  and  $S_{eff}$ ). Top: Sample CT tissue segmentation used to generate head models and simulation setup with superimposed intensity profile. Left: Head models with superimposed point for reference (target location at 50 mm distance from base of transducers). Right: Resulting normalized intensity beam for the shown transducer models. All colorbars are set to the same normalized intensities for ease of comparison.

(see Figure 7.4). In contrast, the simulations based on the physical transducer model were substantially more accurate (see Figure 7.6) for all tested cases after the model was calibrated to fit the measurements obtained for the pure water background. As such, similarly to the ‘effective’ model, our proposed approach for setting up the physical transducer model requires initial reference measurements, but subsequently results in more accurate predictions of the acoustic beam. However, we only varied the radius of curvature to find the best  $S_{\text{eff}}$  (see Section 7.2.7). A better agreement with the measurements might be obtained when using a more complicated effective model, optimizing for additional free parameters, such as the aperture diameter and the focal distance. Accurate transducer modelling is also expected to be a prerequisite for simulation-driven design of acoustic lenses placed on top of transducers, as in [295, 296].

**TRANSDUCER MODELLING IN WATER** Different parameters of the physical transducer model had specific, distinguishable impacts on the intensity distribution (see Figures 7.11 and 7.12). Changing the attenuation parameters (of the acoustic lens material or the obstacle) hardly affected the intensity distribution and only resulted in a change in magnitude scale. Both modification of the lens material speed-of-sound and of the piezo element depth have a similar effect, namely a noticeable impact on the intensity distribution. This is due to the fact that a change in speed-of-sound in the region where the wave is still mostly traveling paraxially corresponds to an effective change in the traveled distance. The curved surface primarily produces a radial distance dependent phase delay, which is slightly affected by the speed-of-sound. The mechanical construction of the transducer (e.g., transducer walls and housing) affect the vibrational modes. We have considered the impact of such an effect on the acoustic pressure wave by introducing an aperture function. A change in aperture function has a small impact on focus sharpness, but its main effect is to modify the location and occurrence of secondary foci.

We have modelled the piezo element as time-harmonic Dirichlet boundary condition (prescribed pressure). This is the natural and common choice when using FDTD. However, other methods exist where boundary conditions are commonly defined in terms of prescribed velocities. Constant velocity and constant pressure are not equivalent, as evident, e.g., when looking at the analytical solution for a vibrating circular disk obtained using Rayleigh-Sommerfeld integrals [17] where velocity is constant across the transducer surface, while pressure is not. However, this should be in-

investigated further as the different boundary conditions will give rise to different intensity distributions. Replacing the 'hard' with a 'soft' boundary condition modifies the exposure in a similar way as shifting the piezo-depth does (i.e., less pronounced secondary peaks in the near-field, sharper focus). This can be understood as a result of the modified internal interference pattern inside the transducer. In the absence of knowledge about the exact internal mechanical structure of the transducer, the associated modelling ambiguity cannot be avoided.

**SENSITIVITY AND TOLERANCES** In line with [283], our results indicate that small variations in acoustic material properties such as speed-of-sound, can have an important impact on the complex interference pattern of (curved) acoustic transducers. Therefore, it is important to reduce uncertainty by properly characterizing the acoustic properties of relevant materials in the sonication setup.

The choice of the tolerances ( $\Delta d_{x,y,z}$  and  $\Delta D$ ) for the Gamma metric – which is used in this study to judge simulation-measurement agreement – is driven by application specific criteria. That is, prediction errors above the tolerances would significantly compromise the accuracy and precision of the conclusions with regards to the targeted position in the brain and the intensity at the target. This approach is unlike that followed in [283] where agreement tolerances were based on a thorough uncertainty analysis. The Gamma tolerances obtained in [283] at similar frequencies (550 kHz rather than 500 kHz) through uncertainty analysis of sonication in the absence of an obstacle (1.3 times the wavelength in water, i.e., 4 mm; 14 % of the peak intensity) are comparable to the ones used in this study (5 mm, 15 %). However, a similar uncertainty assessment in the presence of skull obstacles would have resulted in much larger tolerances. Therefore, the approach chosen for this paper results in much stricter criteria that are hard to meet but reflect application needs.

**STANDING WAVES IN THE OBSTACLE** The large difference in acoustic impedance between Veroblack and water (see Table 7.1) results in strong reflections at the interfaces (32 % of the pressure amplitude for a plane wave with normal incidence). This leads to a standing wave effect within the obstacle [297], which results in resonator behavior (similar to that known from Fabry-Pérot resonators in laser-physics [298]) and is known to be associated with fluctuations in transmitted power as a function of the effective cavity length (see Figure 7.9). When the planar Veroblack slab

is placed at the focus location, varying the frequency (or equivalently the wavelength or obstacle thickness) results in up to 20% changes in pressure transmission (> 40% change in intensity, see Figure 7.9). This standing-wave effect helps explain the focus intensity differences observed with Veroblack obstacles (see Section 7.3.3). Further research should be performed to assess the relevance of such findings for transcranial sonication. It is expected that skull heterogeneity and losses related to absorption or scattering reduce the occurrence of standing waves. On the other hand, the higher density and speed-of-sound of cortical bone compared to Veroblack – and the related increase in acoustic impedance mismatch – leads to a more than fourfold variability of the transmitted intensity for relatively moderate changes in speed-of-sound assignment and skull thickness modelling (computed analytically for a homogeneous cortical bone plate of realistic thickness immersed in water; see Figure 7.9). This results in a high sensitivity to modelling errors. This phenomenon has been discussed by [299], where an approach to optimize transcranial focal-gain by suitably tuning the sonication frequency is proposed.

**STANDING WAVES BEFORE THE OBSTACLE** Similarly, standing waves occur between the transducer and the obstacle. Changing the transducer models affects this standing-wave configuration – as evident when comparing the ‘effective’ with the physical transducer model (see Figure 7.8) –, which in turn affects the skull exposure. This is likely to be an important factor in explaining the observed changes in the pressure distribution.

**LIMITATIONS AND FURTHER WORK** A ‘first principles’ approach would consist in performing proper mechanical modelling (i.e., full dynamic stress-strain simulation) of the transducer, from which the vibrational mode would emerge and might allow for accurate predictions of the acoustic beam without the need for reference measurements. However, this is beyond the scope of this paper.

The simulated sonication intensities for the bone skull samples agreed satisfactorily with the measurements only after resorting to species-specific skull attenuation maps (see Table 7.2). This might reflect different bone compositions between species, which can result in different properties for similar HU values. A more detailed evaluation of CT image-based modelling of skull properties is the subject of a companion paper [288].

A recent work [300] proposed an alternative way of constructing an ultrasound source model, based on holographic projections. Briefly, this method

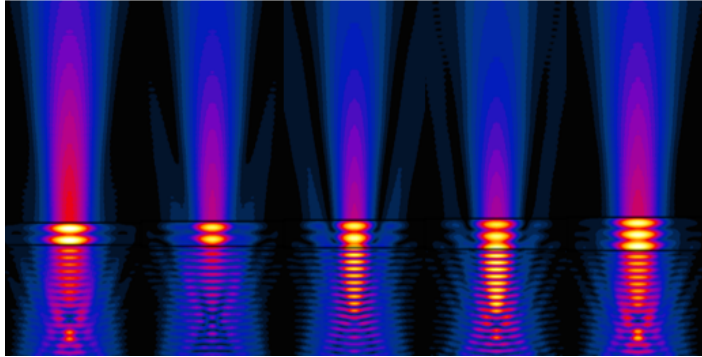
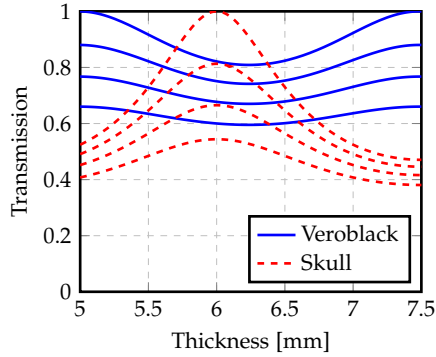


FIGURE 7.9: Impact of the standing wave effect on transmission. (Top) Analytically computed plane wave (pressure) transmission factor past a flat, homogeneous obstacle (blue: Veroblack, red: cortical bone  $c$  and  $\rho$ ; see Table 7.1), as a function of obstacle thickness and for different attenuation factors (0, 10, 20, or 30% attenuation when propagating through the plate). (Bottom) Pressure distribution obtained for a physical transducer model past a Veroblack obstacle of varying thickness (5–7.3 mm, corresponding to 1–1.5 wavelengths in the obstacle, 0.5 mm steps). The color-bar remains identical. Notice that the top figure is computed for plane-wave exposure, while the bottom figure shows results for a focused sonication.

allows the derivation of an equivalent source model from pressure measurements in a plane parallel to the transducer face by iterative optimization of the pressure distribution on the surface of the equivalent source. Similar to the source reconstructed by back-propagation here, the equivalent source can then be employed in a full-wave model to estimate the ultrasound beam through complex and heterogeneous media. In general, both our and their [300] work highlight the need for source models that are more accurate than ‘effective’ models. In contrast to our physical transducer models, the method in [300] has the advantage of not requiring information about the internal structure of the transducer (nor the construction of a corresponding acousto-mechanical model), but depends on measurement data (phases and amplitudes) at very high resolution, accuracy and precision instead, as measurement errors might be amplified in the equivalent source model reconstruction process. Our approach constrains the fitting of the equivalent model to a few key parameters, so that measurement errors are more likely to be identifiable as mismatches between modelled and measured beams.

## 7.5 CONCLUSIONS

Careful transducer modelling and experimental validation is crucial for the reliable simulation of tcFUS fields. The currently commonly employed approaches – i.e., assigning a boundary condition to the real shape of the transducer surface, or using an ‘effective’ transducer shape model that has been constructed to produce a focus at the right location in a homogeneous water setup – are inadequate for flat piston transducers with a curved acoustic lens and, possibly, for other geometrically complex transducer models. This is particularly true in the presence of acoustic obstacles and inhomogeneity. This suggests that effective transducer models should be validated also in the presence of complex and inhomogeneous obstacles in order to ensure that they perform well also in realistic usage scenarios. Even physics-based transducer modelling can sometimes fail to reach the chosen, clinically motivated, agreement criteria (15 % peak intensity, 5 mm for focus position and length). An optimal, but highly demanding and typically impracticable approach would include complete mechanical modelling of the transducer with its housing and fixation. However, a compromise combining improved acoustic modelling of the transducer and its internal structure with an aperture function to account for the missing mechanical modes can be an acceptable solution, but requires the acquisition of reference data using hydrophone measurements. An alternative approach would be to

adapt the transducer model or the transducer placement heuristically, using image-based information, to compensate for, e.g., the skull lens effect [301]. Image-based information, such as MRI data, is readily available and can also be used to optimize the sonication path.

If possible, experimental effort should be invested in characterizing sensitive material properties of the transducer components and obstacle media (particularly speed-of-sound and species-specific attenuation). Comprehensive uncertainty assessment should typically be performed along with computational modelling. Standing wave effects have been found to have a high impact on the sensitivity and accuracy of transmitted intensity predictions for the 3D-printed and other homogeneous obstacles (up to fourfold variation of peak transcranial intensity for relatively small speed-of-sound assignment errors in cortical skull). Additional studies should be performed to investigate how much skull heterogeneity affects the formation of standing-waves. Approaches involving, e.g., stochastic modulation, to suppress standing waves have been proposed [302–304].



## 7.A APPENDIX

## 7.A.1 Results tables and figures

Veroblack Plate Comparison [%]						
		Gamma	$I_{peak}$	$d_z$	$d$	$HWHM_{z+}$
<b>VB Plate (2 cm dist.)</b>	$S_{eff}$	18.9	-77.1	-134.9	134.9	-180.6
	$P_1$	0.0	5.4	-71.9	71.9	-55.1
	$P_2$	0.0	-39.6	-41.9	41.9	-51.6
<b>VB Plate (3 cm dist.)</b>	$S_{eff}$	14.9	-37.4	-11.5	18.9	-190.3
	$P_1$	0.0	-15.4	-29.6	33.9	-10.8
	$P_2$	0.0	-89.8	-29.6	33.9	46.2

TABLE 7.5: Comparison of the difference metrics of simulated and measured intensity distributions with the Veroblack plate obstacles at varying positions (the tolerance-normalized deviation in %).

<b>Veroblack Printed Skulls Comparison [%]</b>				
		<b>Gamma</b>	<b><math>I_{peak}</math></b>	<b><math>WHM_{z+}</math></b>
<b>VB Pig 1</b>	$S_{eff}$	25.4	-284.4	-65.1
	$P_1$	0.0	100.5	-57.0
	$P_2$	0.0	71.1	-41.0
<b>VB Pig 2A</b>	$S_{eff}$	47.7	-530.0	-161.5
	$P_1$	0.0	-74.7	26.5
	$P_2$	0.0	-67.5	26.5
<b>VB Pig 2B</b>	$S_{eff}$	0.0	118.7	-127.2
	$P_1$	44.0	-616.4	-72.3
	$P_2$	48.4	-616.4	-72.3
<b>VB Pig 2C</b>	$S_{eff}$	0.1	287.6	-155.8
	$P_1$	8.0	-113.1	-35.9
	$P_2$	5.6	12.2	-120.9
<b>VB Pig 3</b>	$S_{eff}$	0.0	-32.3	-102.5
	$P_1$	27.6	-454.9	-35.2
	$P_2$	35.5	-524.4	-40.2

TABLE 7.6: Comparison of the difference metrics of simulated and measured intensity distributions with the pig-skull-shaped Veroblack obstacle at varying positions (the tolerance-normalized deviation in %).

Veroblack Printed Skulls Comparison [%]						
		Gamma	$I_{peak}$	$d_z$	$d$	$WHM_{z+}$
<b>VB Sheep 1</b>	$S_{eff}$	3.9	-17.4	-99.7	101.1	-80.6
	$P_1$	0.0	-42.0	-92.2	93.4	27.3
	$P_2$	4.1	-151.2	-94.7	95.6	0.6
<b>VB Sheep 2A</b>	$S_{eff}$	1.7	30.2	-125.0	126.7	-70.5
	$P_1$	1.8	120.3	-122.2	124.2	-11.3
	$P_2$	0.4	132.5	-122.2	124.2	-38.7
<b>VB Sheep 3</b>	$S_{eff}$	31.0	-35.5	-247.1	247.2	-80.0
	$P_1$	2.0	85.2	-136.1	137.3	50.7
	$P_2$	0.7	80.1	-136.1	137.6	48.3

TABLE 7.7: Comparison of the difference metrics of simulated and measured intensity distributions with the sheep-skull-shaped Veroblack obstacle at varying positions (the tolerance-normalized deviation in %).

Skulls Comparison [%]						
		Gamma	$I_{peak}$	$d_z$	$d$	HWHM $_{z+}$
<b>Pig 1</b>	$S_{eff}$	16.4	-134.7	3.4	30.3	-174.9
	$P_1$	0.0	-11.7	10.6	33.7	-53.0
	$P_2$	0.1	-55.6	2.2	31.9	-73.3
<b>Pig 2A</b>	$S_{eff}$	6.3	-238.6	-	-	-46.5
	$P_1$	0.0	-50.5	-	-	67.2
	$P_2$	0.1	-129.5	-	-	62.3
<b>Pig 2B</b>	$S_{eff}$	21.8	-53.6	-	-	-187.1
	$P_1$	0.0	19.1	-	-	-30.0
	$P_2$	0.4	-19.6	-	-	-54.9
<b>Pig 2C</b>	$S_{eff}$	6.8	-	-	-	212.1
	$P_1$	0.3	-	-	-	44.9
	$P_2$	0.4	-	-	-	82.3
<b>Pig 3</b>	$S_{eff}$	4.2	-193.4	-	-	142.1
	$P_1$	0.2	-36.1	-	-	209.4
	$P_2$	0.7	-108.6	-	-	236.9

TABLE 7.8: Comparison of the difference metrics of simulated and measured intensity distributions with the real pig skull obstacle at varying positions (the tolerance-normalized deviation in %).  $d_z$ ,  $d$  and  $I_{peak}$  comparisons omitted for simulation results where maxima occurs at first measurement position.

Skulls Comparison [%]						
		Gamma	$I_{peak}$	$d_z$	$d$	$WHM_{z+}$
<b>Sheep 1</b>	$S_{eff}$	38.7	-105.2	-91.0	101.6	-123.2
	$P_1$	4.2	25.2	-27.5	48.7	3.9
	$P_2$	11.4	75.9	-28.7	50.4	-60.7
	$M_{B-P}$	15.9	49.6	-81.4	90.4	-87.2
	$P_{1-W1492}$	6.4	35.7	-190	192	110.5
<b>Sheep 2A</b>	$S_{eff}$	7.9	-115.8	98.6	101	-241.1
	$P_1$	3.8	-192.4	106.5	110.5	-16.2
	$P_2$	7.6	-256.1	102.8	105.2	-33.5
<b>Sheep 3</b>	$S_{eff}$	21.6	-447.1	1.7	32	-36.9
	$P_1$	4.8	-297.2	5.4	31	286.3
	$P_2$	19.4	-5.6	1.7	31	231.4

TABLE 7.9: Comparison of the difference metrics of simulated and measured intensity distributions with the real sheep skull obstacle at varying positions (the tolerance-normalized deviation in %).  $P_{1-W1492}$  indicates the simulation where the acoustic property of water at 20°C were employed.

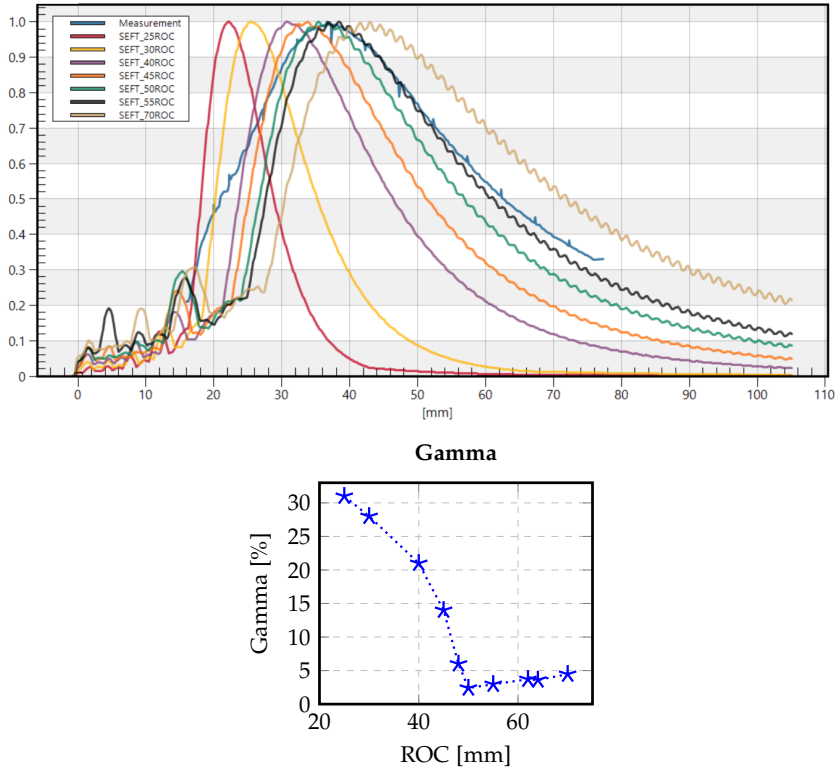


FIGURE 7.10: (Top) The intensity profiles of the measurement and the simplified SEFT transducer models with different radii of curvature (ROC) normalized by the maximum. The x-axis indicates the distance from the base of the transducer in the longitudinal direction. (Bottom) The Gamma metric comparing the disagreement of the measurement and the transducer models with different ROC is shown. Notice that the model with 50 ROC is the best match. We employed the latter throughout the paper and called it  $S_{\text{eff}}$ .

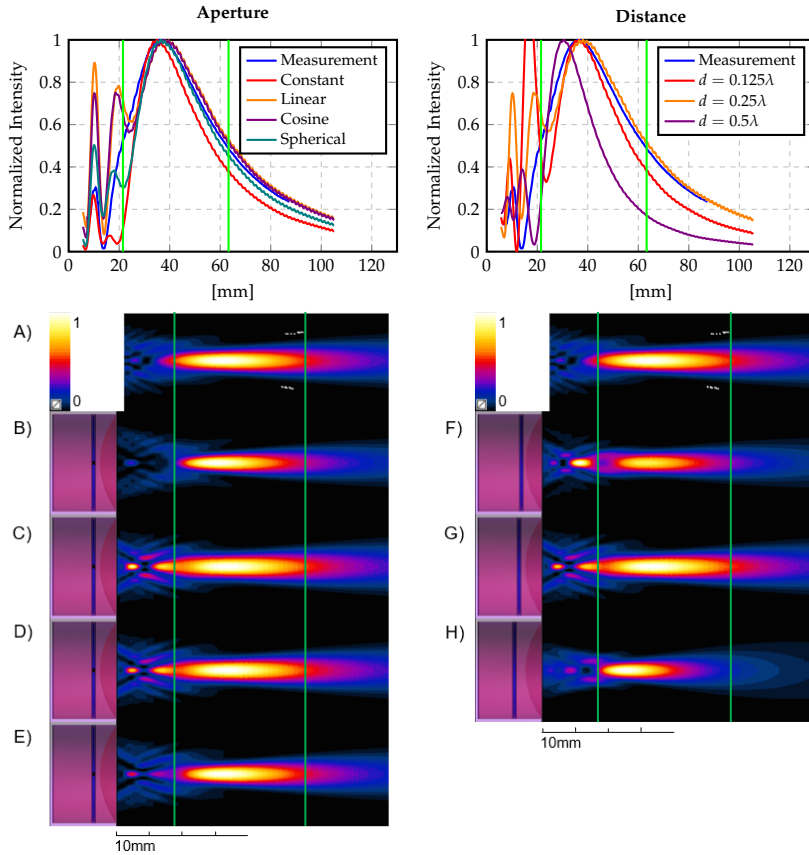


FIGURE 7.11: Variation of the normalized intensity distribution of a physical transducer model resulting from changes: (B-E) to the aperture function (radial pressure variation of the piezo element boundary condition; constant, linear, cosine, and spherical, respectively), and (F-H) to the acoustic lens layer thickness (0.125, 0.25, and 0.5 wavelengths). (A) The measurement reference. (Top) Plot along the symmetry axis.

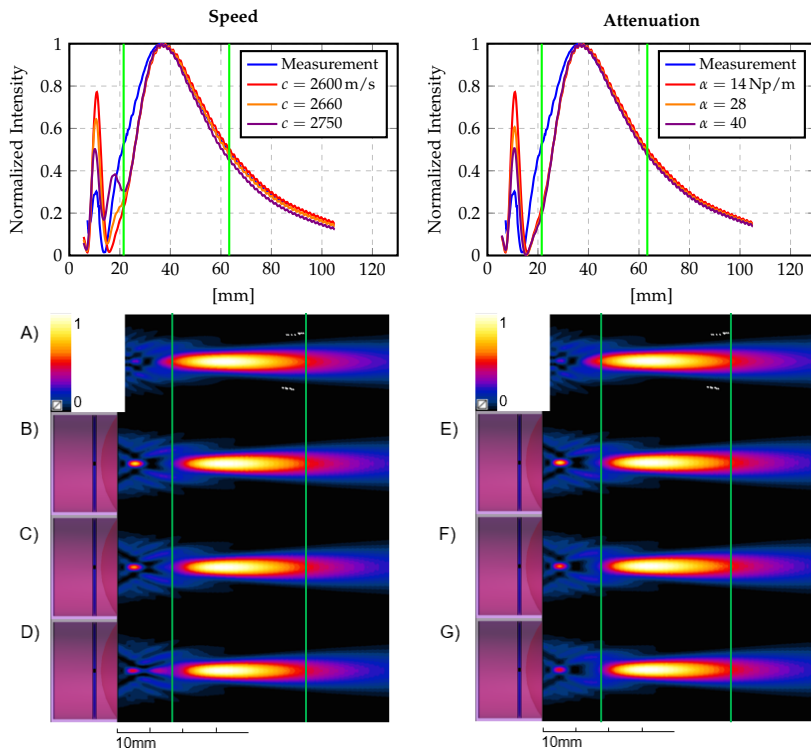


FIGURE 7.12: Variation of the normalized intensity distribution of a physical transducer model resulting from changes: (B-D) to the speed-of-sound of the acrylic acoustic lens (2600, 2660, and 2750 m/s), and (E-G) to the acrylic acoustic lens attenuation (14, 28, and 40 Np/m). (A) The measurement reference. (Top) Plot along the symmetry axis.



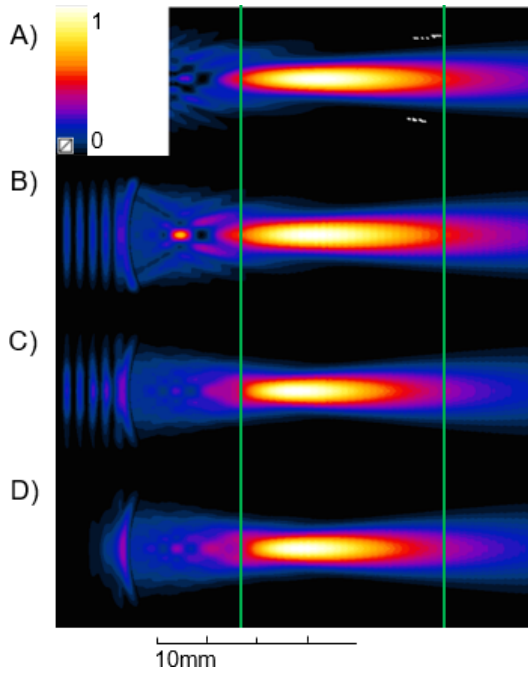


FIGURE 7.13: Comparison between piezo-element boundary conditions in simulations of the beam profile in a pure water background. (A) Reference measurement. Normalized intensity distribution with piezo (B) 'hard' source and (C-D) 'soft' source. The casing is treated as a perfect reflector. The backing layer is modelled with the same density and speed-of-sound as the acoustic lens and is assigned varying absorption values (B-C: 50 Np/m and A: 150 Np/m). The green line is provided as reference to indicate the extent of the FWHM in the measurement.



## THE IMPACT OF CT IMAGE PARAMETERS AND SKULL HETEROGENEITY MODELLING ON THE ACCURACY OF TRANSCRANIAL FOCUSED ULTRASOUND SIMULATIONS

---

### ABSTRACT

**Objective:** Low-intensity transcranial ultrasound stimulation (tcFUS) is a promising non-invasive brain stimulation (NIBS) technique. tcFUS can reach deeper areas and target smaller tissue regions in the brain than other NIBS techniques, but its application in humans is hampered by the lack of a straightforward and reliable procedure to predict the induced ultrasound exposure. Here, we examined how the modelling of the skull affects computer simulations of tcFUS.

**Approach:** We characterized the ultrasonic beam after transmission through a sheep skull with a hydrophone. We then performed computed tomography (CT) image-based simulations of the experimental setup. To study the impact on the skull model, we varied: CT acquisition parameters (tube voltage, dose, filter sharpness), image interpolation, skull segmentation parameters, and mapping of the acoustic properties (speed-of-sound, density, and attenuation). We also studied how slight skull position mismatches affect the predictions. Peak intensity, peak position, total power, and the Gamma metric, as a measure for distribution differences, are used as quantitative criteria.

**Main results:** Skull attenuation assignment and transducer positioning had the most important impact on peak intensity, followed by imaging parameters such as filter sharpness and tube voltage, which require proper calibration of the mapping functions. Positioning also strongly affected the intensity distribution (including focus-shape and location), as does the structure of skull heterogeneity, which must be obtained from patient image-data, rather than simulated as stochastic variability.

**Significance:** Our study reveals the importance of properly modelling the heterogeneity of the skull and its structure, of accurately reproducing the transducer position. Our results also raise red flags in terms of translating modelling approaches among clinical sites without proper standardization

and calibration of the imaging procedures or re-calibration of modelling parameters.

## 8.1 INTRODUCTION

Low intensity transcranial focused ultrasound stimulation (tcFUS) has good spatial resolution and can also target deeper brain areas compared to established transcranial stimulation methods, offering a complementary application profile [123]. Its neuromodulatory effects have been repeatedly demonstrated in animals [11, 109, 130, 269, 270] and humans [12, 269, 271, 272], but its cornerstones still need to be better established in order to move tcFUS from basic research towards clinical applications. In particular, an accurate and precise control of the spatial distribution and intensity of the tcFUS beam is needed to ensure that neurally effective and safe stimulation doses are delivered in the brain.

While standardized procedures have been established to measure the profile of an ultrasound beam in water (for example IEC 62127-1 or [305]), the characterization of the beam profile in the brain after propagation through the dense, heterogeneous skull structure is a difficult problem for *in vivo* applications in humans. The mismatch in acoustic impedance between the skull and the surrounding soft tissue and water strongly affects the tcFUS beam. In addition, the skull itself is composed of two outer layers of cortical bone with a layer of inhomogeneous cancellous bone inside, each having different density and thickness [306].

So far, computer simulations based on computed tomography (CT) images are considered the best choice for dose estimations for human tcFUS [146, 147, 273–276, 307]. CT images offer a strong contrast between bone and other tissues, allowing for an accurate segmentation of the skull surfaces, and can further be used to estimate the bone density. Using the assumption that tissue density systematically relates to acoustic properties, several works [146, 147, 276] established mappings between the CT Hounsfield units (HU) and the acoustic properties of bone. This approach is promising, but still requires further development and validation, as the mapping of HU to density without further calibration typically only applies for soft tissue and not bone [308]. Small variations of the geometry and acoustic skull properties (speed-of-sound, attenuation) can significantly affect the dose shape, location and peak intensity [14], suggesting the need for individualized dosing approaches.

To account for differences in scanner types and settings, CT attenuation grayscale values are typically mapped to the dimensionless linear scale of HU using air ( $-1000$  HU) and water ( $0$  HU) as reference points. The calibrated HU can then be mapped to the density of soft tissue, since most organs behave like water with regards to radiation physics [308]. This, however, does not hold strictly true for bone (between  $300$  and  $3000$  HU), as it further depends on the X-ray spectrum and beam hardening correction, which requires additional calibration [309]. Even after calibration, there is no linear map that correctly fixes the HU and density relation for air, water, and skull. Furthermore, clinical CT images lack the spatial resolution to fully resolve the microstructure of the highly heterogeneous cancellous bone layer.

Practically, this presents a challenge as the HU derived acoustic properties of bone now depend on scanner type and settings (see Figure 8.1a for the impact of tube voltage on HU distribution in the sheep skull). The HU values outside the calibrated linear range of air and water depend on acquisition parameters such as the chosen tube potential, the current-time product, and the reconstruction filter (see Figure 8.2). In practice, CT parameters are set to minimize the radiation dose at the expense of image resolution and signal-to-noise ratio (SNR) for the application at hand. It is so far unclear how sensitive the simulated tcFUS beam profile reacts to variations of the dose and smoothness of clinical CT images, and how this affects the match between the simulated and real beam profile of tcFUS after transcranial transmission.

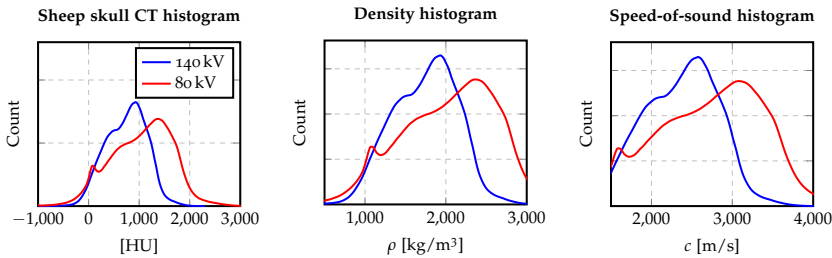


FIGURE 8.1: Histograms of HU values, skull density, and speed-of-sound (mapped linearly using air and water as anchor points) at two different CT tube voltages: 140 (blue line) and 80 (red line) kV. Clearly, the tube voltage affects the image-based property maps when no specific calibration is applied.

Compounding the issue are variations found between different mappings from bone density to acoustic properties (see Figure 8.3). The linear mapping from density to speed-of-sound from [146] has two free parameters that can be adjusted to compensate for the variations in the CT, while the non-linear mapping from [147] is fixed and derived for a particular CT configuration and stimulation frequency. The proper way to map image-derived density to skull acoustic attenuation map is still an open problem and its parameters are normally artificially tuned to match the experimental beam profile [14, 146, 286].

In this study, we investigated the impact of CT image parameters (energy levels, filter sharpness, and noise levels), of the skull shape reconstruction approach, of the different mappings from HU to acoustic properties, and of transducer positioning uncertainties on the simulated acoustic exposure from a single element focused transducer (SEFT) operated at 500 kHz.

Using a state-of-the-art clinical CT, we acquired images of a sheep skull sample. The nominal image resolution was chosen as high as possible to allow for an accurate reconstruction of the object boundaries and the internal heterogeneous structure. The dose was varied to correspond to that of a standard clinical head scan (1–2 mSv), a low-dose scan previously used for research purposes (0.3 mSv) [294] and a high-dose one as comparison baseline. Image reconstruction was repeated with different filters that resulted in varying trade-offs between image smoothness and noise levels. While the majority of the images were acquired at a tube voltage of 140 kV, we also considered one image acquired with a tube voltage of 80 kV. The image HU were mapped to acoustic properties employing different transformations, such as the ones proposed by [146] and [147] (see Figure 8.3), and used to simulate acoustic transmission through a sheep skull, as further described in [307]. Systematic comparisons of the simulations with hydrophone measurements of the beam profiles allowed assessing the impact of the parameter choices on the accuracy of the simulations. The analysis distinguished between effects of the parameter variations on the focus shape and the absolute magnitude, respectively, of the transcranial intensity distribution. As the absolute pressure magnitude strongly depends on the attenuation in the skull that is often experimentally tuned for the particular model, skull attenuation was treated separately.

The goal of this study is to provide guidance on the application of image-based skull modelling (imaging and image processing parameters, skull reconstruction, property mapping), to point out remaining limitations, and

to give insight into the sensitive parameters dominating the modelling uncertainty.

## 8.2 METHODS

### 8.2.1 *Bone sample*

In this study, we tested the same sample of sheep skull used in [307]. Soft tissue from the skull was mechanically removed with tweezers, and the sample was cut to maintain the upper section of the skull. The bone sample was then glued to a holder (see Figure 8.4) and subsequently continuously kept under phosphate-buffered saline (PBS) solution.

### 8.2.2 *Measurements*

A detailed description of how the ultrasound beam was characterized with hydrophone measurements of acoustic intensity in a water tank, with and without the skull, and how we analyzed the data can be found in [307]. Briefly, we employed two function generators (33220A, Agilent Technologies, California, United States) to generate a burst (20 pulses / burst) of sinusoidal waves with a center frequency of 500 kHz, at a pulse repetition frequency of 1 kHz. The pulse was subsequently amplified by a power amplifier (5312, OPHIR, California, USA) and sent to a single element spherical ultrasound transducer (IPBD2, Hagisonic, South Korea, as in [307]). Two custom-designed 3D-printed holders were used to fix the transducer and the skull inside a tank. To sample the pressure wave, we employed a calibrated needle hydrophone (NH1000, Precision Acoustic, Dorset, UK). The hydrophone was moved by a stepper-motor system (Sciencetown Co., Incheon, South Korea) with a plane sampling distance of 0.25 mm, and controlled by custom written software in *MATLAB*. The signal from the hydrophone was transmitted and visualized with an oscilloscope (DSOX2022A, Agilent Technologies, California, United States).

The data analyzed in this paper was acquired with the sheep skull at a distance of 18.2 mm between the transducer and the surface of the skull facing the hydrophone (corresponding to ‘position 1’ in our companion paper [307]).

### 8.2.3 Simulation framework

Acoustic propagation was simulated with the same methodology as in [307] within the *Sim4Life* (ZMT Zurich MedTech AG, Zurich, Switzerland) platform employing the linear acoustic pressure wave solver (LAPWE) from [17]. The LAPWE solver solves the wave equation:

$$\rho \nabla \frac{1}{\rho} \nabla p - \frac{1}{c^2} \frac{\partial^2 p}{\partial t^2} - \frac{\tilde{a}}{c^2} \frac{\partial p}{\partial t} = 0 \quad (8.1)$$

where  $\rho$  is density in  $\text{kg/m}^3$ ,  $c$  is speed-of-sound in  $\text{m/s}$ ,  $p$  is pressure in Pa,  $t$  is time in s,  $\omega$  is angular frequency in  $\text{rad/s}$ , and  $\tilde{a}$  is:

$$\tilde{a} = 2\alpha \sqrt{\frac{\alpha^2 c^4}{\omega^2} + c^2}$$

where  $\alpha$  is attenuation in  $\text{Np/m}$ . The acoustic properties assigned to the materials are listed in Table 8.1.

Voxel size in every material remained below a tenth of its wavelength with the coarsest grid step at 0.3 mm outside the skull region and 0.1 mm in the skull region, resulting in a simulation mesh with about 500 million voxels.

Simulations of the experimental setup were performed for a pure water background, as well as with the skull obstacle in a water background (see Figure 8.4b).

We carefully modelled the transducer in order to account for its internal structure and vibrational modes and to ensure accurate estimations of the beam transmission through complex obstacles [307]. The transducer model is identical to the  $P_1$  model in [307], which distinguishes the outer, concave acoustic lens (matching layer made from acrylic resin, properties as in Table 8.1) and a disk shaped piezo-element (treated as Dirichlet pressure boundary condition with a sinusoidal ‘aperture function’ that accounts for the spatial variation of the pressure magnitude).

HU-based inhomogeneous property assignment was restricted to the skull region. Voxels were assigned to 30 different bone classes based on HU binning. An increase of the number of binning classes beyond 30 was found to not significantly affect the acoustic distributions anymore (less than 1% change in peak intensity).



### 8.2.4 Varied parameters

We defined a baseline configuration for the parameters used in acquiring the CT images and in setting up the simulations, and then varied them individually. Table 8.2 presents all parameter variations and the baseline parameters.

#### 8.2.4.1 CT imaging of the skull

We acquired CT images of the skull attached to its holder in air background using a positron emission tomography / computed tomography (PET / CT) scanner (Biograph 128, Siemens, Germany). We acquired CT data with two tube potentials, 80 and 140 kV. The latter corresponds to the tube potential used in [147] for mapping HU to acoustic properties. Figure 8.1a shows the different distribution of HU for the two tube voltages. For 80 kV, a tube current-time product of 115 mAs was used, together with a sharp filter (H60s) during reconstruction. This corresponds to a low effective dose of  $\sim 0.3$  mSv for a human head scan (roughly one-third of the dose of clinical head scans) [294]. The spatial resolution was  $0.36 \times 0.36 \times 0.6$  mm<sup>3</sup>. For 140 kV, three current-time products were used: 300, 70, and 25 mAs corresponding, respectively, to a high ( $\sim 4.3$  mS), clinical ( $\sim 1$  mS), and low ( $\sim 0.3$  mS) effective dose. The spatial resolution was  $0.39 \times 0.39 \times 0.6$  mm<sup>3</sup>. For each dose, three reconstruction filters were used, corresponding to three different filter levels (H60s: sharp filter, H48s: medium filter, H41s: smooth filter). As the image noise is not only dependent on the parameter settings, but also on properties of the scanned object such as size and density, gaussian noise was added to the images acquired with H60s and H41s filters to emulate the noise levels of human images at low and clinical doses (see Section 8.A.1 for details). Table 8.4 in the Appendix lists the adjusted noise levels of the images depending on the CT parameters. Table 8.2 gives an overview of the acquisition and reconstruction parameters considered here. Figure 8.2 shows six examples of images acquired with different parameters.

#### 8.2.4.2 3D skull geometrical model

Skull model parameters were varied to assess their impact on the simulated beam. The skull models were generated by first thresholding the CT images at 0 HU (the skull CT images are acquired in air-medium where the background is around  $-1000$  HU) to extract a surface model of the skull

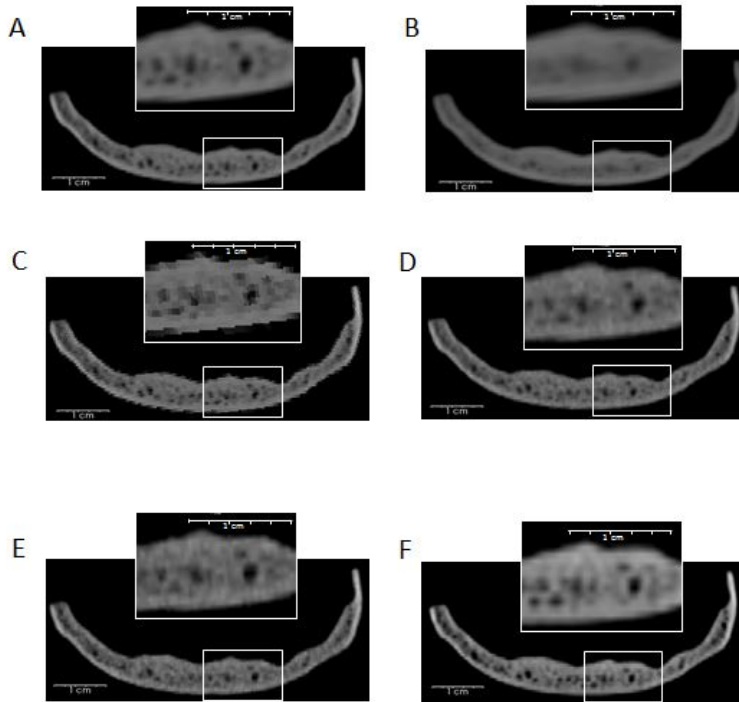


FIGURE 8.2: The figure shows six examples of the same slice of the sheep skull, acquired with different scan / processing parameters: (A) high-dose and sharp filter (H60s), (B) high-dose and smoother filter (H41s), (C) high-dose and sharp filter (H60s), with nearest-neighbor interpolation, (D) clinical-dose, sharp filter (H60s), (E) low-dose and sharp filter (H60s), and (F) with a tube voltage of 80 kV. When not indicated otherwise, the tube voltage was 140 kV, and linear interpolation was used. In images (D) and (E), additional noise was added to emulate typical human imaging conditions, as described in Section 8.A.1. The insets show a zoomed region of the image, indicated by the white square. The images clearly show that the level of detail changes depending on the employed acquisition or reconstruction parameters.

	HU	$\rho$ [kg/m <sup>3</sup> ]	$c$ [m/s]	$\alpha$ [Np/m]
Air	-1000	1.275	343	0
Water	0	1000	1500	0
Sheep skull	<i>variable*</i>	1710	2500	100
Matching layer	-	1190	2600	50

TABLE 8.1: Parameters used for skull property mappings, based on the approach from [146], but using species-specific values from [280]. *variable\** indicates that the HU value of bone is scan parameter-dependent and defined here as the location of the corresponding HU-histogram peak.

component. Image up-sampling via either nearest-neighbor or linear interpolation (baseline: linear) was applied to relate the coarse CT resolution to the fine discretization step in the simulation domain (0.112 mm).

#### 8.2.4.3 Skull acoustic property maps

**HETEROGENEITY** The importance of considering skull heterogeneity and structure was investigated by either modelling the skull as a homogeneous medium or as heterogeneous with image-based tissue properties distributions (baseline, defined below). To test the impact of the structure of the skull heterogeneity on the acoustic beam, virtual images were constructed by replacing the skull’s HU values with random values following a gaussian distribution with the mean and standard deviation of the original HU value distribution (see Figure 8.15) before the different acoustic property maps were applied. The spatial granularity of the assignment of the random values was varied (resolution: 0.1 mm, granularity:  $1 \times 1 \times 1 / 2 \times 2 \times 2 / 3 \times 3 \times 3$  voxels). The mean wavelength inside the skull varies between 4.5–5 mm.

**DENSITY AND SPEED-OF-SOUND** To simulate the inhomogeneity of the skull, we first used an approach similar to the one from [146] to map HU to acoustic properties. This approach was also explored in our previous study [307]. It assumes that the CT HU can be linearly mapped to bone density, which in turn maps to speed-of-sound according to the following relations:

$$\rho = \rho_{ref_1} + \frac{\rho_{ref_2} - \rho_{ref_1}}{HU_{ref_2} - HU_{ref_1}} HU$$

<b>Varied parameters</b>	
CT imaging	
Tube voltage	80, <b>140</b> kV
Filter (smoothing)	H41s, H48s, <b>H60s</b>
Dose	Low, Clinical, <b>High</b>
Skull model generation	
Interpolation	Nearest neighbor, <b>Linear</b>
Acoustic property mapping	
Speed-of-sound	Homogeneous, Gaussian <sub>1</sub> , Gaussian <sub>2</sub> , Gaussian <sub>3</sub> , <b>Linear</b> <sub>w,s</sub> , Linear <sub>a,s</sub> , Pich <sub>836</sub> , Pich <sub>500i</sub> , Pich <sub>270</sub>
Attenuation	0, 50, <b>100</b> , 150, 300 Np/m, Pich <sub>836</sub> , Pich <sub>500i</sub> , Pich <sub>270</sub>
Skull position	
Translation	<b>0</b> , ±1, 2, 3 mm
Rotation	<b>0</b> , ±1, 3°

TABLE 8.2: The different parameters considered in this paper and their baseline parameters (***italic+bold***; individual parameters are varied while keeping the other parameters at their baseline). The mappings are explained in detail in Table 8.3 and Section 8.2.4.3.

<b>Image-based skull map parameters</b>			
	HU $\rightarrow \rho$	$\rho \rightarrow c$	$\alpha$
	$ref_1, ref_2$	$ref_1, ref_2$	Np/m
Linear <sub><i>w,s</i></sub>	water, skull	water, skull	100
Linear <sub><i>a,s</i></sub>	air, skull	air, skull	100
Pich <sub>836</sub>	air, water	[147]	[147]
Pich <sub>836,100</sub>	air, water	[147]	100
Pich <sub>500<i>i</i></sub>	air, water	interpolated [147]	interpolated [147]
Pich <sub>500<i>i</i>,100</sub>	air, water	interpolated [147]	100
Pich <sub>270</sub>	air, water	[147]	[147]

TABLE 8.3: The different acoustic property mapping schemes (density  $\rho$ , speed-of-sound  $c$ , and attenuation  $\alpha$ ).  $\rho$  is mapped from HU, and  $c$  from  $\rho$ .  $\alpha$  is either mapped from density, or kept homogeneous. The mapping can be linear, with water and sheep skull (Linear<sub>*w,s*</sub>), or air and sheep skull (Linear<sub>*a,s*</sub>), as anchor points. In addition, the mapping can be non-linear, following the method proposed by [147]. In [147], mappings relative to two frequencies were studied (270 and 836 kHz, Pich<sub>270</sub> and Pich<sub>836</sub>). We also consider interpolated mapping functions to handle the 500 kHz (Pich<sub>500*i*</sub>) frequency used in this study.

$$c = c_{ref_1} + \frac{c_{ref_2} - c_{ref_1}}{\rho_{ref_2} - \rho_{ref_1}} \rho$$

where  $ref_1$  and  $ref_2$  refer to the reference anchors (air, water or skull) of the linear mappings and their corresponding HU and density values.  $ref_1$  is chosen as either water or air and  $ref_2$  as species specific average skull properties. As mentioned earlier, the HU of water and air are fixed by definition, however the average skull value is not. To set  $HU_{ref_2}$ , a histogram of the skull CT HU data was extracted and the HU value corresponding to the peak of the histogram was used.  $\rho_{ref_2}$  and  $c_{ref_2}$  were set to the species-specific average skull properties (density and speed-of-sound, respectively) as obtained from [280]. Adjusting the linear mapping to the peak HU of skull ensured that the density and speed-of-sound histograms of 80 and 140 kV acquisitions agreed reasonably (see Figure 8.5 vs. 8.1).

Additionally, the non-linear mappings from [147] were also explored (see Figure 8.3). These mappings have no free parameters since the linear HU to density conversion depends uniquely on water and air for calibration (which are independent of CT settings), and the mapping from density to speed-of-sound and attenuation are fixed and only depend on frequency. These mappings were established for a discrete set of frequencies (270 kHz and 836 kHz are the ones closest to the stimulation frequency of 500 kHz employed in this study). Therefore, simulations at 500 kHz were performed using the experimentally determined relationships at 270 kHz and 836 kHz, as well as a point-wise linear interpolation thereof.

Note, however, that these maps were obtained by fitting experimental data from human skulls. The density to speed-of-sound and attenuation curves do not necessarily translate to other species, as discussed in [307]. It is also important to note, that the curves have been fitted to provide good approximations in a certain range of densities. Outside that range, the extrapolated evaluation of these fitting functions is not suitable, and in this study, the mapped properties are treated as constant above 1200 and below 2600 kg/m<sup>3</sup> (corresponding to 200 and 1600 HU, respectively).

Parameters used for the different mappings are shown in Table 8.3. The mappings are reproduced in Figure 8.3 and the resulting distribution of acoustic properties inside the skull for the baseline CT settings are plotted in Figure 8.5.

**ATTENUATION** Previous work has assigned skull attenuation  $\alpha$  based on the bone density  $\rho$ , as in [146] and [147]. However, in [146], this relation is heuristically tuned to better match simulation results with measure-

ments. This is justified as a way to account for microscopic back-scattering effects that cannot be effectively captured by even high resolution CT images [14, 146, 286]. Works by [286, 301] instead suggest using homogeneous absorption maps in the skull, based on the finding that the introduction of heavy stochastic noise (greater than 20%) into a previously homogeneous attenuation distribution has almost no effect on the transcranial field distribution [14].

To investigate the impact of attenuation, first homogeneous attenuation with varying attenuation strengths (0 / 50 / 100 / 150 / 300 Np/m) were applied (baseline: 100 Np/m), and subsequently, the different image-based non-linear mappings from [147] at 270 and 836 kHz were used, as well as a linearly interpolated version at 500 kHz.

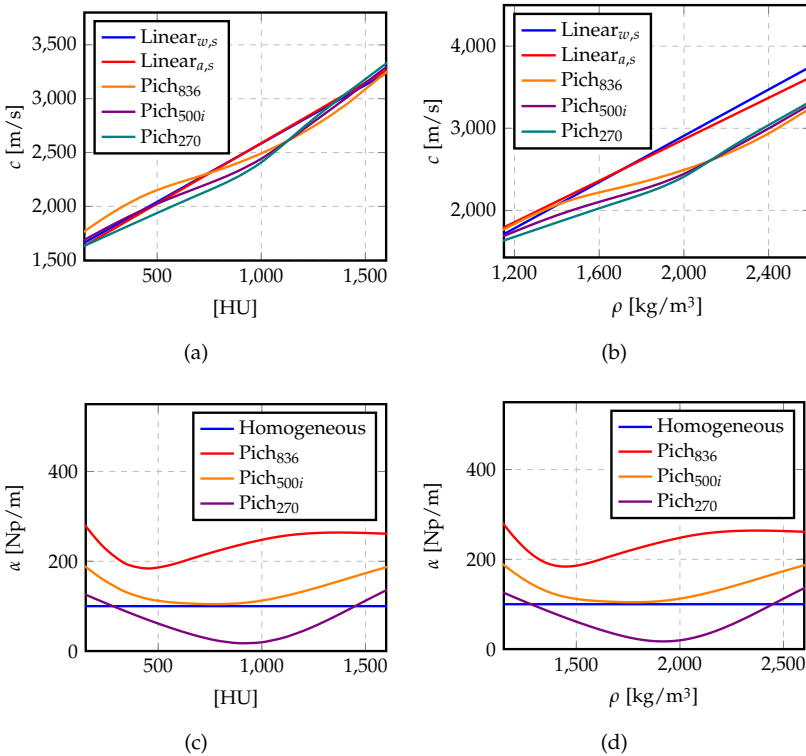


FIGURE 8.3: Speed-of-sound and attenuation mapping as a function of HU (A, B) and density (C, D). Up to 1700 HU, the combined  $\rho$ (HU) and  $c(\rho)$  mapping results in mostly linear and equivalent  $c$ (HU) maps.

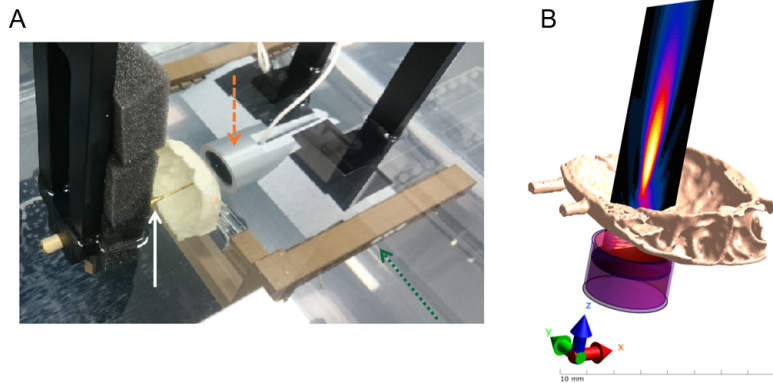


FIGURE 8.4: Setup used to characterize the ultrasound beam (A) and the corresponding simulation setup with results (B). In (A), three parts of the setup are visible: the hydrophone (white arrow), the sheep skull holder (green dotted arrow), and the transducer holder (orange dotted arrow). In the bottom corner of (B), the direction of the three Cartesian axes are indicated. Adapted from [307].

#### 8.2.4.4 Positioning sensitivity

Sensitivity assessment was also conducted by running simulations with the skulls shifted ( $\pm 1 / 2 / 3$  mm) and rotated ( $\pm 1 / 3^\circ$ ) along the principal axes. Positive rotations are defined in a counterclockwise direction around the stated plane with the origin at the skull's bounding box center according to the right hand rule. The direction of the principal axes can be seen in Figure 8.4.

#### 8.2.5 Agreement metrics

We aimed to determine how sensitive the simulations are to changes of the parameters described above. To do so, we used one parameter combination as the reference case (highlighted in *italic and bold* in Table 8.2) and systematically varied single parameters to assess the impact on the simulated transcranial distribution. For quantitative analysis, we defined metrics to characterize both changes in the spatial beam profile (irrespective of the absolute intensity) and changes of the beam intensity.

In a second analysis, we tested how the parameters affected the fit between simulation and measurements, again using metrics that characterized



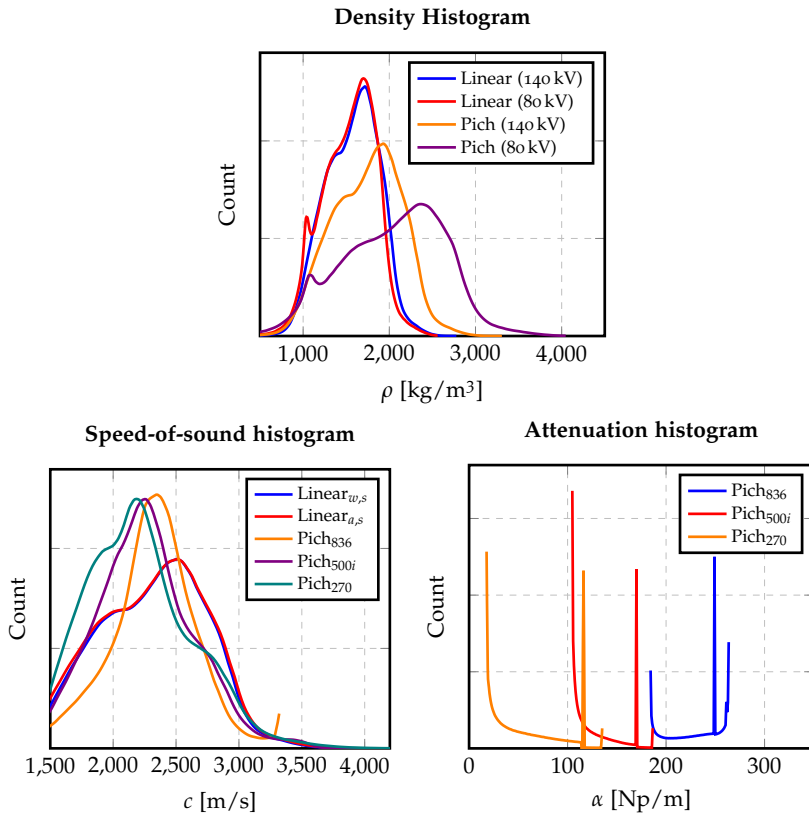


FIGURE 8.5: Density  $\rho$ , speed-of-sound  $c$ , and attenuation  $\alpha$  histograms for the different mappings.

the differences in beam shape and beam intensity, respectively. The employed metrics are described in detail below.

### 8.2.5.1 Comparison between simulations

We defined four measures to compare the spatial distribution and the intensity of the acoustic beam after skull transmission between simulations and the reference simulation:

**GAMMA COMPARISON OF THE BEAM PROFILES** The Gamma method allows for a quantitative comparison of shape and intensity differences between two fields [283, 290, 307]. Here, we apply it to simulations that are first normalized to the total power in the volume after the skull obstacle, resulting in a measure that is mostly sensitive to changes in the spatial beam shape, and not to the overall intensity.

The method relates differences between the distributions to acceptable spatial tolerances and an amplitude tolerance ( $\Delta d_{x,y,z}$  and  $\Delta D$ , respectively) defined by the user (see Section 8.2.5.3). It compares every point in the reference dataset with all points in the second dataset to determine the point in the second dataset that minimizes an Euclidean distance norm combining distance ( $\vec{r}$ ) and value ( $f(\vec{r})$ ) deviations, weighted by the corresponding tolerances:

$$\Gamma(\vec{r}_{\text{model}}, \vec{r}_{\text{meas},i}) = \sqrt{\frac{(f_{\text{model}}(\vec{r}_{\text{model}}) - f_{\text{meas}}(\vec{r}_{\text{meas},i}))^2}{\Delta D^2} + \sum_{j=x,y,z} \frac{(r_{j,\text{model}} - r_{j,\text{meas},i})^2}{\Delta d_j^2}}$$

where  $i$  is the index of a specific point in the reference dataset,  $x$ ,  $y$  and  $z$  are the spatial coordinate system of the two datasets, and the subscripts *ref* and *model* indicate the reference and the second dataset, respectively. A gamma index ( $\gamma$ ) is subsequently assigned to each point by choosing the minimized Euclidean distance norm:

$$\gamma(\vec{r}_{\text{ref},i}) = \min \{ \Gamma(\vec{r}_{\text{model}}, \vec{r}_{\text{ref},i}) \} \forall \vec{r}_{\text{model}}$$

A value of  $\gamma(\vec{r}_{\text{ref},i}) = 0$  corresponds to a perfect match for a point  $i$ , a value of  $\gamma(\vec{r}_{\text{ref},i}) \leq 1$  means that the disagreement lies within the total tolerance, and  $\gamma(\vec{r}_{\text{ref},i}) > 1$  means that the disagreement exceeds the combined tolerances. Finally, we determine the gamma comparison value  $\gamma_{\%}$  for reporting, which is the volume in which gamma exceeds the threshold

criterion, relative to the volume of the full width at half maximum (FWHM) of the beam in water background:

$$\gamma\% = 100 \frac{\text{volume with } \gamma > 1}{\text{volume of FWHM in water}} \quad (8.2)$$

This normalization allows comparison of the volume in which gamma exceeds the threshold to the overall volume of the beam. However, please note that the gamma volume corresponds to positions both in- and outside the FWHM. See Figure 8.6 for an illustrative example of the Gamma comparison method.

**PEAK LOCATION  $|d|$**  We report the Euclidean distance  $|d|$  in mm between the peak locations of the two distributions.

**PEAK INTENSITY** We report the difference between the peak intensities of the two simulations relative to the peak intensity of the reference case in percent:

$$\Delta I_{peak} = 100 \frac{I_{peak,sim} - I_{peak,ref}}{I_{peak,ref}} = 100 \left( \frac{I_{peak,sim}}{I_{peak,ref}} - 1 \right)$$

where  $I_{peak,sim}$  and  $I_{peak,ref}$  are the peak intensity in the simulation and in the reference case, respectively.

**TOTAL POWER** Similarly to the peak intensity, we report the difference between the total power of the distribution after skull transmission, relative to the total power of the reference case:

$$\Delta P = 100 \left( \frac{P_{sim}}{P_{ref}} - 1 \right)$$

where  $P_{sim}$  and  $P_{ref}$  are the total transcranial power of the simulation and of the reference simulation, respectively.

### 8.2.5.2 Comparison of simulations to measurements

The above measures were adapted for the comparison of simulations and measurements as follows:

**GAMMA COMPARISON OF THE BEAM PROFILES** Using the measurement data as reference, we changed the Gamma comparison by normalizing

the intensity distributions of both simulations and measurements to their respective total power in a pure water background without obstacles. Total power calculations for the simulations and measurements were done over the same domain (the measurement volume in water). We refer to this Gamma metric as  $\tilde{\gamma}\%$ .

**PEAK LOCATION**  $|\tilde{d}|$  We determined the Euclidean distance  $|\tilde{d}|$  in mm between the peak locations in the simulation and measurement distributions.

**PEAK INTENSITY** We report the difference between the simulated and measured peak intensities, each normalized to the respective peak intensities in a pure water background, in % relative to the normalized peak intensity of the measurements:

$$\Delta\tilde{I}_{peak} = 100 \left( \frac{I_{peak,sim}/I_{peakWater,sim}}{I_{peak,meas}/I_{peakWater,meas}} - 1 \right)$$

where  $I_{peakWater,sim}$  and  $I_{peakWater,meas}$  are the peak intensities of the simulation and the measurements, respectively, in a pure water background without obstacles.

**TOTAL POWER** We report the difference between the simulated and measured total power of the distribution after skull transmission, each normalized to the respective total power in a pure water background ( $P_{water,sim}$  and  $P_{water,meas}$ , respectively), in % relative to the normalized total power of the measurements:

$$\Delta\tilde{P} = 100 \left( \frac{P_{sim}/P_{water,sim}}{P_{meas}/P_{water,meas}} - 1 \right)$$

### 8.2.5.3 Tolerances for the Gamma comparisons

The chosen tolerances were motivated by the intended application – i.e., the spatially precise targeting of a small cortical patch – and the physical beam properties. Given a focus size of the used transducer with a FWHM in water with no obstacle of 42 mm along the beam axis and 5 mm perpendicular to it, we set  $\Delta d_z = 5$  mm and  $\Delta d_{xy} = 2$  mm as upper thresholds for shifts of the focus position in these directions. Shifts exceeding these criteria would result in the undesired stimulation of a neighboring cortical patch, or in a peak position that is in cerebral spinal fluid (CSF) or white

matter, rather than in gray matter. A criterion of  $\Delta D = 10\%$  was set as the amplitude tolerance, which is more conservative than the  $\Delta D = 15\%$  used in our prior publication [307]. We updated it in order to make the Gamma comparison more sensitive to the impact of parameter changes on the power-normalized distributions, which can be expected to agree better with respect to amplitude.

#### 8.2.5.4 Qualitative comparison

The impact of varying individual parameters on the simulated 3D intensity distributions were compared qualitatively through visualization of the maximum intensity projection (MIP) along the  $y$ -axis (see Figure 8.4b) onto a 2D plane containing the main axis of propagation ( $xz$ -plane). Figure 8.12 shows sample MIPs with two different intensity normalization schemes:  $P_{sim}$  and  $P_{ref}$ , corresponding to the field scaling by the inverse of the simulation's total power or to the reference simulation's total power, respectively. Furthermore, the spatial distribution of  $\gamma(\vec{r}_{ref})$  provides an intuitive visualization of disagreement locations (see Figure 8.6 for an illustrative example of the Gamma comparison method).

## 8.3 RESULTS

In the following, we refer to the Gamma metrics and peak location as measures of the spatial profile distribution (irrespective of the overall average absolute intensity), while we use the peak intensity and total power as measures of the strength or intensity of the distribution.

### 8.3.1 Impact of CT parameters

Figure 8.7 summarizes the sensitivity of the simulations to changes of the imaging parameters (red curves) and the dependence of the fit between simulation and measurements on these parameters (blue curves). Overall, the simulations are only moderately sensitive to the tested imaging parameters. The strongest impact is seen for the peak intensity and total power that vary up to 20% between the two tube voltages and the different filter settings. However, it is worth noting that we fixed the peak of the bone density histogram to the value taken from literature (see Figure 8.5a). The choice of the interpolation scheme for upsampling (nearest-neighbor vs.

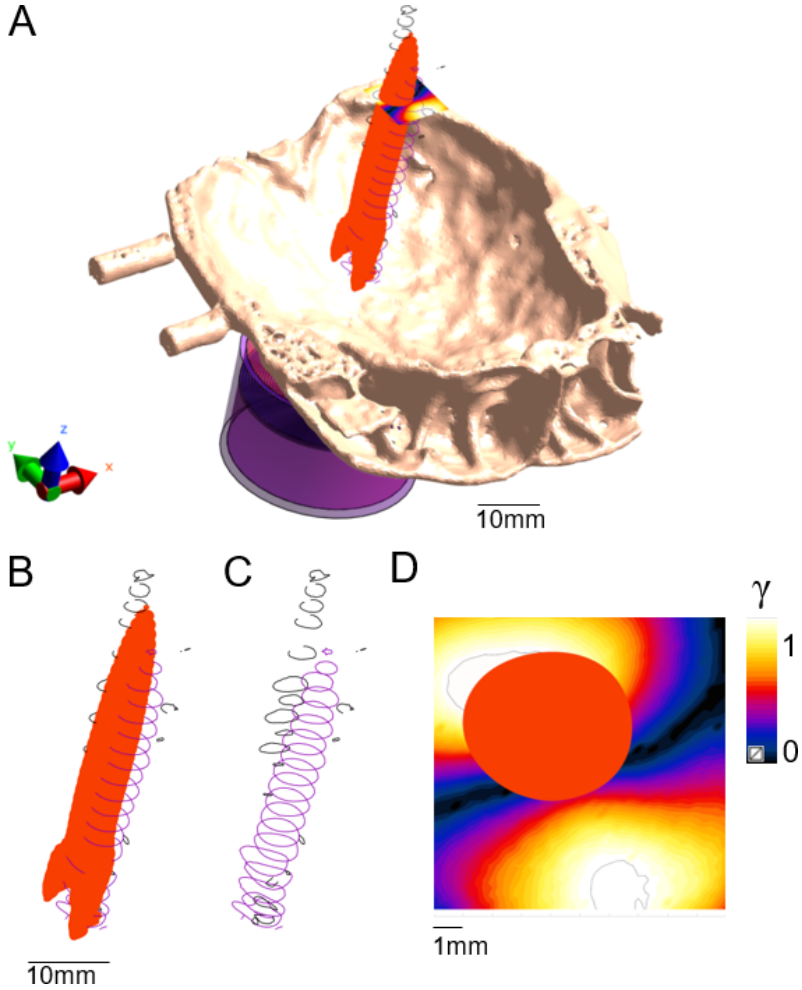


FIGURE 8.6: Simulated focus shape (intensity isolevel). The red iso-surface and violet iso-curves represent the 50% level of the simulated and measured intensity distributions (after deposited power normalization). The black curves demark the regions where a  $\gamma$ -comparison value of 100% is exceeded: (A) simulation setup, (B, C) enlarged focus region with and without simulation iso-surface display, and (D) view from the top displaying the full  $\gamma$ -distribution in a slice. (B) and (C) show that the simulated beam and measured beam point in slightly different directions and as such creates a corresponding mismatch of the gamma metric on one side of the beam (black curves).

linear) had only a small impact on the simulation results, likely due to the inherent smoothness of the underlying images from a clinical CT scanner.

None of the tested parameter variations strongly influenced the fit between simulated and measured spatial distributions (Gamma and Euclidean distance), indicating that error sources such as measurement errors and coregistration errors between simulations and measurements likely contributed to the mismatch (see Section 8.3.3.1 below for details). These error sources might in part also explain the underestimation of the peak intensity and total power by the simulations that was observed in most cases. This is more apparent for the total power that was underestimated in the order of 20–30%. The different behavior for peak intensity and total power indicates that while the simulations underestimate the deposited power, they simultaneously tend to overestimate the focusing quality, thus partially compensating the intensity underestimation in the beam center.

Additional visualizations of the beam distribution can be found in Figures 8.12 and 8.13 in the Appendix. Visual inspection of the MIP of the simulated acoustic intensity maps confirm the overall weak impact of the parameters on the simulated beam, and indicate that the strongest changes occurred in the transducer near-field (see Figure 8.12).

### 8.3.2 *Impact of skull properties and mappings from CT to acoustic properties*

#### 8.3.2.1 *Attenuation*

The spatial distribution of the simulated beam is slightly affected by the attenuation of skull (red curves in Figure 8.8a and b). Correspondingly, the fit between simulated and measured beam profiles did not strongly change with the simulated skull attenuation (blue curves in Figure 8.8a and b). Visual inspection revealed that the beam profile after skull transmission became increasingly smooth with increasing attenuation (right column of Figure 8.14), without a strong change in its distribution. In contrast, the skull attenuation had a profound impact on the absolute intensity of the simulated beam (see Figure 8.8c and d), as expected. A good fit between simulations and measurements was obtained for an attenuation of  $\alpha = 100 \text{ Np/m}$ . However, this value is known to be species-dependent [274, 287, 310, 311] and subject to a large uncertainty. It is thus unclear whether the good fit in intensity observed here would translate to human applications.

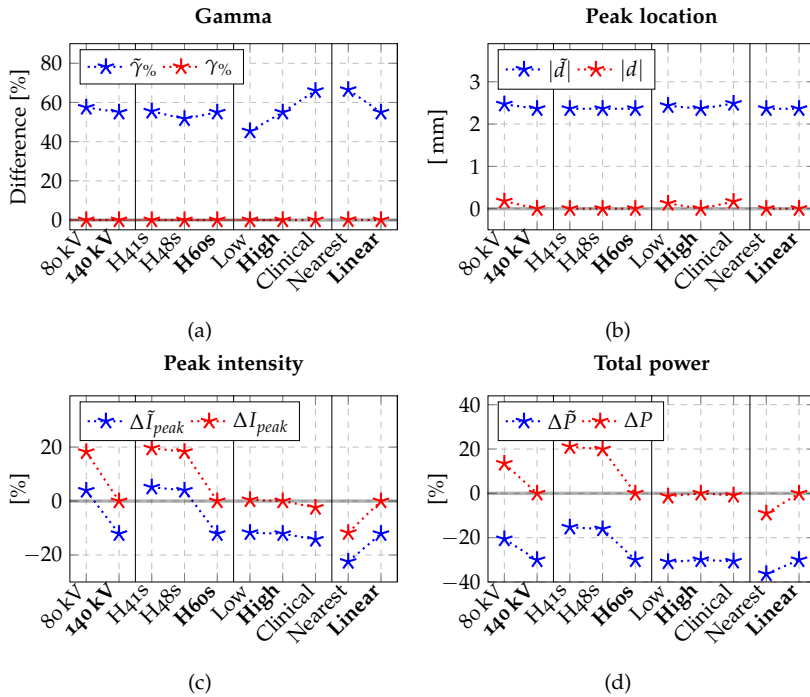


FIGURE 8.7: Dependence of (A) the Gamma metrics ( $\gamma_%$  and  $\tilde{\gamma}_%$ ), (B) the Euclidean distance between the peak positions ( $|d|$  and  $|\tilde{d}|$ ), (C) the peak intensity ( $\Delta I_{peak}$  and  $\Delta\tilde{I}_{peak}$ ), and (D) the total power ( $\Delta P$  and  $\Delta\tilde{P}$ ) on: Tube voltage, reconstruction filter settings, dose, and interpolation scheme during upsampling. The red lines show the comparison with the chosen reference case (the reference parameters are highlighted as bold labels on the x-axis). The blue lines show the comparison to the acoustic measurements. Please see Section 8.2.5 for a detailed description of the metrics.



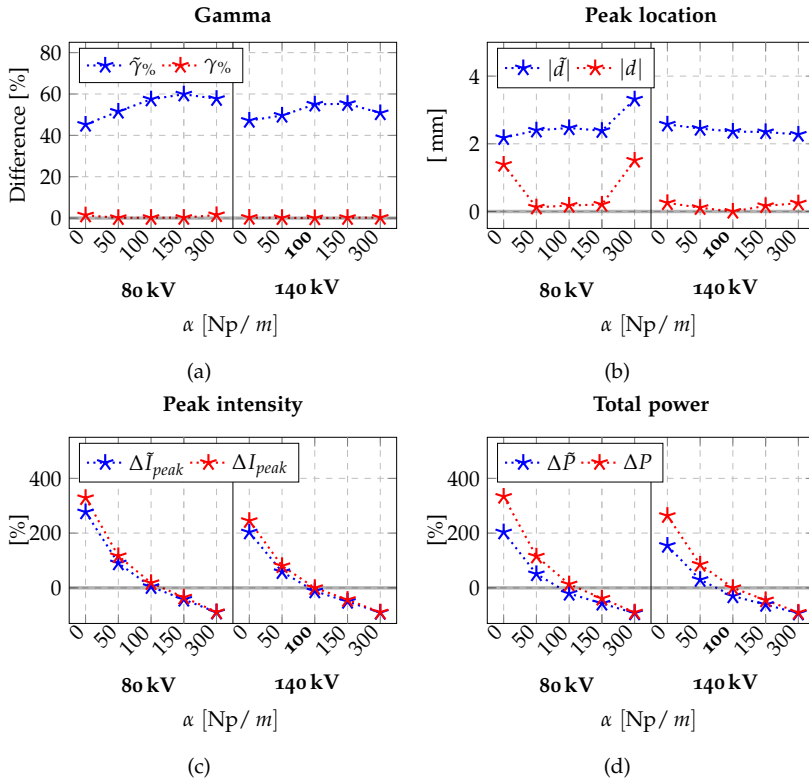


FIGURE 8.8: Dependence of the simulations on tube voltage and skull attenuation. Metrics as in Figure 8.7.

### 8.3.2.2 *Heterogeneity*

**STRUCTURE** Motivated by the weak impact of the skull attenuation on the spatial beam profile, we wanted to additionally test the relevance of accurately modelling the heterogeneous spatial distribution of the skull density and speed-of-sound in the simulations. Therefore, we modelled the skull as a homogeneous medium (using the values for the sheep skull in Table 8.1) and as random heterogeneous region (gaussian distribution with mean and standard deviation matching that of the HU values in the skull, see Figure 8.15 for details). We compared the results to those of our reference case with a linear mapping of the acoustic properties from the CT HU values ( $\text{Linear}_{w,s}$ ). Neglecting the internal structure of the skull and replacing it by a homogeneous region or gaussian noise strongly affects both the spatial distribution and intensity of the simulated beam (red curves in the left part of the four sub-figures in Figure 8.9). Also, the fit to the measurement beam is generally decreased compared to the reference case (see Figure 8.9, left part of the four sub-figures, blue curves). Total power is less affected than peak intensity. This suggests that the tested changes of the internal skull structure mainly affects the spatial profile of the beam while leaving the overall power transmitted through the skull relatively unaffected. Sample cross sections of the speed-of-sound distribution inside the skull with the corresponding beam profiles can be seen in Figure 8.16. Visualizations of the FWHM envelope of the beam together with the  $\gamma$ -distribution show that homogeneous or random-gaussian material properties result in more focused, symmetrical and smoother intensity distributions (see Figure 8.17). This is in disagreement with the measurement results and increases the  $\gamma$ -errors on the two sides of the main lobe.

**HU TO PROPERTIES MAPPING** After confirming the importance of modelling the heterogeneity of the skull, we compared the impact of different linear and non-linear mapping schemes that relate the HU values in the CT to the acoustic properties of bone. The linear maps are only used to generate the distributions of bone density and speed-of-sound, while attenuation is modelled as spatially homogeneous in the skull. We used either water and cortical bone (reference case) or air and cortical bone as reference anchor points to establish the linear mappings. The tested non-linear mappings are based on the approach presented in [147], which includes mapping functions at 270 kHz and 836 kHz. We linearly interpolated these two maps to also construct a mapping function for 500 kHz (Table 8.3 provides a summary of the tested mappings). We aimed to separate the effect of the

mapping of the speed-of-sound and density from the effect of the mapping of the attenuation. Therefore, we also considered two skull models with the non-linear mappings for speed-of-sound and density from [147], but with a constant attenuation of 100 Np/m ( $Pich_{836,100}$ ,  $Pich_{500i,100}$ ). This attenuation was chosen as it gave overall the best match with the measurements (as highlighted in Section 8.3.2.1).

The results for the two linear mappings are nearly identical, independent of the selection of the lower anchor point (right halves in Figure 8.9). Importantly, however, changing the value of the upper anchor point (here set to the peak of cortical bone) can be expected to have a large impact on the simulations.

The non-linear mappings ( $Pich_{836}$ ,  $Pich_{500i}$ ,  $Pich_{270}$ ) that also estimate the position-dependent attenuation from the CT affect the fit between the simulated and measured spatial beam profiles only moderately and the mappings for 270 kHz even improve the Gamma metrics (see Figure 8.9a and b, blue curves). However, the beam intensity varies strongly between the non-linear mappings (see Figure 8.9c and d, right halves).

When non-linear speed-of-sound maps with homogeneous attenuation were employed ( $Pich_{836,100}$ ,  $Pich_{500i,100}$ ), the shape of the normalized pressure distribution were rather similar to those obtained using heterogeneous attenuation maps (see Figure 8.9a and b,  $Pich_{836}$ ,  $Pich_{500i}$ ). However, the intensity prediction improved when the attenuation was kept constant (see Figure 8.9c and d). These results indicate that attenuation mainly affects the overall intensity of the acoustic beam after skull transmission, while the the speed-of-sound and the density mainly affect the spatial distribution.

### 8.3.3 Positioning

The skull was shifted along and rotated around the main axes in the simulations. In general, shifts and rotations have a large, non-linear impact on focus location and intensity. This is due to the variation of skull thickness, skull heterogeneity and the changing orientation of the skull surface relative to the propagation axis. The data are shown in Figures 8.10 and 8.11.

#### 8.3.3.1 Translation

The simulations are sensitive to small translations (red curves in Figure 8.10). In particular, shifts in the y-direction by 1 mm already result in changes of the peak intensity by more than 50 % and a shift of the peak position by 3 mm. The high sensitivity to shifts in this particular direction is likely

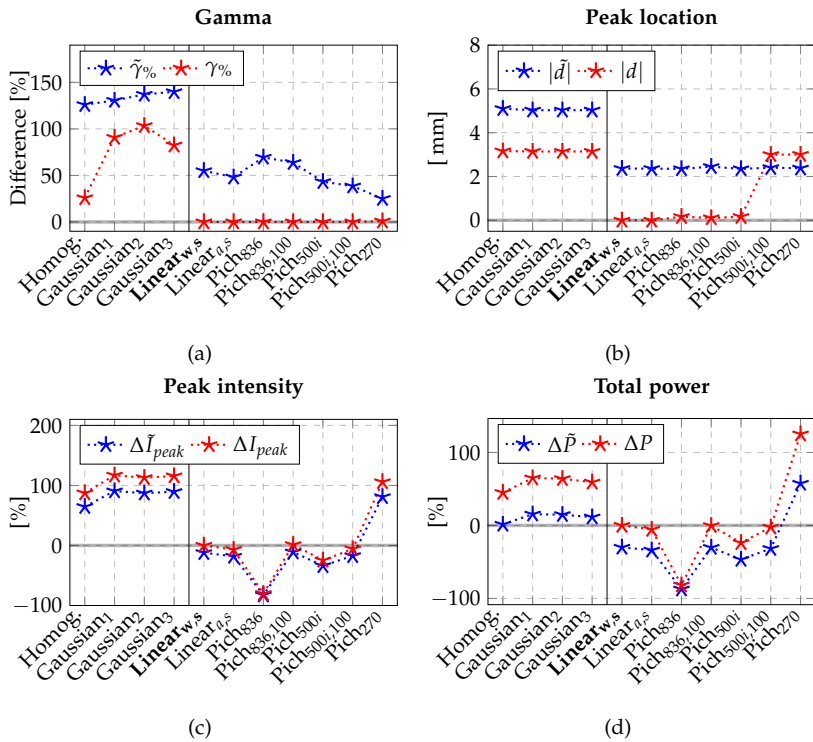


FIGURE 8.9: Dependence of the simulations on the modelling of the acoustic properties of the skull. Metrics as in Figure 8.7. See Table 8.3 for further details.

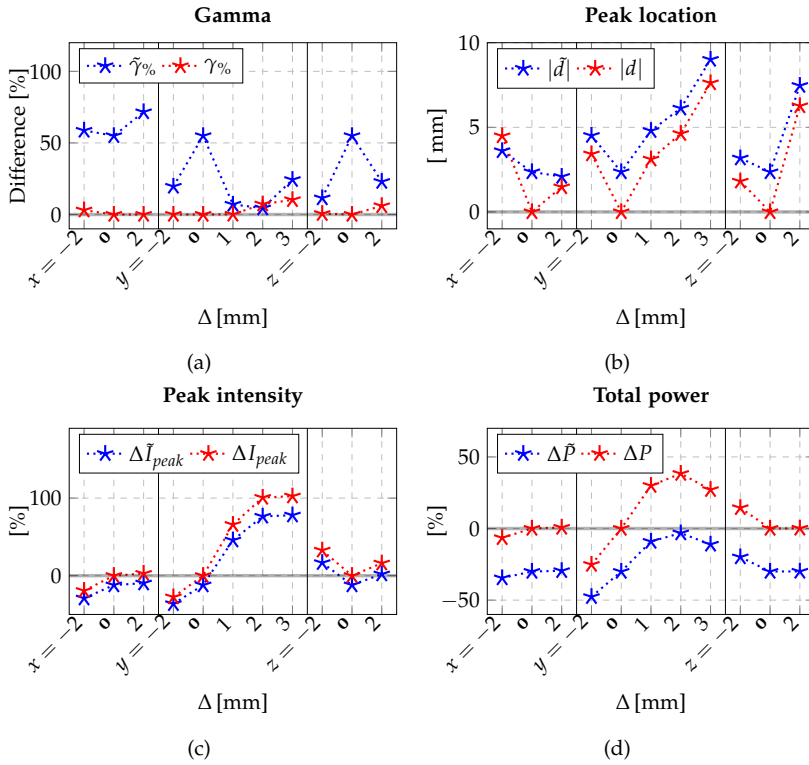


FIGURE 8.10: Dependence of the simulations on translations of the skull. Metrics as in Figure 8.7.

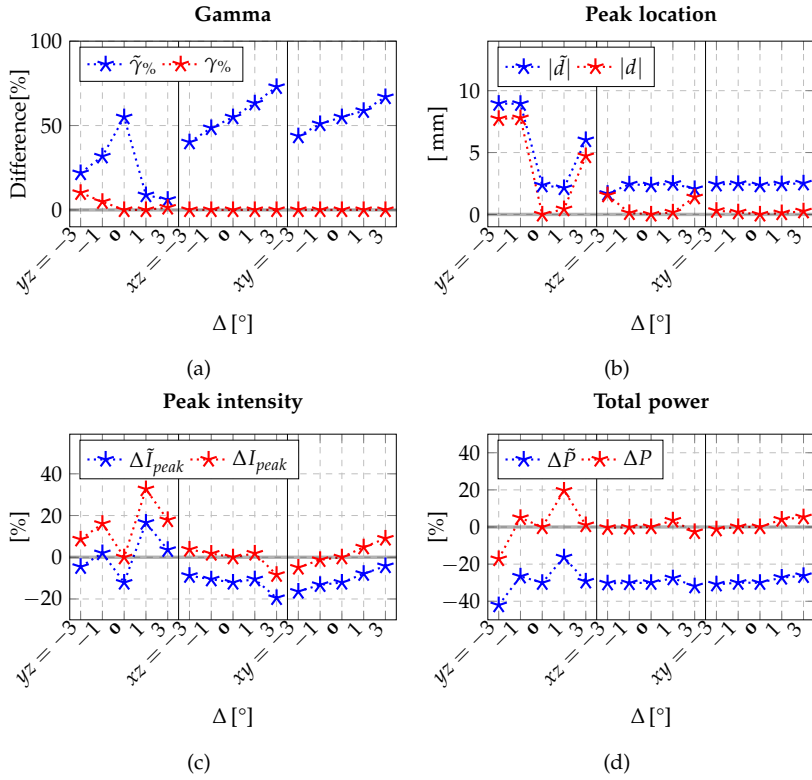


FIGURE 8.11: Dependence of the simulations on rotations of the skull. Metrics as in Figure 8.7.

caused by the associated changes in the distance between the skull interface and the transducer in combination with changes in the incidence angle of the beam due to changes of the orientation of the skull surface in the beam center (see Figure 8.4). Due to the irregular shape of the skull, this effect is more pronounced for shifts in the  $y$ -direction (the anterior - posterior direction) than in the  $x$ -direction (medial - lateral direction). The Gamma metric is on average slightly affected by shifts.

Comparison to the measurements (blue curves in Figure 8.10) in general confirm the importance of an accurate control of the transducer position relative to the skull, but does not allow for a straightforward identification of the cause of the differences between simulations and measurements. Specifically, while the peak position and peak intensity seem to be best matched for the reference case without shifts, Gamma and total power are better matched for shifts in the positive  $y$ -direction. Correspondingly, visualizations of the FWHM envelope of the beam together with the  $\gamma$ -distribution indicates that the  $\gamma$  distribution of the reference case has high values (frequently exceeding 1) on two sides of the main lobe that are reduced for shifts in the positive  $y$ -direction (see Figure 8.18a vs. b). This suggests a systematic slight shift of the lobe relative to the measurements, which can result from a simulation-related focus shift, or of inaccuracy in reproducing the exact skull or sensor position relative to the transducer.

### 8.3.3.2 *Rotation*

In general, the simulations are less affected by rotations in the tested range than they are by the translations (red curves in Figure 8.11). Rotations in the  $yz$ -plane (i.e., rotations around an  $x$ -axis centered in the skull), however, have a strong impact, which is in line with the observed impact of translations along the  $y$ -direction. We suggest that the same structural features of the skull as described above for shifts in the  $y$ -direction also cause the sensitivity of the simulations to the rotations in the  $yz$ -plane.

The fit to the measurements is most sensitive to rotations in the  $yz$ -plane, and counterclockwise rotations improve the fit (see Figure 8.18a vs. c). Conversely, rotations around the  $xz$ -plane gradually sharpens the focus and shifts it further away, resulting in worse agreement (see Figure 8.18d). As in the case of the tested translations, there is no particular rotation that results in the best fit in all measures, making the identification of the root cause of the differences difficult.

## 8.4 DISCUSSION

**IMPACT OF INTERNAL STRUCTURE OF THE SKULL** Our results confirm the importance of accounting for the internal structure of the skull in order to accurately estimate the transmitted acoustic wave [312]. Simulations employing a homogeneous skull model, similar to those used in some prior studies [272], resulted in sharper foci and more regular and symmetric lobe shapes than observed in our measured distributions and in the simulations using CT-based acoustic skull properties (see Figure 8.17). A similar disagreement with the measurements was also seen for simulations based on unstructured, random skull heterogeneities. Presumably, CT-based skull modelling introduces a structured heterogeneity that more profoundly distorts the wave front than homogeneous and random-heterogeneous skull properties. The latter mainly affect the skull transmission through reflections at the skull boundaries that might also cause standing-wave effects [307]. Modeling CT-based structured skull heterogeneity also tends to predict a reduced focus intensity – likely due to scattering and dephasing –, but also predicts suppressed side-foci (also a consequence of dephasing), which would be beneficial effect from a clinical perspective. While it seems generally useful to consider image-based information about skull structure in the simulations, the results can depend strongly on various imaging and image-processing choices made by the user. As detailed in the following paragraphs, this includes the CT imaging parameters, the strategies used to facilitate transferability between CT scanners or scanning protocols, and the mapping functions from CT HU values to acoustic properties.

**IMPACT OF CT PARAMETERS** Varying the imaging parameters and interpolation schemes had small to moderate effects on the simulations and their accuracy. In particular, the result indicate that the chosen CT dose (and by that the noise levels) did hardly affect the simulations that were based on a linear mapping between CT HU values and bone density. This is particularly important for future applications in humans, where it is preferable to minimize the X-ray dose. On the other hand, changing the filter sharpness and tube voltage moderately changed the simulations, in particular the estimated peak intensity and total power. Thus, controlling for these parameters and clearly documenting them in publications seems useful to improve the comparability of simulation results between studies. In this respect, it is important to note that the obtained HU values of the skull sample were clearly affected by the tube voltage. This is not unex-



pected, as the HU values of CT scanners are usually only calibrated and linear within the range corresponding to air ( $-1000$  HU) and water ( $0$  HU). Achieving a good correspondence between the simulation results obtained for the two tube voltages thus required us to rescale the HU values by choosing upper anchor points for the linear mappings that corresponded to the peak of the HU histograms (representing compact bone). While this was effective in reducing the dependence of the simulation results on the CT tube voltage, this approach would in practical applications also remove interindividual differences in bone density and speed-of-sound values.

**SPATIAL DISTRIBUTION OF ACOUSTIC WAVE** Surprisingly, the tested linear and non-linear mappings from HU to acoustic skull properties resulted in similar predictions of the spatial distribution of the transmitted acoustic wave. This was on first sight unexpected, as the modelled range of bone densities differed clearly between the linear and non-linear mappings (see Figure 8.5a), with the non-linear mappings predicting on average higher densities. However, the mappings from density to speed-of-sound also differed between linear and non-linear mappings (see Figure 8.3c). These two differences partly compensated for each other, so that the resulting mappings from HU to speed-of-sound (see Figure 8.3a) were again mostly similar.

However, the spatial distribution of the transmitted wave is also affected by the amount of scattering inside the skull that is estimated by the linear and non-linear mappings. Spatial variations in bone density cause variations in acoustic impedance ( $Z = \rho c$ ) and hence scattering. The term  $\rho \nabla \cdot (\frac{1}{\rho} \nabla p)$  from Equation 8.1 can be rewritten as:

$$\Delta p + \left( \rho \nabla \cdot \frac{1}{\rho} \right) \cdot \nabla p$$

so the contribution of density heterogeneity results from the  $(\rho \nabla \cdot \frac{1}{\rho})$  term. The speed-of-sound histograms (see Figure 8.5b) show that the non-linear mappings result in narrower distributions than the linear ones and thus generally in reduced scattering predictions. Finally, comparing the histograms of the three non-linear mappings with each other reveals a right shift and narrowing of the distribution for 836 kHz compared to 270 kHz, which increases the focality of the predicted acoustic beam.

Obviously, attenuation strongly and predominantly affects the strength of the acoustic intensity distribution (see below). However, comparing the image-based speed-of-sound mapping used with homogeneous attenuation

vs. CT-based heterogeneous attenuation maps indicates an improvement in focus location prediction when considering attenuation heterogeneity – a finding that differs from [14], because only stochastic heterogeneity was considered in that study.

**STRENGTH OF THE TRANSMITTED ACOUSTIC WAVE** While we found that using CT-based acoustic property maps helped to better estimate the spatial distribution of the acoustic wave after skull transmission compared to a homogenous skull model, a more complex pattern arose for the estimation of the magnitude of the transmitted wave. The latter is mostly affected by the acoustic attenuation of the skull. As noted by [146, 286], even high resolution CT is not detailed enough to account for acoustic attenuation related microscopic backscattering effects. Therefore an empirical relationship is employed. Some groups [14, 301] have advocated for a constant skull attenuation. For the linear mappings, we selected a spatially homogeneous attenuation value that resulted in a good match between the simulated and measured intensity. The optimized value fell within a reasonable range, supporting the validity of the simulation framework. The resulting peak intensity and the total power was on average still underestimated by up to 40%, and could likely have been improved further by fine-tuning the chosen attenuation (see Figure 8.7). However, this approach is not feasible for simulations of the tCFUS beam in human *in vivo* applications. Rather, we then have to rely solely on attenuation values reported in the literature. Unfortunately, values between  $\alpha = 10$  and  $\alpha = 300$  Np/m have been reported for humans [147, 313], making the simulated intensities uncertain (see Figures 8.8c and d). In addition, attenuation might exhibit interindividual variations that are lost when assigning a constant value from literature.

The non-linear mappings suggested in [147] aimed to resolve these problems by also estimating a position-dependent attenuation value from the CT image. In addition, they do not involve a rescaling of the CT HU values, as we had to use for the tested linear maps. Thus, the proposed non-linear mappings provide comprehensive informing about the spatial distributions of bone density, speed-of-sound and attenuation inside the skull, including interindividual differences of the acoustic properties. In its current form, however, this approach unfortunately still suffers from two major limitations. First, as already discussed above, CT images are usually not calibrated in the higher HU ranges. Thus, a mapping from HU values to bone density that was established for a particular CT scanner cannot be unambiguously applied to data acquired from another scanner. Even for the

same scanner, the mappings will change when changing the tube voltage (see Figure 8.1). Here, we aimed to ameliorate the latter problem by using the same tube voltage as in [147] (140 kV, personal communication by the authors). It is still likely that the data from the CT scanners used here and in [147] differed in the upper HU range.

Second, the mappings were established for specific ultrasound frequencies, and need to be adapted when applied at other frequencies. In our results, this becomes apparent when using the original mappings for 270 kHz and 836 kHz to estimate the acoustic wave at 500 kHz. The simulated peak intensity and total power strongly deviates by around 100 % for Pich<sub>270</sub> and by -90 % for Pich<sub>836</sub> (see Figures 8.9c and d), which corresponds to the results for constant attenuation values of the skull of about 50 and 300 Np/m, respectively, when using a linear mapping (see Figures 8.8c and d). This can be understood when analyzing the mapping functions. Attenuation as a function of HU are non-monotonous relationships for the Pichardo models (see Figure 8.3c). The 270 kHz transfer function oscillates around the constant attenuation value used for the homogeneous model, being lower in the 300–400 HU range and higher elsewhere. Applied to our CT data, the resulting histogram of the attenuation values inside the skull (see Figure 8.5c) has two peaks – one around 20 Np/m (reflecting the shallow minimum of the transfer function at medium HU) and one around 115 Np/m (reflecting the flat transfer function at high HU) – and is on average clearly lower than the constant attenuation value of  $\alpha = 100$  Np/m used for the linear mappings. The 836 kHz transfer function is much higher than the constant attenuation value used for the homogeneous modelling throughout the spectrum. Correspondingly, also the histogram of the attenuation values ranges from 180 Np/m to 270 Np/m (see Figure 8.5c).

While it was expected that the non-linear mappings that were established at too low (270 kHz) and high (836 kHz) frequencies resulted in under- and overestimated attenuation values, our results indicate that estimating a transfer function at an intermediate frequency through interpolation improves the results. However, as the shape of the transfer functions strongly and non-linearly depends on the frequency and the transfer functions are only available for a sparse set of frequencies, interpolation to other frequencies, e.g., at 500 kHz in our case, should be performed with caution and awareness. The comparison of Pichardo mappings used with homogeneous vs. image-based attenuation demonstrates that deviations from the measurements are influenced (and probably caused) by both speed-of-sound and attenuation heterogeneity.

The Pichardo [147] models were established for human skulls, so that a part of the mismatch between simulated and measured intensities might also stem from species- and age-specific differences in acoustic skull properties, e.g., differences in the skull microstructure or composition that are not resolved at the spatial resolution of clinical CT scanners [312]. Irrespective of this, the limitations outlined above generally apply and affect the reliability of the simulations. Resolving them would likely require reestablishing the mappings based on a CT scanner that is calibrated at higher HU for a specific tube voltage so that they could be transferred to data acquired from other similarly calibrated scanners. Alternatively, dual-energy CT might be used to reliably estimate bone density [314], probably at the expense of increasing the radiation dose.

**IMPACT OF THE POSITIONING ACCURACY** Our results confirm the high sensitivity of the simulations to translations and rotations of the transducer relative to the skull. Even changes in the order of 1–2 mm or 2–3° can affect the predictions of both shape and intensity. Here, this was particularly apparent for shifts and direction in the direction along which the curvature or structure of the skull changed the most. For the human skull, the effect might be often less pronounced as the skull composition and curvature does not change as quickly as seen here for the smaller sheep skull. However, the results still point to the need to control the transducer position very accurately in practical applications. For human non-invasive brain stimulation, neuronavigation based on frameless stereotaxy is considered the gold standard for position control. However, its reported accuracy lies within a few millimeter, i.e., in the range that resulted in clear errors in our simulations [315], suggesting the need for improvements. It is also likely that a slight systematic mismatch of the modelled transducer position contributed to the differences between the simulated and measured acoustic beam shape in our case, despite our efforts to precisely control the position.

**STUDY LIMITATIONS** The presented results reflect measurements performed on a single sample of a sheep skull. Considering the known interspecies and interindividual (e.g., age-related) differences of the acoustic properties of bone [316], it can be expected that the reported absolute result values are sample specific and would vary if repeated for other samples. However, we find it unlikely that our conclusions on, e.g., the relevance of specific CT parameters would fundamentally change. In particular, most of our main findings help to reveal general limitations of CT-informed tcfUS

simulations that are independent of the tested sample, but are caused by the procedures used for the CT image acquisition.

Our results indicate that a part of the observed mismatch between simulations and measurements might be due to positioning errors in the measurement. An even more careful position control might be needed to resolve the remaining mismatch between the spatial distribution of the simulated and measured acoustic waves. Considering the highlighted limitations of the CT data, it is less obvious whether an improved position control would also help to improve the estimation of the strength of the acoustic waves.

## 8.5 CONCLUSIONS

Properly modelling skull heterogeneity is important to accurately predict the acoustic intensity distribution. Interestingly, the structure of the heterogeneity has a much larger impact than the degree of heterogeneity and must be considered to reliably and accurately predict the beam shape. Our study confirms the value of informing tFUS simulations by CT-images of the skull heterogeneity. In particular, the image information helps to estimate relative spatial variations of bone density and speed-of-sound within the skull, which improves the accuracy of the simulated spatial distribution of the transmitted wave. Of note, this also works for low-dose CT scans of the head that minimize the exposure of the participants to radiation at the expense of having a lower SNR than standard diagnostic clinical CT scans. On the other hand, reliable estimation of the strength of the transmitted wave is still a challenge even when CT information is available. CT scanners are usually not calibrated in the upper HU range that covers bone. Consequently, CT images do not provide reliable quantitative information about the absolute bone density, which in turn reduces the reliability of the estimated speed-of-sound and acoustic attenuation. The uncertainty of these parameters affects mostly the simulated strength of the acoustic wave, while its relative spatial distribution seems to be more robustly estimated. In order to ameliorate this problem, some studies chose to use a spatially homogenous attenuation value for the skull that was either empirically adjusted to match the measurements, or – as this is not feasible for human applications – was based on literature values. Indeed, it seems that the best option so far is to base the simulations on linear mappings of the CT information to bone density and speed-of-sound that are adjusted for a scanner-specific upper reference point for compact skull, in combination

with using a homogenous skull attenuation. Literature values can be used for the purpose of fixing the reference point properties and attenuation, at the cost of losing part of the subject-specific information.

Besides their importance in the context of personalized tcFUS modelling and treatment planning / optimization, the presented results make it evident that particular care is needed when translating a modelling approach from one clinical site to another, as imaging conditions are likely to change.

Our findings also confirm that the transmitted acoustic wave is sensitive to small changes (1–2 mm, 2–3°) of the transducer position relative to the skull. When aiming to use acoustic simulations to inform personalized tcFUS applications, a precise control of the transducer placement is thus needed that seems to be at the limit of the accuracy provided by currently available neuronavigation systems.

Future progress would benefit from the use of CT scans that are calibrated and quantitative in the upper HU range, which can for example be achieved by using dual-energy scans. This would improve the comparability of simulation results across studies. Transferability would be further improved when controlling for the image smoothness caused by the reconstruction filter. Importantly, calibrated and standardized CT scans would also ensure that mapping functions between CT information and acoustic bone properties are not scanner-specific, but can be transferred between studies. Our results indicate that this is a key requisite for improving the reliability of CT-based estimates of the acoustic properties of the skull, in particular when aiming to also estimate the attenuation of the skull.

## 8.A APPENDIX

8.A.1 *Adjustment of CT noise levels*

The level of noise in a CT image does not only depend on the dose and the reconstruction filter, but also on the amount of absorbed X-rays by the scanned object and the surrounding background medium. CT scans of a human head will thus have more noise than a scan of the rather small sheep skull sample used here when keeping the scan settings unchanged. Therefore, we mimic the noise levels of human clinical- or low-dose CT images by adding gaussian noise to our images taken in a air background to re-create realistic patient scanning conditions. To do that, we considered the noise distribution in a region of interest (ROI) in the brain in a human CT image acquired at low-dose and with H60s reconstruction filter [294]. We first verified that the values in the ROI were normally distributed (Kolmogorov-Smirnov test), and added corresponding gaussian noise to the CT images of the sheep skull (air background). When two normally distributed random variables  $X$  and  $Y$  with variances of  $\sigma_x^2$  and  $\sigma_y^2$  are summed up, the sum  $Z$  has a variance which is the sum of the variances ( $\sigma_z^2 = \sigma_x^2 + \sigma_y^2$ ). In our case, we determined the variance in a ROI in the center of a human low-dose CT image (i.e., not involving skull and assuming that the values for brain and cerebrospinal fluid are close to water) and a ROI in a water glass in the CT data of the sheep skull sample (same CT parameters). We then adjusted the noise level of the sheep skull image by adding gaussian noise with a variance that corresponded to the difference between the variances of the human and sheep CT scans.

As we had no human CT scan with clinical dose available, we estimated the corresponding noise variance by comparing the variances in ROIs placed in water and in air of sheep CT scans with low versus clinical dose. The variance of the sheep CT scans with clinical dose was then adjusted accordingly by adding gaussian noise.

Dose	Filter	$\sigma$ [HU]
High	H60s	17.0
High	H48s	5.2
High	H41s	4.0
Low	H60s	171.0
Clinical	H60s	126.2
Low*	H60s	45.0
Clinical*	H60s	33.9

TABLE 8.4: HU standard deviations ( $\sigma$ ) in a water region of interest of  $100 \times 100$  pixels. Images were acquired at tube voltage 140 kV with varying doses (high, clinical, low) and smoothing filters (H60s, H48s, H41s). The rows marked with an asterisk refer to the original CT data without added noise.



## 8.A.2 Results figures

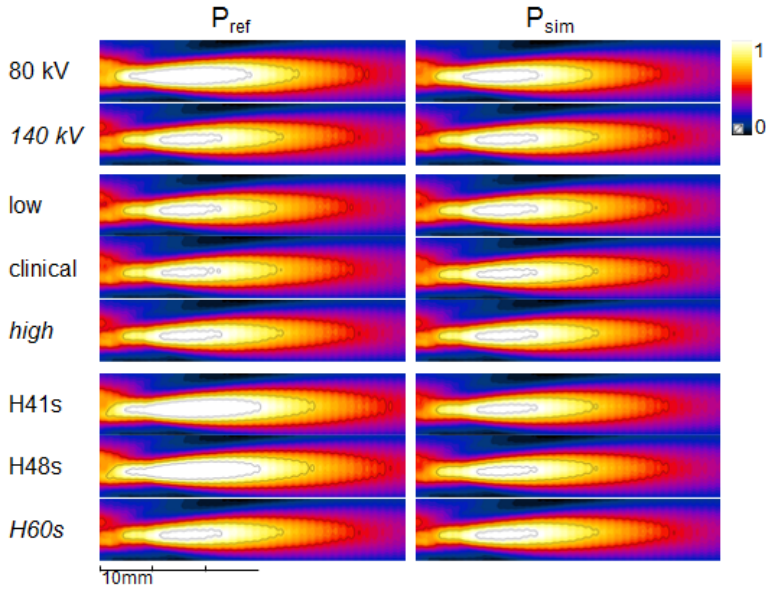


FIGURE 8.12: Assessment of the scan parameter impact on the intensity distribution shape (left: before normalization, right: after normalization to the case-specific deposited power). The same scale ranging from zero to the peak value in the measurement is used throughout. Isolines demark 50, 75, and 100% of that peak value.

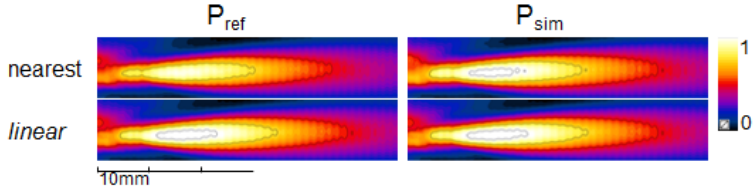


FIGURE 8.13: Same as in Figure 8.12, but for the different interpolation schemes for upsampling.

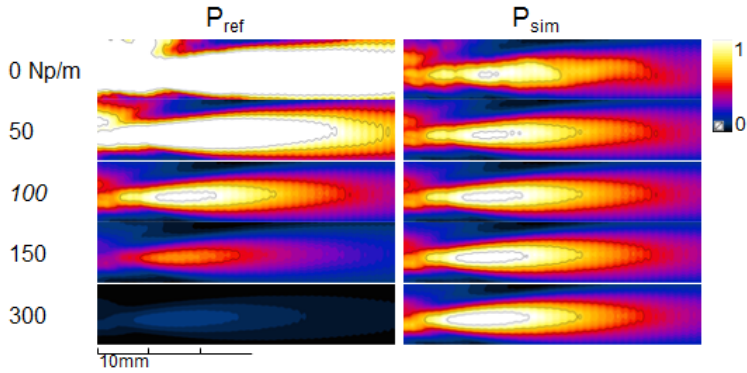


FIGURE 8.14: Same as in Figure 8.12, but for different homogeneous skull attenuation values.

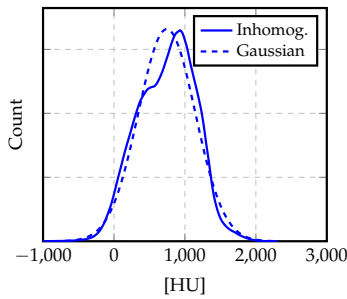


FIGURE 8.15: HU histogram of the skull, as well as fitted gaussian distribution used to investigate the impact of heterogeneity structure (as opposed to only the heterogeneity level) on transcranial sonication.

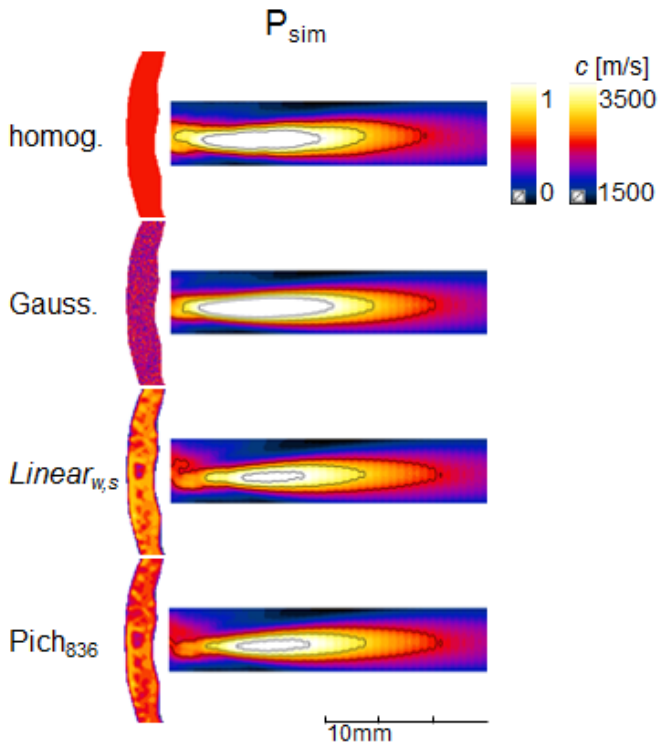


FIGURE 8.16: Impact of skull heterogeneity on the intensity distribution. The color map refers to the skull speed-of-sound distributions (intensity distributions are displayed as in the left columns of Figures 8.12–8.14).

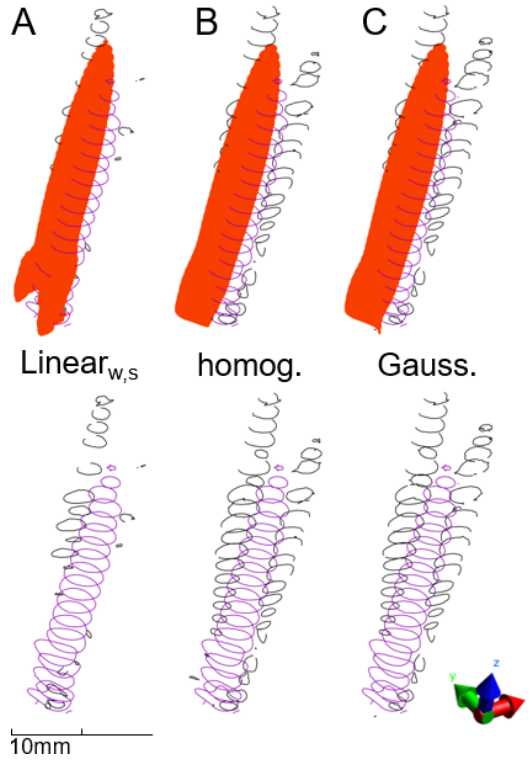


FIGURE 8.17: Impact of skull heterogeneity modelling on the focus shape and  $\gamma$ -distribution. See Figure 8.6 for an explanation of the different iso-contours and surfaces.

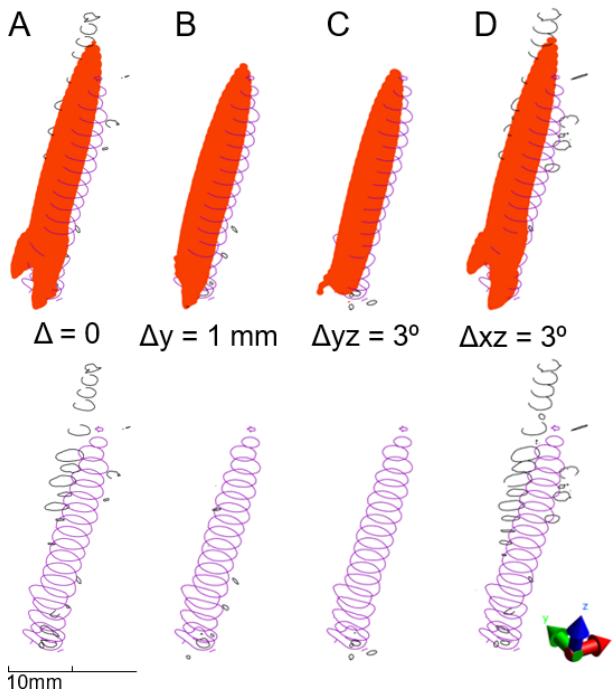


FIGURE 8.18: Same as in Figure 8.17, but with varying skull alignment.



## COUPLED ULTRASOUND-ELECTROPHYSIOLOGY-EEG MODELLING

---

### 9.1 BACKGROUND

It has been recently demonstrated that low intensity focused ultrasound (LIFUS) can stimulate neural activity non-invasively [10, 12, 113, 130, 132, 317, 318]. This is of high value for both therapeutic (stimulation, neuroprosthetics, etc.) and diagnostic (preoperative mapping, etc.) purposes. A multi-scale simulation platform for image-based and personalized modelling of transcranial LIFUS stimulation would be an important tool to support ongoing efforts in this research area. Such a platform would not only provide useful information during device development and the design of experiments, but also allow the performance of mechanistic studies, hypothesis formulation and testing, and, ultimately, personalized treatment planning, safety, and efficacy assessment of LIFUS.

In this chapter, a preliminary study is presented to illustrate how the research and results described in the previous chapters – combined with IT'IS research on the mechanisms of acoustic stimulation, as well as neural network dynamics and EEG modelling – can be used to achieve such (personalized) multi-scale LIFUS modelling. The presented model is highly speculative and greatly simplified, but it contains the building blocks and approaches that can be used to establish physics- and physiology-based modelling of acoustic neuromodulation to assess the impact of LIFUS on brain network function.

### 9.2 METHOD

#### 9.2.1 *Multi-scale model*

A multi-scale model was set up, ranging from the cell membrane-level to the head anatomy level (see Figure 9.1). On the macroscopic level, acoustic propagation in a transcranial LIFUS sonication setup targeting the cortex was simulated. A micro-scale model based on the NICE model for acoustic neuromodulation [193] was used to relate acoustic exposure to the result-

ing change in the spiking activity of specific neuron populations. On the mesoscopic level, cortical activity was simulated using a distributed neural mass model (NMM) approach [319]. This models populations as recurrent feedback and feedforward nodes of excitation and inhibition affecting population firing rates. Combining the macroscopic and mesoscopic levels allowed the simulation of the impact of acoustic exposure on cortical activity maps. In a last step, this neural activity information is combined with electromagnetic simulations on the macroscopic level to obtain virtual EEG traces.

### 9.2.2 *Anatomical head model*

Simulations were performed using the MIDA anatomical head model [258], a highly detailed (resolution  $< 0.5$  mm,  $> 160$  distinguished tissues and structures) computational head model implemented for computational life sciences applications (with a particular focus on neurostimulation applications). The model has been created based on extensive, high resolution MRI data, obtained from a healthy volunteer. The segmentation was performed based on various structural image data sets, with different contrasts to facilitate the detection of a large number of structures. In addition, DTI was performed, which permits to obtain information about the orientation of neural fibers in the brain, dielectric heterogeneity and anisotropy, as well as neural connection strengths (see Figure 9.2). The latter was particularly important for the generation of the cortical activity model (see Section 9.2.4).

### 9.2.3 *Acousto-neural interaction model*

**MODEL** Despite intense investigation in the past decade, the underlying mechanisms by which ultrasound waves interact with neural tissue at the cellular scale are still unclear. Several theories have emerged to try and explain this interaction. Among them, the Neuronal Intramembrane Cavitation Excitation (NICE) model [193] hypothesizes that ultrasound waves excite neurons through the complex interplay of two phenomena occurring at distinct time scales: (1) microsecond mechanical oscillations of 'bilayer sonophores' in the plasma membrane resonating at the ultrasound frequency, and (2) millisecond ion channel's gating transitions driving a progressive neuronal electrical response. This model provides quantitative predictions of cell-type-specific neural responses upon ultrasound exposure [320] that correlate indirectly with the results of numerous animal



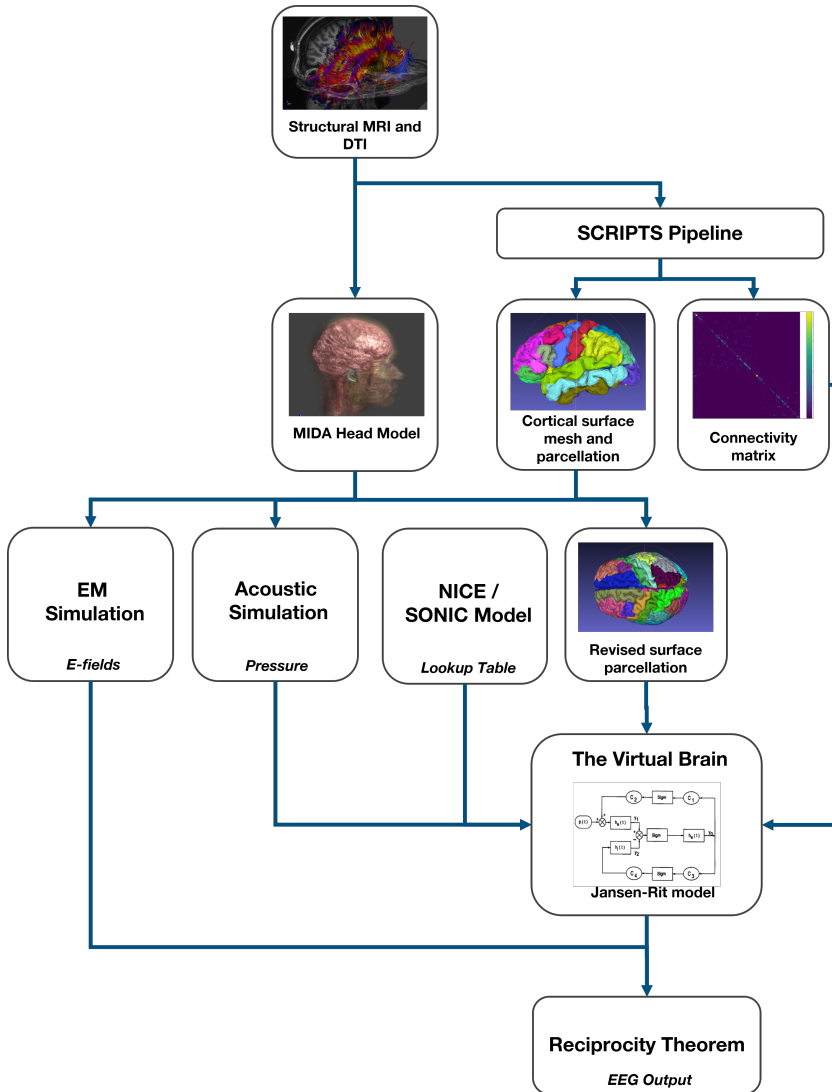


FIGURE 9.1: Schematic representation of the different processes and components involved in the multi-scale modelling of acoustic brain activity modulation and its impact on EEG.

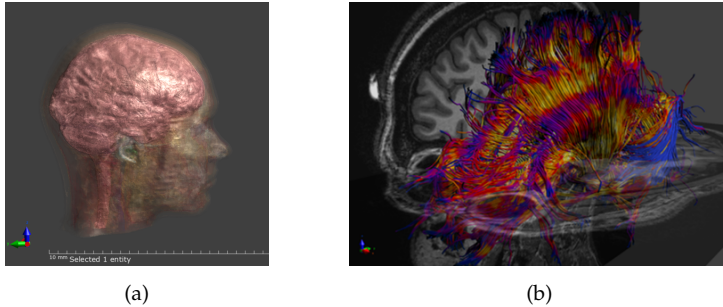


FIGURE 9.2: The MIDA head model (left), as well as underlying MRI image data and DTI tractography (right).

*in vivo* studies sonicating the central nervous system (CNS) [10, 11, 115, 317, 321, 322]. However, as it establishes a bi-directional link between mechanical membrane oscillations at the US frequency and the millisecond development of an electrical neural response, the NICE model effectively couples two dynamical systems evolving at significantly different time scales. As such, it is computationally expensive and difficult to interpret. Furthermore, the NICE model predicts a very singular membrane dynamics upon sonication that has not been directly observed experimentally, hindering a potential validation. Recently, a multi-Scale Optimized Neuronal Intramembrane Cavitation (SONIC) model has been proposed to alleviate those limitations [195]. It partly decouples the NICE model by integrating the coarse-grained evolution of effective electrical variables as a function of a pre-computed, cycle-averaged impact of the mechanical system. The SONIC model accurately reproduces cell-type-specific neural responses of cortical and thalamic neurons predicted by the full NICE model, while drastically reducing computational costs, thereby facilitating systematic explorations of dense parametric spaces and the study of connected neuron populations. Moreover, it offers an increased interpretability to the effects of ultrasonic stimuli in terms of effective membrane dynamics, which explains the predicted singular signature of ultrasound-triggered spikes compared to electrically induced and physiological spikes.

Based on the literature, we selected two point-neuron models of cortical neurons whose functional characteristics corresponded to those of the excitatory and inhibitory elements of the distributed neural mass model: a pyramidal, regular spiking (RS) excitatory neuron and an aspiny, fast spiking (FS) inhibitory interneuron [323]. Both neuron models are composed of

a fast voltage-gated sodium channel, fast and slow voltage-gated potassium sodium channels, as well as a passive leakage channel. They display very similar electrophysiological behaviors upon electrical stimulation, differing only in their firing rate adaptation to prolonged stimuli (enhanced for the RS neuron).

**SETUP** We used the SONIC model to measure the isolated neuromodulatory effect of continuous-wave ultrasound stimuli on each neuron type, for a wide range of post-synaptic states. To do so, the SONIC-neuron model was simulated for numerous combinations of ultrasound amplitudes (ranging from 0–600 kPa) and intracellular driving currents ( $Q$ , ranging from  $-300$ – $1000$  mA/m<sup>2</sup>) meant to represent excitatory or inhibitory input. For each combination, the model was simulated for 1000 ms, neural spikes were detected over the last 500 ms of stimulus delivery, and the resulting firing rate was stored in a two-dimensional lookup table. The necessary automation and evaluations were implemented using *Python* scripting. Look-up tables have been computed for continuous exposure and pulsed exposure (duty cycle: 25 %, pulse repetition rate: 100 Hz).

#### 9.2.4 Cortical oscillation model

**MODEL** A modified version of the Jansen-Rit model [319] was used to simulate the activity of a single cortical column. The Jansen-Rit model consists of three interacting populations, representing inhibitory interneurons, excitatory interneurons, and pyramidal cells, which together represent the activity of a single cortical column (see Figure 9.7). Both classes of interneurons synapse onto pyramidal cells, which in turn synapse onto the interneurons. The membrane potential of each population is determined by the convolution of an alpha function (representing delays and synaptic dynamics) and the firing rates of the inputs to the population. Membrane potentials ( $v$ ) are converted to a firing rate by a sigmoid function.

A network of coupled Jansen-Rit oscillators was implemented in order to represent activity across the entire cortical surface. From each node, an output, scaled by connectivity weight, is added to the excitatory interneuron inputs of the other nodes. We separate short-range and long-range inter-column connectivity. The short range connectivity from node  $m$  to node  $n$  is proportional to the difference between the membrane potentials of excitatory and inhibitory interneurons in node  $m$ ; long-range connectivity is proportional to the membrane potential of the pyramidal cells; the long-

# The NICE electromechanical model

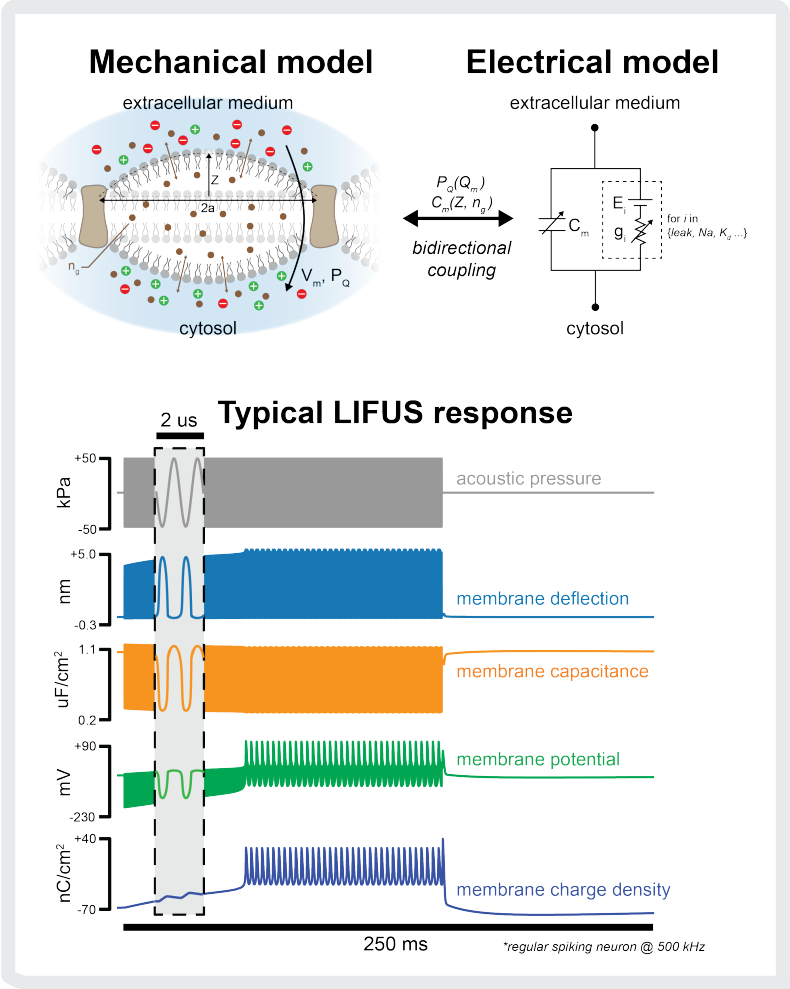


FIGURE 9.3: The sonophore cavitation (NICE) model of acoustic neuromodulation.

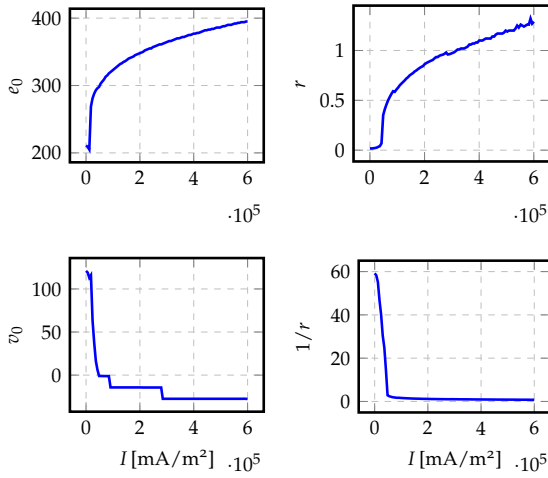


FIGURE 9.4: Pressure-dependence of the sigmoid parameters ( $v_0$ ,  $r$  and its inverse, and  $e_0$ ) for the RS neuron, as obtained through fitting.

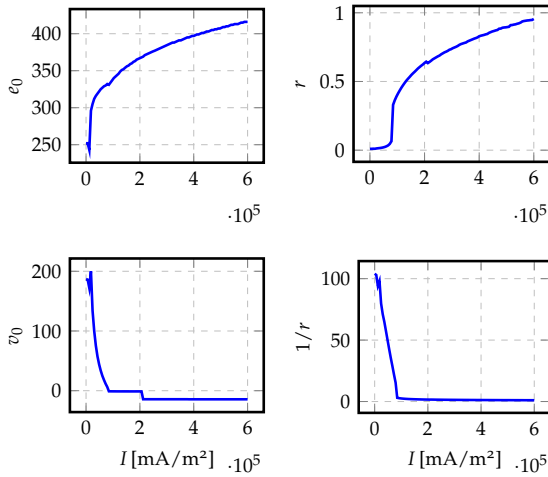


FIGURE 9.5: Pressure-dependence of the sigmoid parameters ( $v_0$ ,  $r$  and its inverse, and  $e_0$ ) for the FS neuron, as obtained through fitting.

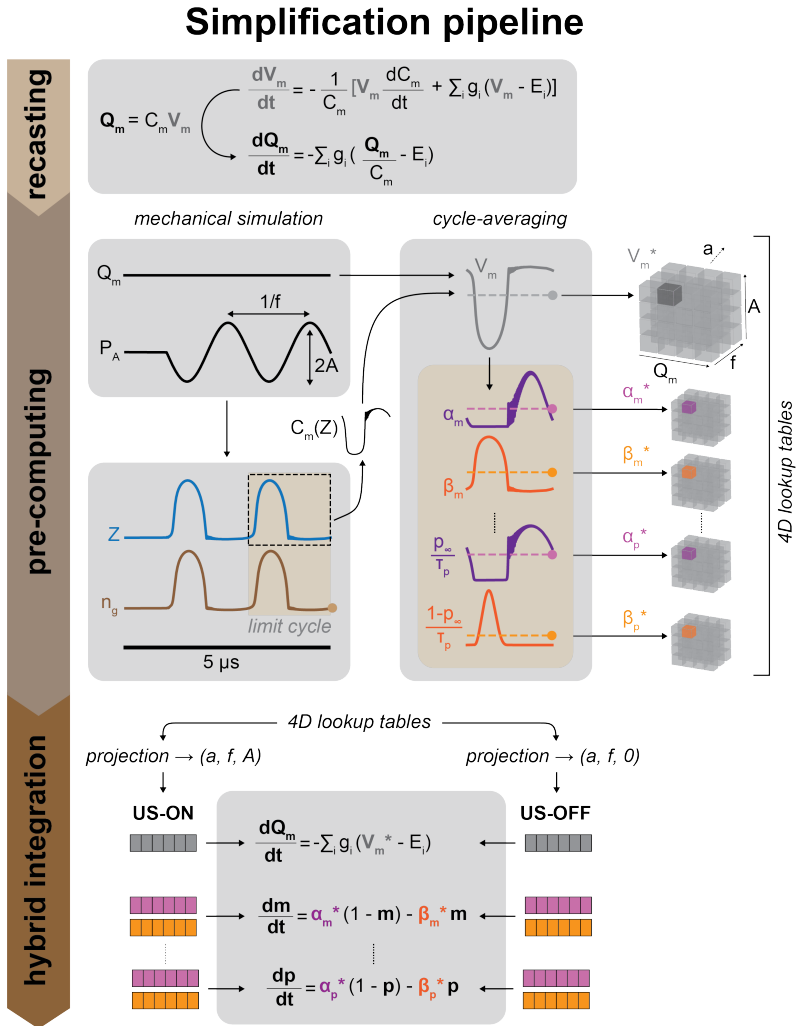


FIGURE 9.6: Principal steps for the derivation of the SONIC model from the NICE model [195]

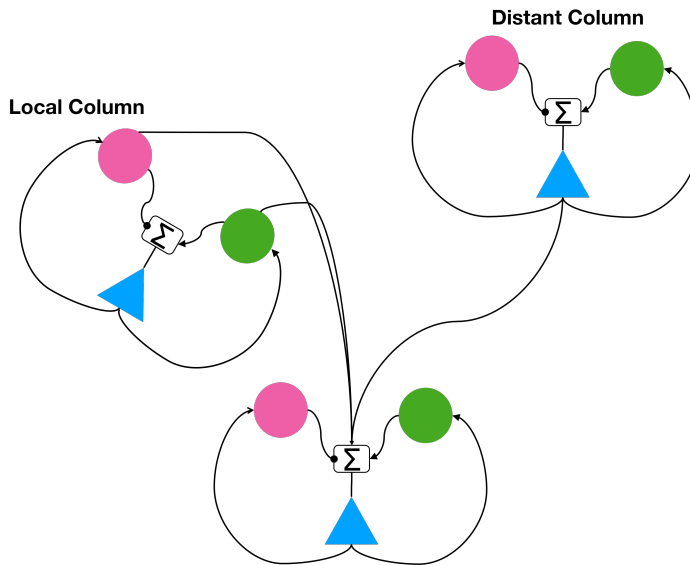


FIGURE 9.7: Schematic representation of the different neuron populations in the Jansen-Rit model. Three column models, each featuring three distinct neural populations (pyramidal cells, excitatory and inhibitory interneurons), as well as their short and long range connectivity are illustrated.

range, but not short-range, input to node  $n$  is delayed according to the spatial distance between nodes  $m$  and  $n$ .

Our model is therefore defined at each node  $n$  by the system of differential equations:

$$\begin{aligned}\dot{y}_0 &= y_3 \\ \dot{y}_3 &= Aas_0(y_1 - y_2) - 2ay_3 - a^2y + 0 \\ \dot{y}_1 &= y_4 + \frac{(0.5Aa(p_{max} - p_{min}))^2}{2}\sigma(t) \\ \dot{y}_4 &= Aa(\mu + a_2Js_{0,1} + c_n + l_n) - 2ay_4 - a^2y_1 \\ \dot{y}_2 &= y_5 \\ \dot{y}_5 &= Bb(a_4Js_{1,3}) - 2by_5 - b^2y_2\end{aligned}$$

The sigmoid functions which define the mapping from membrane potential to firing rate are given by the following relations:

$$s_j = \frac{2e_0}{1.0 + e^{r_j(v_{0j} - y_j)}}$$

$$s_{j,k} = \frac{2e_0}{1.0 + e^{r_j(v_{0j} - a_k l y_j)}}$$

Here,  $c_n$  and  $l_n$  are the  $n^{th}$  terms of the vectors  $\vec{c} = M_c \vec{y}'_0$  and  $\vec{l} = M_l (y_1 - \vec{y}_2)$ , where  $M_c$  and  $M_l$  are the long-range and short-range connectivity matrices,  $\vec{y}_j$  is the vector of values  $y_j$  from each node  $m$ , and  $\vec{y}'_0$  is the vector of values  $y_0$  from each node  $m$ , delayed by the distance between node  $m$  and node  $n$ .  $M_c$  is derived from DTI data as described below.  $M_l$  is defined according to a gaussian scaling function that depends on the spatial distance between nodes.  $\sigma(t)$  is a gaussian white noise input, which is scaled by a function of  $p_{min}$  and  $p_{max}$ , the minimum and maximum noise input rates used in [319].

**IMPLEMENTATION** A network of approximately 600,000 coupled Jansen-Rit neural mass models (NMM) was implemented in The Virtual Brain (TVB) [324]. A single cortical column NMM was positioned at each vertex of a cortical surface mesh derived from the MIDA head model [258]. In addition, single cortical NMMs were used to represent each subcortical region of the MIDA head model. Using SCRIPTS [325], a cortical surface mesh was generated, parcellated, and combined with a DTI-based inter-region connectivity map (obtained from original DTI data of the same



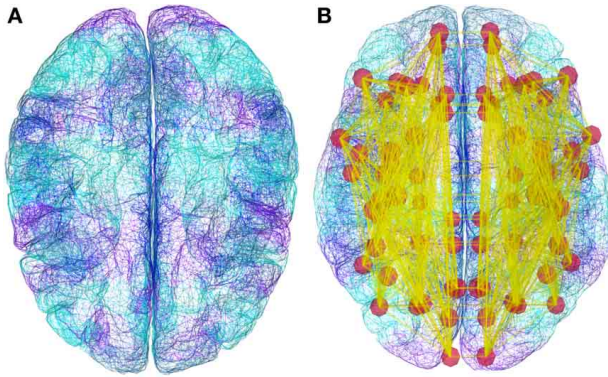


FIGURE 9.8: Illustration of neural-mass networks in TVB [39].

volunteer on whose MRI structural images the MIDA head model is based). The cortical surface mesh derived using the SCRIPTS pipeline was manually aligned to the mesh used in the acoustic simulation. The mesh used in the acoustic simulation was parcellated in accordance to the SCRIPTS mesh, using a nearest neighbor algorithm, and the parcellation information was injected in the TVB model (vertices parcellated as ‘unknown’ were assigned to ‘left cortex unknown’ or ‘right cortex unknown’ based on their position relative to the midline). Subcortical regions were positioned arbitrarily in space, distant from the cortex, such that their connectivity to cortical regions was defined entirely by the DTI-based inter-region connectivity map and not by anatomical geometry. This approach ensures that the computational model is consistently personalized with regard to both anatomical geometry and network connectivity.

For each node in the network, a current dipole proportional to the difference between the Jansen-Rit state variables  $y_1 - y_2$  (corresponds to post-synaptic potential) was computed, and aligned with the cortical surface normal. An EEG trace was calculated from the current dipoles using the reciprocity theorem [326] (described below in Section 9.2.7).

**SETUP** The inherent ambiguity of the connectivity scaling is resolved by rescaling connectivity matrices  $M_c$  and  $M_l$  to reproduce approximately the total input to each node in TVB’s pre-defined and published setup (in the absence of acoustic exposure).  $M_c$  was multiplied by the ratio between the average weight of the TVB default connectivity matrix and that of the connectivity matrix obtained from SCRIPTS, and by the ratio between the

number of nodes in the TVB example Jansen-Rit simulation (76) and the number of nodes the present simulation (to compensate for the much larger number of simulated cortical nodes). As the TVB Jansen-Rit simulation did not include local connectivity,  $M_I$  was scaled by  $2^{-10}$  (as found in a published TVB simulation for a different NMM) and by the node number ratio. As described in Section 9.2.6, the values  $r_j$ ,  $e_{0_j}$  and  $v_{0_j}$  are made local pressure dependent, as described below (distinguishing between excitatory and inhibitory cell types). Thus, values of  $r$ ,  $e_0$  and  $v_0$  are identical for pyramidal cells and excitatory interneurons. At zero acoustic pressure, the parameterized, pressure-dependent sigmoid parameters are identical to those previously published in the absence of exposure and they are identical for the inhibitory and excitatory populations. Numerical values for all parameters are given in Table 9.1.

### 9.2.5 *Acoustic propagation model*

**MODEL AND IMPLEMENTATION** As in Chapters 7–8, the FDTD implementation of the linear acoustic pressure wave equation (LAPWE) from *Sim4Life* was used to simulate acoustic exposure. It considers heterogeneity-related scattering and employs anisotropic, adaptive, rectilinear meshes (voxels) for discretization.

**SETUP** For consistency and to allow straightforward mapping from the acoustic propagation model to the distributed cortical oscillation model, the MIDA head model was also used for the acoustic simulations. Image-based skull heterogeneity modelling was not possible due to the absence of CT data for the MIDA model. Therefore, only cortical and cancellous bones could be distinguished. Tissue properties were assigned according to the IT'IS tissue properties database [155], which includes dispersive relationships for acoustic properties of a large number of tissues, that have been carefully curated based on an extensive literature review.

The exposure model was based on [12] and [272]. Transducer placement was done as in [12], with the transducer normal to the skull surface and at a comparable distance (see Figure 9.9), targeting the left primary somatosensory cortex ( $S_1$ ). A single element focused transducer (SEFT) with 30 mm aperture and curvature operating at 500 kHz was modelled (as in [12]). The SEFT was driven at a constant pressure of 1 MPa, and the output field subsequently scaled to the desired peak pressure value in the skull.

The simulation domain is large enough to encompass the entire brain region of the MIDA head model, the acoustic transducer, as well as the structures in between. A high resolution grid of 0.1 mm (30 points per minimum wavelength) was used in a domain of  $40 \times 40 \times 50 \text{ mm}^3$  comprising the transducer and its geometric focus. The rest of the grid was discretized at a resolution of 0.2 mm (15 points per minimum wavelength). The total grid size was 812 MCells. Simulation was performed in continuous wave mode and over a sufficient amount of periods to reach convergence. PML boundary conditions were used at the boundaries and no reflections were observed.

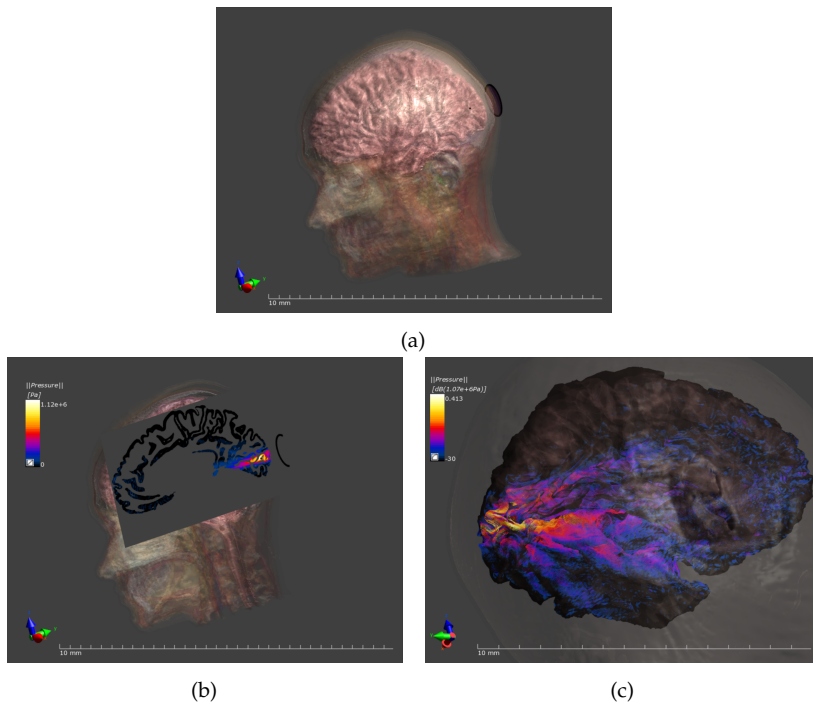


FIGURE 9.9: Visualization of the pressure distribution resulting from tcFUS sonication using a SEFT.

### 9.2.6 Coupling

**MODEL** The integration of pressure-modulation of neural activity in the cortical oscillation model was achieved on the level of the sigmoid functions that translate the average membrane potential ( $v$ ) of a neuronal sub-population to its average spiking frequency  $f$  according to:

$$f(v) = \text{Sigm}(v; e_0, v_0, r) = 2e_0 / (1 + e^{r(v_0 - v)})$$

This transformation had to be extended to consider the local LIFUS exposure:  $f(v, p, s)$ , where  $p$  is the acoustic pressure and  $s$  stands for the pulse form (e.g., duty cycle (DC), pulse repetition frequency (PRF)). The following steps and assumptions were made for that purpose:

- It is assumed that a linear relationship between the average postsynaptic membrane potential (PSP) and the injected current  $Q$  exists. This is a reasonable assumption while the transmembrane voltage is in a range where leakage current dominate. Once the non-linear active channels become relevant, their effective contribution will quickly dominate over the PSP contribution.
- It is further assumed that the average population action potential density is proportional to the spiking frequency of a single neuron with a membrane potential similar to the average membrane potential of the population.
- Finally, based on the observed behavior, to avoid strong modifications to the TVB Jansen-Rit implementation, and for simplicity reasons, it is assumed that  $f(v, p, s) = \text{Sigm}(v; e_0(p, s), v_0(p, s), r(p, s))$ . This is not a fundamental assumption and could be generalized rather easily.
- Therefore, first the  $f_Q(Q; p, s)$  curves were fitted with sigmoids to obtain  $e_{0,Q}(p, s)$ ,  $v_{0,Q}(p, s)$  and  $r_Q(p, s)$ .
- $e_0(p, s)$ ,  $v_0(p, s)$  and  $r(p, s)$  were then obtained through the transformations  $e_0(p, s) = e'_{0,Q}(p, s) \frac{e_0}{e'_{0,Q}(0, s)}$ ,  $r(p, s) = r'_{Q}(p, s) \frac{r}{r'(0, s)}$ , and  $v_0(p, s) = v_0 + \frac{r}{r'(0, s)} (v'_{0,Q}(p, s) - v'_{0,Q}(0, s))$ . These transformations reflect the linearity assumptions above and ascertain that the original Jansen-Rit parameterization is obtained in the absence of acoustic exposure.

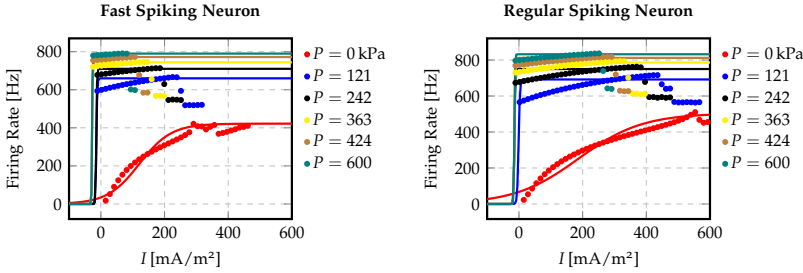


FIGURE 9.10: Illustration of the sigmoid fitting to the injected current-dependent spiking frequencies of the FS (left) and RS (right) neurons.

**IMPLEMENTATION** The sigmoid fits of the  $f_Q(Q; p, s)$  were performed in Scipy [256, 257] with the `curve_fit` function using the `dogbox` method, and look-up tables (NumPy arrays) for  $e_{0,Q}(p, s)$ ,  $v_{0,Q}(p, s)$  and  $r_Q(p, s)$  were produced. The acoustic pressure field was interpolated at the locations of the cortical-column NMMs. In the TVB implementation of the Jansen-Rit model, the pressure distribution calculated from the acoustic simulation was imported and scaled. For each node, values of  $e_{0,Q}(p, s)$ ,  $v_{0,Q}(p, s)$  and  $r_Q(p, s)$  were interpolated based on the pressure at the corresponding node.

### 9.2.7 EEG computation

**MODEL** EEG traces resulting from the transient current dipole activities in the cortex are computed using the reciprocity theorem [326]. The reciprocity theorem provides a relation between the potential difference ( $V$ ) of an electrode pair originating from an electric dipole ( $\vec{d}$ ) and the electric field ( $\vec{E}$ ) at the dipole location originating from a current ( $J$ ) injected through the electrode pair:  $J \cdot V = -\vec{d} \cdot \vec{E}$ . It allows to efficiently compute transient electrode voltages at an electrode pair from a given set of distributed dipole activities (obtained in this study from the cortical network NMM) and a single simulation of the  $E$ -field distribution resulting from the application of a current to that electrode pair.

**IMPLEMENTATION** The reciprocity theorem-based computation of transient electrode voltage was implemented using *Sim4Life's Python* scripting functionality. The EEG trace is the sum of the dot products of each current dipole and the  $E$ -field at the corresponding point on the cortical surface.

**SETUP** Square-shaped electrodes (diameter: 12.5 mm) with rounded corners were positioned on the MIDA head model according to the 10–20 system and  $E$ -field maps for electrode pairs were computed using the *Sim4Life* ohmic-current dominated electro-quasistatic solver (structured rectilinear grid with  $(x, y, z)$  mesh resolution ranging from (0.47, 0.42, 0.45)–(1.8, 1.95, 11.75) mm; tissue properties assignment based on the low-frequency conductivity values from [155]; Dirichlet boundary conditions at the electrodes and insulating boundary conditions at the head surface). The applied current at an electrode was computed by applying the flux-integration functionality of *Sim4Life* to a box surrounding the electrode and the current density distribution  $\mathbf{J}$ .

### 9.3 RESULTS AND DISCUSSION

**ACOUSTIC EXPOSURE** Figure 9.9 illustrates the predicted acoustic exposure of the cortex. The distribution is in good qualitative agreement with the focus location, extent, and intensity from [12]. The focus is located in the S1 area of the cortex, and has a length / diameter of of 17/4 mm (quantified by looking measuring the half-peak isosurface inside the skull). The pressure can be flexibly scaled (linearly) to mimic different exposure strengths, as non-linear effects do not matter at the investigated LIFUS intensities.

**SIGMOID PARAMETERS** Figures 9.4–9.5 show the pressure dependence of the sigmoid parameters. As the pressure increases, the sigmoidal transitions (inversely proportional to  $r$ ) become much sharper and resulting in near-instantaneous transitions (on-off switch). The peak firing rates (proportional to  $e_0$ ) of the inhibitory and excitatory populations increase and firing starts at increasingly low membrane voltages. The pressure sensitivity of FS neurons is stronger than that of RS neurons, such acoustic exposure strengthens the inhibitory populations at lower acoustic intensities than the intensities required to further activate the excitatory populations.

**SINGLE COLUMN ACTIVITY** To get a better understanding of the response of the cortical network model building blocks – the cortical column NMM – simulations have been performed that feature a single, decoupled column exposed to pressures ranging from 0–10 kPa. No stochastic noise is added, to get a unperturbed picture of the temporal dynamics. Two interesting transitions are observed: In the absence of pressure, the Jansen-Rit model has a well known resonance around 10 Hz. As the pressure increases,

that single resonance frequency shifts slightly downwards. Subsequently, additional resonances appear at what seem to be multiples of half of the principal resonance frequency. As the pressure increases further, oscillations are suppressed and a flat plateau is observed (see Figure 9.10).

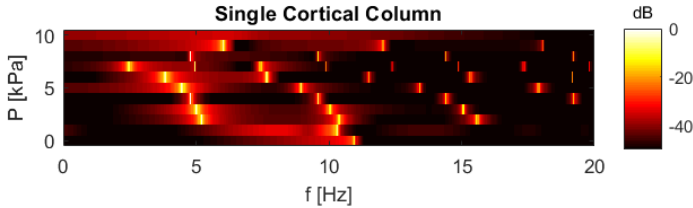


FIGURE 9.11: Pressure dependence of the frequency spectrum of the noise-less single-column Jansen-Rit model.

**CORTICAL NETWORK ACTIVITY** Figure 9.12 illustrates selected spectra of  $y_2 - y_1$  for a range of nodes in the network. The frequency domain power spectra for different regions are shown. The spectra of nodes corresponding to the same cortical region (from the parcellation) are averaged to statistically reduce noise. The overall average of the spectra of all nodes is also shown in Figure 9.12 for a range of pressures. Similar behavior as for the single column is observed. In the absence of acoustic exposure, a single, well defined peak around 10 Hz is observed (at a slightly lower frequency than the single column resonance). With increasing pressure additional peaks at half that frequency and multiple thereof appear. In the regional spectra, these additional peaks are only prominent in exposed regions (e.g., left cuneus), as well as regions with strong connections to exposed regions (e.g., parahippocampal gyrus).

**EEG** The computed EEG traces and spectra are shown in Figure 9.13. They still show the same resonance frequencies, but the peaks are not as distinct anymore. Instead, they feature broad tails. As the EEG traces are weighted averages of the individual dipole traces (due to the linearity of Maxwell's equations), which all show much more distinct peaks in their regionally averaged spectra, that difference is unexpected. The likely explanation is the averaging spectra – as performed for the regional spectra – hides correlations between the individual contributions, whereas computation of the spectrum of an average – as performed for the EEG – conserves

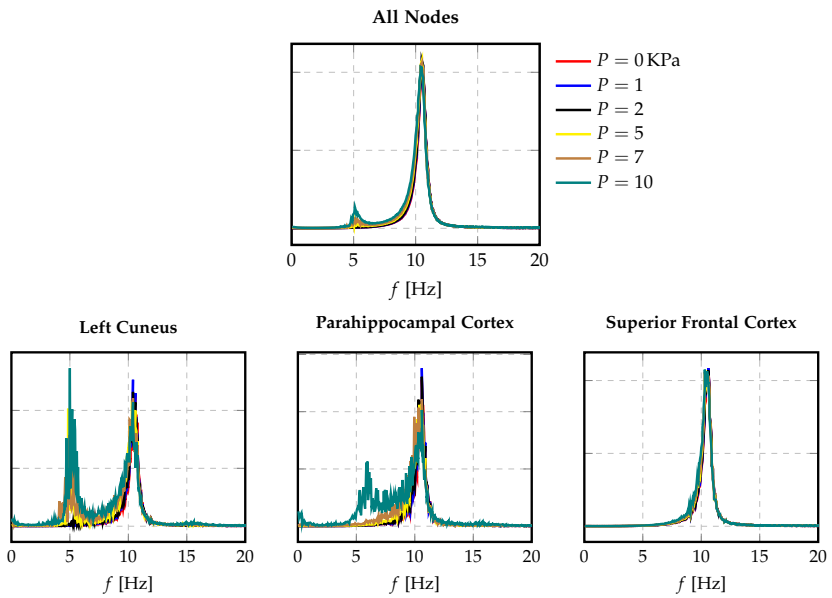


FIGURE 9.12: Averaged spectra of all nodes of the cortical model and of the nodes in the 'Left Cuneus' region, the 'Parahippocampal Gyrus' region, and the 'Frontal Cortex' region at different exposure levels (peak pressure).



correlations. The coupling of correlated dipoles appears to induce a broader range of frequencies in the averaged behavior.

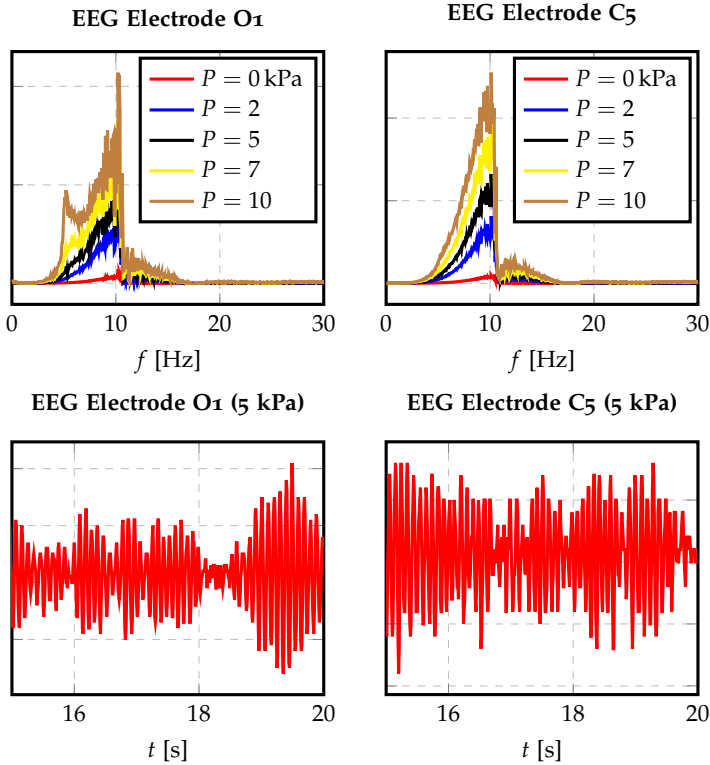


FIGURE 9.13: Trace of the EEG at C5, as well as spectra at C5 and O1 for different exposure levels (peak pressure).

### 9.3.1 Limitations

In addition to the limitations inherent to the EM, acoustic, NICE / FOCUS, and NMM modelling (discussed throughout this thesis, as well as in the relevant literature), additional assumptions and limitations apply to the specific multi-scale model setup:

- It is assumed that the RS and FS neurons are representative of the inhibitory, excitatory, and pyramidal neuron populations. A similar assumption has been made by [320].

- It is assumed the the averaged membrane potential of a neuronal subpopulation can be linearly mapped to input current to obtain a pressure dependent spiking frequency.
- It is assumed that the average membrane potential dependence of spiking frequency can be approximated by a sigmoid, as it is commonly done in NMMs, across all the relevant pressure range.
- The scaling of the local and global connectivity matrices is set somewhat arbitrarily. While the raw matrices are based on subject-specific MRI, the connectivity strengths are scaled by the default prefactors used in TVB, adjusted for the increased number of nodes in our network relative to the TVB default. While this is likely to produce reasonable results, the default connectivity strengths used had not been previously confirmed to be appropriate for a Jansen-Rit model. In the future, a full bifurcation analysis should be performed on the connectivity strengths. In addition, while delays between brain regions are based on DTI tract lengths, conduction speed is assumed to be uniform throughout the brain.
- Our model does not accurately model the behavior of subcortical regions, instead treating each subcortical region as a single cortical NMM. We also assume that the parcellation of the cortical surface obtained through the SCRIPTS pipeline can be projected to the MIDA mesh using a nearest-neighbor algorithm. The projection of the data from the SCRIPTS pipeline to the MIDA mesh inadvertently led to the creation of an 'extra' cortical region consisting of two vertices. As this region is spatially distant from the rest of the mesh, and has no long-range connectivity to any other region, it is not expected to influence the behavior of the model.

#### 9.4 CONCLUSIONS

A prototype multi-scale framework for the computational investigation of LIFU neuro-stimulation was developed. It enables personalized, image-based modelling and combines microscale modelling of neural membrane sonophore cavitation (a mechanistic model for acoustic neuromodulation), effective single neuron dynamics, cortical network NMM, and macroscopic acoustic and EM propagation modelling in realistic anatomical models to compute EEG traces.

The multi-scale model is an important step towards the goal of allowing mechanistic studies, hypothesis formulation and testing, device development, and, ultimately, personalized treatment planning, safety, and efficacy assessment.

The proposed multi-scale modelling approach can be easily extended, for example, to incorporate other neuronal dynamics models than the RS and FS neurons (extension to multi-compartmental models is more challenging, but feasible), to employ more realistic network models, as well as to more accurately model acoustic propagation (e.g., if image-based skull heterogeneity information is available).

The presented prototype multi-scale model relies on a large number of simplifying assumptions that should be carefully investigated and refined in future research work. The experimentally measurable EEG signals will be valuable for validation of the computational model, as they can be readily obtained and compared with model predictions.

## 9.A APPENDIX

9.A.1 *Tables and figures*

Parameter	Value
A	3.25 mV
a	0.1 1/ms
$p_{\min}$	0.12 1/ms
$p_{\max}$	0.32 1/ms
$a_1$	1.0
$a_2$	0.8
$a_3$	0.25
$a_4$	0.25
$\mu$	0.22
J	135
B	22 mV
b	0.05 1/ms
$e_{0,\text{Zero-Pressure}}$	0.0025 1/ms
$r_{\text{Zero-Pressure}}$	0.56 1/mV
$V_{0,\text{Zero-Pressure}}$	6 mV

TABLE 9.1: Values of the different cortical model parameters.

## CONCLUSIONS

---

The work performed in this thesis focuses on computational modelling of neuromodulation by EM or LIFUS exposure that is typically applied for therapeutic purposes. In addition to establishing requirements for reliable treatment modelling and planning, the simulation approaches have also been validated experimentally, principal uncertainty contributors have been identified, mechanistic insights have been gained, a novel treatment optimization approach has been established, and the developed framework has been applied to a range of clinical applications. This includes contributing to the development of spinal-cord stimulation for the restoration of locomotion of paraplegics.

Many of the issues and shortcomings that were identified within the critical review of the current state of research (such as going beyond physical exposure quantification to assess physiological impact, avoiding oversimplification, performing careful verification, validation, sensitivity analyses, and uncertainty quantification, developing personalized modelling for precision medicine, and reducing the difficulty for researchers to implement hybrid modelling pipelines; see Section 2.3) have been addressed in this thesis, and important contributions to resolving them have been made. This chapter summarizes the main achievements and proposes potential future research directions.

### 10.1 ACHIEVEMENTS

- Modelling framework
  - The *Sim4Life* platform, which already included extensive functionality for modelling EM fields and acoustic propagation in complex anatomical environments as well as EM-induced neuromodulation, has been successfully extended. Specifically, the functionality required to realistically and reliably simulate EM and acoustic neuromodulation applications has been added.
  - One important extension of the *Sim4Life* platform concerns the addition of tissue heterogeneity support. This includes image-based heterogeneity, which provides a high degree of realism, as

well as the option of personalizing simulations. Heterogeneity support has been added to the acoustic solver to support, e.g., CT-based skull heterogeneity modelling, as well as to a range of EM-solvers, e.g., to support DTI-based conductivity maps.

- Another important extension of the *Sim4Life* platform relates to the support for anisotropic (tensorial) electrical conductivity. The significance of considering neural tissue anisotropy is demonstrated in great detail in the context of SCS in this thesis, and a mechanistic explanation for the non-trivial behavior in terms of activating functions has been developed.
- Furthermore, the *Sim4Life* acoustic solver has been extended to offer multi-GPU acceleration that allows detailed simulations to be performed within an acceptable time frame thanks to a speed boost by two orders of magnitude. The extended solver also includes a large variety of boundary conditions, non-sinusoidal user-defined sources, as well as numerical enhancements to increase the stability of non-linear simulations (required to study frequency mixing, higher harmonics formation, and dispersive attenuation).
- All these extensions have been carefully validated (analytically and against numerical benchmarks) and stability analyses have been performed. This is required to provide the reliability (and the related confidence in the models) needed for life-sciences applications.
- The use of the simulation framework in a range of high-impact therapeutic and exposure safety applications has been demonstrated. This includes applications in neuroprosthetics (device development and treatment optimization for the restoration of locomotion of paraplegics, as part of the RESTORE collaboration), SCS for pain relief, and tCFUS modelling (e.g., for LIFUS neurostimulation).
- Experimental validation of coupled EM-neuro modelling
  - In addition to the careful verification of the newly developed simulation functionality, experimental validation has been performed to ascertain the suitability of the EM-neuro interaction modelling approach.
  - Successful experimental validation in the context of retinal prosthetics has not only provided validity evidence supporting the

model and modelling approach, but also resulted in an understanding of the three different mechanisms that can be involved in electric stimulation of alpha retinal ganglion cells. These new insights are very valuable as they can help, e.g., with the design of improved neuroprosthetic devices for the visually impaired.

- For that purpose, the first computational ganglion cell models using electrophysiological and cell-morphological data from the same cell (per model) have been generated, assuring cell model consistency. The observed variability between cells indicates the necessity for building cell specific models, rather than combining measurements obtained from different cells.
  - The retinal stimulation study (conducted jointly with the FDA) has also been used to demonstrate how careful uncertainty quantification in the context of EM-neuromodulation modelling can be performed. This is of particular importance as the work helps to establish the basis for regulatory-grade neurostimulation modelling.
  - Further validity evidence is currently being gathered in the context of the RESTORE project by comparing computational predictions with experimental data from patients that have been treated using simulation-based treatment planning and optimization.
- Activation function
    - The predictive value of the activation function concept has been studied in two clinically important neurostimulation applications: SCS for pain-relief and DBS.
    - It was demonstrated that this concept not only provides tractability to stimulation selectivity and the impact of different tissues and their properties on stimulation thresholds, but also has quantitative predictive value.
    - This has been exploited to develop a new stimulation parameter optimization approach that is capable of increasing the stimulation selectivity. The approach is superior to simple *E*-field optimization as it uses a functional which directly relates to an electrophysiologically meaningful quantity. At the same time it retains the advantages of *E*-field optimization by not requiring computationally costly neuronal dynamics simulations (acceleration by more than three orders of magnitude). Exploitation

of linearity can further accelerate optimization, resulting in an approach capable of optimizing selectivity by controlling the voltage or current of a large number of electrode contacts.

- The activation function-driven optimization has been used to achieve superior focusing and steerability in a computational model of SCS for pain therapy, permitting the targeting of selected dermatomal zones.
  - On that basis, a new approach for pulse-shape optimization has also been proposed.
  - The limitations of the activation function approach for very localized sources (producing narrow activation function peaks) have been investigated.
- Transcranial FUS modelling and experimental validation
    - The extended simulation framework has been applied to tcFUS applications, which is a recently introduced attractive approach to non-invasive neural modulation.
    - Careful investigations of the correct modelling of acoustic transducers and of the complex structured skull have been performed. These investigations have been experimentally validated, using *ex vivo* tcFUS hydrophone measurements (with explanted skulls from different species), and complemented by extensive sensitivity and uncertainty assessment.
    - The importance of modelling the physics and internal structure of transducers to reliably predict tcFUS has been demonstrated, and commonly applied approaches have been shown to be unsuitable.
    - The critical impact of standing waves in the skull has been established, which primarily affects focus intensity.
    - Consideration for the heterogeneous nature of the skull has been found to be crucial for the reliable prediction of tcFUS (intensity and distribution). Not only the degree of heterogeneity, but also its structure. This makes it necessary to use personalized models, established based on patient image data (CT). However, the details of the imaging parameters have an important impact on the HU-to-acoustic-parameters mapping functions, such that site-specific calibration is necessary and translation of modelling approaches between clinics can be complicated.



- The high sensitivity to transducer positioning errors has been confirmed. Clinically suitable approaches are needed to ensure reliable reproduction of the treatment planning setup during the treatment administration.
- Multiscale modelling of tcFUS neuromodulation
  - A first multi-scale model of acoustic neuromodulation of brain rhythms has been established which combines macroscale modelling of tcFUS exposure and the generation of EEG signals from cortical activity maps (using a novel, reciprocity theorem-based approach), mesoscale modelling of pressure modulated brain network activity, and microscale modelling of a promising mechanistic model for acousto-neuron interaction.
  - The modular design of this multi-scale model readily permits extension, e.g., by more realistic brain network models.
  - The implemented pipeline supports models that are personalized with regard to anatomy, tissue properties, and network connectivity.

## 10.2 NEXT STEPS AND FUTURE RESEARCH

Considering the needs of the scientific and medical communities, the following next steps and future research directions should be considered:

- The work performed on tcFUS should be extended to cover anatomical inter-subject and inter-species variability and age effects. It should also be generalized to more transducer types.
- The developed activation function-based optimization approach is expected to be of high value in optimizing stimulation selectivity in the area of bioelectronic medicine and neuroprosthetics. It should particularly be applied to the problem of selectively stimulating certain spatially or electrophysiologically distinct fiber populations within complex, fascicular nerve structures.
- While important contributions to establishing verification and validation approaches for regulatory grade neurostimulation modelling have been made, they principally focus on the impact of exposure uncertainty on the electrophysiological response; they do not yet address the question of electrophysiological uncertainty. This problem is

hard to solve as even the equations used to describe neuronal activity are only mathematical approximations to capture the extraordinarily complex underlying physics.

- Extensive, application-specific *in vivo* validation is required. This is particularly true for cases when predictions on physiological responses are made (such as neuromuscular, behavioral, or EEG responses). Some validation effort is ongoing in the context of the RESTORE project on restoring locomotion to paraplegics, where *in vivo* electrophysiology and motor-response measurements are being carried out.
- The multi-scale model of acoustic brain-activity modulation presented in the last chapter is strongly simplified and includes a wide range of assumptions. The model is flexible and can easily be extended, but further research is required before this promising approach can yield meaningful predictions.

## BIBLIOGRAPHY

---

1. Dobkin, B. H. Strategies for stroke rehabilitation. *The Lancet Neurology* **3**, 528 (2004).
2. Gybels, J. M. & Sweet, W. H. Neurosurgical treatment of persistent pain (1989).
3. Marangell, L. B., Martinez, M., Jurdi, R. A. & Zboyan, H. Neurostimulation therapies in depression: a review of new modalities. *Acta Psychiatrica Scandinavica* **116**, 174 (2007).
4. Gross, R. E. & Lozano, A. M. Advances in neurostimulation for movement disorders. *Neurological research* **22**, 247 (2000).
5. Wagner, T., Valero-Cabre, A. & Pascual-Leone, A. Noninvasive human brain stimulation. *Annu. Rev. Biomed. Eng.* **9**, 527 (2007).
6. Perlmutter, J. S. & Mink, J. W. Deep brain stimulation. *Annu. Rev. Neurosci.* **29**, 229 (2006).
7. Kent, A. R., Min, X., Rosenberg, S. P. & Fayram, T. A. *Computational modeling analysis of a spinal cord stimulation paddle lead reveals broad, gapless dermatomal coverage in Engineering in Medicine and Biology Society (EMBC), 2014 36th Annual International Conference of the IEEE (2014)*, 6254.
8. Capogrosso, M., Wenger, N., Raspopovic, S., Musienko, P., Beauparlant, J., Luciani, L. B., Courtine, G. & Micera, S. A computational model for epidural electrical stimulation of spinal sensorimotor circuits. *Journal of Neuroscience* **33**, 19326 (2013).
9. Wagner, F. B., Mignardot, J. B., Le Goff-Mignardot, C. G., Demesmaeker, R., Komi, S., Capogrosso, M., Rowald, A., Seáñez, I., Caban, M., Pirondini, E., Vat, M., McCracken, L. A., Heimgartner, R., Fodor, I., Watrin, A., Seguin, P., Paoles, E., Van Den Keybus, K., Eberle, G., Schurch, B., Pralong, E., Becce, F., Prior, J., Buse, N., Buschman, R., Neufeld, E., Kuster, N., Carda, S., von Zitzewitz, J., Delattre, V., Denison, T., Lambert, H., Minassian, K., Bloch, J. & Courtine, G. Targeted neurotechnology restores walking in humans with spinal cord injury. *Nature* **563**, 65 (2018).

10. King, R. R. L., Brown, J. R. J., Newsome, W. W. T. & Pauly, K. K. B. Effective parameters for ultrasound-induced in vivo neurostimulation. *Ultrasound in Medicine and Biology* **39**, 312 (2013).
11. Yoo, S. S., Bystritsky, A., Lee, J. H., Zhang, Y., Fischer, K., Min, B. K., McDannold, N. J., Pascual-Leone, A. & Jolesz, F. F. A. Focused ultrasound modulates region-specific brain activity. *NeuroImage* **56**, 1267 (2011).
12. Legon, W., Sato, T. F. T., Opitz, A., Mueller, J., Barbour, A., Williams, A. & Tyler, W. J. W. Transcranial focused ultrasound modulates the activity of primary somatosensory cortex in humans. *Nature Neuroscience* **17**, 322 (2014).
13. Elias, W. J., Huss, D., Voss, T., Loomba, J., Khaled, M., Zadicario, E., Frysinger, R. R. C., Sperling, S. S. A., Wylie, S., Monteith, S. S. J., Harrison, M., Wintermark, M., *et al.* A pilot study of focused ultrasound thalamotomy for essential tremor. *New England Journal of Medicine* **369**, 640 (2013).
14. Robertson, J., Martin, E., Cox, B. & Treeby, B. E. Sensitivity of simulated transcranial ultrasound fields to acoustic medium property maps. *Physics in Medicine and Biology* **62**, 2559 (2017).
15. MedTech, Z. M. T. Z. *Sim4Life 5.0 User Manual* (ZMT Zurich MedTech, Zurich, Switzerland, 2019).
16. Rattay, F. The basic mechanism for the electrical stimulation of the nervous system. *Neuroscience* **89**, 335 (1999).
17. Kyriakou, A. *Multi-Physics Computational Modeling of Focused Ultrasound Therapies* PhD thesis (ETH Zürich, 2015).
18. Benabid, A. L., Pollak, P., Louveau, A., Henry, S. & De Rougemont, J. Combined (thalamotomy and stimulation) stereotactic surgery of the vim thalamic nucleus for bilateral parkinson disease. *Stereotactic and Functional Neurosurgery* **50**, 344 (1987).
19. Odekerken, V. J., Boel, J. A., Schmand, B. A., De Haan, R. J., Figeet, M., Van Den Munckhof, P., Schuurman, P. R. & De Bie, R. M. GPi vs STN deep brain stimulation for Parkinson disease. *Neurology* **86**, 755 (2016).
20. Baizabal-Carvallo, J. F., Kagnoff, M. N., Jimenez-Shahed, J., Fekete, R. & Jankovic, J. The safety and efficacy of thalamic deep brain stimulation in essential tremor: 10 years and beyond. *Journal of Neurology, Neurosurgery and Psychiatry* **85**, 567 (2014).

21. Benabid, A. L., Pollak, P., Hoffmann, D., Gervason, C., Hommel, M., Perret, J. E., de Rougemont, J. & Gao, D. M. Long-term suppression of tremor by chronic stimulation of the ventral intermediate thalamic nucleus. *The Lancet* **337**, 403 (1991).
22. Boccard, S. G., Fitzgerald, J. J., Pereira, E. A., Moir, L., Van Hartevelt, T. J., Kringelbach, M. L., Green, A. L. & Aziz, T. Z. Targeting the affective component of chronic pain: A case series of deep brain stimulation of the anterior cingulate cortex. *Neurosurgery* **74**, 628 (2014).
23. Fisher, R. *et al.* Electrical stimulation of the anterior nucleus of thalamus for treatment of refractory epilepsy. *Epilepsia* **51**, 899 (2010).
24. Tronnier, V. & Rasche, D. in *Handbook of Clinical Neurology* 343 (2013).
25. Fitzgerald, P. B. Non-pharmacological biological treatment approaches to difficult-to-treat depression. *The Medical journal of Australia* **199**, S48 (2013).
26. Amiaz, R., Levy, D., Vainiger, D., Grunhaus, L. & Zangen, A. Repeated high-frequency transcranial magnetic stimulation over the dorsolateral prefrontal cortex reduces cigarette craving and consumption. *Addiction* **104**, 653 (2009).
27. McClelland, J., Kekic, M., Campbell, I. C. & Schmidt, U. Repetitive Transcranial Magnetic Stimulation (rTMS) Treatment in Enduring Anorexia Nervosa: A Case Series. *European Eating Disorders Review* **24**, 157 (2016).
28. Otto, S. R., Shannon, R. V., Wilkinson, E. P., Hitselberger, W. E., McCreery, D. B., Moore, J. K. & Brackmann, D. E. Audiologic outcomes with the penetrating electrode auditory brainstem implant. *Otology and Neurotology* **29**, 1147 (2008).
29. Lewis, P. M., Ackland, H. M., Lowery, A. J. & Rosenfeld, J. V. *Restoration of vision in blind individuals using bionic devices: A review with a focus on cortical visual prostheses* 2015.
30. Berg, J. A., Dammann, J. F., Tenore, F. V., Tabot, G. A., Boback, J. L., Manfredi, L. R., Peterson, M. L., Katyal, K. D., Johannes, M. S., Makhlin, A., Wilcox, R., Franklin, R. K., Vogelstein, R. J., Hatsopoulos, N. G. & Bensmaia, S. J. Behavioral demonstration of a somatosensory neuroprosthesis. *IEEE Transactions on Neural Systems and Rehabilitation Engineering* **21**, 500 (2013).

31. Miranda, P. C., Correia, L., Salvador, R. & Basser, P. J. *The role of tissue heterogeneity in neural stimulation by applied electric fields in Annual International Conference of the IEEE Engineering in Medicine and Biology - Proceedings* (2007), 1715.
32. Miranda, P. C., Correia, L., Salvador, R. & Basser, P. J. Tissue heterogeneity as a mechanism for localized neural stimulation by applied electric fields. *Physics in Medicine and Biology* **52**, 5603 (2007).
33. Salvador, R., Mekonnen, A., Ruffini, G. & Miranda, P. C. *Modeling the electric field induced in a high resolution realistic head model during transcranial current stimulation in 2010 Annual International Conference of the IEEE Engineering in Medicine and Biology Society, EMBC'10* (2010), 2073.
34. Salvador, R., Silva, S., Basser, P. J. & Miranda, P. C. Determining which mechanisms lead to activation in the motor cortex: A modeling study of transcranial magnetic stimulation using realistic stimulus waveforms and sulcal geometry. *Clinical Neurophysiology* **122**, 748 (2011).
35. Rahman, A., Reato, D., Arlotti, M., Gasca, F., Datta, A., Parra, L. C. & Bikson, M. Cellular effects of acute direct current stimulation: Somatic and synaptic terminal effects. *Journal of Physiology* **591**, 2563 (2013).
36. Kandel, E. R., Schwartz, J. H. & Jessell, T. M. *Principles of Neural Science* 4th (McGraw-Hill, 2000).
37. Butson, C. R., Cooper, S. E. S., Henderson, J. J. M. & McIntyre, C. C. Patient-specific analysis of the volume of tissue activated during deep brain stimulation. *NeuroImage* **34**, 661 (2007).
38. Markram, H. *The Blue Brain Project* 2006.
39. Ritter, P., Schirner, M., McIntosh, A. R. & Jirsa, V. K. The Virtual Brain Integrates Computational Modeling and Multimodal Neuroimaging. *Brain Connectivity* **3**, 121 (2013).
40. Van Essen, D. C., Ugurbil, K., Auerbach, E., Barch, D., Behrens, T. E., Bucholz, R., Chang, A., Chen, L., Corbetta, M., Curtiss, S. W., Della Penna, S., Feinberg, D., Glasser, M. F., Harel, N., Heath, A. C., Larson-Prior, L., Marcus, D., Michalareas, G., Moeller, S., Oostenveld, R., Petersen, S. E., Prior, F., Schlaggar, B. L., Smith, S. M., Snyder, A. Z., Xu, J. & Yacoub, E. *The Human Connectome Project: A data acquisition perspective* 2012.
41. Brocker, D. T. & Grill, W. M. in *Handbook of Clinical Neurology* **3** (2013).

42. Paulus, W. Chapter 26 Transcranial direct current stimulation (tDCS). *Supplements to Clinical Neurophysiology* **56**, 249 (2003).
43. Nitsche, M. A., Fricke, K., Henschke, U., Schlitterlau, A., Liebetanz, D., Lang, N., Henning, S., Tergau, F. & Paulus, W. Pharmacological modulation of cortical excitability shifts induced by transcranial direct current stimulation in humans. *Journal of Physiology* **553**, 293 (2003).
44. Struijk, J. J., Holsheimer, J., van Veen, B. K. & Boom, H. B. Epidural Spinal Cord Stimulation: Calculation of Field Potentials with Special Reference to Dorsal Column Nerve Fibers. *IEEE Transactions on Biomedical Engineering* **38**, 104 (1991).
45. Wiethoff, S., Hamada, M. & Rothwell, J. C. Variability in response to transcranial direct current stimulation of the motor cortex. *Brain Stimulation* **7**, 468 (2014).
46. Walter, B. L. & Vitek, J. L. Surgical treatment for Parkinson's disease. *The Lancet Neurology* **3**, 719 (2004).
47. Kim, D., Jun, S. C. & Kim, H. I. *Computational study of subdural and epidural cortical stimulation of the motor cortex in Proceedings of the Annual International Conference of the IEEE Engineering in Medicine and Biology Society, EMBS* (2011), 7226.
48. Manola, L., Roelofsen, B. H., Holsheimer, J., Marani, E. & Geelen, J. Modelling motor cortex stimulation for chronic pain control: Electrical potential field, activating functions and responses of simple nerve fibre models. *Medical and Biological Engineering and Computing* **43**, 335 (2005).
49. Wongsarnpigoon, A. & Grill, W. M. Computational modeling of epidural cortical stimulation. *Journal of Neural Engineering* **5**, 443 (2008).
50. Bezard, E., Boraud, T., Nguyen, J. P., Velasco, F., Keravel, Y. & Gross, C. Cortical stimulation and epileptic seizure: A study of the potential risk in primates. *Neurosurgery* **45**, 346 (1999).
51. Woolley, A. J., Desai, H. A. & Otto, K. J. Chronic intracortical micro-electrode arrays induce non-uniform, depth-related tissue responses. *Journal of Neural Engineering* **10** (2013).
52. Wang, C., Brunton, E., Haghgooie, S., Cassells, K., Lowery, A. & Rajan, R. Characteristics of electrode impedance and stimulation efficacy of a chronic cortical implant using novel annulus electrodes in rat motor cortex. *Journal of Neural Engineering* **10** (2013).

53. Overstreet, C. K., Klein, J. D. & Helms Tillery, S. I. Computational modeling of direct neuronal recruitment during intracortical microstimulation in somatosensory cortex. *Journal of Neural Engineering* **10** (2013).
54. Nitsche, M. A., Kuo, M. F., Karrasch, R., Wächter, B., Liebetanz, D. & Paulus, W. Serotonin Affects Transcranial Direct Current-Induced Neuroplasticity in Humans. *Biological Psychiatry* **66**, 503 (2009).
55. Kuo, M. F., Grosch, J., Fregni, F., Paulus, W. & Nitsche, M. A. Focusing effect of acetylcholine on neuroplasticity in the human motor cortex. *Journal of Neuroscience* **27**, 14442 (2007).
56. Batsikadze, G., Paulus, W., Grundey, J., Kuo, M. F. & Nitsche, M. A. Effect of the nicotinic  $\alpha 4\beta 2$ -receptor partial agonist varenicline on non-invasive brain stimulation-induced neuroplasticity in the human motor cortex. *Cerebral Cortex* **25**, 3249 (2015).
57. Delgado, J. M., Hamlin, H. & Chapman, W. P. Technique of intracranial electrode placement for recording and stimulation and its possible therapeutic value in psychotic patients. *Confinia neurologica* **12**, 315 (1952).
58. Bekhtereva, N. P., Grachev, K. V., Orlova, A. N. & Iatsukl. Utilization of multiple electrodes implanted in the subcortical structure of the human brain for the treatment of hyperkinesia. *Zhurnal nevropatologii i psikiatrii imeni S.S. Korsakova (Moscow, Russia : 1952)* **63**, 3 (1963).
59. Hosobuchi, Y., Adams, J. E. & Rutkin, B. Chronic Thalamic Stimulation for the Control of Facial Anesthesia Dolorosa. *Archives of Neurology* **29**, 158 (1973).
60. Agnesi, F., Johnson, M. D. & Vitek, J. L. in *Handbook of Clinical Neurology* 39 (2013).
61. Ranck, J. B., Ranck Jr., J. & Ranck, J. B. *Which elements are excited in electrical stimulation of mammalian central nervous system: A review* 1975.
62. Marks, W. J. *Deep brain stimulation management* 1 (2010).
63. Pouclet-Courtemanche, H., Rouaud, T., Thobois, S., Nguyen, J. M., Brefel-Courbon, C., Chereau, I., Cuny, E., Derost, P., Eusebio, A., Guehl, D., Laurencin, C., Mertens, P., Ory-Magne, F., Raoul, S., Regis, J., Ulla, M., Witjas, T., Burbaud, P., Rascol, O. & Damier, P. Long-term efficacy and tolerability of bilateral pallidal stimulation to treat tardive dyskinesia. *Neurology* **86**, 651 (2016).



64. Udupa, K. & Chen, R. *The mechanisms of action of deep brain stimulation and ideas for the future development* 2015.
65. Alhourani, A., McDowell, M. M., Randazzo, M. J., Wozny, T. A., Kondylis, E. D., Lipski, W. J., Beck, S., Karp, J. F., Ghuman, A. S. & Richardson, R. M. *Network effects of deep brain stimulation* 2015.
66. Butson, C. R., Cooper, S. E. S., Henderson, J. J. M., Wolgamuth, B. & McIntyre, C. C. Probabilistic analysis of activation volumes generated during deep brain stimulation. *NeuroImage* **54**, 2096 (2011).
67. Maks, C. B., Butson, C. R., Walter, B. L., Vitek, J. L. & McIntyre, C. C. Deep brain stimulation activation volumes and their association with neurophysiological mapping and therapeutic outcomes. *Journal of Neurology, Neurosurgery and Psychiatry* **80**, 659 (2009).
68. Nowak, L. G. & Bullier, J. Axons, but not cell bodies, are activated by electrical stimulation in cortical gray matter. II. Evidence from selective inactivation of cell bodies and axon initial segments. *Experimental Brain Research* **118**, 489 (1998).
69. Moffitt, M. A., McIntyre, C. C. & Grill, W. M. Prediction of Myelinated Nerve Fiber Stimulation Thresholds: Limitations of Linear Models. *IEEE Transactions on Biomedical Engineering* **51**, 229 (2004).
70. Melzack, R. & Wall, P. D. Pain mechanisms: A new theory. *Pain Forum* **5**, 3 (1996).
71. Holsheimer, J., Demeulemeester, H., Nuttin, B. & De Sutter, P. Identification of the target neuronal elements in electrical deep brain stimulation. *European Journal of Neuroscience* **12**, 4573 (2000).
72. Grady, K. M., Severn, A. M. & Eldridge, P. R. *Key topics in chronic pain* (CRC Press, 2002).
73. Angeli, C. A., Boakye, M., Morton, R. A., Vogt, J., Benton, K., Chen, Y., Ferreira, C. K. & Harkema, S. J. Recovery of over-ground walking after chronic motor complete spinal cord injury. *New England Journal of Medicine* **379**, 1244 (2018).
74. Formento, E., Minassian, K., Wagner, F., Mignardot, J. B., Le Goff-Mignardot, C. G., Rowald, A., Bloch, J., Micera, S., Capogrosso, M. & Courtine, G. Electrical spinal cord stimulation must preserve proprioception to enable locomotion in humans with spinal cord injury. *Nature Neuroscience* **21**, 1728 (2018).

75. George, M. S., Wassermann, E. M., Williams, W. A., Callahan, A., Ketter, T. A., Basser, P., Hallett, M. & Post, R. M. Daily repetitive transcranial magnetic stimulation (rTMS) improves mood in depression. *NeuroReport* **6**, 1853 (1995).
76. Grisaru, N., Yaroslavsky, U., Abarbanel, J., Lamberg, T. & Belmaker, R. H. *Transcranial magnetic stimulation in depression and schizophrenia in European Neuropsychopharmacology* **4** (1994), 287.
77. Höflich, G., Kasper, S., Hufnagel, A., Ruhrmann, S. & Möller, H. -J. Application of transcranial magnetic stimulation in treatment of drug-resistant major depression—a report of two cases. *Human Psychopharmacology: Clinical and Experimental* **8**, 361 (1993).
78. Kolbinger, H. M., Höflich, G., Hufnagel, A., Müller, H.-J. -J. & Kasper, S. Transcranial magnetic stimulation (TMS) in the treatment of major depression — a pilot study. *Human Psychopharmacology: Clinical and Experimental* **10**, 305 (1995).
79. Pascual-Leone, A., Rubio, B., Pallardó, F. & Catalá, M. D. Rapid-rate transcranial magnetic stimulation of left dorsolateral prefrontal cortex in drug-resistant depression. *Lancet* **348**, 233 (1996).
80. Ueno, S., Tashiro, T. & Harada, K. Localized stimulation of neural tissues in the brain by means of a paired configuration of time-varying magnetic fields. *Journal of Applied Physics* **64**, 5862 (1988).
81. Wassermann, E. M. Risk and safety of repetitive transcranial magnetic stimulation: Report and suggested guidelines from the International Workshop on the Safety of Repetitive Transcranial Magnetic Stimulation, June 5-7, 1996. *Electroencephalography and Clinical Neurophysiology - Evoked Potentials* **108**, 1 (1998).
82. Chen, R., Classen, J., Gerloff, C., Celnik, P., Wassermann, E. M., Hallett, M. & Cohen, L. G. Depression of motor cortex excitability by low-frequency transcranial magnetic stimulation. *Neurology* **48**, 1398 (1997).
83. Hamada, M., Murase, N., Hasan, A., Balaratnam, M. & Rothwell, J. C. The role of interneuron networks in driving human motor cortical plasticity. *Cerebral Cortex* **23**, 1593 (2013).
84. Maeda, F., Keenan, J. P., Tormos, J. M., Topka, H. & Pascual-Leone, A. Interindividual variability of the modulatory effects of repetitive transcranial magnetic stimulation on cortical excitability. *Experimental Brain Research* **133**, 425 (2000).

85. Rohan, M. L., Yamamoto, R. T., Ravichandran, C. T., Cayetano, K. R., Morales, O. G., Olson, D. P., Vitaliano, G., Paul, S. M. & Cohen, B. M. Rapid mood-elevating effects of low field magnetic stimulation in depression. *Biological Psychiatry* **76**, 186 (2014).
86. Bonmassar, G., Lee, S. W., Freeman, D. K., Polasek, M., Fried, S. I. & Gale, J. T. Microscopic magnetic stimulation of neural tissue. *Nature Communications* **3** (2012).
87. Park, H. J., Bonmassar, G., Kaltenbach, J. A., Machado, A. G., Manzoor, N. F. & Gale, J. T. Activation of the central nervous system induced by micro-magnetic stimulation. *Nature Communications* **4** (2013).
88. Peeples, L. The rise of bioelectric medicine sparks interest among researchers, patients, and industry. *Proceedings of the National Academy of Sciences of the United States of America* **116**, 24379 (2019).
89. Lopshire, J. C. & Zipes, D. P. Device therapy to modulate the autonomic nervous system to treat heart failure. *Current Cardiology Reports* **14**, 593 (2012).
90. Vinci, T., Ganzer, P., Fetzek, C., Hamlin, R., Muir, W., Zmarowski, A., Hanjora, K., Bresler, H. & Hawk, M. A. Non-invasive bioelectronic medicines for treating cardiopulmonary disease. *Journal of Pharmacological and Toxicological Methods* **99**, 106595 (2018).
91. Farajidavar, A. Bioelectronics for mapping gut activity. *Brain research* **1693**, 169 (2018).
92. Edwards, C. A., Kouzani, A., Lee, K. H. & Ross, E. K. *Neurostimulation devices for the treatment of neurologic disorders in Mayo Clinic Proceedings* **92** (2017), 1427.
93. Famm, K. Drug discovery: a jump-start for electroceuticals (vol 496, pg 159, 2013). *Nature* **496**, 300 (2013).
94. Horn, C. C., Ardell, J. L. & Fisher, L. E. Electroceutical targeting of the autonomic nervous system. *Physiology* **34**, 150 (2019).
95. Mickle, A. D. & Gereau IV, R. W. A bright future? Optogenetics in the periphery for pain research and therapy. *Pain* **159**, S65 (2018).
96. Mickle, A. D., Won, S. M., Noh, K. N., Yoon, J., Meacham, K. W., Xue, Y., McIlvried, L. A., Copits, B. A., Samineni, V. K., Crawford, K. E., *et al.* A wireless closed-loop system for optogenetic peripheral neuromodulation. *Nature* **565**, 361 (2019).

97. Anderson, H. E. *et al.* On the development of optical peripheral nerve interfaces. *Neural regeneration research* **14**, 425 (2019).
98. Grill, W. M. & DeBerry, J. J. Innovative device illuminates the horizon of bioelectronic medicines. *Nature Reviews Urology* **16**, 209 (2019).
99. Coterio, V., Graf, J., Zachs, D. P., Tracey, K. J., Ashe, J., Lim, H. H. & Puleo, C. Peripheral Focused Ultrasound Stimulation (pFUS): New Competitor in Pharmaceutical Markets? *SLAS Technology* **24**, 448 (2019).
100. Hicks, J. *Wirelessly Powering Medical Chips Inside Your Body* 2014.
101. Tanabe, Y., Ho, J. S., Liu, J., Liao, S. Y., Zhen, Z., Hsu, S., Shuto, C., Zhu, Z. Y., Ma, A., Vassos, C., Chen, P., Tse, H. F. & Poon, A. S. High-performance wireless powering for peripheral nerve neuromodulation systems. *PLoS ONE* **12** (2017).
102. Carreno, F. R. & Frazer, A. Vagal nerve stimulation for treatment-resistant depression. *Neurotherapeutics* **14**, 716 (2017).
103. Conway, C. R. & Xiong, W. The mechanism of action of vagus nerve stimulation in treatment-resistant depression: current conceptualizations. *Psychiatric Clinics* **41**, 395 (2018).
104. Thompson, N., Mastitskaya, S. & Holder, D. Avoiding off-target effects in electrical stimulation of the cervical vagus nerve: Neuroanatomical tracing techniques to study fascicular anatomy of the vagus nerve. *Journal of neuroscience methods* **325**, 108325 (2019).
105. Charkhkar, H., Christie, B. P., Pinault, G. J., Tyler, D. J. & Triolo, R. J. A translational framework for peripheral nerve stimulating electrodes: Reviewing the journey from concept to clinic. *Journal of Neuroscience Methods* **328**, 108414 (2019).
106. Grill, W. M. in *Computational Neurostimulation* (ed Bestmann, S.) 147 (Elsevier, 2015).
107. Musselman, E. D., Pelot, N. A. & Grill, W. M. Empirically based guidelines for selecting vagus nerve stimulation parameters in epilepsy and heart failure. *Cold Spring Harbor Perspectives in Medicine* **9** (2019).
108. Yadav, A. P., Li, D. & Nicoletis, M. A. L. A Brain to Spine Interface for Transferring Artificial Sensory Information. *bioRxiv*, 807735 (2019).
109. Tufail, Y., Matyushov, A., Baldwin, N., Tauchmann, M. L. M., Georges, J., Yoshihiro, A., Tillery, S. S. I. H. & Tyler, W. J. W. Transcranial pulsed ultrasound stimulates intact brain circuits. *Neuron* **66**, 681 (2010).

110. Min, B.-K., Yang, P., Bohlke, M., Park, S., R.vago, D., Maher, T. & Yoo, S.-S. Focused ultrasound modulates the level of cortical neurotransmitters: Potential as a new functional brain mapping technique. *International Journal of Imaging Systems and Technology* **21**, 232 (2011).
111. Yoo, S.-S., Kim, H., Min, B.-K., Franck, E. & Park, S. Transcranial focused ultrasound to the thalamus alters anesthesia time in rats. *NeuroReport* **22**, 783 (2011).
112. Yang, P., Kim, H., Lee, W., Bohlke, M., Park, S., Maher, T. & Yoo, S.-S. Transcranial focused ultrasound to the thalamus is associated with reduced rxtacellular GABA levels in rats. *Neuropsychobiology* **65**, 153 (2012).
113. Younan, Y., Deffieux, T., Larrat, B., Fink, M., Tanter, M. & Aubry, J. F. Influence of the pressure field distribution in transcranial ultrasonic neurostimulation. *Medical Physics* **40** (2013).
114. Mehić, E., Xu, J., Caler, C., Coulson, N., Moritz, C. & Mourad, P. Increased anatomical specificity of neuromodulation via modulated focused ultrasound. *PLoS ONE* **9** (2014).
115. Kim, H., Chiu, A., Lee, S. S. D., Fischer, K. & Yoo, S. S. S.-S. Focused ultrasound-mediated non-invasive brain stimulation: Examination of sonication parameters. *Brain Stimulation* **7**, 748 (2014).
116. Hynynen, K. & Jolesz, F. Demonstration of potential noninvasive ultrasound brain therapy through an intact skull. *Ultrasound in Medicine and Biology* **24**, 275 (1998).
117. Postema, M. *Fundamentals of Medical Ultrasonics* (2014).
118. Ebbini, E. & Cain, C. A Spherical-Section Ultrasound Phased Array Applicator for Deep Localized Hyperthermia. *IEEE Transactions on Biomedical Engineering* **38**, 634 (1991).
119. White, J., Clement, G. T. & Hynynen, K. Transcranial ultrasound focus reconstruction with phase and amplitude correction. *IEEE Transactions on Ultrasonics, Ferroelectrics, and Frequency Control* **52**, 1518 (2005).
120. Pinton, G., Aubry, J.-F. F., Bossy, E., Muller, M., Pernot, M. & Tanter, M. Attenuation, scattering, and absorption of ultrasound in the skull bone. *Medical Physics* **39**, 299 (2012).
121. Hynynen, K. The threshold for thermally significant cavitation in dog's thigh muscle in vivo. *Ultrasound in Medicine and Biology* **17**, 157 (1991).

122. Torr, G. R. The acoustic radiation force. *American Journal of Physics* **52**, 402 (1984).
123. Bystritsky, A., Korb, A. S., Douglas, P. K., Cohen, M. S., Melega, W. P., Mulgaonkar, A. P., Desalles, A., Min, B. K. & Yoo, S. S. *A review of low-intensity focused ultrasound pulsation* 2011.
124. Gavrilov, L. & Tsurulnikov, E. Focused ultrasound as a tool to input sensory information to humans (review). *Acoustical Physics* **58**, 1 (2012).
125. Gavrilov, L. R. *Use of focused ultrasound for stimulation of various neural structures* (Nova Biomedical New York, 2014).
126. Fry, F. J., Ades, H. W. & Fry, W. J. Production of reversible changes in the central nervous system by ultrasound. *Science* **127**, 83 (1958).
127. Adrianov, O. S., Vykhodtseva, N. I., Fokin, V. F., Uranova, N. A., Avirom, V. M. & Galogazha, M. Reversible functional blocking of the optic tract by focused ultrasound. *Bulletin of Experimental Biology and Medicine* **97**, 844 (1984).
128. Velling, V. A. & Shklyaruk, S. P. Modulation of the functional state of the brain with the aid of focused ultrasonic action. *Neuroscience and Behavioral Physiology* **18**, 369 (1988).
129. Adrianov, O. S., Vykhodtseva, N. I., Fokin, V. F. & Avirom, V. M. Method of local application of focused ultrasound to deep brain structures of an unrestrained unanesthetized animal. *Bulletin of Experimental Biology and Medicine* **98**, 992 (1984).
130. Deffieux, T., Younan, Y., Wattiez, N., Tanter, M., Pouget, P. & Aubry, J. F. Low-intensity focused ultrasound modulates monkey visuomotor behavior. *Current Biology* **23**, 2430 (2013).
131. Bachtold, M., Rinaldi, P., Jones, J., Reines, F. & Price, L. Focused ultrasound modifications of neural circuit activity in a mammalian brain. *Ultrasound in Medicine and Biology* **24**, 557 (1998).
132. Tyler, W., Tufail, Y., Finsterwald, M., Tauchmann, M., Olson, E. & Majestic, C. Remote excitation of neuronal circuits using low-intensity, low-frequency ultrasound. *PLoS ONE* **3** (2008).
133. Takagi, S. F., Higashino, S., Shibuya, T. & Osawa, N. The Actions of Ultrasound on the Myelinated Nerve, the Spinal Cord and the Brain. *The Japanese Journal of Physiology* **10**, 183 (1960).

134. Lele, P. Effects of focused ultrasonic radiation on peripheral nerve, with observations on local heating. *Experimental Neurology* **8**, 47 (1963).
135. Mihran, R., Barnes, F. & Wachtel, H. Temporally-specific modification of myelinated axon excitability in vitro following a single ultrasound pulse. *Ultrasound in Medicine and Biology* **16**, 297 (1990).
136. Muratore, R., LaManna, J., Szulman, E., Kalisz, A., Lamprecht, M., Simon, M., Yu, Z., Xu, N. & Morrison, B. *Bioeffective ultrasound at very low doses: Reversible manipulation of neuronal cell morphology and function in vitro* in *AIP Conference Proceedings* **1113** (2009), 25.
137. Lee, Y. F., Lin, C. C., Cheng, J. S. & Chen, G. S. Nerve conduction block in diabetic rats using high-intensity focused ultrasound for analgesic applications. *British Journal of Anaesthesia* **114**, 840 (2015).
138. Fry, F. J. & Johnson, L. K. Tumor irradiation with intense ultrasound. *Ultrasound in Medicine and Biology* **4**, 337 (1978).
139. Krishna, V., Sammartino, F. & Rezaei, A. *A review of the current therapies, challenges, and future directions of transcranial focused ultrasound technology advances in diagnosis and treatment* 2018.
140. Della Flora, E., Perera, C. L., Cameron, A. L. & Maddern, G. J. *Deep brain stimulation for essential tremor: A systematic review* 2010.
141. Min, B.-K., Bystritsky, A., Jung, K.-I., Fischer, K., Zhang, Y., Maeng, L.-S., In Park, S., Chung, Y.-A., Jolesz, F. & Yoo, S.-S. Focused ultrasound-mediated suppression of chemically-induced acute epileptic EEG activity. *BMC Neuroscience* **12** (2011).
142. Hindman, J. C. Proton Resonance Shift of Water in the Gas and Liquid States. *The Journal of Chemical Physics* **44**, 4582 (1966).
143. Bednarz, G., Downes, M. B., Corn, B. W., Curran, W. J. & Goldman, H. W. Evaluation of the spatial accuracy of magnetic resonance imaging-based stereotactic target localization for gamma knife radiosurgery of functional disorders. *Neurosurgery* **45**, 1156 (1999).
144. Kyriakou, A., Neufeld, E., Werner, B., Paulides, M. M., Szekely, G. & Kuster, N. A review of numerical and experimental compensation techniques for skull-induced phase aberrations in transcranial focused ultrasound. *International Journal of Hyperthermia* **30**, 36 (2014).
145. Hynynen, K. & Sun, J. Trans-skull ultrasound therapy: The feasibility of using image-derived skull thickness information to correct the phase distortion. *IEEE Transactions on Ultrasonics, Ferroelectrics, and Frequency Control* **46**, 752 (1999).

146. Aubry, J.-F., Tanter, M., Pernot, M., Thomas, J.-L. & Fink, M. Experimental demonstration of noninvasive transskull adaptive focusing based on prior computed tomography scans. *The Journal of the Acoustical Society of America* **113**, 84 (2003).
147. Pichardo, S., Sin, V. V. W. & Hynynen, K. Multi-frequency characterization of the speed of sound and attenuation coefficient for longitudinal transmission of freshly excised human skulls. *Physics in Medicine and Biology* **56**, 219 (2011).
148. Chavrier, F., Chapelon, J., Gelet, A. & Cathignol, D. Modeling of high-intensity focused ultrasound-induced lesions in the presence of cavitation bubbles. *Journal of the Acoustical Society of America* **108**, 432 (2000).
149. Yee, K. S., Chen, J. S. & Chang, A. H. Conformal finite difference time domain (FDTD) with overlapping grids in *IEEE Antennas and Propagation Society, AP-S International Symposium (Digest)* **1992-June** (Institute of Electrical and Electronics Engineers Inc., 1992), 1949.
150. Tuch, D. S., Wedeen, V. J., Dale, A. M., George, J. S. & Belliveau, J. W. Conductivity tensor mapping of the human brain using diffusion tensor MRI. *Proceedings of the National Academy of Sciences of the United States of America* **98**, 11697 (2001).
151. Chaturvedi, A., Butson, C. R., Lempka, S. S. F., Cooper, S. E. S. & McIntyre, C. C. Patient-specific models of deep brain stimulation: Influence of field model complexity on neural activation predictions. *Brain Stimulation* **3**, 65 (2010).
152. Parent, M., Lvesque, M. & Parent, A. Two types of projection neurons in the internal pallidum of primates: Single-axon tracing and three-dimensional reconstruction. *Journal of Comparative Neurology* **439**, 162 (2001).
153. Geddes, L. A. & Baker, L. E. The specific resistance of biological material-A compendium of data for the biomedical engineer and physiologist. *Medical and biological engineering* **5**, 271 (1967).
154. Gabriel, S., Lau, R. W. & Gabriel, C. The dielectric properties of biological tissues: II. Measurements in the frequency range 10 Hz to 20 GHz. *Physics in Medicine and Biology* **41**, 2251 (1996).
155. Havgall, P. A., Neufeld, E., Gosselin, M. C., Klingenböck, A. & Kuster, N. IT'IS Database for thermal and electromagnetic parameters of biological tissues. *Version 3.0* (2015).



156. Hodgkin, A. L. & Huxley, A. F. A quantitative description of membrane current and its application to conduction and excitation in nerve. *The Journal of Physiology* **117**, 500 (1952).
157. Frankenhaeuser, B. & Huxley, A. F. The action potential in the myelinated nerve fibre of *Xenopus laevis* as computed on the basis of voltage clamp data. *The Journal of Physiology* **171**, 302 (1964).
158. Sweeney, J. D., Mortimer, J. T. & Durand, D. *Modeling of mammalian myelinated nerve for functional neuromuscular stimulation in IEEE 9th Annual Conference of the Engineering in Medicine and Biology Society* **3** (1987), 1577.
159. Richardson, A. G., McIntyre, C. C. & Grill, W. M. Modelling the effects of electric fields on nerve fibres: Influence of the myelin sheath. *Medical and Biological Engineering and Computing* **38**, 438 (2000).
160. Carnevale, N. N. T. & Hines, M. M. L. *The NEURON book* **1** (Cambridge University Press, 2006).
161. Hines, M. L., Morse, T., Migliore, M., Carnevale, N. T. & Shepherd, G. M. ModelDB: A Database to Support Computational Neuroscience. *Journal of computational neuroscience* **17**, 7 (2004).
162. McNeal, D. R. D. Analysis of a Model for Excitation of Myelinated Nerve. *IEEE Transactions on Biomedical Engineering* **BME-23**, 329 (1976).
163. D'Haese, P. F., Cetinkaya, E., Konrad, P. E., Kao, C. & Dawant, B. M. Computer-aided placement of deep brain stimulators: From planning to intraoperative guidance. *IEEE Transactions on Medical Imaging* **24**, 1469 (2005).
164. Castro, F. J. S., Pollo, C., Meuli, R., Maeder, P., Cuisenaire, O., Bach Cuadra, M., Villemure, J. G. & Thiran, J. P. A cross validation study of deep brain stimulation targeting: From experts to atlas-based, segmentation-based and automatic registration algorithms. *IEEE Transactions on Medical Imaging* **25**, 1440 (2006).
165. Duay, V., Bresson, X., Castro, J. S., Pollo, C., Cuadra, M. B. & Thiran, J. P. *An active contour-based atlas registration model applied to automatic subthalamic nucleus targeting on MRI: Method and validation in Lecture Notes in Computer Science (including subseries Lecture Notes in Artificial Intelligence and Lecture Notes in Bioinformatics)* **5242 LNCS** (2008), 980.

166. Chen, S. Y., Tsai, S. T., Hung, H. Y., Lin, S. H., Pan, Y. H. & Lin, S. Z. *Targeting the subthalamic nucleus for deep brain stimulation - A comparative study between magnetic resonance images alone and fusion with computed tomographic images* 2011.
167. Rubin, J. E. & Terman, D. High frequency stimulation of the subthalamic nucleus eliminates pathological thalamic rhythmicity in a computational model. *Journal of Computational Neuroscience* **16**, 211 (2004).
168. Hahn, P. J. & McIntyre, C. C. Modeling shifts in the rate and pattern of subthalamopallidal network activity during deep brain stimulation. *Journal of Computational Neuroscience* **28**, 425 (2010).
169. Humphries, M. D. & Gurney, K. Network effects of subthalamic deep brain stimulation drive a unique mixture of responses in basal ganglia output. *European Journal of Neuroscience* **36**, 2240 (2012).
170. Sweet, J. A., Walter, B. L., Gunalan, K., Chaturvedi, A., McIntyre, C. C. & Miller, J. P. Fiber tractography of the axonal pathways linking the basal ganglia and cerebellum in Parkinson disease: Implications for targeting in deep brain stimulation: Clinical article. *Journal of Neurosurgery* **120**, 988 (2014).
171. Miocinovic, S., Parent, M., Butson, C. R., Hahn, P. J., Russo, G. S., Vitek, J. L. & McIntyre, C. C. Computational analysis of subthalamic nucleus and lenticular fasciculus activation during therapeutic deep brain stimulation. *Journal of neurophysiology* **96**, 1569 (2006).
172. Van Wijk, B. C., Beudel, M., Jha, A., Oswal, A., Foltynie, T., Hariz, M. I., Limousin, P., Zrinzo, L., Aziz, T. Z., Green, A. L., Brown, P. & Litvak, V. Subthalamic nucleus phase-amplitude coupling correlates with motor impairment in Parkinson's disease. *Clinical Neurophysiology* **127**, 2010 (2016).
173. Bériault, S., Xiao, Y., Bailey, L., Collins, D. L., Sadikot, A. F. & Pike, G. B. *Towards computer-assisted deep brain stimulation targeting with multiple active contacts* in *Lecture Notes in Computer Science (including subseries Lecture Notes in Artificial Intelligence and Lecture Notes in Bioinformatics)* **7510 LNCS** (2012), 487.
174. Butson, C. R. & McIntyre, C. C. Current steering to control the volume of tissue activated during deep brain stimulation. *Brain Stimulation* **1**, 7 (2008).

175. Ladenbauer, J., Minassian, K., Hofstoetter, U. S., Dimitrijevic, M. R. & Rattay, F. Stimulation of the human lumbar spinal cord with implanted and surface electrodes: A computer simulation study. *IEEE Transactions on Neural Systems and Rehabilitation Engineering* **18**, 637 (2010).
176. Rattay, F., Minassian, K. & Dimitrijevic, M. R. Epidural electrical stimulation of posterior structures of the human lumbosacral cord: 2. Quantitative analysis by computer modeling. *Spinal Cord* **38**, 473 (2000).
177. Holsheimer, J. Which neuronal elements are activated directly by spinal cord stimulation. *Neuromodulation* **5**, 25 (2002).
178. Gerasimenko, Y. P., Lavrov, I. A., Courtine, G., Ichiyama, R. M., Dy, C. J., Zhong, H., Roy, R. R. & Edgerton, V. R. Spinal cord reflexes induced by epidural spinal cord stimulation in normal awake rats. *Journal of Neuroscience Methods* **157**, 253 (2006).
179. Struijk, J. J., Holsheimer, J., van der Heide, G. G. & Boom, H. B. Recruitment of Dorsal Column Fibers in Spinal Cord Stimulation: Influence of Collateral Branching. *IEEE Transactions on Biomedical Engineering* **39**, 903 (1992).
180. Shealy, C. N., Mortimer, J. T. & Reswick, J. B. Electrical inhibition of pain by stimulation of the dorsal columns: preliminary clinical report. *Anesthesia and analgesia* **46**, 489 (1967).
181. Coburn, B. Electrical stimulation of the spinal cord: two-dimensional finite element analysis with particular reference to epidural electrodes. *Medical & Biological Engineering & Computing* **18**, 573 (1980).
182. Howell, B., Lad, S. P., Grill, W. M. & Glorioso, J. C. Evaluation of intradural stimulation efficiency and selectivity in a computational model of spinal cord stimulation. *PLoS ONE* **9** (2014).
183. Lempka, S. F., McIntyre, C. C., Kilgore, K. L. & Machado, A. G. *Computational Analysis of Kilohertz Frequency Spinal Cord Stimulation for Chronic Pain Management in Anesthesiology* **122** (Lippincott Williams and Wilkins, 2015), 1362.
184. Westervelt, P. J. The Theory of Steady Forces Caused by Sound Waves. *Journal of the Acoustical Society of America* **23**, 312 (1951).
185. Colucci, V., Strichartz, G., Jolesz, F., Vykhodtseva, N. & Hynynen, K. Focused Ultrasound Effects on Nerve Action Potential in vitro. *Ultrasound in Medicine and Biology* **35**, 1737 (2009).

186. Juan, E. J., González, R., Albors, G., Ward, M. P. & Irazoqui, P. Vagus nerve modulation using focused pulsed ultrasound: Potential applications and preliminary observations in a rat. *International Journal of Imaging Systems and Technology* **24**, 67 (2014).
187. Iwasa, K., Tasaki, I. & Gibbons, R. C. Swelling of nerve fibers associated with action potentials. *Science* **210**, 338 (1980).
188. Tasaki, I., Iwasa, K. & Gibbons, R. C. Mechanical changes in crab nerve fibers during action potentials. *The Japanese Journal of Physiology* **30**, 897 (1980).
189. Tasaki, I. & Iwasa, K. Rapid Pressure Changes and Surface Displacements in the Squid Giant Axon Associated with Production of Action Potentials. *The Japanese Journal of Physiology* **32**, 69 (1982).
190. Heimburg, T. & Jackson, A. D. On soliton propagation in biomembranes and nerves. *Proceedings of the National Academy of Sciences of the United States of America* **102**, 9790 (2005).
191. Petrov, A. G. *Electricity and mechanics of biomembrane systems: Flexoelectricity in living membranes* 2006.
192. Todorov, A. T., Petrov, A. G. & Fendler, J. H. First observation of the converse flexoelectric effect in bilayer lipid membranes. *Journal of Physical Chemistry* **98**, 3076 (1994).
193. Plaksin, M., Shoham, S. & Kimmel, E. Intramembrane cavitation as a predictive bio-piezoelectric mechanism for ultrasonic brain stimulation. *Physical review X* **4**, 11004 (2014).
194. Menz, M. D., Ye, P., Firouzi, K., Nikoozadeh, A., Pauly, K. B., Khuri-Yakub, P. & Baccus, S. A. Radiation Force as a Physical Mechanism for Ultrasonic Neurostimulation of the Ex Vivo Retina. *The Journal of neuroscience : the official journal of the Society for Neuroscience* **39**, 6251 (2019).
195. Lemaire, T., Neufeld, E., Kuster, N. & Micera, S. Understanding ultrasound neuromodulation using a computationally efficient and interpretable model of intramembrane cavitation. *Journal of Neural Engineering* **16**, 046007 (2019).
196. Kubanek, J., Shi, J., Marsh, J., Chen, D., Deng, C. & Cui, J. Ultrasound modulates ion channel currents. *Scientific Reports* **6** (2016).
197. Ibsen, S., Tong, A., Schutt, C., Esener, S. & Chalasani, S. Sonogenetics is a non-invasive approach to activating neurons in *Caenorhabditis elegans*. *Nature Communications* **6** (2015).

198. Prieto, M., Oralkan, Ö., Khuri-Yakub, B. & Maduke, M. Dynamic Response of Model Lipid Membranes to Ultrasonic Radiation Force. *PLoS ONE* **8** (2013).
199. Gosselin, M.-C. M. C., Neufeld, E., Moser, H., Huber, E., Farcito, S., Gerber, L., Jedensjo, M., Hilber, I., Gennaro, F. F. D., Lloyd, B., Kainz, W., Kuster, N., Cherubini, E., Szczerba, D., Kainz, W. & Kuster, N. Development of a new generation of high-resolution anatomical models for medical device evaluation: The Virtual Population 3.0. *Physics in Medicine and Biology* **59**, 5287 (2014).
200. Balay, S., Gropp, W. D., McInnes, L. C. & Smith, B. F. in *Modern Software Tools for Scientific Computing* 163 (1997).
201. Neufeld, E., Cassará, A. M., Montanaro, H., Kuster, N. & Kainz, W. Functionalized anatomical models for EM-neuron interaction modeling. *Physics in Medicine and Biology* **61**, 4390 (2016).
202. Wenger, N., Moraud, E. M., Gandar, J., Musienko, P., Capogrosso, M., Baud, L., Le Goff, C. G., Barraud, Q., Pavlova, N., Dominici, N., Minev, I. R., Asboth, L., Hirsch, A., Duis, S., Kreider, J., Mortera, A., Haverbeck, O., Kraus, S., Schmitz, F., DiGiovanna, J., Van Den Brand, R., Bloch, J., Detemple, P., Lacour, S. P., Bézard, E., Micera, S. & Courtine, G. Spatiotemporal neuromodulation therapies engaging muscle synergies improve motor control after spinal cord injury. *Nature Medicine* **22**, 138 (2016).
203. Schroeder, W., Martin, K. & Lorensen, B. *The Visualization Toolkit: An Object Oriented Approach to 3D Graphics* 3rd Edition (2003).
204. Raspopovic, S., Capogrosso, M. & Micera, S. A computational model for the stimulation of rat sciatic nerve using a transverse intrafascicular multichannel electrode. *IEEE Transactions on Neural Systems and Rehabilitation Engineering* **19**, 333 (2011).
205. Carras, P. L., Coleman, P. A. & Miller, R. F. Site of action potential initiation in amphibian retinal ganglion cells. *J. Neurophysiol* **67**, 292 (1992).
206. Cohen, E. D. Interactions of inhibition and excitation in the light-evoked currents of X type retinal ganglion cells. *J. Neurophysiol* **80**, 2975 (1998).
207. Cohen, E. D. Synaptic mechanisms shaping the light-response in retinal ganglion cells. *Concepts and Challenges in Retinal Biology* **131**, 215 (2003).

208. O'Brien, B. J., Isayama, T., Richardson, R. & Berson, D. M. Intrinsic physiological properties of cat retinal ganglion cells. *Journal of Physiology* **538**, 787 (2002).
209. Greenberg, R. J., Veite, T. J., Humayun, M. S., Scarlatis, G. N., De Juan, E., Velte, T. J., Humayun, M. S., Scarlatis, G. N., De & Juan Jr., E. A computational model of electrical stimulation of the retinal ganglion cell. *IEEE Transactions on Biomedical Engineering* **46**, 505 (1999).
210. Rattay, F. & Resatz, S. Effective electrode configuration for selective stimulation with inner eye prostheses. *IEEE Trans Biomed Eng* **51**, 1659 (2004).
211. Schiefer, M. A. & Grill, W. M. Sites of neuronal excitation by epiretinal electrical stimulation. *IEEE Trans Neural Syst Rehabil Eng* **14**, 5 (2006).
212. Dreher, B., Sefton, A. J., Ni, S. Y. & Nisbelt, G. The morphology, number, distribution and central projections of class i retinal ganglion cells in albino and hooded rats. *Brain, Behavior and Evolution* **26**, 10 (1985).
213. Peichl, L., Buhl, E. H. & Boycott, B. B. Alpha ganglion cells in the rabbit retina. *Journal of Comparative Neurology* **263**, 25 (1987).
214. Peichl, L. & Wassle, H. The structural correlate of the receptive field centre of alpha ganglion cells in the cat retina. *J. Physiol. (Lond)* **341**, 309 (1983).
215. Caldwell, J. H. & Daw, N. W. New properties of rabbit retinal ganglion cells. *The Journal of Physiology* **276**, 257 (1978).
216. Boiko, T., Van Wart, A., Caldwell, J. H., Levinson, S. R., Trimmer, J. S. & Matthews, G. Functional specialization of the axon initial segment by isoform-specific sodium channel targeting. *J Neurosci* **23**, 2306 (2003).
217. Fried, S. I., Lasker, A. C. W., Desai, N. J., Eddington, D. K., Rizzo 3rd, J. F. & Rizzo, J. F. Axonal sodium-channel bands shape the response to electric stimulation in retinal ganglion cells. *J Neurophysiol* **101**, 1972 (2009).
218. Ames 3rd, A., Nesbett, F. B., Ames, A. & Nesbett, F. B. In vitro retina as an experimental model of the central nervous system. *J Neurochem* **37**, 867 (1981).
219. Muller, J. F. & Dacheux, R. F. Alpha ganglion cells of the rabbit retina lose antagonistic surround responses under dark adaptation. *Vis. Neurosci* **14**, 395 (1997).

220. Neher, E. Correction for liquid junction potentials in patch clamp experiments. *Methods Enzymol* **207**, 123 (1992).
221. Neher, E. & Sakmann, B. The patch clamp technique. *Sci Am* **266**, 44 (1992).
222. Brandon, C. & Criswell, M. H. Antiserum to lucifer yellow: preparation, characterization, and use for immunocytochemical localization of dye-filled retinal neurons. *J Histochem Cytochem* **39**, 1547 (1991).
223. Pu, M., Berson, D. M. & Pan, T. Structure and function of retinal ganglion cells innervating the cat's geniculate wing: an in vitro study. *J. Neurosci* **14**, 4338 (1994).
224. Hines, M. L. & Carnevale, N. T. *NEURON: A tool for neuroscientists* 2001.
225. Fohlmeister, J. F. & Miller, R. F. Impulse encoding mechanisms of ganglion cells in the tiger salamander retina. *J. Neurophysiol* **78**, 1935 (1997).
226. Fohlmeister, J. F., Cohen, E. D. & Newman, E. A. Mechanisms and distribution of ion channels in retinal ganglion cells: using temperature as an independent variable. *J Neurophysiol* **103**, 1357 (2010).
227. Minnikanti, S., Cohen, E. & Peixoto, N. *Quasi-static analysis of electric field distributions by disc electrodes in a rabbit eye model in 26th Southern Biomedical Engineering Conference SBEC 2010, April 30-May 2, 2010, College Park, Maryland, USA* **32 IFMBE** (Springer, 2010), 385.
228. BIPM, IEC, IFCC, ILAC, ISO, IUPAC, IUPAP & OIML. Guide to the Expression of Uncertainty in Measurement,(1995), with Supplement 1, Evaluation of measurement data, JCGM 101. *Organization for Standardization, Geneva, Switzerland* **3**, 352 (2008).
229. Rockhill, R. L., Euler, T. & Masland, R. H. Spatial order within but not between types of retinal neurons. *Proceedings of the National Academy of Sciences of the United States of America* **97**, 2303 (2000).
230. Azouz, R., Jensen, M. S. & Yaari, Y. Ionic basis of spike afterdepolarization and burst generation in adult rat hippocampal CA1 pyramidal cells. *J Physiol* **492** ( Pt 1, 211 (1996).
231. Coombs, J. S., Curtis, D. R. & Eccles, J. C. The generation of impulses in motoneurons. *The Journal of physiology* **139**, 232 (1957).
232. Van Wart, A. & Matthews, G. Impaired firing and cell-specific compensation in neurons lacking nav1.6 sodium channels. *J Neurosci* **26**, 7172 (2006).

233. Pu, M., Berson, D. & Pan, T. Structure and function of retinal ganglion cells innervating the cat's geniculate wing: an in vitro study. *Journal of Neuroscience* **14**, 4338 (1994).
234. Hadjinicolaou, A. E., Savage, C. O., Apollo, N. V., Garrett, D. J., Cloherty, S. L., Ibbotson, M. R. & O'Brien, B. J. Optimizing the electrical stimulation of retinal ganglion cells. *IEEE Trans Neural Syst Rehabil Eng* **23**, 169 (2015).
235. Azouz, R., Jensen, M. S. & Yaari, Y. Ionic basis of spike afterdepolarization and burst generation in adult rat hippocampal CA1 pyramidal cells. *Journal of Physiology* **492**, 211 (1996).
236. Destexhe, A., Babloyantz, A. & Sejnowski, T. J. Ionic mechanisms for intrinsic slow oscillations in thalamic relay neurons. *Biophys J* **65**, 1538 (1993).
237. Araki, T. & Otani, T. Response of single motoneurons to direct stimulation in toad's spinal cord. *J Neurophysiol* **18**, 472 (1955).
238. Boiko, T., Rasband, M. N., Levinson, S. R., Caldwell, J. H., Mandel, G., Trimmer, J. S. & Matthews, G. Compact myelin dictates the differential targeting of two sodium channel isoforms in the same axon. *Neuron* **30**, 91 (2001).
239. Vacher, H. & Trimmer, J. S. Trafficking mechanisms underlying neuronal voltage-gated ion channel localization at the axon initial segment. *Epilepsia* **53**, 21 (2012).
240. Van Wart, A., Trimmer, J. S. & Matthews, G. Polarized distribution of ion channels within microdomains of the axon initial segment. *Journal of Comparative Neurology* **500**, 339 (2007).
241. Werginz, P., Fried, S. I. & Rattay, F. Influence of the sodium channel band on retinal ganglion cell excitation during electric stimulation—a modeling study. *Neuroscience* **266**, 162 (2014).
242. Almog, M. & Korngreen, A. Is realistic neuronal modeling realistic? *J Neurophysiol* **116**, 2180 (2016).
243. Chen, Y., Yu, F. H., Sharp, E. M., Beacham, D., Scheuer, T. & Catterall, W. A. Functional properties and differential neuromodulation of Nav1.6 channels. *Molecular and Cellular Neuroscience* **38**, 607 (2008).
244. Rudy, B. Slow inactivation of the sodium conductance in squid giant axons. Pronase resistance. *J Physiol* **283**, 1 (1978).



245. Jensen, R. J., Ziv, O. R. & Rizzo, J. F. Thresholds for activation of rabbit retinal ganglion cells with relatively large, extracellular micro-electrodes. *Investigative ophthalmology & visual science* **46**, 1486 (2005).
246. Reilly, J. P. & Diamant, A. M. *Electrostimulation: Theory, Applications, and Computational Model* 352 (Artech House, 2011).
247. Majdi, J. A., Minnikanti, S., Peixoto, N., Agrawal, A. & Cohen, E. D. Access resistance of stimulation electrodes as a function of electrode proximity to the retina. *J Neural Eng* **12**, 16006 (2015).
248. Feucht, M., Laube, T., Bornfeld, N., Walter, P., Velikay-Parel, M., Hornig, R. & Richard, G. Development of an epiretinal prosthesis for stimulation of the human retina. *Der Ophthalmologe: Zeitschrift der Deutschen Ophthalmologischen Gesellschaft* **102**, 688 (2005).
249. Humayun, M. S., Weiland, J. D., Fujii, G. Y., Greenberg, R., Williamson, R., Little, J., Mech, B., Cimmarusti, V., Van Boemel, G., Dagnelie, G. & De Juan, E. Visual perception in a blind subject with a chronic microelectronic retinal prosthesis. *Vision research* **43**, 2573 (2003).
250. Keserü, M., Feucht, M., Bornfeld, N., Laube, T., Walter, P., Rössler, G., Velikay-Parel, M., Hornig, R. & Richard, G. Acute electrical stimulation of the human retina with an epiretinal electrode array. *Acta Ophthalmologica* **90**, e1 (2012).
251. Grubb, M. S. & Burrone, J. Activity-dependent relocation of the axon initial segment fine-tunes neuronal excitability. *Nature* **465**, 1070 (2010).
252. Hu, W., Tian, C., Li, T., Yang, M., Hou, H. & Shu, Y. Distinct contributions of Na(v)1.6 and Na(v)1.2 in action potential initiation and backpropagation. *Nat Neurosci* **12**, 996 (2009).
253. Harkema, S., Gerasimenko, Y., Hodes, J., Burdick, J., Angeli, C., Chen, Y., Ferreira, C., Willhite, A., Rejc, E., Grossman, R. G. & Edgerton, V. R. Effect of epidural stimulation of the lumbosacral spinal cord on voluntary movement, standing, and assisted stepping after motor complete paraplegia: A case study. *The Lancet* **377**, 1938 (2011).
254. Fénelon, G., Goujon, C., Gurruchaga, J. M., Cesaro, P., Jarraya, B., Palfi, S. & Lefaucheur, J. P. *Spinal cord stimulation for chronic pain improved motor function in a patient with Parkinson's disease* 2012.
255. Hines, M. L. & Carnevale, N. T. *The NEURON Simulation Environment* 1997.

256. Gao, F. & Han, L. Implementing the Nelder-Mead simplex algorithm with adaptive parameters. *Computational Optimization and Applications* **51**, 259 (2012).
257. Virtanen, P., Gommers, R., Oliphant, T. E., Haberland, M., Reddy, T., Cournapeau, D., Burovski, E., Peterson, P., Weckesser, W., Bright, J., van der Walt, S. J., Brett, M., Wilson, J., Millman, K. J., Mayorov, N., Nelson, A. R. J., Jones, E., Kern, R., Larson, E., Carey, C., Polat, İ., Feng, Y., Moore, E. W., VanderPlas, J., Laxalde, D., Perktold, J., Cimrman, R., Henriksen, I., Quintero, E. A., Harris, C. R., Archibald, A. M., Ribeiro, A. H., Pedregosa, F., van Mulbregt, P. & Contributors, S. 1. o. SciPy 1.0—Fundamental Algorithms for Scientific Computing in Python (2019).
258. Iacono, M. I., Neufeld, E., Akinnagbe, E., Bower, K., Wolf, J., Oikonomidis, I. V., Sharma, D., Lloyd, B., Wilm, B. J., Wyss, M., Pruessmann, K. P., Jakab, A., Makris, N., Cohen, E. D., Kuster, N., Kainz, W. & Angelone, L. M. MIDA: A multimodal imaging-based detailed anatomical model of the human head and neck. *PLoS ONE* **10** (ed Jespersen, S. N.) e0124126 (2015).
259. Parent, A. Giovanni Aldini: from animal electricity to human brain stimulation. *Canadian journal of neurological sciences* **31**, 576 (2004).
260. McIntyre, C. C., Mori, S., Sherman, D. D. L., Thakor, N. V. N. & Vitek, J. L. J. Electric field and stimulating influence generated by deep brain stimulation of the subthalamic nucleus. *Clinical Neurophysiology* **115**, 589 (2004).
261. Min, X., Rosenberg, S. & Fayram, T. *Modeling of Spinal Cord Stimulation for the PENTA Paddle Lead with Various Stimulation Configurations* in (Las Vegas, Nevada, USA, 2013).
262. Moffitt, M. A., Lee, D. C. & Bradley, K. in, 155 (2009).
263. Lee, D., Hershey, B., Bradley, K. & Yearwood, T. Predicted effects of pulse width programming in spinal cord stimulation: A mathematical modeling study. *Medical and Biological Engineering and Computing* **49**, 765 (2011).
264. Hameroff, S., Trakas, M., Duffield, C., Annabi, E., Gerace, M. B., Boyle, P., Lucas, A., Amos, Q., Buadu, A. & Badal, J. J. Transcranial ultrasound (TUS) effects on mental states: A pilot study. *Brain Stimulation* **6**, 409 (2013).

265. McDannold, N., Clement, G., Black, P., Jolesz, F. & Hynynen, K. Transcranial magnetic resonance imaging-guided focused ultrasound surgery of brain tumors: Initial findings in 3 patients. *Neurosurgery* **66**, 323 (2010).
266. McDannold, N., Vykhodtseva, N., Raymond, S., Jolesz, F. A. & Hynynen, K. MRI-guided targeted blood-brain barrier disruption with focused ultrasound: Histological findings in rabbits. *Ultrasound in Medicine and Biology* **31**, 1527 (2005).
267. Fry, W., Barnard, J., Fry, F., Krumins, R. & Brennan, J. Ultrasonic lesions in the mammalian central nervous system. *Science* **122**, 517 (1955).
268. Fry, F. J. Transkull transmission of an intense focused ultrasonic beam. *Ultrasound in Medicine and Biology* **3** (1977).
269. Lee, W., Lee, S. S. D., Park, M. Y. M., Foley, L., Purcell-Estabrook, E., Kim, H., Fischer, K., Maeng, L. S. L.-S. & Yoo, S. S. S.-S. Image-Guided Focused Ultrasound-Mediated Regional Brain Stimulation in Sheep. *Ultrasound in Medicine and Biology* **42**, 459 (2016).
270. Daniels, D., Sharabi, S., Last, D., Guez, D., Salomon, S., Zivli, Z., Castel, D., Volovick, A., Grinfeld, J., Rachmilevich, I., Amar, T., Liraz-Zaltsman, S., Sargsyan, N., Mardor, Y. & Harnof, S. Focused Ultrasound-Induced Suppression of Auditory Evoked Potentials in Vivo. *Ultrasound in Medicine and Biology* **44**, 1022 (2018).
271. Lee, W., Kim, H., Jung, Y., Song, I.-U., Chung, Y. A. & Yoo, S.-S. Image-guided transcranial focused ultrasound stimulates human primary somatosensory cortex. *Scientific reports* **5**, 8743 (2015).
272. Lee, W., Kim, H. C., Jung, Y., Chung, Y. A., Song, I. U., Lee, J. H. & Yoo, S. S. Transcranial focused ultrasound stimulation of human primary visual cortex. *Scientific Reports* **6** (2016).
273. Fry, F. J. & Barger, J. E. Acoustical properties of the human skull. *The Journal of the Acoustical Society of America* **63**, 1576 (1978).
274. White, D. N., Curry, G. R. & Stevenson, R. J. The acoustic characteristics of the skull. *Ultrasound in Medicine and Biology* **4**, 225 (1978).
275. Evans, J. A. A. & Tavakoli, M. B. B. *Ultrasonic attenuation and velocity in bone Related content Ultrasonic attenuation and velocity in bone* tech. rep. 10 (1990), 1387.

276. Connor, C. W., Clement, G. T. & Hynynen, K. A unified model for the speed of sound in cranial bone based on genetic algorithm optimization. *Physics in Medicine and Biology* **47**, 3925 (2002).
277. Hagisonic. *Characterization of Ultrasonic Probe* tech. rep. (Hagisonic, 2016).
278. Teja, J. L., Lopez-Haro, S. A., Leija, L. & Vera, A. A finite element simulation of High Intensity Focused Ultrasound with polyacrylamide as coupling material for acoustic hemostasis. *Pan American Health Care Exchanges, PAHCE*, **1** (2013).
279. Mueller, J. K., Ai, L., Bansal, P. & Legon, W. Computational exploration of wave propagation and heating from transcranial focused ultrasound for neuromodulation. *Journal of Neural Engineering* **13**, **1** (2016).
280. Pelekanos, M., Leinenga, G., Odabae, M. M., Odabae, M. M., Saifzadeh, S., Steck, R. & Götz, J. Establishing sheep as an experimental species to validate ultrasound-mediated blood-brain barrier opening for potential therapeutic interventions. *Theranostics* **8**, 2583 (2018).
281. Martin, E., Ling, Y. T. & Treeby, B. E. Simulating Focused Ultrasound Transducers Using Discrete Sources on Regular Cartesian Grids. *IEEE Transactions on Ultrasonics, Ferroelectrics, and Frequency Control* **63**, 1535 (2016).
282. Selfridge, A. R. Isotropic Materials. *Ieee Transactions on Sonics and Ultrasonics* **32**, 381 (1985).
283. Neufeld, E., Kyriacou, A., Kainz, W. & Kuster, N. Approach to Validate Simulation-Based Distribution Predictions Combining the Gamma-Method and Uncertainty Assessment: Application to Focused Ultrasound. *Journal of Verification, Validation and Uncertainty Quantification* **1**, 31006 (2016).
284. Renaud, G., Callé, S., Remenieras, J. P. & Defontaine, M. Exploration of trabecular bone nonlinear elasticity using time-of-flight modulation. *IEEE Transactions on Ultrasonics, Ferroelectrics, and Frequency Control* **55**, 1497 (2008).
285. Mueller, J. K., Ai, L., Bansal, P. & Legon, W. Numerical evaluation of the skull for human neuromodulation with transcranial focused ultrasound. *Journal of Neural Engineering* **14** (2017).

286. Tanter, M., Fink, M., Marsac, L., Aubry, J.-F. F., Pernot, M., Montaldo, G., Marquet, F., Pernot, M., Aubry, J.-F. F., Montaldo, G., Marsac, L., Tanter, M. & Fink, M. Non-invasive transcranial ultrasound therapy based on a 3D CT scan: protocol validation and in vitro results. *Physics in Medicine and Biology* **54**, 2597 (2009).
287. Hatakeyama, R., Yoshizawa, M. & Moriya, T. Method for the measurement of acoustic impedance and speed of sound in a small region of bone using a fused quartz rod as a transmission line. *Japanese Journal of Applied Physics, Part 1: Regular Papers and Short Notes and Review Papers* **39**, 6449 (2000).
288. Montanaro, H., Pasquinelli, C., Lee, H. J., Hanson, L. G., Kuster, N., Siebner, H. R., Thielscher, A. & Neufeld, E. The effects of CT image parameters and noise on the accuracy of simulations of transcranial focused ultrasound. *submitted* (2020).
289. Postema, M. *Fundamentals of Medical Ultrasonics* 248 (Spon Press, 2018).
290. Low, D. A. *Gamma dose distribution evaluation tool in Journal of Physics: Conference Series* **250** (IOP Publishing, 2010), 349.
291. King, R. L., Brown, J. R., Newsome, W. T. & Pauly, K. B. Effective parameters for ultrasound-induced in vivo neurostimulation. *Ultrasound in Medicine and Biology* **39**, 312 (2013).
292. Shewell, J. R. & Wolf, E. Inverse Diffraction and a New Reciprocity Theorem\*. *Journal of the Optical Society of America* **58**, 1596 (1968).
293. Schafer, M. E. & Lewin, P. A. Transducer Characterization Using The Angular Spectrum Method. *Journal of the Acoustical Society of America* **85**, 2202 (1989).
294. Farcito, S., Puonti, O., Montanaro, H., Saturnino, G. B., Nielsen, J. D., Madsen, C. G., Siebner, H. R., Neufeld, E., Kuster, N., Lloyd, B. A. & Thielscher, A. *Accurate anatomical head segmentations: a data set for biomedical simulations* in (Institute of Electrical and Electronics Engineers (IEEE), 2019), 6118.
295. Maimbourg, G., Houdouin, A., Deffieux, T., Tanter, M. & Aubry, J. F. 3D-printed adaptive acoustic lens as a disruptive technology for transcranial ultrasound therapy using single-element transducers. *Physics in Medicine and Biology* **63**, 25026 (2018).

296. Ferri, M., Bravo, J. M., Redondo, J. & Sánchez-Pérez, J. V. Enhanced Numerical Method for the Design of 3-D-Printed Holographic Acoustic Lenses for Aberration Correction of Single-Element Transcranial Focused Ultrasound. *Ultrasound in Medicine and Biology* **45**, 867 (2019).
297. Cobbold, R. S. *Foundations of biomedical ultrasound*. (Oxford university press, 2006).
298. Ismail, N., Kores, C. C., Geskus, D. & Pollnau, M. Fabry-Pérot resonator: spectral line shapes, generic and related Airy distributions, linewidths, finesses, and performance at low or frequency-dependent reflectivity. *Optics express* **24**, 16366 (2016).
299. White, P. J., Clement, G. T., Hynynen, K. & Clement, G. T. *Longitudinal and shear mode ultrasound propagation in human skull bone in AIP Conference Proceedings* **829** (2006), 251.
300. Treeby, B., Lucka, F., Martin, E. & Cox, B. T. Equivalent-Source Acoustic Holography for Projecting Measured Ultrasound Fields Through Complex Media. *IEEE Transactions on Ultrasonics, Ferroelectrics, and Frequency Control* **65**, 1857 (2018).
301. Deffieux, T. & Konofagou, E. Numerical study of a simple transcranial focused ultrasound system applied to blood-brain barrier opening. *IEEE Transactions on Ultrasonics, Ferroelectrics, and Frequency Control* **57**, 2637 (2010).
302. Samoudi, M. A., Van Renterghem, T. & Botteldooren, D. Computational modeling of a single-element transcranial focused ultrasound transducer for subthalamic nucleus stimulation. *Journal of neural engineering* **16**, 26015 (2019).
303. Ye, P. P., Brown, J. R. & Pauly, K. B. Frequency dependence of ultrasound neurostimulation in the mouse brain. *Ultrasound in Medicine and Biology* **42**, 1512 (2016).
304. Tang, S. C. & Clement, G. T. Standing-wave suppression for transcranial ultrasound by random modulation. *IEEE Transactions on Biomedical Engineering* **57**, 203 (2010).
305. Phillips, R. ( & Harris, G. ( Information for Manufacturers Seeking Marketing Clearance of Diagnostic Ultrasound Systems and Transducers. *FDA Guidance*, 1 (2008).
306. Voie, A., Dirnbacher, M., Fisher, D. & Hölscher, T. Parametric mapping and quantitative analysis of the human calvarium. *Computerized Medical Imaging and Graphics* **38**, 675 (2014).

307. Pasquinelli, C., Montanaro, H., Lee, H. J., Hanson, L., Kim, H., Kuster, N., Siebner, H. R., Neufeld, E. & Thielscher, A. Transducer modeling for accurate acoustic simulations of transcranial focused ultrasound stimulation. *Journal of Neural Engineering* **17**, 46010 (2020).
308. Buzug, T. M. & Mihailidis, D. Computed tomography from photon statistics to modern cone-beam CT. *Medical Physics* **36**, 3858 (2009).
309. Morneburg, H. *Diagnostic Imaging Systems: Diagnostics and Angiography, Computed Tomography, Nuclear Medicine, Magnetic Resonance Imaging, Sonography, Integrated Information Systems* (Publicis MCD-Publisher, 1995).
310. White, P. J., Clement, G. T. & Hynynen, K. Transcranial longitudinal and shear sound speeds in animal models. *The Journal of the Acoustical Society of America* **119**, 3319 (2013).
311. Yoon, K., Lee, W., Croce, P., Cammalleri, A. & Yoo, S. S. Multi-resolution simulation of focused ultrasound propagation through ovine skull from a single-element transducer. *Physics in Medicine and Biology* **63**, 1 (2018).
312. Robertson, J., Urban, J., Stitzel, J. & Treeby, B. E. The effects of image homogenisation on simulated transcranial ultrasound propagation. *Physics in Medicine and Biology* **63** (2018).
313. Top, C. B., White, P. J. & McDannold, N. J. Nonthermal ablation of deep brain targets: A simulation study on a large animal model. *Medical Physics* **43**, 870 (2016).
314. Webb, T. D., Leung, S. A., Rosenberg, J., Ghanouni, P., Dahl, J. J., Pelc, N. J. & Pauly, K. B. Measurements of the Relationship between CT Hounsfield Units and Acoustic Velocity and How It Changes with Photon Energy and Reconstruction Method. *IEEE Transactions on Ultrasonics, Ferroelectrics, and Frequency Control* **65**, 1111 (2018).
315. Schönfeldt-Lecuona, C., Thielscher, A., Freudenmann, R. W., Kron, M., Spitzer, M. & Herwig, U. Accuracy of stereotaxic positioning of transcranial magnetic stimulation. *Brain Topography* **17**, 253 (2005).
316. Goss, S. A., Johnston, R. L. & Dunn, F. Comprehensive compilation of empirical ultrasonic properties of mammalian tissues. *Journal of the Acoustical Society of America* **64**, 423 (1978).
317. Kim, H., Park, M. Y., Lee, S. D., Lee, W., Chiu, A. & Yoo, S. S. Suppression of EEG visual-evoked potentials in rats through neuromodulatory focused ultrasound. *NeuroReport* **26**, 211 (2015).

318. Mueller, J., Legon, W., Opitz, A., Sato, T. & Tyler, W. Transcranial focused ultrasound modulates intrinsic and evoked EEG dynamics. *Brain Stimulation* **7**, 900 (2014).
319. Jansen, B. H. & Rit, V. G. Electroencephalogram and visual evoked potential generation in a mathematical model of coupled cortical columns. *Biological Cybernetics* **73**, 357 (1995).
320. Plaksin, M., Kimmel, E. & Shoham, S. Cell-type-selective effects of intramembrane cavitation as a unifying theoretical framework for ultrasonic neuromodulation. *eNeuro* **3**, 229 (2016).
321. Kim, H., Taghados, S. S. J., Fischer, K., Maeng, L. S. L.-S., Park, S. & Yoo, S. S. S.-S. Noninvasive Transcranial Stimulation of Rat Abducens Nerve by Focused Ultrasound. *Ultrasound in Medicine and Biology* **38**, 1568 (2012).
322. Tufail, Y., Yoshihiro, A., Pati, S., Li, M. M. & Tyler, W. J. W. Ultrasonic neuromodulation by brain stimulation with transcranial ultrasound. *Nature Protocols* **6**, 1453 (2011).
323. Pospischil, M., Toledo-Rodriguez, M., Monier, C., Piwkowska, Z., Bal, T., Frégnac, Y., Markram, H. & Destexhe, A. Minimal Hodgkin-Huxley type models for different classes of cortical and thalamic neurons. *Biological Cybernetics* **99**, 427 (2008).
324. Sanzleon, P., Knock, S. A., Woodman, M. M., Domide, L., Mersmann, J., Mcintosh, A. R. & Jirsa, V. The virtual brain: A simulator of primate brain network dynamics. *Frontiers in Neuroinformatics* **7** (2013).
325. Proix, T., Spiegler, A., Schirner, M., Rothmeier, S., Ritter, P. & Jirsa, V. K. How do parcellation size and short-range connectivity affect dynamics in large-scale brain network models? *NeuroImage* **142**, 135 (2016).
326. Plonsey, R. Reciprocity Applied to Volume Conductors and the ECG. *IEEE Transactions on Bio-medical Electronics* **10**, 9 (1963).



# CURRICULUM VITAE

---

## PERSONAL DATA

Name Hazael Fabrizio Montanaro Ochoa  
Date of Birth November 6, 1987  
Place of Birth Asunción, Paraguay  
Citizen of Paraguay

## EDUCATION

2015 – 2020 ETH Zurich and IT'IS Foundation  
Zurich, Switzerland  
*PhD* Information Tech. and Electrical Engineering

2011 – 2014 ETH Zurich and University of Zurich  
Zurich, Switzerland  
*MSc* Neural Systems and Computation

2006 – 2011 Yale University  
New Haven, CT, USA  
*BSc* Electrical Engineering (ABET certification)

1992– 2006 American School of Asunción  
Asunción, Paraguay

## EMPLOYMENT

2011– 2014 Researcher, Neuromorphic Sensors Group  
*Institute of Neuroinformatics, University of Zurich*  
Zurich, Switzerland

2008– 2011 Researcher, e-Lab  
*Department of Electrical Engineering, Yale University*  
New Haven, CT, USA



## PUBLICATIONS

---

### Articles in peer-reviewed journals:

1. Montanaro, H., Pasquinelli, C., Lee, H. J., Hanson, L. G., Kuster, N., Siebner, H. R., Thielscher, A. & Neufeld, E. The effects of CT image parameters and noise on the accuracy of simulations of transcranial focused ultrasound. *Journal of Neural Engineering* (submitted) (2020).
2. Pasquinelli, C., Montanaro, H., Lee, H. J., Hanson, L., Kim, H., Kuster, N., Siebner, H. R., Neufeld, E. & Thielscher, A. Transducer modeling for accurate acoustic simulations of transcranial focused ultrasound stimulation. *Journal of Neural Engineering* **17**, 46010 (2020).
3. Neufeld, E., Cassarà, A. M., Montanaro, H., Kuster, N. & Kainz, W. Functionalized anatomical models for EM-neuron Interaction modeling. *Physics in Medicine and Biology* **61**, 4390 (2016).

### Conference contributions:

4. Farcito, S., Puonti, O., Montanaro, H., Saturnino, G. B., Nielsen, J. D., Madsen, C. G., Siebner, H. R., Neufeld, E., Kuster, N., Lloyd, B. A. & Thielscher, A. *Accurate anatomical head segmentations: A data set for biomedical simulations* in *41st Annual International Conference of the IEEE Engineering in Medicine and Biology Society (EMBC)* (2019).
5. Rowald, A., Neufeld, E., Paoles, E., Mandija, S., Montanaro, H., Alaia, A., Cassarà, A., Lloyd, B., Froeling, M., Bakker, J., Minassian, K., Wagner, F., Delattre, V., van der Berg, N., Kuster, N., Bloch, J., Courtine, G. & Capogrosso, M. *Computational models steering the personalization of targeted spinal cord stimulation to restore motor function in humans with spinal cord injury* in *Society for Neuroscience (SfN) Meeting* (2018).
6. Pasquinelli, C., Montanaro, H., Neufeld, E., Poni, R., Kuster, N. & Thielscher, A. *Pitfalls in acoustic transducer modeling for focused ultrasound (FUS)* in *32nd Annual Meeting of the European Society for Hyperthermic Oncology (ESHO)* (2018).
7. Montanaro, H., Neufeld, E., Kuster, N., Pasquinelli, C., Hanson, L. & Thielscher, A. *Investigation of fallacies in focused ultrasound transducer acoustic modeling* in *18th International Symposium for Therapeutic Ultrasound (ISTU)* (2018).

## BIBLIOGRAPHY

8. Montanaro, H., Ozdas, M. S., Neufeld, E., Lemaire, T., Micera, S., Fatih, Y. & Kuster, N. *Towards Multiscale Modeling of Transcranial Focused Ultrasound Neurostimulation in 20th Swiss Society for Neuroscience Meeting* (2018).
9. Pasquinelli, C., Montanaro, H., Neufeld, E., Lee, H. J. & Thielscher, A. *Impact of the skull model on simulated TFUS beam profiles in 40th International Conference of the IEEE Engineering in Medicine and Biology Society (EMBC)* (2018).
10. Montanaro, H., Ozdas, M. S., Neufeld, E., Lemaire, T., Micera, S., Yanik, M. F. & Kuster, N. *Multiscale Modeling of transcranial focused ultrasoundneurostimulation and experimental validation: initial results in 17th International Society for Therapeutic Ultrasound Symposium (ISTU)* (2017).
11. Cohen, E., Montanaro, H., Neufeld, E., Angelone, L. M., Kuster, N. & Kainz, W. *Development and Validation of Alpha Retinal Ganglion Cell Model for Epiretinal Electrode Stimulation and Simulation Platform for Coupled EM-Neuron Dynamics Modeling in 8th International IEEE EMBS Neural Engineering Conference (NER)* (2017).
12. Cassarà, A. M., Neufeld, E., Montanaro, H. & Kuster, N. *Mechanism Investigation, Device Development, and Treatment Personalization Using Anatomical Models Functionalized with Electrophysiological Neuron Models in 2017 XXXIInd General Assembly and Scientific Symposium of the International Union of Radio Science (URSI GASS)* (2017).
13. Teixeira, F., Neufeld, E., Montanaro, H., Morel, S., Kwak, B., Schilling, S., Hirsch, S. & Kuster, N. *Multiscale, Personalized Modeling of Blood-Flow-Related Vessel-Wall Evolution in 3rd International SystemsX.ch Conference on Systems Biology* (2017).
14. Cassarà, A. M., Neufeld, E., Montanaro, H., Kainz, W. & Kuster, N. *Insights Gained from Electrophysiologically Functionalized Anatomical Models: Exposure Safety and Targetted Therapeutic Stimulation in 6th International Workshop on Computational Human Phantoms (CP)* (2017).
15. Cassarà, A. M., Neufeld, E., Montanaro, H. & Kuster, N. *Neuro-functionalized Anatomical Human Models for Neuromodulation Related Mechanism and Safety Investigations, Device Development, Personalized Treatment Planning, and in silico Trials in 47th Annual Meeting of the Society for Neuroscience (Neuroscience)* (2017).

16. Montanaro, H., Neufeld, E., Cassarà, A. M., Guidon, M. & Kuster, N. *Optimization of Targeted Neurostimulation Based on Activating Functions and Validation by Coupled Electromagnetic-Neuronal Dynamics Modelling in The Joint Meeting of the Bioelectromagnetics Society (BEMS) and the European BioElectromagnetics Association (EBEA) (2017).*
17. Cassara, A. M., Neufeld, E., Montanaro, H. & Kuster, N. *Vagus Nerve Stimulation: Comparison of Thresholds for A-, B-and C-Fiber Recruitment for Cuff Electrodes and Alternative Stimulation Configurations in Functionalized Generic and Anatomical Models in The Joint Meeting of the Bioelectromagnetics Society (BEMS) and the European BioElectromagnetics Association (EBEA) (2017).*
18. Neufeld, E., Cassarà, A. M., Kainz, W., Montanaro, H. & Kuster, N. *Neuro-Functionalized Anatomical Models for Mechanism Investigation, Device Development, and Treatment Personalization in 3rd Annual BMES/FDA Frontiers in Medical Devices Conference (2017).*
19. Montanaro, H., Neufeld, E., Capstick, M. & Kuster, N. *Treatment Planning for Magnetic Nanoparticle-Based Hyperthermia in 12th International Congress of Hyperthermic Oncology (ICHO) (2016).*
20. Montanaro, H., Neufeld, E., Capstick, M. & Kuster, N. *Image-Based Modeling of Superparamagnetic Iron-Oxide Nanoparticle Hyperthermia Therapy in Joint Meeting of the Bioelectromagnetics Society and the European BioElectromagnetics Association (BioEM) (2016).*
21. Neufeld, E., Cassarà, A. M., Montanaro, H., Kainz, W. & Kuster, N. *Investigation of Electric and Magnetic Stimulation Time Constants Through Neuronal Dynamics Functionalized Anatomical Models in Joint Meeting of the Bioelectromagnetics Society and the European BioElectromagnetics Association (BioEM) (2016).*
22. Cohen, E., Montanaro, H., Neufeld, E., Iacono, M., Leonardo, A. & Kainz, W. *Development of an alpha retinal ganglion cell model for epiretinal electrode stimulation in ARVO Imaging in the Eye Conference (ARVO) (2016).*
23. Kyriakou, A., Neufeld, E., Lloyd, B., Montanaro, H., Lloyd, B. & Kuster, N. *Automatized and Environment-Adaptive Optimization of Target Locations for Point-by-Point and Volumetric Ablation of Large Tumors in 15th International Society for Therapeutic Ultrasound Symposium (ISTU) (2015).*